Katholieke Universiteit Leuven
Faculteit Wetenschappen
Departement Natuurkunde en Sterrenkunde
Laboratorium voor Halfgeleiderfysica

Electron spin resonance probing of point defects in functional oxides and Si/high-κ structures

Katrijn Clémer

Promotor:
Prof. Dr. A. Stesmans

Proefschrift ingediend tot
het behalen van de graad van
Doctor in de Wetenschappen

2007

Proefschrift voorgedragen tot het behalen van het doctoraat
in de Wetenschappen door
Katrijn Clémer

En daarvoor publiekelijk verdedigd
op 25 oktober 2007 om 17 u in auditorium 05.11,
Celestijnenlaan 200 D
3001 Heverlee
België

De examencommissie is samengesteld uit:

Promotor
Prof. Dr. A. Stesmans

Leden
Prof. Dr. G. Adriaenssens
Prof. Dr. V.V. Afanas'ev
Prof. Dr. M. Van der Auweraer
Prof. Dr. C. Glorieux
Dr. M. Houssa

Acknowledgments

Dank aan allen die mede verantwoordelijk gesteld kunnen worden voor het tot stand komen en volbrengen van deze thesis.

Voor de talrijke wetenschappelijke discussies en begeleiding dank ik de promotor van dit werk Prof. Dr. A. Stesmans, Prof. Dr. V. V. Afanas'ev, Pieter en alle andere leden van de afdeling Halfgeleiderfysica.

Voor het kritisch lezen en becommentariseren van dit werk dank ik de leden van de jury: Prof. Dr. A. Stesmans, Prof. Dr. V. V. Afanas'ev, Prof. Dr. G. Adriaenssens, Prof. Dr. M. Van der Auweraer, Prof. Dr. C. Glorieux, en Dr. M. Houssa.

Voor de persoonlijke ondersteuning in goede en in moeilijke tijden dank ik, Pieter, Sheron, Koen, Maria, mijn familie, en in het bijzonder Marc.

Follow the yellow brick road...

–L. F. Baum–

Contents

List of abbreviations

ALCVD	atomic layer chemical vapor deposition
BET	Brunauer-Emmet-Teller
$BHODC$	bridged hole-trapping oxygen deficiency center
BPSG	borophosphosilicate
CVD	chemical vapor deposition
cw	continuous wave
DFT	density functional theory
EOT	equivalent oxide thickness
ESR	electron spin resonance
FESEM	field emission scanning electron microscopy
FTIR	fourier transform infrared absorption
FWHM	full width at half amplitude
hf	hyperfine
HRTEM	high-resolution transmission electron microscopy
IC	integrated circuit
ITRS	international technology roadmap for semiconductors
LCAO	linear combination of atomic orbitals
MBD	molecular beam deposition
MD	molecular dynamics
MEIS	medium-energy ion scattering
MOCVD	metallo-organic chemical vapor deposition
MOS	metal-oxide-semiconductor
MOSFET	metal-oxide-semiconductor field-effect transistor
$NBOHC$	non-bridging oxygen hole center
NCVD	ALCVD using the nitro precursor $Hf(NO_3)_4$
NMR	nuclear magnetic resonance
OHC	oxygen-related hole center
PDA	post-deposition annealing
PL	photoluminescence
$POHC$	phosphorus oxygen hole center
POR	peroxy-radical
PSG	phosphosilicate
RTA	rapid thermal annealing
SIMS	secondary ion mass spectroscopy
VUV	vacuum ultra violet
XPS	x-ray photoelectron spectroscopy

List of symbols

α^2	s character of the orbital composition of the unpaired electron
α_{SiO_2}	thermal expansion coefficient of quartz
β^2	p character of the orbital composition of the unpaired electron
$\Delta\gamma$	g matrix anisotropy
η^2	localization of the electron wave function on an atom
θ	O–Si–defect bond angle
κ	dielectric constant
κ_{ls}	line shape factor
$\vec{\mu}$	magnetic moment
μ_B	Bohr magneton
$\vec{\mu_e}$	intrinsic angular momentum
$\vec{\mu_L}$	orbital angular momentum
ν	microwave frequency
τ_c	correlation time
χ	magnetic susceptibility

$\hat{A}$	hyperfine tensor
$A_\parallel$, $A_\perp$	parallel and perpendicular components of an axial $\hat{A}$
A_{iso}, b, c	isotropic, anisotropic, and orthorhombic part of $\hat{A}$
A_s, A_p	atomic hyperfine coupling constants
A_{pp}	peak-to-peak hight
$\vec{B}$	magnetic field induction
B_m	modulation amplitude
ΔB_{pp}	peak-to-peak line width
d_{ox}	grown oxide thickness
g, $\hat{g}$	spectroscopic splitting factor/matrix
$g_\parallel$, $g_\perp$	parallel and perpendicular components of an axial $\hat{g}$
g_0	free electron g factor
g_c	zero crossing g value, central g value
g_{av}	average g value
h	Planck's constant
$\mathcal{H}_S$	spin Hamiltonian
$\mathcal{H}_{ez}$	electronic Zeeman Hamiltonian
$\mathcal{H}_D$	spin-spin Hamiltonian
$\mathcal{H}_{hf}$	hyperfine Hamiltonian

$\mathcal{H}_{\mathrm{nz}}$	nuclear Zeeman Hamiltonian
$\mathcal{I}$	signal intensity
$\vec{J}$	total angular momentum
$\vec{L}$	orbital angular momentum
M_I	nuclear spin quantum number
M_J	magnetic quantum number
N^S	number of spins
P_μ	incident microwave power
$\vec{S}$	electron spin angular momentum
T	measurement temperature
T_{an}	(observation) temperature
T_C	Curie temperature

Samenvatting

Tegenwoordig verwachten we dat onze gadgets gebaseerd op halfgeleidertechnologie steeds kleiner, sneller, multifunctioneler, en –als het even kan– ook nog goedkoper worden. Gedurende jaren is de industrie er in geslaagd om tegemoet te komen aan deze eisen door onder andere miniatuur GSMs, MP3-spelers, foto- en videocamera's, en labtops op de markt brengen. Het woord 'nano' is zelfs boven zijn wetenschappelijke betekenis (eenheid prefix) uitgestegen en werd het toverwoord in de reclame wereld om alles, van elektronica tot waspoeder, aan de man te brengen.

De elementaire eenheid die decennia lang aan de basis lag van alle geavanceerde toepassingen was de Si/SiO_2-structuur. Het succes van de halfgeleiderindustrie was tot nu toe gebaseerd op de schaalbaarheid van de Si/SiO_2-gebaseerde micro-elektronica: Krachtigere chips konden bekomen worden door de afmetingen van de metaal-oxide-halfgeleider (MOS) componenten steeds kleiner te maken. Op dit moment is het punt echter bereikt waar verdere 'schaling' van de Si/SiO_2-gebaseerde componenten onmogelijk wordt vermits dit zou leiden tot zware problemen met de performantie en betrouwbaarheid van de MOS componenten. De nieuwe generatie transistoren zal alternatieve 'nieuwe' isolerende poort materialen nodig hebben. Een voor de hand liggende oplossing is het gebruik van een isolator met een hogere dilektrische constante (κ) waardoor een fysisch dikkere oxide laag kan gebruikt worden zonder dat de capaciteit van de poort hierbij moet inboeten.

Het gebruik van zulk een alternatief poort oxide in de plaats van het uitgebreid bestudeerde SiO_2 oxide brengt natuurlijk onverwachte problemen met zich mee zoals de vorming van een tussenlaag en diffusie van additieven. Er zijn al talrijke studies die handelen over verschillende van deze kandidaat hoge-κ materialen maar uiteindelijk blijven we achter met meer vragen dan antwoorden. In een poging om enkele van deze vragen te beantwoorden werden in deze thesis drie van deze hoge-κ materialen bestudeerd: ZrO_2, HfO_2, en $LaAlO_3$.

Een ander gevolg van de huidige nano-rage is de stijgende populariteit van, o.a., nano-deeltjes, nano-draden, en nano-buisjes. Wanneer men oxides schaalt tot deze kleine dimensies ($\sim 10^{-8}$-10^{-9} m) veranderen echter hun elektrische en optische eigenschappen, waardoor onderzoekers weer van voor af aan kunnen beginnen met het bepalen van de materiaaleigenschappen.

Verwikkeld in een strijd om oplossingen te vinden voor al deze nieuwe problemen die zich aandienen is zowel het toegepaste als het fundamentele onderzoek naar nano-structuren de laatste jaren exponentieel gegroeid. Hierbij werd de toenemende impact van de aanwezigheid van defecten blootgelegd, zowel in de kern van de nano-materialen als aan de halfgeleider/oxide grenslaag in MOS structuren. De aanwezigheid van n enkel puntdefect kan een bepalend vaak negatief effect hebben op de optische en elektrische eigenschappen zoals fotoluminescentie, geleiding, en dopering van nano-deeltjes. Om een beter begrip te krijgen van de negatieve invloeden die deze puntdefecten kunnen hebben is het van cruciaal belang dat we kennis kunnen verwerven aangaande de fysische structuur van die defecten. Elektron spin resonantie (ESR) is hiervoor de uitgelezen techniek. Voorwaarden zijn dat de defecten een magnetisch moment ("spin") hebben en in voldoende aantallen aanwezig zijn in het te onderzoeken systeem (typisch 10^{10}-10^{12} magnetisch centra). In deze thesis zal ESR dan ook aangewend worden om optredende puntdefecten te monitoren, karakteriseren, en identificeren in een aantal materialen die mogelijk gebruikt kunnen worden in toekomstige halgeleider nano-technologien.

In een eerste fase werden pyrolytisch gevormde SiO_2 nano-deeltjes bestudeerd, met de bedoeling om via de analyse van de ESR-eigenschappen van ingebedde intrinsieke puntdefecten, informatie te verkrijgen op rele atomaire schaal van de invloed van de sterke dimensionele reductie. Ter verhoging van de detectiviteit en resolutie werd het ESR-onderzoek uitgevoerd in combinatie met verschillende types van bestraling, zoals UV, VUV, ^{60}Co-gamma straling. Voor het eerst werden in de nano-deeltjes verschillende puntdefecten gedetecteerd zoals E', het zuurstof peroxy-radicaal, het methyl radicaal, en een ongekend signaal met axiale symmetrie ($g_\parallel$=2.0041, $g_\perp$=2.0027). Een grondige studie van de ESR-parameters van deze defecten in functie van onder andere de bestraling en de postdepositie warmtebehandeling leverde een bijkomend inzicht in de specifieke structuur van de nano-deeltjes op atomair niveau. Er werd experimenteel bewijs geleverd dat er in deze nano-deeltjes twee verschillende systemen E' centers aanwezig zijn. De specifieke ESR parameters (bvb. g matrix) van de E' centers van een eerste bad werden zeer gelijkend gevonden aan deze van het goed gekende

E'_γ center in bulk fused SiO_2. De E' centers behorende tot het tweede bad geven blijk van een verschillende nuldoorgang g waarde en lijnvorm. Deze verschillen werden toegeschreven aan variaties in de locale structuur. Dit laatste E' systeem lijkt zich te bevinden in de buitenste SiO_2 lagen van de nano-deeltjes structureel verschillend van bulk SiO_2. Verder kon uit een gedetailleerde studie van de hyperfijn splitsing van de E' centers in de kern van de nano-deeltjes worden afgeleid dat deze kern dichter is. Deze verdichting is waarschijnlijk geassocieerd met de aanwezigheid van meer kleinere ringen in het SiO_2 netwerk.

Een volgend hoofdstuk handelt over de observatie van P-gerelateerde puntdefecten in nm-dikke P-gemplanteerde HfO_2 lagen op (100)Si onderworpen aan een postfabricatie thermische behandeling (verhitting in N_2-gas voor temperaturen tussen 500 en 900 $°C$) en in ZrO_2 poeder. De hoofd g matrices en hyperfijn tensoren van de geobserveerde defecten werden bekomen door de X, K, en Q-band spectra consistent te simuleren. De bekomen resultaten werden vergeleken met de goed gekende P-geassocieerde defecten in silica. Na deze analyse werden beide geobserveerde defecten toegewezen aan een P_2-type defect –een P atoom dat een Hf of Zr atoom vervangt. Beide defecten werden geobserveerd in de monokliene fase van de hoge-κ oxiden met het ongepaarde elektron sterk gelokaliseerd op het P atoom. Een beduidende fractie van de gencorporeerde P onzuiverheden resulteerde in een ESR actief P_2 defect. Vermits er een versterkte diffusie van additieven (P) werd vastgesteld in HfO_2 lagen is de identificatie van resulterende P-geassocieerde defecten van cruciaal belang. Deze defecten kunnen immers optreden als schadelijke ladingsvallen.

De atomaire natuur van de (100)Si/$LaAlO_3$ grenslaag is het onderwerp van hoofdstuk vier. De nm-dunne amorfe $LaAlO_3$ lagen hebben een hoge diëlectrische constante ($\kappa\sim$20-27). In de oorspronkelijke samples wezen de K-band ESR metingen op de afwezigheid van een Si/SiO_2 type grenslaag vermits de archetypische Si/SiO_2 grenslaag defecten (P_{b1}, P_{b0}) niet werden geobserveerd. De situatie blijft onveranderd na verdere warmtebehandelingen to 800 $°C$. De Si/$LaAlO_3$ grenslaag blijkt thermisch stabiel en abrupt in tegenstelling tot andere Si/hoge-κ structuren. Na warmtebehandelingen in het temperatuursgebied 800-860 $°C$ begint zich echter een Si/SiO_2-type grenslaag te vormen: P_{b0} defecten worden geobserveerd en iets later in temperatuur ook het EX center –een SiO_2-geassocieerd defect. Dit laatste wijst op een substantile structurele/compositie modificatie. Het pieken van de defect dichtheden vs. warmtebehandelingstemperaturen curven duidt erop dat de SiO_x natuur van de grenslaag terug opbreekt na warmtebehan-

delingen bij temperaturen groter dan 930 $°C$. Dit is mogelijk gerelateerd met kristallisatie en/of silicaat vorming.

In een laatste hoofdstuk werd gekeken naar de invloed van ionenimplantatie (O en Si) in amorf SiO_2. In samenwerking met R. Weeks (*Vanderbilt University, USA*), R. Magruder (*Belmont University, USA*) en R. Weller (*Vanderbilt University, USA*) werden de geobserveerde ESR-defect dichtheden vergeleken met de optische absorptie banden rond 4.8 eV en 5.3 eV. Zo kon informatie verkregen worden over de bron van de geobserveerde optische absorpties.

Introduction

Today, we want our devices based on semiconductor devices to be ever smaller, faster, more multi-functional, and, if possible, also cheaper. For years now industry has been able to meet these demands bringing e.g., tiny cell phones, MP3-players, photo and video cameras, and laptops on the market. The word 'nano' has even surpassed its scientific meaning (unit prefix) and became the magic word to sell electronic devices and even washing-powder.

Up to present, the success of semiconductor-based industry has been the scalability of the microelectronics. More powerful chips could be realized through scaling of the metal-oxide-semiconductor (MOS) device dimensions. Using the Si/SiO_2 entity as basic building block, this down-scaling was successfully accomplished for gate thicknesses down to the 1-nm range. At this very moment, however, semiconductor industry has reached the end of the road for pure Si/SiO_2 based technology.

Further down-scaling of the SiO_2 gate oxide layer would induce excessive leakage currents because of direct tunneling, and moreover, serious reliability problems. This means that to keep on track with the requested advances in semiconductor devices an alternative "new" gate insulating material will be required for future generations of MOS devices. As an obvious solution, an insulator with a higher value of dielectric constant (κ) would allow one to use a physically thicker oxide layer retaining the same gate capacitance.

The use of such an alternative insulator instead of the extensively studied SiO_2 oxide brings about unforeseen problems associated with, e.g., inter-layer formation and dopant penetration. Many candidate materials have been studied, leaving us with more questions than answers. In search for some fundamental answers three of these so-called high-κ materials, ZrO_2, HfO_2, and $LaAlO_3$, were studied in this thesis and are the subject of chapters 3 and 4.

Another outcome of the current nano-wave is the rising popularity of, e.g., nanoparticles, nanowires, and nanotubes. Scaling down the SiO_2 di-

electric to such small dimensions, however, changes its electrical and optical properties, opening a whole new area of research. The characterization of the structure of SiO_2 nanoparticles is the subject of chapter 2.

The last few years, applied and fundamental research of nano-structures has grown exponentially revealing the upcoming relative impact of defects in the core of the nano-materials (nanoparticles, nanotubes, ultrathin layers) as well as at the interface. The study of point defects subsequently became of general interest since the presence of one single point defect can play a crucial definite part in the optical and electronic properties, such as, e.g., photoluminescence, doping of semiconductor nanoparticles, and conduction (in e.g., carbon nanotubes), of the nano-structures. To gain a better understanding of the detrimental influence of the presence of point defects atomic identification of occurring point defects is of vital importance. Up to the present the only known technique able to reveal the required atomic-scale information is electron spin resonance. Hence, in this thesis we will use electron spin resonance to monitor, characterize, and hopefully identify occurring point defects in a range of materials of interest for future developments in semiconductor nano-technology.

The outline of this thesis is as follows: Chapter 1 starts with a summary of some elementary notions of the theory and practice of electron spin resonance experiments. Further a brief overview of the characteristics of some occurring defects is Si/SiO_2 and in $Si/high-\kappa$ structures is given.

In chapter 2 an extensive electron spin resonance study is presented of fumed silica nanoparticles. Monitoring occurring point defects as a function of post-formation heating and treatment revealed interesting atomic-scale information concerning the particles' network structure.

The third chapter reports on the observation of P-impurity related point defects in nm-thick P-implanted HfO_2 films on (100)Si and in ZrO_2 powder –two oxides prominent in current high-κ insulator research. It is shown that the incorporation of P in these high-κ oxides results in ESR-active defects possibly acting as hole traps. This finding is important in view of the observed enhanced dopant penetration through HfO_2 layers during the necessary dopant activation anneals.

The study of the nature and stability of the $(100)Si/LaAlO_3$ interface is the subject of chapter 4. Here it is demonstrated that the interface is abrupt and stable for annealing up to about 800 $^\circ C$. It is evidenced that upon annealing in the range 800-860 $^\circ C$ a Si/SiO_2-type interlayer starts forming. Upon annealing at temperatures higher then 930 $^\circ C$ the interlayer with SiO_x nature is found to break up. The latter is possibly

related crystallization and possibly silicate formation.

In the last chapter the influence of ion implantation in amorphous bulk SiO_2 was studied. In cooperation with R. Weeks (*Vanderbilt University, USA*), R. Magruder (*Belmont University, USA*), and R. Weller (*Vanderbilt University, USA*) the densities of observed defects were compared to the optical absorption bands around 4.8 and 5.3 eV. In this manner information could be obtained concerning the source of the optical absorptions.

This thesis ends with a summary and general conclusions of the experimental work performed.

Chapter 1

Electron spin resonance probing of defects

1.1 Electron spin resonance: theory and experiment

When it comes to the atomic-scale characterization and identification of defects in solids, electron spin resonance (ESR) has proven to be a valuable technique. Of course only paramagnetic states can be studied with this technique, with a limited sensitivity –operated at low temperatures (4.2-100 K) typically a detection limit of 10^{10} spins per Gauss line width is quoted. Continuous wave (cw) ESR experiments generally consist of measuring the (derivative) absorption of the microwave power (P_μ) at a fixed frequency ν as a function of an externally applied magnetic field induction $\vec{B}$. The theory and practice of ESR has been accurately dealt with in numerous textbooks [1, 2, 3] and review papers [4]. Here, we will restrict to a very brief introduction to those ESR elements most commonly encountered in semiconductor ESR research.

1.1.1 Theory

The resonance condition

The energy of the interaction of a magnetic moment $\vec{\mu}$ in a magnetic field induction $\vec{B}$ may be written as

$$E = -\vec{\mu} \cdot \vec{B}. \qquad (1.1)$$

The magnetic moments concerned in ESR originate from electrons, to which there are two contributions: the intrinsic angular moment ($\vec{\mu_e}$) –the so called spin– and the orbital angular moment ($\vec{\mu_L}$). The magnetic moment arising from the electron spin can be written as

$$\vec{\mu}_e = -g_0\mu_B\vec{S}, \tag{1.2}$$

where $\hbar\vec{S}$ ($\hbar$ is Planck's constant h divided by 2π) is the electron spin angular momentum operator, $\mu_B \equiv \frac{|e|h}{2m_e}$ (e is the electron charge and m_e the rest mass of the electron) the Bohr magneton, and g_0 the so called free electron g factor. Experimentally as well as theoretically g_0 has been determined to equal 2.0023193043718(75) [5]. The orbital angular momentum of an electron is formally written the same as Eq. 1.2, but without the proportionality factor g_0,

$$\vec{\mu}_L = -\mu_B\vec{L}, \tag{1.3}$$

where $\hbar\vec{L}$ is the orbital angular momentum operator.

For a spin system of total angular momentum $\vec{J}$ placed in an applied magnetic field induction $\vec{B}$ the possible energies are quantized. The Zeeman levels can be written as

$$E_{M_J} = g\mu_B B M_J, \tag{1.4}$$

with $M_J = -J, -J+1, ..., J-1, J$ the magnetic quantum number. The energy levels are equidistant with an energy difference $\Delta E = g\mu_B B$ between two adjacent levels.

During an ESR experiment 'physical' information about the spin system is obtained through inducing transitions between the Zeeman levels. According the basic theory of quantum mechanics, such transition can be accomplished by a time dependent perturbation, e.g., an alternating magnetic field $\vec{B}_1 \cos(2\pi\nu t)$, if $h\nu = \Delta E$ and $\Delta M_J = \pm 1$. The resonance condition then easily follows from Eq. 1.4 as

$$h\nu = g\mu_B B. \tag{1.5}$$

In Fig. 1.1 the Zeeman energies of Eq. 1.4 are diagrammed, for a single electron with S=1/2, as a function of B together with the resonant absorption of microwaves occurring when the resonance condition (Eq. 1.5) is fulfilled.

The effective spin Hamiltonian

Within the context of an ESR experiment, a spin system can be described by a unique spin Hamiltonian ($\mathcal{H}_S$), i.e., a Hamiltonian build up of useful

$$E_\downarrow = \frac{1}{2} g_0 \mu_B B$$

$$h\nu = g_0 \mu_B B_r$$

$$E_\uparrow = -\frac{1}{2} g_0 \mu_B B$$
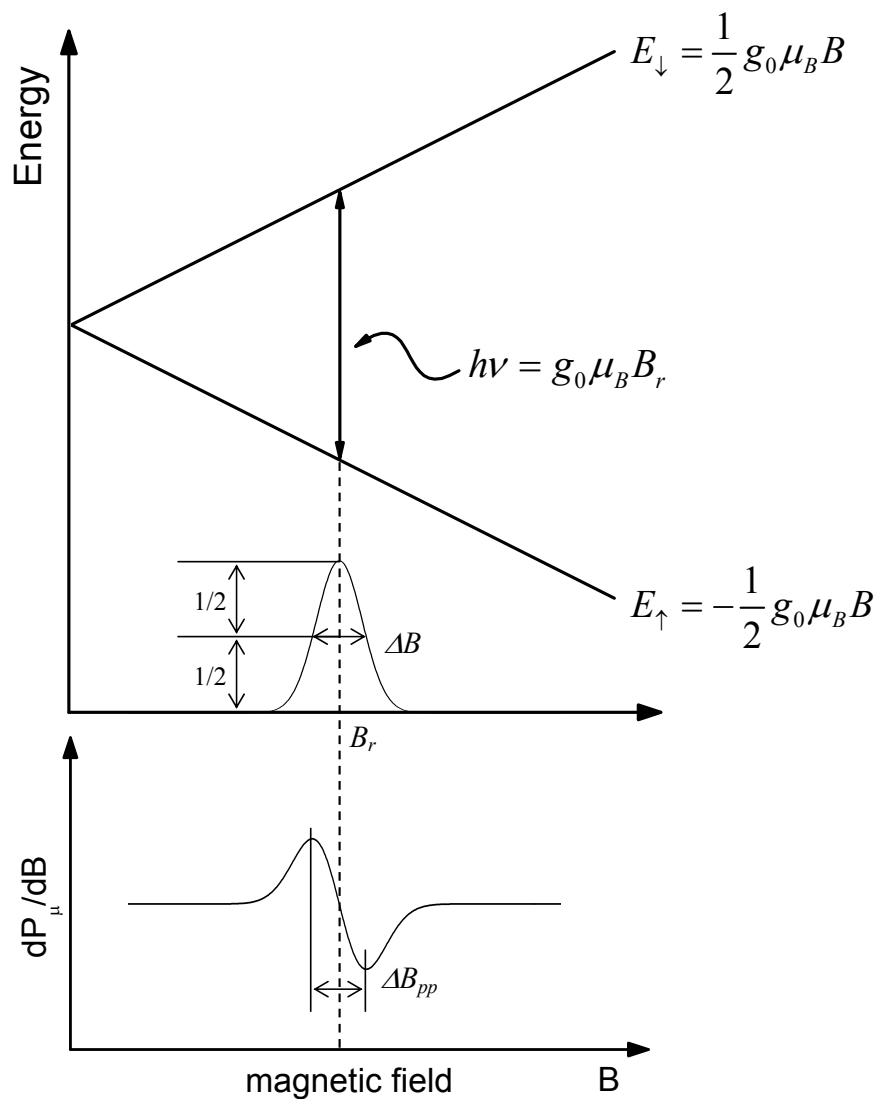
Figure 1.1: *Energy levels scheme as a function of magnetic field for the Zeeman interaction of a single electron (S=1/2) together with the ESR resonance absorption and its first derivative occurring at $B = B_r$. Various indicated symbols, used to describe signals, are discussed in the text.*

terms only comprising spin operators and parameters involving quantitative information about the nature of the defect under study. This is true when $\vec{L}$ is quenched by the crystal field so that mixing of higher lying levels in the ground state via spin-orbit coupling is small –a condition satisfied for most defects embedded in a solid, and certainly for all defects studied in this thesis. Thus for the purpose of this work the full Hamiltonian can be replaced by a reduced effective spin Hamiltonian

$$\mathcal{H}_S = \mathcal{H}_{ez} + \mathcal{H}_D + \mathcal{H}_{hf} + \mathcal{H}_{nz}, \tag{1.6}$$

where $\mathcal{H}_{ez}$ represents the operator of the electronic Zeeman interaction (0-1 cm^{-1}), $\mathcal{H}_D$ describes the spin-spin interactions (0-1 cm^{-1}), $\mathcal{H}_{hf}$ the hyperfine (hf) interaction (0-10^2 cm^{-1}), and $\mathcal{H}_{nz}$ represents the nuclear Zeeman interaction (0-10^{-3} cm^{-1}). We will now describe the theoretical expressions for the different terms in Eq. 1.6.

For a simple $S=1/2$, $I=0$ spin system the only non-zero interaction included in Eq. 1.6 is the electronic Zeeman interaction. The effective spin Hamiltonian can be reduced to

$$\mathcal{H}_S = \mathcal{H}_{ez} = \mu_B \vec{B} \cdot \hat{g} \cdot \vec{S}. \tag{1.7}$$

If the angular orbital momentum $\vec{L}$ is largely quenched, as assumed in the construction of the effective spin Hamiltonian, the remaining small residual mixing of the exited state $|\Psi_n\rangle$ spatial wave functions of the unpaired spin in the ground state $|\Psi_0\rangle$ wave function by the spin-orbit coupling coefficient λ can be described by replacement of the real spin by an "effective" spin $\hat{g} \cdot \vec{S}/g_0$, effectuated by the replacement of the free electron g value g_0 by a $\hat{g}$ matrix. Using perturbation theory, accurate to second order in the spin-orbit coupling, the $\hat{g}$ matrix becomes

$$\hat{g} = g_0 \hat{1} + 2\lambda \hat{\Lambda}, \tag{1.8}$$

where $\hat{1}$ the unitary matrix. For unpaired spins localized on a single atom (or a cluster of like atoms), the elements of the symmetric matrix $\hat{\Lambda}$ are given by

$$\Lambda_{ij} = \sum_{n \neq 0} \frac{\langle \Psi_0 | L_i | \Psi_n \rangle \langle \Psi_n | L_j | \Psi_0 \rangle}{E_0 - E_n} \tag{1.9}$$

where E_0 and E_n are the energy levels of the ground state and the excited state of the unpaired electron, respectively. From Eq. 1.9 it is evident that the symmetry of Ψ_0 and Ψ_n is projected into the symmetry of the $\hat{g}$ matrix. This way, the $\hat{g}$ matrix can reveal information regarding the electronic

symmetry of the paramagnetic defect and provides a unique fingerprint of the center.

In general the g factor forms a symmetric matrix with six components. It is, however, always possible to find the principal axes (x, y, z) where the $\hat{g}$ matrix is diagonal

$$\hat{g} = \begin{pmatrix} g_x & 0 & 0 \\ 0 & g_y & 0 \\ 0 & 0 & g_z \end{pmatrix} \tag{1.10}$$

For an arbitrary orientation of a crystal in a magnetic field one obtains a resonance characterized by the g factor

$$g = (g_x^2 \cos^2 \theta_x + g_y^2 \cos^2 \theta_y + g_z^2 \cos^2 \theta_z)^{1/2} \tag{1.11}$$

where, for example θ_x is the angle between the x axis and the magnetic field direction and $\cos \theta_x$ is called the direction cosine of x. The three direction cosines obey the relation

$$\cos^2 \theta_x + \cos^2 \theta_y + \cos^2 \theta_z = 1 \tag{1.12}$$

In spherical coordinates Eq. 1.11 assumes the form

$$g = (g_x^2 \sin^2 \theta \cos^2 \phi + g_y^2 \sin^2 \theta \sin^2 \phi + g_z^2 \cos^2 \theta)^{1/2} \tag{1.13}$$

It is frequently found that the $\hat{g}$ matrix has axial symmetry, in which case

$$\begin{aligned} g_\parallel &= g_z \\ g_\perp &= g_x = g_z \end{aligned} \tag{1.14}$$

where the z axis is taken as the symmetry axis. For this case Eq. 1.13 becomes

$$g = (g_\perp^2 \sin^2 \theta + g_\parallel^2 \cos^2 \theta)^{1/2} \tag{1.15}$$

where θ is the angle between the symmetry axis (along $g_\parallel$) and the magnetic field direction.

For $S > 1/2$ spin systems the spin-spin interaction comes into play and must be included in the effective spin Hamiltonian

$$\mathcal{H}_\mathrm{S} = \mathcal{H}_\mathrm{ez} + \mathcal{H}_\mathrm{D} = \mu_B \vec{B} \cdot \hat{g} \cdot \vec{S} + \vec{S} \cdot \hat{D} \cdot \vec{S}. \tag{1.16}$$

The last term is often referred to as the fine structure or zero-field splitting and is most frequently expressed in its alternative form

$$\mathcal{H}_\mathrm{D} = D[S_z{}^2 - \frac{1}{3}S(S+1)] + E(S_x{}^2 - S_y{}^2), \tag{1.17}$$

with

$$D = D_{zz} - \frac{1}{2}(D_{xx} + D_{yy}),$$

and

$$E = \frac{1}{2}(D_{xx} - D_{yy}).$$

For $I \neq 0$ the nuclear Zeeman interaction and the hf interaction –the interaction of the unpaired electron with nearby nuclear magnetic moments– need to be included in the spin Hamiltonian describing the magnetic behavior of the ground state of the spin system. The effective spin Hamiltonian for an S=1/2 electron interaction with a magnetic nucleus is

$$\mathcal{H}_\mathrm{S} = \mathcal{H}_\mathrm{ez} + \mathcal{H}_\mathrm{hf} + \mathcal{H}_\mathrm{nz} = \mu_B \vec{B} \cdot \hat{g} \cdot \vec{S} + \vec{S} \cdot \hat{A} \cdot \vec{I} - g_N \mu_N \vec{B} \cdot \vec{I}, \quad (1.18)$$

where the symbols $\vec{I}$, $\hat{A}$, g_N, and μ_N represent the nuclear spin vector operator, the hf tensor, the nuclear g factor, and the nuclear magneton. The last term in Eq. 1.18, representing the nuclear Zeeman interaction, can often be neglected except when the nucleus in question has a large magnetic moment (e.g., the H atom). The middle term, representing the hf interaction, is replaced by a sum of similar terms when the electron spin interacts with several magnetic nuclei at different neighboring sites or different $\vec{I}$.

The hf interaction can be divided in two parts: the isotropic Fermi-contact interaction and the anisotropic electron nuclear dipole-dipole coupling. Consequently the hf tensor $\hat{A}$ can be written as

$$\hat{A} = a_{iso}\hat{1} + \hat{T}, \quad (1.19)$$

the sum of the isotropic hf interaction tensor $a_{iso}\hat{1}$ and the anisotropic hf interaction tensor $\hat{T}$. The Fermi-contact Hamiltonian $\mathcal{H}_\mathrm{f}$ can be written as

$$\mathcal{H}_\mathrm{f} = a_{iso}\vec{S} \cdot \vec{I}, \quad (1.20)$$

where

$$a_{iso} = \frac{2}{3}\mu_0 g_e \mu_B g_N \mu_N |\Psi_0(0)|^2,$$

μ_0 the permeability of free space, and $\Psi_0(0)$ the ground state electron wave function at the interacting nucleus. From Eq. 1.20 it is evident that the measurement of the isotropic hf interaction may result in the determination of the probability density of the electron at the site of the interactive nucleus if the chemical identity of the nucleus is known. Obviously, there is only an a_{iso} contribution for s-state wave functions of the magnetic nucleus.

The electron nuclear dipole-dipole coupling Hamiltonian $\mathcal{H}_{\mathrm{dd}}$ can be written as

$$\mathcal{H}_{\mathrm{dd}} = \frac{\mu_0}{4\pi} g_e \mu_B g_N \mu_N \left[\frac{(3\vec{S}\cdot\vec{r})(\vec{r}\cdot\vec{I})}{r^5} - \frac{\vec{S}\cdot\vec{I}}{r^3} \right] = \vec{S}\cdot\hat{T}\cdot\vec{I}. \qquad (1.21)$$

Detection of occurring hf structures is, without doubt, the most powerful ESR observation. From the hf spectra the nuclear spin of the interacting nuclei and their (natural) abundance can be determined together with $\hat{A}$. In this way it is possible to identify the atoms involved, their arrangement, and, in favorable cases, distances. In conjunction with theoretical modeling, the observation of the hf structures can often lead to full atomic identification of the defect.

Linear Combination of Atomic Orbitals analysis of the hyperfine interaction

The LCAO (Linear Combination of Atomic Orbitals) approximation is based on the expansion of the molecular orbital Ψ_0 containing the unpaired electron in terms of atomic wave functions that consist of a linear combination of atomic orbitals ϕ_j. If all N atoms on which the ground state wave function Ψ_0 has an appreciable probability density are identical and their atomic functions on each consist of M atomic orbitals then

$$\Psi_0 = \sum_{i=1}^{N} \eta_i \left[\sum_{j=1}^{M} \alpha_j \phi_j \right], \qquad (1.22)$$

where η_i is the localization of the wave function on atom i and α_j is its ϕ_j orbital character.

For the analysis of the hf interaction in this thesis the number of atoms is restricted to those causing a detectable hf splitting. The expansion is also restricted to s and p orbitals only. This is a good approximation for the analysis of defects in solids with top valence and conduction bands are constructed from sp^3 hybrid orbitals. Thus Ψ_0 can be approximated as

$$\Psi_0 = \sum_{i=1}^{N} \eta_i [\alpha_i \phi_{ns} + \beta_i \phi_{np}], \qquad (1.23)$$

with the normalization conditions

$$\forall i, i = 1...N : \alpha_i^2 + \beta_i^2 = 1$$

$$\sum_i \eta_i^2 = 1.$$

A last assumption is that the wave function density on atom i totally arises from the atomic wave function of atom i. Any contributions on atom i from the atomic wave function of an atom $j \neq i$ are neglected. This last assumption and the restriction to s and p orbitals imply that the hf matrix $\hat{A}$ is axially symmetric. In general, principal values of $\hat{A}$ can be written in terms of an isotropic (A_{iso}) part (s part: Fermi contact interaction), an anisotropic (b) part (p part: dipolar interaction), and an orthorhombic (c) part (deviation from perfect sp character):

$$
\begin{aligned}
A_1 &= A_{iso} + 2b \\
A_2 &= A_{iso} - b + c \\
A_3 &= A_{iso} - b - c.
\end{aligned}
\tag{1.24}
$$

Within the assumption of perfect sp^3 hybridization ($c{=}0$), the combination of Eqs. 1.18, 1.20, 1.21, 1.23, and 1.24 renders:

$$
\begin{aligned}
|<\phi_{ns}\,|\,\Psi_0>|^2 &= \eta^2\alpha^2 = \frac{A_{iso}}{A_s}, \\
|<\phi_{np}\,|\,\Psi_0>|^2 &= \eta^2\beta^2 = \frac{b}{A_p}, \\
1 &= \alpha^2 + \beta^2,
\end{aligned}
\tag{1.25}
$$

where A_s and A_p are, respectively, the atomic s and p-state hf coupling constants, inferred from theory. Thus the LCAO analysis of the hf interaction presents a simple method to investigate the localization (η^2) of the electron wave function on an atom and the s (α^2) and p (β^2) character of the orbital composition of the unpaired electron.

As evident from Eq. 1.25, it should be noted that the inferred values for α^2, β^2, and η^2 will depend on the used atomic set for A_s and A_p. Some of the atomic hf coupling constants existing in literature are listed in Table 1.1 for Si and P. Comparison of the numbers in Table 1.1 reveals the limited accuracy of the calculations ($\sim 30\%$). It is therefore necessary, when comparing various sources of hybridization and localization parameters, to make sure whether the data were all obtained from interpretations based on the same set of atomic hf coupling constants. In this thesis the values calculated by Morton and Preston [8] are used, as those are still regarded as the most accurate. Results from literature presented in this work are, if necessary, recalculated from the hf matrix using the atomic set from Ref. [8].

Table 1.1: *List of various theoretical estimates of A_s and A_p, the hyperfine coupling constants for 3s and 3p electrons on atomic silicon and phosphorus.*

Atom	A_s (MHz)	A_p (MHz)	Ref.
Si	4788		[6]
		95	[7]
	4594	114	[8]
	3380	86	[9]
	4191	106	[10]
P	13306	367	[8]
	11175	308	[11]

1.1.2   Practice

Detection modes

In general first derivatives of absorption curves (dP_μ/dB) are detected in cw ESR, due to the use of lock-in detection techniques to improve sensitivity. The modulation amplitude B_m of the applied magnetic field B and incident microwave power P_μ were restricted to levels not causing (noticeable) signal distortion. The latter is very pertinent with respect to inferring reliable ESR parameters of highly saturable point defects, such as most defects encountered in this thesis. In the case of highly saturable defect centers it is sometimes just impossible to detect these undistorted as the proper spectrometer settings cannot be attained due to the loss of sensitivity when decreasing P_μ. A possible solution may then come from switching to the second harmonic phase-quadrature (out-of-phase) mode [12] using relatively high B_m and P_μ, as demonstrated in chapters 2 and 3. Even though the second harmonic detection technique has not been finalized theoretically, empirical evidence has been provided that the observed spectra resemble the direct absorption shapes [13, 14, 15]. The down side is that quantitative determination of defect densities from second harmonic saturation spectra is not straightforward and requires extreme care.

To enhance the signal-to-noise ratio, in both modes the spectrometer signal averaging capabilities are extensively used: if necessary typically up to several hundred field scans were added.

Physical parameters

Depending on sample and measurement conditions, various physical parameters occurring in Eq. 1.6 can be obtained by interpretation of experimentally observed ESR spectra. The main parameters one attempts to measure are the three principal-axis components and directions of the $\hat{A}$ tensor and of the $\hat{g}$ matrix. For accurate g value calibration use was made, in this work, of a calibrated Si:P marker [16] sample [S=1/2, g(100 K)=1.99891] or a Li:F marker [17] sample [S=1/2, g=2.00229] co-mounted with the studied sample and recorded in one trace. Chapter 3 of this work deals with the detailed analysis of the hf interactions leading to the identification of the observed defect centers. In chapter 2 the observation of changes in $\hat{g}$ and $\hat{A}$, in conjunction with elementary theoretical modeling, reveals changes in the network structure.

In general $\hat{g}$ and $\hat{A}$ are not isotropic and the observed g value and hf splitting depend on the orientation of $\hat{g}$ and $\hat{A}$, respectively, relative to the direction of $\vec{B}$. The orientation and symmetry of $\hat{g}$ and $\hat{A}$ reflect those of the involved electronic wave function, as can be seen from Eqs. 1.8, 1.20, and 1.21, which is co-determined by the defect's local surrounding. Especially in a crystalline environment, where defects occur in discrete orientations determined by the lattice symmetry, useful information concerning defect and lattice orientation may be obtained. In disordered media, such as poly-crystalline or amorphous materials, however, anisotropic spectral properties are continuously averaged over all orientations of the defect, leading to the observation of less informative, smeared out spectra. If all orientations of the local coordinate system of the defect with respect to the magnetic field are present in the sample, the resulting ESR spectrum will then be a so called *powder* spectrum –of importance in chapters 2, 3, and 5. The powder spectrum is a summation of all individual spectra over all possible orientations of the principal axes of the defect relative to the direction of the magnetic field, each multiplied with its transition probability. Many approximations exist for the calculation of such a powder spectrum. Examples of calculated powder spectra for an axial and orthorhombic system are illustrated in Fig. 1.2.

Other salient spectral features are line width and line shape. The first derivative absorption signal is characterized by the peak-to-peak width ΔB_{pp}, the added result of various line broadening mechanisms. The most frequently encountered basic absorption shapes are the Gaussian, Lorentzian, and Voigt line, i.e. where the latter is the convolution of a Gaussian and Lorentzian line. The full width at half the amplitude of the absorption
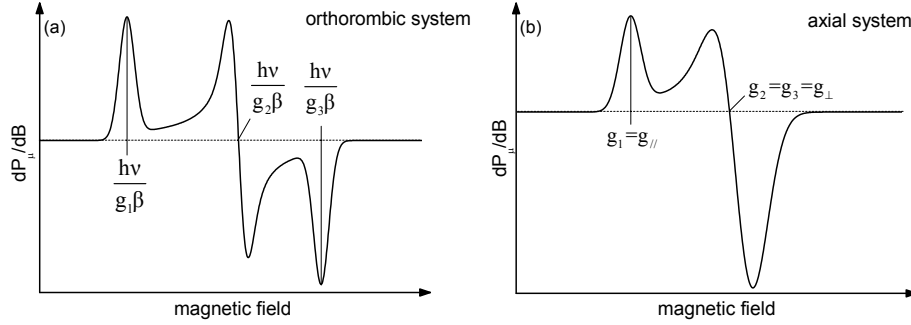
Figure 1.2: *Illustration of first derivative powder pattern spectra (Gaussian convoluting line shape) for a S=1/2 system exhibiting (a) orthorhombic (the principal values of $\hat{g}$ are $g_1 \neq g_2 \neq g_3$) and (b) axial symmetry ($g_1 \neq g_2 = g_3$, or $g_1 = g_\parallel$ and $g_2 = g_3 = g_\perp$, with $g_\parallel > g_\perp$).*

line (ΔB) is related to ΔB_{pp} through the expressions $\Delta B = \sqrt{2ln2}\Delta B_{pp}$ and $\Delta B = \sqrt{3}\Delta B_{pp}$ for a Gaussian and Lorentzian line shape, respectively. The line shape can be typified by the line shape factor

$$\kappa_{ls} \equiv \frac{2\mathcal{I}}{A_{pp}\Delta B_{pp}^2}, \qquad (1.26)$$

where A_{pp} is the peak-to-peak height of the signal, equal to twice the signal amplitude, and $\mathcal{I}$ the signal intensity, defined as the area under the absorption curve. The line shape factors for Lorentzian, Voigt, and Gaussian line shapes are κ_{ls}=3.63, 1.03<κ_{ls}<3.63, and κ_{ls}=1.03, respectively.

The ESR parameters are often inferred from the observed spectra through spectra simulations. The accuracy of the inferred g and hf values can be improved through independent fitting of the spectra of ESR measurements at different microwave frequencies. When this can be accomplished using one set (within experimental error) of $\hat{g}$ and $\hat{A}$, the inferred data can be regarded as highly reliable. It should be noted that in cases of 'large' hf values ($A \gtrsim 40$ G) the fitting needs to be done using a code based on exact matrix diagonalization incorporating the Breit-Rabi formula [18].

Defect density calibration

The signal intensity $\mathcal{I}$ is, apart from obvious experimental factors such as, e.g., the incident microwave power P_μ and the applied modulation field B_m, proportional to the magnetic susceptibility χ. As a result $\mathcal{I}$ displays a dependence on the number of spins in the sample. In this work defect

densities are determined by comparing $\mathcal{I}^S$ for the sample under study with $\mathcal{I}^M$ from a calibrated co-mounted marker sample. For this purpose the same markers were used, i.e., Si:P and Li:F [16, 17], as for the g value calibration described before. A major difference between the two types of markers is their paramagnetic behavior: Like most paramagnetic spin systems, the χ of the Si:P marker displays a Curie-Weiss type behavior, i.e.,

$$\chi \sim \frac{1}{T - T_C}, \tag{1.27}$$

where T_C is the Curie temperature [T_C(Si:P)=-2.7±0.3 K] [16]. For the Li:F marker the ESR signal originates from the conduction electrons of the metallic Li particles. Consequently, the marker exhibits a Pauli paramagnetic behavior giving rise to a χ essentially independent of the temperature. All Li:F markers were calibrated at room temperature relatively to a Curie-Weiss paramagnetic primary marker (MgO:Cr^{3+}), and then used as intermediate spin marker with, however, always paying attention to its specific T-independent susceptibility.

When the ESR spectrum of an S=1/2 (spin) system exhibiting Curie-Weiss paramagnetism and g values close to the g value of the marker is recorded –using the proper spectrometer settings– in the same trace as the co-mounted S=1/2 marker sample, the number of defects (spins) (N^S) can be obtained by

$$N^S = \frac{\mathcal{I}^S}{\mathcal{I}^M} N^M \frac{< B_1^2 >^M}{< B_1^2 >^S} \frac{T - T_C^S}{T + 2.7}, \tag{1.28}$$

or

$$N^S = \frac{\mathcal{I}^S}{\mathcal{I}^M} N^M \frac{< B_1^2 >^M}{< B_1^2 >^S} (T - T_C^S), \tag{1.29}$$

when comparing to the Si:P and Li:F marker, respectively. In Eqs. 1.28 and 1.29 N^M is the total number of spins in the co-mounted marker sample and $< B_1^2 >$ represents the value of the square of the applied magnetic microwave field component averaged over the sample. The assumption made in order to construct these equations are valid for all defects studied in this thesis.

Correct signal intensities must be determined through double numerical integration of the recorded first derivative ESR spectrum. However, this sometimes becomes inapplicable because of overlap and entanglement of signals originating from different types of defect centers. In that case reliable intensities can only be obtained through reliable fitting of the ESR

spectra and double numerical integration of the individual simulations of the different defect centers making up the measured ESR spectrum.

Spectrometers

The ESR measurements reported in this work were carried out employing three experimental setups: One home built system operated at K-band ($\nu \sim 20.5\ GHz$) frequencies, a commercial Q-band ($\nu \sim 34\ GHz$) setup (Bruker EMX) and a commercial X-band ($\nu \sim 9.2\ GHz$) setup (Jeol JES-FA 100). The systems show some similarities: all are equipped with a cylindrical TE_{011} microwave reflection cavity, routinely driven in absorption mode under conditions of slow adiabatic passage. Modulation of the externally applied magnetic field induction $\vec{B}$ typically at 100 kHz, allows phase sensitive signal detection.

The **K-band** spectrometer is equipped with a liquid He bath cryostat which allows variations of the measurement temperature T in the range 1-300 K. Usually, however, it is operated at 4.2 K, i.e., the temperature of liquid He at atmosphere pressure. The K-band cavity has a very high quality factor Q compared to the commercial setups: the typically loaded Q at $\sim 10\ K$ was ~ 10000. Moreover, the distinct differences in microwave circuitry and related detection scheme, enabled the K-band spectrometer to be operated, still with superb sensitivity, at much lower P_μ –below nW range– than the Q or X-band setups. This quality is crucial for the successful conventional absorption-derivative detection of highly saturable defect centers. The **Q-band** spectrometer is equipped with a He flow cryostat and operates generally at temperatures $T > 20\ K$ to room temperature. For the Q-band setup a maximum loaded Q of ~ 4000 could be attained. The Q-band spectrometer can be operated at P_μ in the range 160 nW - 160 mW. The Q-band setup was found to be the most suited for second harmonic out-of-phase mode measurements. The **X-band** spectrometer is equipped with a N_2 flow cryostat and operates generally at temperatures $T \sim 120$ - 470 K. A loaded Q of maximum ~ 6000 could be attained and the spectrometer can be operated at P_μ in the range 200 mW - 0.1 μW.

1.2 Defects in the Si/SiO$_2$ system

For decades, the Si/SiO$_2$ structure has dominated the semiconductor industry. Some of the reasons are that this native insulator to Si provides thermodynamical and electrical stability, a large band gap ($\sim 9\ eV$, making it an excellent electrical isolator), and an outstanding Si/SiO$_2$ interface

(a)

(b)
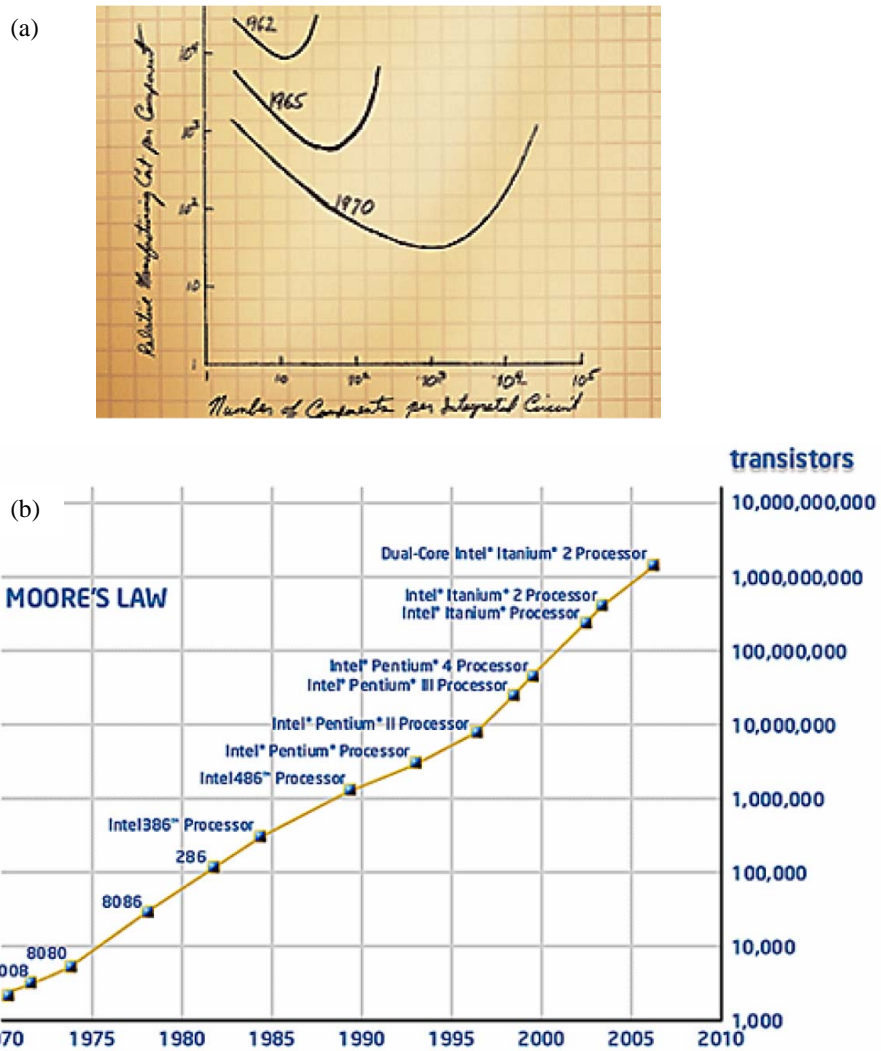
Figure 1.3: *Illustration of Moore's law stating that the number of transistors on a chip doubles every 18 months: (a) Gordon Moore's original graph from 1965, and (b) growth of transistor counts for Intel processors following Moore's law up to the present.*

because of the passivation behavior (very efficient possibility for passivation by H) of the inherently present interface defects. Up to now there is no interface exhibiting electrical properties approaching those of the Si/SiO$_2$ interface.

Over the years improvement of the performance of integrated circuits (ICs) was successfully achieved by scaling down the metal-oxide-semiconductor (MOS) entity, as illustrated in Fig. 1.3 by Moore's law. Lateral scaling of the MOS devices and thus the gate oxide mandates compensation for the loss in areal gate capacitance. This may be realized by reducing the gate oxide thickness. For the SiO$_2$ or the nitrided silicate (SiO$_x$N$_y$) gate dielectric down-scaling could be successfully accomplished for gate thicknesses down to the 1-nm range [19, 20]. There is, however, a fundamental limit to this scaling being the loss of bulk SiO$_2$ properties below $\sim$7 $\AA$. From a technological point of view the ultimate failure of standard SiO$_2$ as gate insulator is mainly due to issues such as intolerable (tunneling) leakage currents, problems with intrinsic reliability, and dopant penetration. Consequently, the ongoing scaling of MOS based devices will demand, amongst others, the introduction of new wide band gap insulators of dielectric constant κ higher than that of conventional SiO$_2$ or SiO$_x$N$_y$ ($\kappa_{SiO_2} = 3.9, \kappa_{SiO_xN_y} = 3.9 - 7.5$) in the near future, known as the high-κ issue [21, 19]. In that manner a physically thicker oxide layer of equivalent SiO$_2$ electrical oxide thickness (EOT, defined as d$_{EOT}$=d$_{high-\kappa}$ $\kappa_{SiO_2}/\kappa_{high-\kappa}$) can be used retaining the same gate capacitance but possibly reducing the leakage current and improving the gate reliability.

To set the stage for the discussion of Si/high-κ structures studied in Chapter 3 and 4, an overview is given of the defects, relevant to this work, observed in Si/SiO$_2$ structures. Even though it seems that the conventional Si/SiO$_2$-age will soon come to an end, the Si/SiO$_2$ entity will remain of interest as it appears inevitably present in the Si/high-κ structures. On the other hand, the oxide itself has regained attention in the form of nm-sized particles for their potential applications in optical and electronic nanodevices [22, 23]. (Chapter 2)

1.2.1 P_b-type interface defects

Three Si dangling-bond type Si/SiO$_2$ interface defects have so far been substantiated by ESR, commonly denoted as the P_b-type defects. It has been demonstrated in conjunction with electrical measurements [25, 26] that these P_b-type defects are the dominant class of interface traps invariably introduced at the Si/SiO$_2$ interface as a result of lattice mismatch between
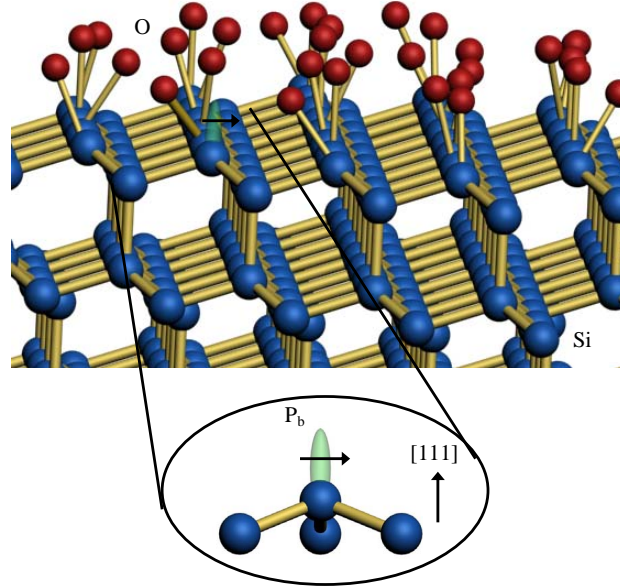
Figure 1.4: *A schematic representation of the (111)Si/SiO$_2$ interface with an incorporated P$_b$ defect structure [24].*

c-Si and a-SiO$_2$ [27, 28, 29]. The different types of Si dangling-bond type defects observed correlate with interface orientation, in registry with the crystallinity of the underlying Si substrate.

At the (111)Si/SiO$_2$ interface, the only type observed –specifically termed P$_b$– was identified as trivalent interfacial Si ($Si_3 \equiv Si\bullet$, where the dot represents an unpaired electron in a dangling Si sp^3 hybrid) back bonded to three Si atoms in the bulk. A schematic representation of the atomic structure of the (111) surface and the incorporated P$_b$ defect are shown in Fig. 1.4. The P$_b$ center was observed for the first time by Nishi [30]. Later, more extensive measurements performed by the group of Poindexter and Caplan [31, 32] linked the P$_b$ densities to the densities of interface traps in Si/SiO$_2$ capacitors and provided an accurate g map. Figure 1.5 illustrates the calculated g map of the P$_b$ center. The principal axis g values used are $g_\parallel$=2.0013 and $g_\perp$=2.0086. The center exhibits C_{3v} symmetry (axial along the [111]), for which four equivalent orientations in the Si lattice exist. Yet, only one orientation along the [111] interface normal is generally observed [29]. The other orientations, however, have been observed as well [33]. Conclusive evidence for the atomic model of the P$_b$ center was provided by the observation of a strong ^{29}Si (natural abundance 4.7%; $I = 1/2$) hf interaction
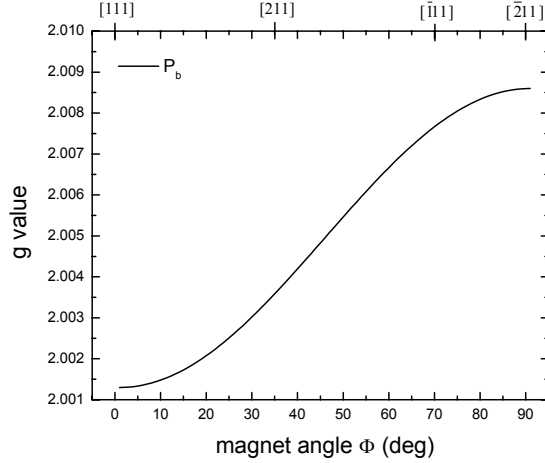
Figure 1.5: *Angular g map of the P$_b$ center observed at the (111)Si/SiO$_2$ interface for $\vec{B}$ rotating in the $(0\bar{1}1)$ plane with respect to the interface normal $\vec{n}$. The curve represents the theoretical calculation for trigonal symmetry using the principal axis g values $g_{\parallel}$=2.0013 and $g_{\perp}$=2.0086. Only the experimentally observed branch is shown.*

with a single Si site [24]. LCAO analysis of the hf tensor indicated that 80% of the unpaired electron density is located on the central Si atom. The orbital lobe pointing into the oxide was found to exhibit 12% s and 88% p character, confirming its expected sp^3 hybrid like character.

The technologically favored (100)Si/SiO$_2$ interface exhibits two types of dangling-bond type centers, termed P_{b0} and P_{b1}, again first observed by the group of Poindexter and Caplan [32]. Their atomic assignment, however, remained long obscure mainly because of the lack of convincing ESR data due to the inherently smaller defect densities ($\sim$1/5 as compared to the occurrence of P_b on (111) interfaces) and the spectral overlap. Later, measurements on thermal (100)Si/SiO$_2$ predominantly exhibiting either the P_{b0} or P_{b1} defect allowed accurate g mapping of both interface defects [34, 35]. The calculated g map is shown in Fig. 1.6. The principal g values used are $g_{\parallel}$=2.00185 and $g_{\perp}$=2.0081 for the P_{b0} defect center and g_1=2.0058, g_2=2.00735, and g_3=2.0022 for the P_{b1} defect center. The experimental evidence is that P_{b0} is chemically identical to P_b, but now residing at microscopically (111)-oriented Si/SiO$_2$ facets [34, 36, 37]. In agreement, both were conclusively established as major systems of detrimental electrical interface traps [25, 26]. The P_{b1} center is assigned to a distorted defected
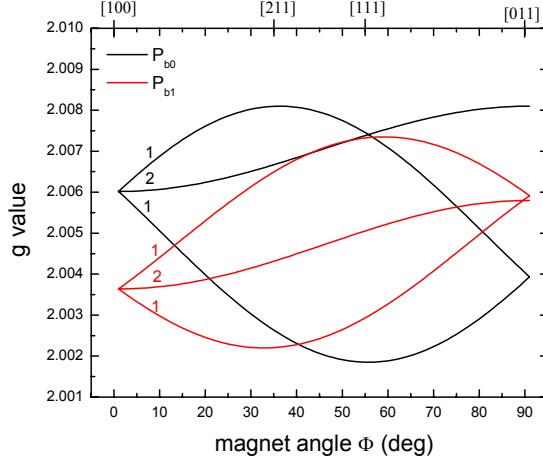
Figure 1.6: *Angular g map of the P_{b0} (black curves) and P_{b1} (red curves) centers observed at the (100)Si/SiO$_2$ interface for $\vec{B}$ rotating in the (0$\bar{1}$1) plane with respect to the interface normal $\vec{n}$. The curves represents the theoretical calculations for trigonal symmetry using the principal axis g values $g_\parallel$ =2.00185 and $g_\perp$ =2.0081 for the P_{b0} defect center and for triclinic symmetry using the principal axis g values g_1 =2.0058, g_2 =2.00735, and g_3 =2.0022 for the P_{b1} defect center. Only the experimentally observed branches are shown. The added numbers indicate relative branch intensities.*

interfacial Si-Si dimer (a $\equiv$ Si—Si$^{\bullet}$=Si$_2$ defect, where the long hyphen symbolizes a strained bond, with an approximately <211> oriented unpaired Si sp^3 hybrid) [38]. An (100)Si/SiO$_2$ interface with incorporated P_{b0} and P_{b1} defects is illustrated in Fig. 1.7.

At the (110)Si/SiO$_2$ interface also, only one type, the P_b variant, is observed [27].

Thus all three variants were shown to be interfacial trivalent Si centers [28, 38, 34], naturally occurring, for standard oxidation temperatures T_{ox} (800-960 $^\circ$C), in areal densities of $[P_b] \sim 5 \times 10^{12}$ cm^{-2} [39, 40] and $[P_{b0}]$, $[P_{b1}] \sim 1 \times 10^{12}$ cm^{-2} [39]. Both P_b and P_{b0} were demonstrated to be adverse electrical interface traps [25, 26].

As a key characteristic, the thermochemical properties of the P_b-type defects appear dominated by reversible interaction with hydrogen. The defects may be readily electrically inactivated (passivated) by heating ($T_{an} \gtrsim 230$ $^\circ$C) in molecular H$_2$ pictured as chemical saturation of the unpaired sp^3 Si hybrid by hydrogen [28, 41, 42, 43], denoted as SiH formation. The chemical reaction is modeled as $P_b + H_2 \rightarrow P_bH + H\uparrow$, proceeding with
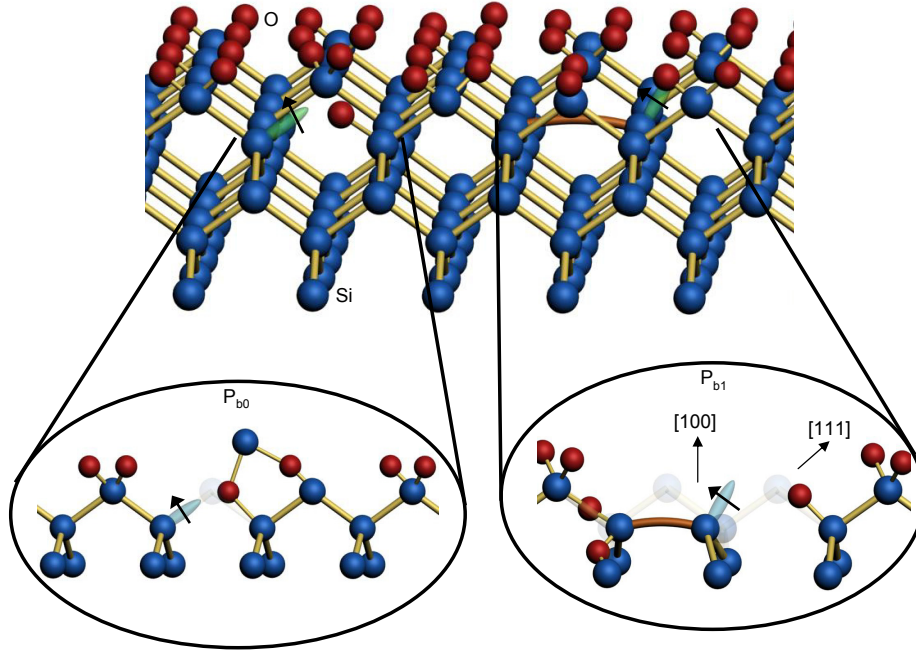
Figure 1.7: *A schematic representation of the (100)Si/SiO$_2$ interface with incorporated P_{b0} and P_{b1} defect structures [37, 38].*

an activation energy E_f=1.51±0.04 eV [41, 42, 43]. Heating to $T_{an} \gtrsim$ 500 $^{\circ}C$ results in dissociation of H, according to the reaction P_bH $\rightarrow$ P_b + H↑ turning the defects again into the ESR-active paramagnetic state [44, 41, 42, 43]. The latter reaction proceeds with an activation energy of E$_d$=2.83±0.2 eV [45].

1.2.2   Intrinsic defects in a-SiO$_2$

A range of intrinsic defects have been reported in a-SiO$_2$ including the E'-type defects, EX, the non-bridging oxygen hole center ($NBOHC$), and the peroxy-radical (POR). In the following we will discuss those intrinsic defects in a-SiO$_2$ of relevance to this work. Models of the various defects are discussed and compiled in Figs. 1.8, 1.9, 1.10, and 1.11.

Table 1.2: *Comparison of experimental principal axis g matrix values of generic E′ centers.*

	E'_1 [a]	E'_γ [b]	E'_α [b]	E'_β [b]	E'_δ [b]	E'_s [c]
g_1	2.0018	2.0018	2.0018	2.0018	2.0018	2.0018
g_2	2.0005	2.0006	2.0013	2.0004	2.0021	2.0003
g_3	2.0003	2.0003	1.9998	2.0004	2.0021	2.0003

[a] Observed in fast neutron irradiated crystalline quartz, see Ref. [47].
[b] Observed in synthetic fused silica subjected to 100 keV x-rays at 77 K, see Ref. [48].
[c] Observed in natural and synthetic quartz crushed in UHV at 300 K, see Ref. [49].

The E'_γ center

The E'_γ center is a subclass of the most widely studied radiation-induced defect centers in a-SiO$_2$, i.e., the so called E'-type defects. Most of the E' defects share the same basic structural feature –the so called generic E' entity– pictured as an O$_3$ $\equiv$Si$\bullet$ moiety, where $\bullet$ and $\equiv$ represent an unpaired electron and three Si-O bonds respectively, with the unpaired electron highly localized in an sp^3-type hybrid orbital on the defect Si, back bonded to three O atoms. Their presence is closely related to the oxide quality. Beside the E'_γ center, previous ESR studies have demonstrated the existence of several variants of E'-type centers in a-SiO$_2$ [4], that exhibit subtle differences in their ESR signals as shown in Table 1.2. The models for the different E'-type defects in a-SiO$_2$ are still under discussion. An overview is presented in Ref. [46].

For the E'_γ center Griscom *et al.* pointed out that the model is most probably essentially identical with that of the 'crystalline' equivalent of this defect [14] –termed E'_1 center– first observed in neutron irradiated α-quartz [50], because the ESR characteristics of these two types of E' centers are very similar. The observed larger spread both in the nearly equal g_2 and g_3 components and in the isotropic ^{29}Si hf coupling constant [51] of the E'_γ center compared to the E'_1 center were attributed to small random variations in the defect bond angles in the glass.

A detailed study of the E'_1 center [47] revealed the principal values of the g matrix (see Table 1.2), and reported the observation of one strong hf interaction ($\sim$ 420 G doublet), which allowed identification of the unpaired
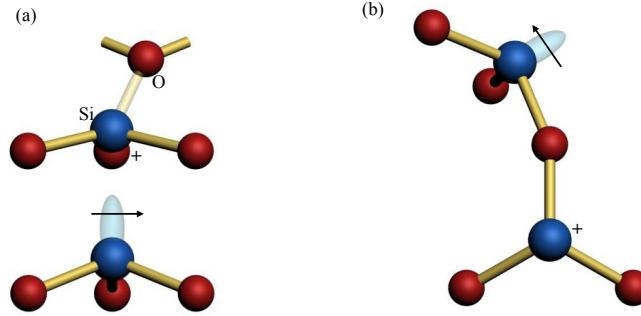
Figure 1.8: *A schematic representation of the suggested models of the E'_γ center: (a) The conventional model [51, 53] and (b) the new BHODC model [54].*

electron state as occupying a sp^3 hybrid orbital on a single Si site. In addition, two more weak hf interactions were observed, also attributed to (more distant) Si atoms. The formation mechanism of the E'_1 center in α-quartz, proposed by Feigl, Fowler, and Yip [52], is well accepted; that is, a positive hole h$^+$ trapped at a neutral oxygen monovacancy can be localized on one silicon atom and then lower its energy by relaxing back into the plane of its three remaining oxygen neighbors. This reaction can be written as follows:

$$\equiv Si - Si \equiv +h^+ \rightarrow \equiv Si \bullet (E'_1)+ \equiv Si^+, \qquad (1.30)$$
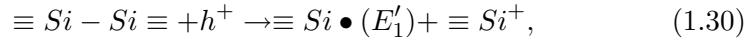
where $\bullet$ and $\equiv$ represent an unpaired electron and three Si-O bonds, respectively. Importantly, as modeled, the E'_1 center in its paramagnetic state would thus be a positively charged entity. This model was subsequently refined by Rudra and Fowler [53], who suggested that the relaxation of the positively charged silicon is further stabilized by forming an additional weak backward Si—O bond ("backward puckering" through the plane formed by the three back bonded O atoms) with a nearby oxygen atom, making the oxygen atom threefold coordinated. The latter model is illustrated in Fig. 1.8 (a).

More recently, Uchino *et al.* questioned the assumption that the E'_γ center in a-SiO$_2$ has the same microscopic origin as the E'_1 center in α-quartz [54, 55]. Based on density functional theory (DFT) calculations, a different model –named the bridged hole-trapping oxygen deficiency center ($BHODC$)– was proposed, as shown in Fig. 1.8 (b). In this model a paramagnetic silicon shares a common oxygen with a neighboring hole-trapping silicon. It is, however, important to notice that this model concerns one of the more theoretical suggestions, that still need experimental verification.

Both models described here hold that the E' center is positively charged. Over the years various experimental studies have questioned this assumed positive charge state of the paramagnetic E' center in thermal SiO_2 on Si [56, 57, 58]. Based on the comparison between the densities of positive charge and paramagnetic E' centers generated in thermal SiO_2 on Si by VUV irradiation at different electrical field strengths in the oxide, Afanas'ev and Stesmans [59] have demonstrated that an uncharged E'_γ center does exist in amorphous thermal SiO_2 on Si and proposed that the E'_γ center mainly involved the O≡Si• moiety only, i.e., the positively charged counterpart is absent. The E'_γ system here operates as a potential H-storage system (O≡Si–H formation).

The S center

Holzenkämpfer *et al.* carried out an ESR study on thin amorphous SiO_x layers deposited by electron-beam evaporation of Si under different oxygen pressures, where x was varied between 0 and 2 [60]. After irradiation with He^+ ions, a broad resonance line was observed which the authors interpreted as a superposition of three singlet lines having different g values –in the range $\sim$2.0060 to $\sim$2.0008– and line widths. From the variation of the effective g value with the oxygen stoichiometry x, they inferred that the higher g values are associated with regions of the network which are progressively more oxygen deficient. In the samples with x $\geq$ 0.8 a narrow resonance line centered near g$\sim$2.001 was observed in increasing intensity with rising oxygen content. Based on the signal's observed g matrix anisotropy, the signal was identified as the E'_γ center. The broad resonances were interpreted in terms of superpositions of three additional signals arising from E' or P_b variants wherein the defected silicon is bonded to one oxygen and two silicons, two oxygens and one silicon, or three silicons (the latter being the P_b defect.
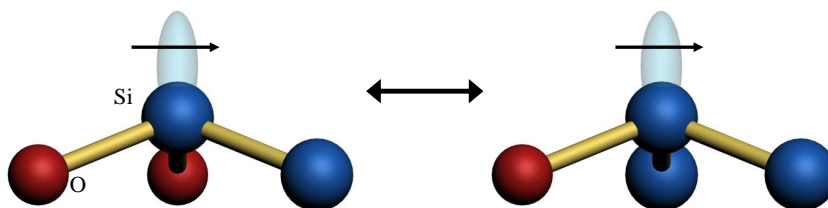
Figure 1.9: *A schematic representation of the suggested model of the S center.*

Later, Griscom *et al.* observed a singlet (g~2.0030; ΔB_{pp}~2.6 G) in γ-irradiated P$_2$O$_5$-SiO$_2$ glasses annealed at $T_{an}\geq700$ K, the corresponding defect of which they labeled the S center [61]. Within the framework of the work of Holzenkämpfer [60], they suggested the S center to correspond to the centers "intermediate" between the E' and P_b defects, namely defects of the type OSi$_2\equiv$Si$^\bullet$ and/or O$_2$Si$\equiv$Si$^\bullet$, as illustrated in Fig. 1.9.

Stesmans and Afanas'ev for the first time observed a signal similar to that of the S center –characteristic isotropic signal at g(4.2 K)=2.0028 and ΔB_{pp}=4.5-5.8 G– in thermal SiO$_2$ on (100)Si subjected to post-oxidation vacuum annealing at $T_{an}\geq950$ $^\circ C$ [62]. The S center generation during degradation was found attendant with the appearance of other oxide point defects: EX, E'_γ, and E'_δ [62, 63, 64]. A similar center (g=2.0028; ΔB_{pp}=3.6-6 G) was also observed in fused silica upon the interaction with gaseous SiO during annealing at ~1140 $^\circ C$ [65]. Later two hf doublets (162$\pm$5 G and 279$\pm$2 G) could be discerned in thermal SiO$_2$ on Si subjected to 1 h vacuum annealing at ~1250 $^\circ C$ and additional VUV irradiation [64]. These doublets were centered at the (central) Zeeman signal of the S center, and accordingly, interpreted as corresponding hf structure. The spectral intensity of the outer doublet appeared somewhat larger as compared to the inner doublet; However, given the large experimental uncertainty, the intensity of these might well be equal within the experimental error. Further interpretation required more discriminative experimental information.

The experimental breakthrough realized by observation of two additional doublets, in the S defect ESR spectrum, assigned as hf structure, has stimulated further theoretical work. Based on generalized-gradient DFT work [66], the defect has been identified with the Si$\equiv$SiO$_2$ center, where the two doublets could be successfully modeled: The principal outer doublet would arise from the defect Si atom, while the weaker inner doublet would arise from the delocalized spin density on the Si atom in the first neighbor shell of the defect Si atom.

The EX center

Another defect of interest for the current work is EX: An SiO$_2$-associated defect generally observed in Si/SiO$_2$-entities after thermal treatment. The EX center was first reported [67] for as-prepared SiO$_2$ thermally grown on (111)Si in dry O$_2$ at 700-850 $^\circ C$. Using K-band ESR at low temperatures a narrow isotropic signal was observed with a g value of g=2.00246$\pm$0.00003 and line width ΔB_{pp}=1.0$\pm$0.05 G together with a ^{29}Si hf doublet of splitting A=16.1$\pm$0.1 G. Later Stesmans *et al.* [69] reported the observation of EX
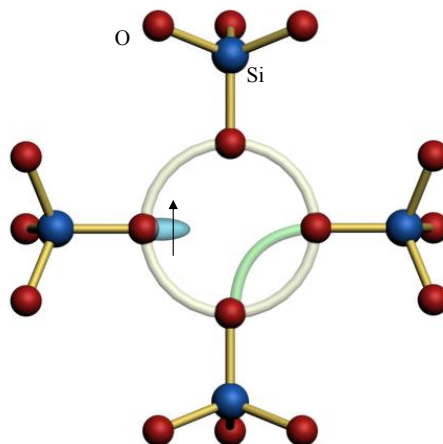
Figure 1.10: *A schematic representation of the proposed model of the EX center [68].*

in dry thermal SiO_2 in (100) and (111)Si/SiO_2 entities. From this study it was shown that the EX areal defect density depends on the grown oxide thickness (d_{ox}), that EX is only detected from $d_{ox} \sim 70$ Å onwards with a maximum density at $d_{ox} \sim 125$ Å and is mainly located in the top 45 Å of the oxide layer. The detection of part of the ^{17}O hf structures of EX in ^{17}O enriched (111)Si/SiO_2 structures [68] resulted in the suggestion of a preliminary model where EX consists of a hole delocalized over four oxygen dangling bonds formally at the site of a Si vacancy. In another view, it has been described as an agglomorate of four oxygen-related hole centers (OHC's) [70]. A schematic representation of the suggested model for the EX center is shown in Fig. 1.10.

Over the years EX has been observed in a variety of Si/SiO_2 entities and SiO_2 samples such as, e.g., oxidized porous Si layers [71, 70, 36], thermally degraded Si/SiO_2 [63], silicon nanowires [72, 73, 74], ultra fine silicon particles [75], and in stacks of nm-thick layers of SiO_x, Al_2O_3, ZrO_2, and HfO_2 on (100)Si [76, 77, 78]. Dohi *et al.* suggested the presence of two different variants in ultra fine Si particles [75], exhibiting the same g value but a different saturation behavior, which they labeled EX_L and EX_H. This work further suggested that the EX_H center observed upon annealing of the particles in vacuum at 900-1000 $°C$ is similar to the EX center described above, and that the EX_L center observed upon annealing at 600-700 $°C$ is identical to the defect reported by Kusumoto [79] in Si powders crushed in room ambient which Dohi *et al.* suggest to be related to the
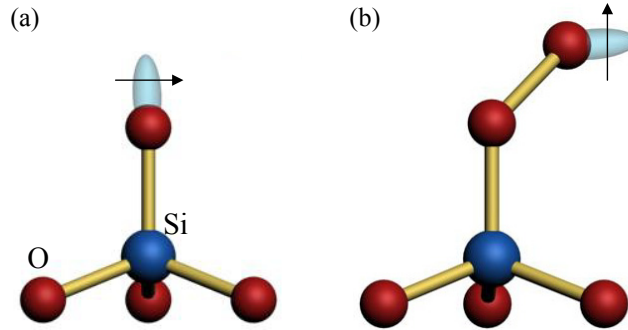
Figure 1.11: *A schematic representation of the proposed generic entity of two OHCs: (a) the NBOHC [80], and (b) the POR [81].*

Si-OH structure; however, no detailed atomic model has been provided.

The oxygen associated hole centers

For reasons of completeness we will briefly discuss two types of *OHCs*: the *POR* which is relatively more prevalent in silicas with a low OH content and the *NBOHC* which tends to dominate in silicas with a high OH content [4]. The latter is attributed to ≡Si-O• species, as illustrated in Fig. 1.11 (a). Originally it was isolated by ESR in γ-irradiated fused silica with a high OH content [80] and a first confirmation of this model was obtained by Stapelbroek *et al.* [82] who measured the unpaired electron hf interaction with ^{17}O nuclei in an isotopically enriched sample. Further experimental evidence was provided by the observation of the hf interaction with just one silicon in a ^{29}Si enriched sample [83].

The *POR* was identified as a Si-O-O• entity in a study on 36 % ^{17}O enriched neutron irradiated silica glass [81]. The suggested model is presented in Fig. 1.11 (b). This assignment was later corroborated by a study of the same defect in ^{29}Si enriched samples, which, in agreement with the model, demonstrated the hf interaction with a single silicon atom [83].

1.2.3 Extrinsic defects in a-SiO$_2$

In addition to the intrinsic point defects various extrinsic, or impurity related, point defects have been observed in a-SiO$_2$ [4]. In undoped irradiated a-SiO$_2$ atomic hydrogen H^0 is one of the most commonly encountered impurity associated defects, although it should be specified as a low temperature
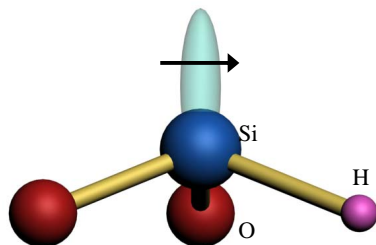
Figure 1.12: *A schematic representation of the generic entity of the 73-G doublet.*

defect. As generally created by ionizing radiation, it remains relatively stable below $\sim$100 K, but it anneals out rapidly above $\sim$130 K, mainly as a result of dimerization (H_2 formation). Its ESR resonance signal is made up of a pair of sharp lines centered on g=2.00 with a splitting of $\sim$505 G due to the hf interaction with ^{1}H (99.98% natural abundance, I=1/2).

Another H-impurity related defect observed in various types of undoped a-SiO$_2$ [15, 84] is the so-called *73-G doublet* attributed to an E' type defect with a H atom in the back bond instead of O, as shown in Fig. 1.12.

In doped a-SiO$_2$ and in silicate glasses, the number of impurity related defects observed by ESR is almost unlimited. Here we will focus on P-associated point defects in SiO$_2$ as their discussion will constitute a basis for the analysis of P-associated defects in high-κ oxides, presented in chapter 3.

P-associated defects in SiO$_2$-based materials

Uchida *et al.* succeeded in the incorporation of P ions in hydrothermally grown quartz crystals [85, 86]. Upon x or γ-irradiation of the doped crystals, ESR measurements performed at $\sim$40, 120, and 290 K revealed three sets of ^{31}P hf lines labeled $P(I)$, $P(II)$, and $P(A)$, where $P(I)$ and $P(II)$ were observed as separate ESR signals at low temperatures ($T < 140\ K$) and $P(A)$ appears at high T. It was demonstrated that the three sets of resonances are separate but related appearances of an unpaired electron localized at a pentavalent P ion which occupies substitutionally a Si site: $P(I)$ is the ground state of $[PO_4]^0$, $P(II)$ is the first accessible excited state of $P(I)$, and $P(A)$ is the dynamic average. Based on the symmetry properties a structural model was proposed as presented schematically in Fig. 1.13 (a), introducing an appreciable displacement of the P nucleus. Calculations based on DFT of the hf parameters agree well with the experimental values and also indicated that the incorporation of P in the c-SiO$_2$ network results in a significant perturbation of the α-quartz structure surrounding

Table 1.3: *Overview of the ESR data in the literature on the different P-associated defect centers observed in SiO$_2$-based glasses and P-doped c-SiO$_2$ together with the corresponding principal values of the g and A matrices. Results are obtained at X-band frequency.*

Defect label	Oxide and damage	g	A(G)
P_1	10P$_2$O$_5$-90SiO$_2$	g_1=2.002	A_1=1030
	x- or γ-irradiated [a]	g_2=1.999	A_2=850
		g_3=1.999	A_3=850
	PSG films on Si	g_1=2.003	A_1=989
	VUV irradiated [b]	g_2=1.998	A_2=789
		g_3=1.998	A_3=785
P_2	10P$_2$O$_5$-90SiO$_2$	g_1=2.001	A_1=1300
	x- or γ-irradiated [a]	g_2=2.001	A_2=1150
		g_3=2.001	A_3=1150
	PSG films on Si	g_1=2.010	A_1=1360
	VUV irradiated [b]	g_2=1.980	A_2=1120
		g_3=1.980	A_3=1120
$P(I)$-variant of	P-doped α-quartz	g_1=2.0012	A_1=1228.93
P_2 [d]	x- or γ-irradiated [c]	g_2=2.0032	A_2=1086.86
		g_3=1.9991	A_3=1074.84
$P(II)$-variant of		g_1=2.0013	A_1=1159.72
P_2 [d]		g_2=2.0034	A_2=1025.14
		g_3=1.9991	A_3=1012.22
$P(A)$-variant of		g_1=2.0010	A_1=1139.02
P_2 [d]		g_2=2.0025	A_2=1120.99
		g_3=2.0003	A_3=1057.79
P_4	10P$_2$O$_5$-90SiO$_2$	g_1=2.0014	A_1=355.2
	x- or γ-irradiated [a]	g_2=1.9989	A_2=-43.8
		g_3=1.9989	A_3=-43.8
	PSG films on Si	g_1=2.016	A_1=274.5
	VUV irradiated [b]	g_2=1.9989	A_2=-43.5
		g_3=1.9989	A_3=-43.5
$POHC^s$	10P$_2$O$_5$-90SiO$_2$	g_1=2.0179	A_1=54
	x- or γ-irradiated [a]	g_2=2.0097	A_2=52
		g_3=2.0075	A_3=48
	PSG films on Si	g_1=2.0185	A_1=54
	x-irradiated [e]	g_2=2.0115	A_2=49
		g_3=2.0082	A_3=47
$POHC^m$	PSG films on Si	g_1=2.0514	A_1=55
	x-irradiated [e]	g_2=2.0079	A_2=50
		g_3=2.0032	A_3=44

[a] See Refs. [4, 61].
[b] Deposited by pressure induced CVD, see Ref. [87].
[c] See Ref. [85, 86].
[d] $P(I)$ is ascribed to the ground state of P_2, $P(II)$ is the first accessible excited state of $P(I)$, and $P(A)$ is the dynamic average. $P(I)$ and $P(II)$ are observed as separate ESR signals at low temperatures ($T < 140\ K$) and $P(A)$ appears at high T [85, 86].
[e] Deposited by subatmospheric CVD, see Ref. [88].
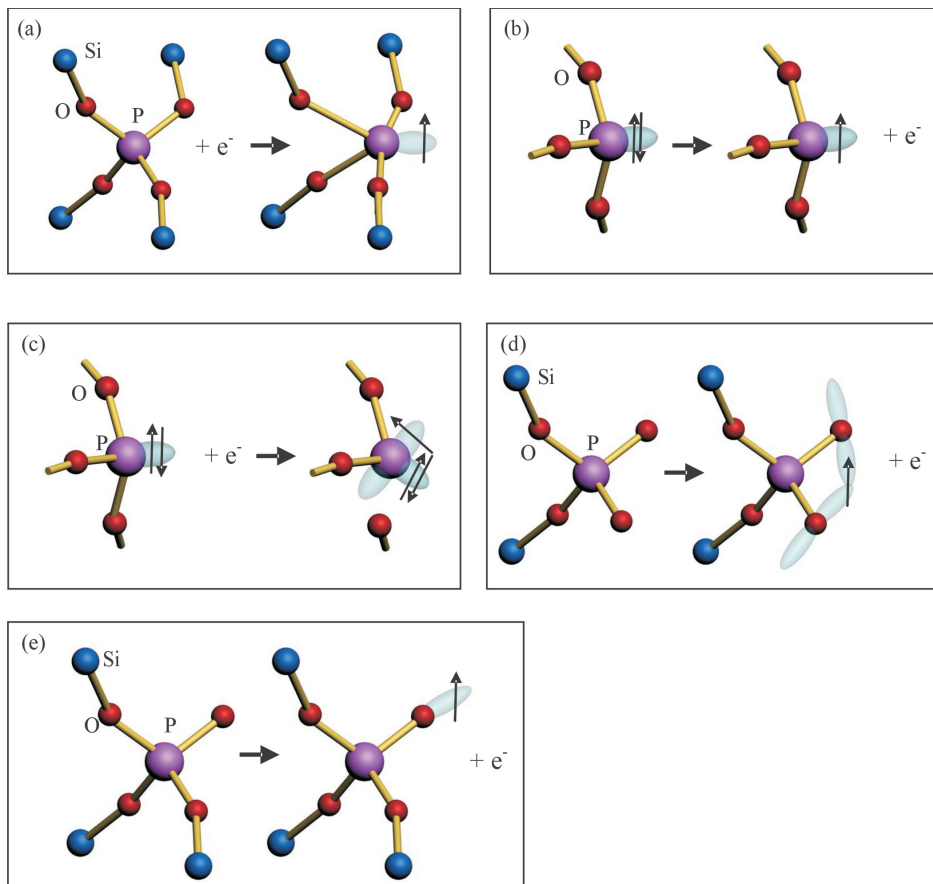
Figure 1.13: *Overview of the conceptual models proposed in literature for the formation of P-associated defects in SiO$_2$-based glasses: (a) P(I), P$_2$ [85, 86], (b) P$_1$ [61], (c) P$_4$ [61], (d) POHC^s [61], and (e) POHC^m [61].*

the impurity [89, 90].

Griscom *et al.* reported on the observation of four different ^{31}P doublets in glassy 10P$_2$O$_5$-90SiO$_2$ subjected to x- or γ-irradiation which they labeled P_1, P_2, P_4, and $POHC$ [61]. The nomenclature P_1 and P_2 was taken from Weeks and Bray [91] who studied P-associated defects in γ-irradiated P$_2$O$_5$ and alkali phosphate glasses as these defects appeared to be essentially identical to those observed in P-doped SiO$_2$. The P_1 and P_2 centers are characterized by a very large hf splitting (A_{iso}~910 G and ~1200 G, respectively; cf. Table 1.3 for $A_{iso}=\frac{A_1+A_2+A_3}{3}$). The P_1 defect is suggested to be the phosphorous analogue of the Si E' center in SiO$_2$ presumably formed by trapping a hole on a three fold coordinated P atom substitutionally occupying a three fold coordinated Si atom at an E' center site. The proposed steric model is shown in Fig. 1.13 (b). The P_2 center appeared to be identical to the $[PO_4]^0$ center reported by Uchida *et al.* [85, 86].

The P_4 and $POHC$ defects both exhibit a much smaller hf splitting than P_1 and P_2 (cf. Table 1.3). The P_4 center has been suggested to originate from the three fold coordinated P precursor site as P_1 but is formed by trapping an electron as depicted in Fig. 1.13 (c). Two different variants of the $POHC$ (phosphorus oxygen hole center) were observed: A stable variant ($POHC^s$) and a metastable variant ($POHC^m$) only observed at low temperatures ($T \leq 300$ K). The $POHC^s$ was fully characterized and suggested to be a hole trapped on a pair of non bridging oxygens bonded to the same phosphorous, see Fig. 1.13 (d). The $POHC^m$ was tentatively assigned to a hole metastably trapped on the lone non-bridging oxygen, as depicted in Fig. 1.13 (e).

The P-associated defect centers have not only been observed in bulk P-doped silica glass but also in thin films of SiO$_2$-based glasses on Si [92, 13, 87, 88]. Warren *et al.* observed the $POHC^s$ in phosphosilicate (PSG) and borophosphosilicate (BPSG) dielectrics deposited on Si by chemical vapor deposition (CVD) subjected to VUV, x-ray irradiation, or hole injection [92]. Based on the charge trapping behavior of the defect, a different model was proposed for the $POHC^s$ where the spin active state would be positively charged instead of neutral. This alternative model is the same as the model proposed by Griscom *et al.* for the metastable variant of the POHC. Later on Fanciulli *et al.* rejected this alternate model for the $POHC^s$ and retained the model proposed by Griscom *et al.* based on the combination of DFT calculations and UV-Raman and ESR measurements on PSG films deposited on Si in a single chamber using subatmo-
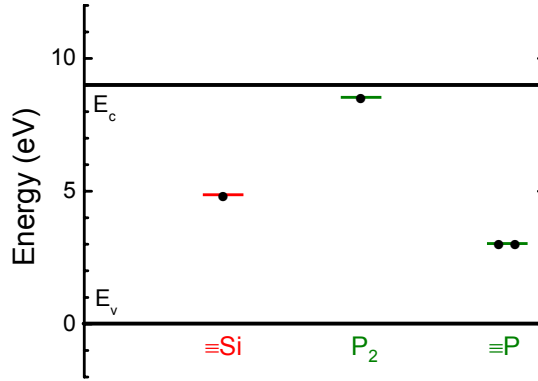
Figure 1.14: *Calculated energy levels, based on DFT, associated with various defect configurations located in the band gap (∼9 eV) of SiO_2. Defects shown include the silicon dangling bond ($\equiv Si$), the P_2 center, and the precusor of the P_1 and P_4 defects ($\equiv P$).*

spheric CVD, and subsequently subjected to x-ray irradiation [88]. Both the $POHC^s$ and $POHC^m$ centers were observed and modeled. In a different work, in addition to the $POHC^s$, the P_1 and P_2 centers were observed in atmospheric pressure CVD deposited BPSG films on Si subjected to VUV irradiation, electron, and/or hole injection [13]. The P_1, P_2, and P_4 defect centers have been observed as well in PSG films deposited on Si by pressure induced CVD, after subjection to VUV irradiation [87].

Theoretical work based on DFT studies showed that the introduction of P impurities in silica introduces defect states in the band gap, as shown in Fig. 1.14. In particular, the P_2 defect has been assigned to be a hole trap [93].

1.3   Defects in the Si/high-κ system

As outlined in the International Technology Roadmap for semiconductors (ITRS) [21], continued scaling of complementary metal-oxide-semiconductor (MOS) technology will require the replacement of the conventional SiO_2 gate insulator by an alternative dielectric of higher κ in the near term years. The projected advancement in technology nodes and the related scaling of some of the device dimensions over the predicted years of production are shown in Table 1.4. As already outlined, high-κ gate dielectric metal oxides permit the usage of physically thicker gate dielectrics to obtain the same effective capacitance as with thinner SiO_2 gate dielectrics, while

Table 1.4: *Technology nodes, gate lengths, and gate dielectric EOTs for future high performance applications [21] in current MOSFET-based technology.*

Year of production	2007	2010	2013	2016
Technology node (nm)	65	45	32	22
Physical gate length (nm)	25	18	13	9
EOT (nm)	0.8-0.9	0.7	0.6	0.5

significantly reducing the probability for direct tunneling [19]. For that purpose, a large variety of (metal) oxides have been investigated as possible candidates, including metal oxides in their simplest form such as HfO_2, ZrO_2, Al_2O_3, La_2O_3, and others [19, 94], as well as more complex varieties such as silicates, aluminates, pseudo binary mixtures and multi metal oxide compounds. Currently, HfO_2 or better stated HfO_2-based composites (e.g., $HfSi_xO_yN_z$), have emerged as most promising future gate oxides [21, 95].

In order to be successful the replacing oxide must meet various requirements [21, 19, 20]: The dielectric constant should be somewhere between 10 and 30, the high-κ oxide must be an insulator with a band gap over 5 eV and exhibiting sufficient band offsets with Si, it should have a high quality interface with Si and a low interface trap defect density, it should exhibit good thermodynamic stability with Si, and good dopant barrier properties.

The various candidate materials have been intensively studied by numerous material characterization techniques providing a wealth of useful information on the microstructure, bonding chemistry, and composition of the newly composed Si/high-κ stacks [96, 97, 98, 99, 100, 101, 102, 103, 104, 105, 106, 107]. Also, using electrical techniques such as capacitance-voltage (C-V) and current-voltage (I-V), the investigation of the electrical performance (transport, charge trapping, and presence of detrimentally active interface traps) has received much attention [108, 109, 110, 111]. However, when it comes to assessing the atomic nature of these electrically active traps these techniques, superb as they are, inherently fall short. That information can in principle be obtained by ESR probing of occurring point defects at the Si/high-κ interface and in the high-κ oxide.

1.3.1   The Si/high-κ interface

The first ESR study of paramagnetic point defects at the interface of a
Si/high-κ structure was conducted by Stesmans and Afanas'ev [112, 113].
The initial K-band work studied (100)Si/SiO$_x$/ZrO$_2$ and (100)Si/Al$_2$O$_3$/ZrO$_2$
stacks (SiO$_x$ refers to nonstoiciometric Si dioxide, with $1{\leq}$x${\leq}2$) with nm-
thin layers grown at 300 $^\circ C$ by atomic layer CVD (ALCVD) using trimethy-
laluminium, ZrCl$_4$, and H$_2$O as precursors. The only defects observed in all
stacks were the P_b-type defects P_{b0} and P_{b1} –generally the unique ESR fin-
gerprint of an Si/SiO$_2$ interface. Their presence indicated that not only the
(100)Si/SiO$_x$/ZrO$_2$ interface, but also the (100)Si/Al$_2$O$_3$/ZrO$_2$ interface is
Si/SiO$_2$-type, in terms of inherent interface defects. In the as-deposited
samples the observed signals were weak, but upon VUV activation the de-
fect densities exceed those generally observed for standard (100)Si/SiO$_2$.
The g matrix appeared to be identical, within experimental error, to that
observed for the P_{b0} and P_{b1} defects in SiO$_2$, but the observed signals were
somewhat broadened, indicating that the interface is under enhanced stress.
However through subsequent application of an appropriate thermal treat-
ment, an interface quality close to that of standard thermal Si/SiO$_2$ could
be realized.

   This was confirmed by electrically detected magnetic resonance on AL-
CVD (100)Si/Al$_2$O$_3$ and (100)Si/ZrO$_2$ entities [114] and two X-band ESR
works on ALCVD grown (100)/Al$_2$O$_3$ [115, 116]. Cantin *et al.* [115] also re-
ported on an additional center, the D center, generally ascribed to unpaired
Si bonds in disordered a-Si. The authors suggested that part of the defects
is present at the interface or in the dielectric. It is, however, more likely
that all the D centers were located in the lateral cleavage planes and/or
substrate back. This was suggested by Stesmans *et al.* [77] and later on
demonstrated by Jones and Barklie [116].

   Two more works focussed on the interface defects in Si/HfO$_2$ struc-
tures [117, 118]. One work compared (100)Si/HfO$_2$ entities grown by three
variants of CVD [117]. also here, in the as-deposited state, the P_b-type de-
fects were reported as predominant defects. In agreement, a second X-band
work reported the observation of P_b defects at the interface of nominally
(111)Si/HfO$_2$($145\ nm$) entities manufactured via ALCVD using the nitrato
precursor Hf(NO$_3$)$_4$ (NCVD) [118].

   One work focussed on the observation of point defects in the SiO$_2$-type
interlayer in Si/SiO$_x$/ZrO$_2$, Si/Al$_2$O$_3$, Si/Al$_2$O$_3$/ZrO$_2$ and Si/SiO$_x$/HfO$_2$
stacks with nm-thick high-κ layers deposited at 300 $^\circ C$ in an ALCVD re-
actor [77]. Upon post-deposition oxidation at 650-800 $^\circ C$ the E' and EX

defects –SiO$_2$ associated defects– were observed in all stacks, as well as a 95-G doublet in the Si/SiO$_x$/ZrO$_2$ system. It was suggested that the appearance of the SiO$_2$-specific point defects indicated a modification and/or additional growth of the SiO$_2$-interlayer. The results on the E' center also revealed that the established interlayer in Si/SiO$_x$/ZrO$_2$ is electrically drastically inferior to standard thermal SiO$_2$ on Si, while the quality of the inter layer in the Si/HfO$_2$ system was found to be qualitatively close to standard thermal SiO$_2$.

There appears to be a consensus in ESR literature that P_b-type defects are inevitably present at the Si/high-κ interface, indicating that the formation of an SiO$_{2(x)}$ interlayer is endemic for these Si/high-κ metal oxide systems. This way, as evidenced by both independent electrical measurements [108, 109, 110, 111] as well as ESR observations [112, 113, 77], an interface is realized of technological quality in terms of interface state density and passivation behavior in hydrogen, much like the standard thermal Si/SiO$_2$ system. However the presence of such an interlayer is undesired in terms of EOT consideration, the more so with increasing relative thickness of the 'low-κ' SiO$_2$ interlayer. Yet, since its occurrence seems hard to prevent in any realistic application, the insertion of an (in thickness) well-controlled SiO$_2$ layer of minimal thickness is currently adopted as a *modus vivendi* route of progress [94, 119]. The presence of an SiO$_{2(x)}$ interlayer
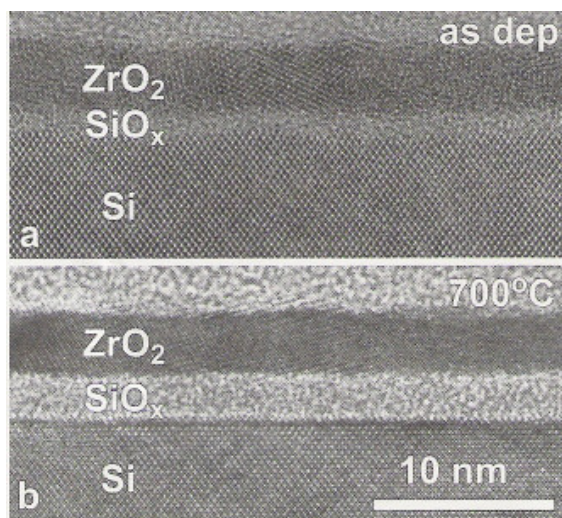
Figure 1.15: *HRTEM images of a Si/SiO$_x$/ZrO$_2$ stack (a) before and (b) after post deposition annealing in O$_2$ at 700 °C for 15 min.*

has more directly been demonstrated by numerous topographic/imaging techniques, such as medium-energy ion scattering (MEIS), high-resolution transmission electron microscopy (HRTEM) and x-ray photoelectron spectroscopy (XPS) [19, 94, 120, 121, 122, 107, 101]. Fig. 1.15 shows a HRTEM picture of a $Si/SiO_x/ZrO_2$ stack before and after post deposition annealing in O_2 at 700 $°C$ for 15 min [123]. The 100 nm thin ZrO_2 layers were deposited by ALCVD at 300 $°C$ using $ZrCl_4$ and H_2O sources. The presence and additional growth upon annealing (by a factor $\sim$2.5 in thickness) of the SiO_x layer is nicely demonstrated.

1.3.2   Intrinsic defects in high-κ oxides

Very little is known about occurring intrinsic point defects in high-κ oxides. Only ZrO_2 has been intensively studied as it has been widely used as active catalyst for many reactions [124, 125, 126, 127]. Three types of defects are generally observed in ZrO_2: (a) an axial symmetric signal generally attributed to Zr^{3+} ions in the bulk or at the surface, (b) an isotropic or slightly axial symmetric signal attributed to electrons trapped in oxygen vacancies (F-centers), and (c) a paramagnetic oxygen related center (O_2^--type). However, since the only isotope of Zr with a nuclear spin different from zero has a rather low natural abundance (^{91}Zr; 11.22%) and a high nuclear spin (I=5/2), the observation of any hf splitting originating from Zr may appear quite hopeless. Consequently, the observed ESR signals cannot be conclusively identified and their origin and/or location is still under discussion.

For the high-κ oxide currently considered of most technological relevance, HfO_2, only a few ESR studies, concerning possible intrinsic point defects in the dielectric, exist: One work reports on the observation of two paramagnetic defects in thin ALCVD deposited HfO_2 layers on (100)Si after photoinjection of electrons [128]. This is the only work so far existing in the literature reporting on the ESR observation of intrinsic point defects in high-κ layers deposited on Si. Other work reports on the characterization of defects in monoclinic HfO_2 powders [129, 130]. Here a brief overview will be given of the different "intrinsic" point defects observed by ESR in ZrO_2 and HfO_2, with the observed g values gathered in tables 1.5, 1.6, and 1.7. To our knowledge no point defects have been observed by ESR in other high-κ oxides than ZrO_2 or HfO_2.

The Zr^{3+}/Hf^{3+} defect

In ZrO_2 outgassed in vacuum at 623 K and subsequently heated in air, Torralvo *et al.* observed an axial symmetric ESR signal [124]. Based on crystal field theory stating that for a d^1 ion in a tetragonally or orthorombically distorted cube or in trigonally distorted octahedra the corresponding g values always fulfill $g_\perp < g_e$ and $g_\parallel < g_\perp$, the observed ESR resonance was assigned to Zr^{3+} ions. The possibility of an impurity, however, was also considered. Later, Azzoni *et al.* observed a similar axial symmetric signal in single crystals of yttria stabilized zirconia subjected to x-ray irradiation [131, 132]. Based on symmetry properties of the observed spectra, concerning g values and line broadening, the authors assigned the defect to a trapped electron in a 4d^1 configuration of the 7-fold coordinated zirconium atoms near an oxygen vacancy. Morterra *et al.*, however, concluded that the axial symmetric signal they observed [125] during their study of the formation and reactivity of paramagnetic centers in ZrO_2 annealed in vacuum originates from Zr^{3+} ions located on the surface of zirconia. This assignment was followed by many others [126, 133, 127, 134, 135]. However, Orera *et al.* did not agree with the surface location of the observed Zr^{3+} defects: Studying intrinsic defects in yttria and calcia stabilized zirconia single crystals subjected to x-ray irradiation through combining ESR, optical absorption, and photo emission techniques, the authors assigned the observed axial symmetric signal to electrons trapped by Zr^{4+} ions perturbed by two oxygen vacancies placed at the opposite corners of the anions cube [136]. The idea of the Zr^{3+} sites located in the bulk of the dielectric near oxygen vacancies, as originally proposed by Azzoni *et al.* [131], was also adopted by many authors [137, 138, 139, 140, 127].

From the above, it would thus appear there to exist some disagreement in the literature on the location of the Zr^{3+} sites. It could, however, also be that there exist in fact two types of Zr^{3+} entities exhibiting similar g values, one located at or near the surface and another located in the bulk of the oxide [127]. But it should be kept in mind that without the observation of any hf structure originating from the low abundant ^{91}Zr nuclei, the assignments of the observed axial symmetric signals to Zr^{3+} entities is merely suggestive and definitively not conclusive.

One other possibility is that the defect is not intrinsic but impurity related. Ben-Michael *et al.* observed a sample dependence of the defect density of the axial symmetric signal they observed in yttria and calcia stabilized zirconia single crystals [141]. Supported by the results of Ermakovich [143] who found a very similar signal in γ-irradiated Ti doped

Table 1.5: *Comparison of the different axial symmetric defects observed by ESR in different ZrO_2 and HfO_2 samples. The list is not exhaustive.*

Sample	$g_\parallel$	$g_\perp$	Assignment	Ref.
ZrO_2 gels	1.956	1.981	Zr^{3+} or impurity	[124]
yttria stabilized ZrO_2	1.989	1.852	Zr^{3+} near O vacancy	[131]
ZrO_2 powder	1.953-1.975	1.978	Zr^{3+} at surface	[125]
yttria and calcia stabilized ZrO_2	1.989	1.860	impurity (Ti^{3+})	[141]
yttria and calcia stabilized ZrO_2	1.989	1.852	Zr^{3+} near two O vacancies	[136]
ZrO_2 nanopowder	1.961	1.974	Zr^{3+} near O vacancy in bulk	[137]
calcinated zirconium hydroxide	1.956	1.973	Zr^{3+} at surface	[133]
zirconium silicates	1.982	1.973-1.963	Zr^{3+} inside pore structure	[127]
zirconium silicates	1.958	1.977	Zr^{3+} at surface	[127]
pure and Cr doped ZrO_2	1.953	1.978	Cr impurity	[142]
sulfated ZrO_2	1.951	1.979	Zr^{3+} at surface	[126]
ZrO_2 powder	1.957	1.975	Zr^{3+} at surface	[134]
(100)Si/HfO_2	1.96	1.96	Hf^{3+}	[128]
m-HfO_2 powder	1.938-1.941	1.971-1.970	Hf^{3+} or impurity (Ti^{3+}, Zr^{3+})	[129]

samples, the authors pointed towards the Ti^{3+} reduced state as being responsible for the defect. This attribution was supported by Merino *et al.* who found a correlation between the defect density and the Ti concentration [144]. Recently, another work [142] reported on the correlation of the defect density of the axial symmetric defect observed in pure zirconia and Cr doped zirconia with the Cr concentration. The assignment was substantiated by the observation of the most intense hf component of the [53]Cr-induced (I=3/2 and 9.501% natural abundant) hf structure.

Also in the HfO_2 powders similar axial symmetric signals were observed [129, 130]. The authors suggest that the associated defect is probably located in the bulk of the material, but are very cautious with the assign-

ment. They suggest that in accordance with the ZrO_2 cases reported, the defect most probably involves Hf^{3+}, but Zr^{3+} and Ti^{3+} cannot be ruled out. In (100)Si/HfO$_2$ subjected to a post-deposition N$_2$ anneal at 420 $°C$ and negative charge injection (using the UV light corona ion technique) a weak signal at zero crossing g=1.96 is tentatively assigned to a Hf^{3+}-related ion defect [128] in the HfO$_2$ layer.

It seems that the observation by ESR of the axial symmetric signal in ZrO$_2$ and HfO$_2$ (after the appropriate heat treatment or irradiation) is quite systematic. There is however a substantial spread in the reported g values for this signal observed in ZrO$_2$: $g_\perp$ ranges from 1.981 to 1.852 and $g_\parallel$ from 1.989 to 1.951 (see Table 1.5). This inconsistency in the reported g values indicates that either the originating defect center must be extremely sensitive to small variations in the ZrO$_2$ matrix leading to the observation of different g values for different ZrO$_2$ samples, or that the observed signals originate from different defect centers. The proposed intrinsic Zr^{3+} center located in the bulk or at the surface possibly near one ore more oxygen vacancies and the impurity centers may all be valid possibilities, but without the observation of any hf structure the real origin of these signals remains obscure.

The F-center

Another signal observed in ZrO$_2$ samples [124, 126, 137, 145, 133, 142, 134, 135] and in HfO$_2$ powders [129, 130] exhibits slightly axial or spherical

Table 1.6: *Overview of some ESR signals observed in ZrO$_2$ or HfO$_2$ assigned to an F-center.*

Sample	$g_\parallel$	$g_\perp$	Ref.
ZrO$_2$ gels	2.002	2.004	[124]
ZrO$_2$ nanopowder[a]	2.003	2.003	[137]
calcinated zirconium[a]	2.0018	2.0018	[133]
pure and Cr doped ZrO$_2$	2.002	2.002	[142]
sulfated ZrO$_2$	2.003	2.003	[126]
ZrO$_2$ powder[a]	2.000	2.000	[134]
m-HfO$_2$ powder[b]	2.003	2.000-1.994	[129]

[a] The observed signal was assigned to an F-center located near the surface.
[b] The observed signal exhibited orthorombic symmetry.

Table 1.7: *Overview of some ESR signals observed in ZrO_2 or HfO_2 assigned to an O_2^- ion center.*

Sample	g_1	g_2	g_3	Ref.
ZrO_2 gels	2.012	2.012	2.004	[124]
calcinated zirconium	2.034	2.010	2.010	[133]
sulfated ZrO_2	2.027	2.010	2.002	[126]
ZrO_2 powder	2.031	2.009	2.000	[134]
(100)Si/HfO_2	2.04	2.01	2.000	[128]
m-HfO_2 powder	2.014	2.013	2.006	[129]

symmetry and has a zero crossing g value around g=2.002-2.003, see Table 1.6. Since this g value is close to the free electron g value (g_0=2.0023) it has been assigned to and F-type defect, i.e., an electron trapped in an O^- oxygen vacancy. Again, also regarding this defect there is some discussion between the different authors whether the vacancy is located in the bulk or near the surface.

The O_2^--type defects

A third defect center observed by ESR in ZrO_2 [124, 126, 145, 133, 127, 134] and HfO_2 [129, 130, 128] exhibits an othorombic g matrix with one g value close to g_0 (see Table 1.7). This signal is attributed to an O_2^- ion based on the *Känzig* and Cohen model [146] for the g matrix of the O_2^- ion in alkali halids widely accepted in literature. From the first order perturbation approximation of the expressions for the principal g values of an O_2^- ion it can be seen that one g value should be close to g_0 and the other two should be greater. The observed O_2^- ions in ZrO_2 and HfO_2 are most probably adsorbed on the surface.

1.3.3   Impurity related defects in high-κ oxides

It still remains undecided whether the defect centers observed in ZrO_2 and HfO_2 described in the previous section should be classified as intrinsic or extrinsic point defects. However, up to the current work (chapter 3), the only undisputable extrinsic defect observed in a high-κ dielectric was the NO_2 radical. Stesmans *et al.* revealed the incorporation of N in NCVD deposited thin HfO_2 films on (100)Si subjected to ^{60}Co γ-irradiation through

the observation of a prominent ESR powder pattern [147]. The spectrum could not be observed in metallo-organic CVD (MOCVD) nor ALCVD deposited HfO_2 on (100)Si. The spectrum only appeared in the NCVD deposited samples after γ-irradiation and not after VUV irradiation.

From measurements performed at two different microwave frequencies the three observed resonance lines were clearly found to originate from a S=1/2, I=1 (with 100 % natural abundance such as ^{14}N) center. The principal values of the g and hf matrices could be obtained (g_1=1.99122, g_2=2.00192, and g_3=2.00555; A_1=49.0 G, A_2=68.5 G, and A_3=51.0 G) incontestably indicating that the spectrum originates from NO_2 radicals (density $\geq$ 55 at. ppm). The ESR spectrum was observed to remain essentially unchanged up to 35 K [148], indicating the NO_2 entities to remain immobilized within the HfO_2 matrix. The molecules were found to be stabilized and likely homogeneous distributed in the a-HfO_2 network. The defects precursor was suggested to be the N$\equiv$[O–HfO$_3$]$_3$ network entity, the NO_2 defects being formed through γ-ray induced structural rearrangements.

Chapter 2

Fundamental point defects in nm-sized silica particles: probing of the network structure

2.1 Introduction

That the Si/SiO_2 entity is likely to soon lose its position as one of the main building blocks of MOS entities in semiconductor industry, does not necessarily result in a loss of all interest in the SiO_2 dielectric. As a result of the current nano-rage the oxide has attracted renewed interest in the form of nanospheres, nano-agglomerates, nanowires, and nanotubes for their potential use in e.g., opto-electronic nanodevices, catalysis, chromatography, and biosensors [149, 22, 23]. In this chapter we will focus on flame aerosol manufactured silica nanoparticles. Interesting for industry is that these fumed silica particles can easily be produced in industrial quantities [150]. Consequently, from their commercial production in the 1940's on, the nanoparticles were introduced in numerous applications. For instance, the material can be found as fillers in toothpaste and car tires, as starting material for optical fibers it may serve as a general gel former [151], and it is found in various food such as bread, ice cream, and margarine [152].

But, even though it is well established experimentally that the electrical and optical properties associated with fumed silica distinctly differ from the bulk silica counterparts [153, 154, 155], very little is known about the exact network structure of the silica particles. One known

piece of information is that the nanoparticles are in the amorphous phase, interpreted as being caused by the extremely fast cooling of the pyrogene silica aggregates formed at 1400-1800 $^{\circ}C$. Consequently, recently a variety of theoretical [156, 157, 158, 159] as well as experimental studies [160, 161, 154, 153, 162, 163, 164, 155, 165, 166] using a range of sensitive techniques such as positron annihilation [161], x-ray diffraction [153], and key photon-solid interaction probes including optical [162, 163, 155] and Fourier transform infrared (FTIR) absorption [160, 154, 153], Raman spectroscopy [153], nuclear magnetic resonance (NMR) [165], and ESR [161, 166], have been reported.

Surprisingly, in the few ESR studies reported, no ESR signals originating from the nanoparticles could be observed [161, 166] which would leave two possibilities: The nanoparticles either differ drastically from the bulk counterparts and to such an extend that the particles would exhibit no point defects such as the E' center, or the occurring (inherent) point defects may be left passivated by bonding to hydrogen in the as-prepared state, thus rendering them ESR inactive. In view of the particular (H-rich) preparation method of fumed silica nanoparticles (*vide infra*) and based on build up experience in the Leuven ESR group, the latter seems more likely. The phenomenon of H-passivation is indeed well known for Si dangling bond type defects such as the P_b [29, 167, 28] and E'-type defects [168] in thermal Si/SiO$_2$. Irradiation by VUV photons ($\sim$10 eV) has been proven to be a most suitable approach to dissociate H from passivated defects [62, 63, 169].

Encouraged by the latter idea, ESR research of fumed silica nanoparticles was re-opened and indeed, the combination of photon excitation and ESR analysis revealed the presence of several (inherent) point defects. The occurring ESR resonances are monitored as a function of post-formation heating and treatment (aging, VUV excitation) in this way using the point defects as atomic probes of the local network structure. Careful characterization and identification of the occurring point defects could possibly provide access to the structural nature of the nanoparticles and reveal possible differences as compared to bulk silica. In a next step, inspired by previous work in our group concerning the structural degradation of thermal SiO$_2$ by high-temperature vacuum annealing [63], the possible influence of SiO on the fumed silica network at elevated temperatures was studied.

2.2 Former studies

From a technological as well as a fundamental point of view, it is of much interest to obtain a good understanding of the properties of the nanoparticles *vis-à-vis* those of the macroscopic counterparts. Here an overview is presented of former studies on fumed silica. Since the *nm*-sized particles have a very high specific surface area ($\sim$100-400 m^2g^{-1}), their surface reactivity and related surface properties have been intensively studied [165, 170, 160]. Bunker *et al.* studied the dissociative chemisorption of various gas species on the dehydroxylated surface of fumed silica [160]. Using FTIR spectroscopy their results showed the presence of highly reactive defect sites. The fast hydrolization of these defects, a factor 10^5 to 5×10^6 higher as compared to fused silica, indicates that the reactivity of the Si–O bonds is promoted by bond strain. An extensive NMR research [165] points out that both mutually hydrogen-bonded and isolated silanols (Si–OH groups) are present at the surface of fumed silica, but only the isolated ones remain after heating at a temperature $T_{an} > 350$ °C. This work also concluded that the high temperature production of the nanoparticles leads to a wider range of variation of Si–O–Si bond angles at the surface of the particles.

Glinka *et al.* extensively studied the photoluminenscence (PL) properties of 7 and 15 *nm* sized nanoparticles compared to bulk silica [164, 163]. In addition to the PL bands observed for bulk silica –i.e., 1.9 and 2.35 *eV* PL bands assigned to bulk $NBOHCs$ and hydrogen related species (such as $\equiv$Si–H), respectively– an additional PL band was observed at 1.79 *eV*. This extra PL band was attributed to a large concentration of surface $NBOHCs$ in the nanoparticles. They suggested that large concentrations of surface structural defects, i.e., E' ($\equiv$Si$^\bullet$) and OHC ($\equiv$Si–O$^\bullet$) defects, result from $\equiv$Si–O–Si$\equiv$ bond splitting during particle formation. The intensity of the PL band attributed to $NBOHCs$ (bulk and surface related) was found to increase as a function of heat treatment in air ($\sim$2 *h*) in the range T_{an}=600-900 °C and dominated the spectrum after annealing at $T_{an} \sim$900 °C. From these results the authors concluded that heat treatment of the silica powders in air at $T_{an} \geq$600 °C gives rise to the formation of $NBOHCs$ by the following process:

$$2(\equiv Si - OH) \longrightarrow (\equiv Si - O\bullet) + (\equiv Si\bullet) + H_2O \uparrow . \qquad (2.1)$$

The concentration of the $NBOHCs$ should thus increase with increasing anneal temperature and become dominant for the sample annealed at $T_{an} \sim$900 °C.

This picture was partially retained when Altman *et al.* ascribed the non-exponential behavior of light absorption in the visible range of the fumed silica nanoparticles to $NBOHCs$ [155]. They suggest that these defects are formed during particle formation. Moreover, the authors believe that the concentration of these defects may be so high that corresponding strong Coulomb disorder leads to a significant narrowing of the optical band gap. A recent paper [162] reports on white light emission from transparent SiO_2 glass prepared from fumed silica, a property that can be of importance for the field of display and lightning technology. The exact origin of the white PL lightening is yet unknown. It was, however, demonstrated that the white PL emission cannot arise from the same defects as the previously observed red ($\sim 2.35 \, eV$) and green ($\sim 1.9 \, eV$) PL bands originating from silica nanoparticles.

Uchino *et al.* extensively studied the microscopic structure of fumed silica combining FTIR spectroscopy, Raman spectroscopy, and high-energy x-ray diffraction [154, 153]. In an initial work they studied the modification of the fumed silica structure under pressure [154]. Compressing the nanoparticles at room temperature at 2 and 5.5 GPa resulted in opaque and translucent samples. At higher pressures (6 and 8 GPa) transparent SiO_2 glass was obtained structurally different from normal a-SiO_2. This irreversible pressure-induced structural transition occurs at lower pressures (2-8 GPa) than would be expected for bulk silica glass ($>10 \, GPa$). As
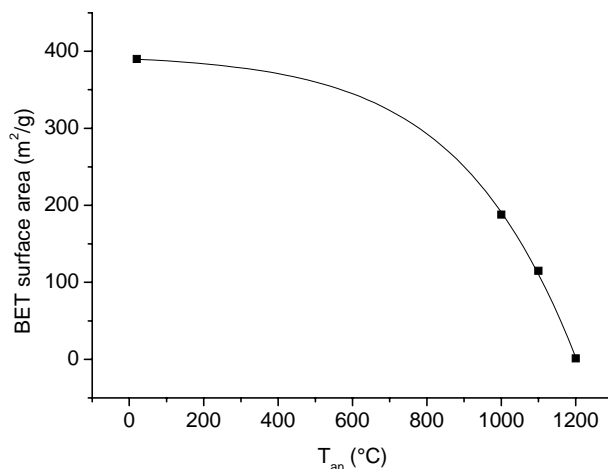
Figure 2.1: *BET surface areas of fumed silica samples heated in air at different temperatures. (Data taken from Ref. [153].)*

these results are most likely linked with the intrinsic structural characteristics of the nanoparticles, this stimulated the authors to extend their structural analysis of fumed silica [153].

Looking at the Brunauer-Emmet-Teller (BET) specific surface areas of the as-recieved and heat-treated ($\sim$2 h in air) fumed silica particles Uchino *et al.* found that the surface area decreases upon heating as illustrated in Fig. 2.1. This decrease was attributed to sintering of the nanoparticles with an onset temperature of $\sim$850 $^\circ C$, as proposed previously [171]. Upon heating at $\sim$1200 $^\circ C$ the surface area dropped below the detection limit ($\sim$1 $m^2 g^{-1}$). This was explained as resulting from the coalescence of the primary particles into bulk-like silica. These changes in the particles morphology could also nicely be seen from the field emission scanning electron microscopy (FESEM) pictures shown in Fig. 2.2.

The FTIR spectra of the fumed silica particles heated up to $\sim$1100 $^\circ C$ distinctly differ from those of the sample heated at $\sim$1200 $^\circ C$ which was very similar to that of bulk silica, as can be seen from Fig. 2.3. Their results thus indicated that the nanoparticles in the as-received state or after annealing in the range 900-1100 $^\circ C$ are structurally different from bulk silica while the fumed silica sample heated at $\sim$1200 $^\circ C$ becomes very bulk silica like. In agreement with the FTIR spectra, the fourier trans-
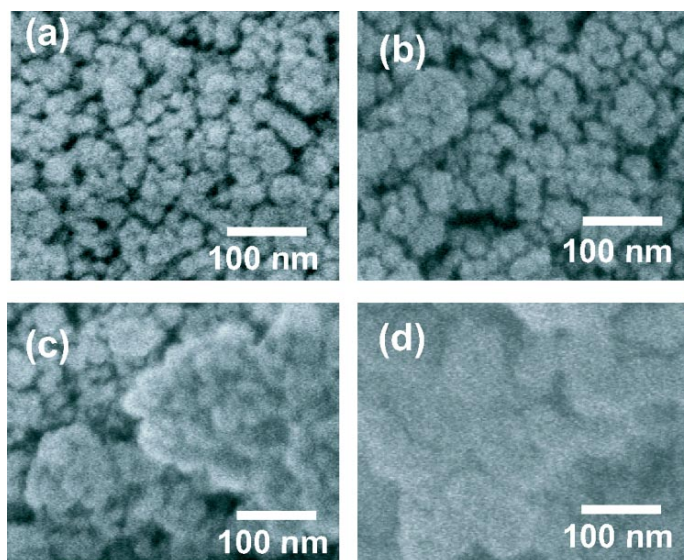
Figure 2.2: *FESEM images of fumed silica after heat treatment in air for 2 h at (a) 900 °C, (b) 1000 °C, (c) 1100 °C, and (d) 1200 °C (taken from Ref. [153]).*

form Raman spectra of the as-received sample and samples heat treated at $T_{an} \sim 900\text{-}1100$ $^{\circ}C$ differ from bulk silica, but nicely coalesce when heated at ~ 1200 $^{\circ}C$ (see Fig. 2.4). The bands at 495 and 606 cm^{-1} attributed to four and three membered silica rings, respectively, were found to be more pronounced for the as-received particles than for bulk silica indicating that the population of small membered rings in the nm-sized silica particles is larger than in bulk silica. From their in situ infrared absorption spectra the authors concluded that the fumed silica network is more flexible and more rigid against applied pressure than bulk silica.

The fumed nanoparticles did not only attract the attention of experimentalists, but were also studied theoretically [156, 157, 158, 159]. Several molecular dynamics (MD) simulations have been reported for silica clusters containing $\sim 10^3$ to $\sim 10^4$ atoms, revealing specific structural properties for the nm-sized particles [159, 156, 157]. From the simulations it was concluded that the nanoparticles have a shell-like structure: The structure and density of the surface of the nanoparticles are substantially different from those of the interior of the cluster. The interior of the cluster was suggested to be structurally equivalent to bulk silica. These results, however, are not completely consistent with the experimental results obtained by Uchino *et al.* [153] as they concluded from their measurements that the structure of the interior of the nanoparticles cannot be equivalent to that of macroscopic SiO_2.

It has been demonstrated that inherent structural defects, as studied by the ESR technique, may serve as atomic sized probes of utmost sensitivity to structural aspects of their local environment (see, e.g., Refs. [172, 29, 173]). So, their characterization and identification may appear a key means to assess the structural nature of the nanoparticles and to reveal possible differences as compared to the bulk silica counterpart. Though being a tool with atomic level physico-chemical sensitivity, very little research has so far been carried out using ESR: Some ESR work has been done on fumed silica in the as-grown state [166] as well as after UV irradiation [161] with photons (~ 5 eV) obtained from a low pressure Hg lamp. However, as mentioned before, in both cases no ESR signals originating from the silica nanoparticles could be observed, likely explaining the faded interest over the years in applying ESR to this field of research.
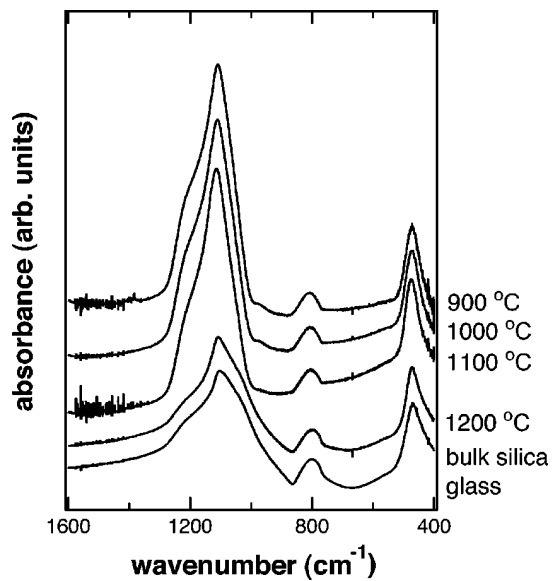
Figure 2.3: *FTIR absorption spectra of fumed silica after heat treatment in air for 2 h in the range $T_{an}\sim$900-1200 °C together with the FTIR spectrum of normal bulk silica glass. All spectra are taken from Ref. [153].*
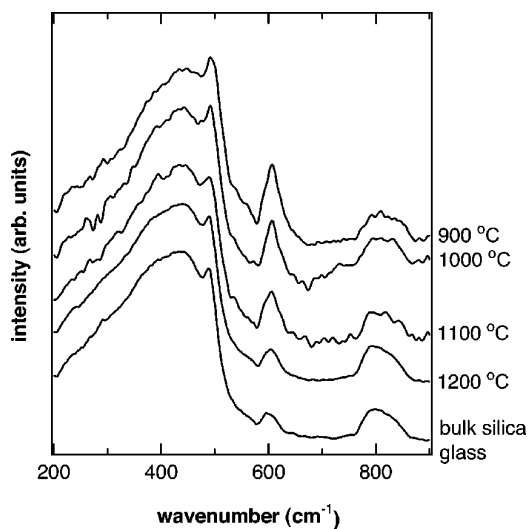
Figure 2.4: *Fourier transform Raman spectra of fumed silica after heat treatment in air for 2 h in the range $T_{an}\sim$900-1200 °C together with the Fourier transform Raman spectrum of normal bulk silica glass. All spectra are taken from Ref. [153].*

2.3   Interactions with SiO at elevated temperatures

In previous work on the structure of thermal oxide on Si [63], the influence of post-deposition heat treatment in an O_2-deficient ambient in the temperature range T_{an}=950-1250 $^{\circ}C$ was studied. The main motive for this work was probing by ESR via generated point defects of the electrically and morphologically well known thermal degradation process effectuated by such annealings to the thermal Si oxide on Si (see, e.g., Refs [174, 62]). In another ESR work the interaction of fused silica with gaseous SiO, in situ provided from co-inserted solid SiO, during annealing at ~1140 $^{\circ}C$ was studied [65]. One of the incentives for these studies was the suspicion raised about the influence of Si/SiO_2 interface-released SiO molecules: Indeed previous work had observed the formation of pores (voids) through the SiO_2 film evidencing the freeing of volatile SiO at the Si/SiO_2 interface through the net reduction reaction Si (s) + SiO_2 (s) → 2SiO (volatile) [174]. Later,
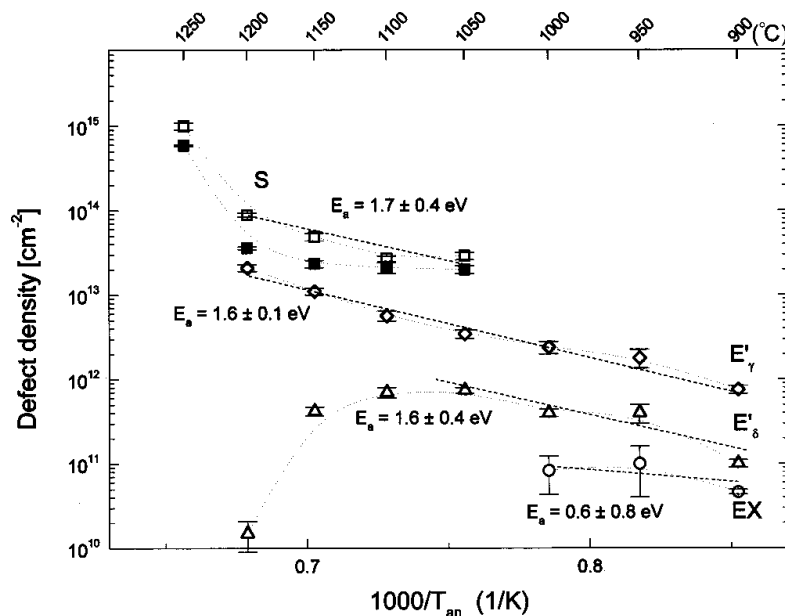
Figure 2.5: *Areal defect densities of $S(\square)$, $E'_\gamma(\diamond)$, $E'_\delta(\triangle)$, and $EX(\bigcirc)$ defects inferred from K-band ESR in standard thermal Si/SiO_2 after ~1 h vacuum anneal at various temperatures, before (solid symbols) and after VUV irradiation under positive bias (standardly +20 V). The figure was taken from Ref. [113].*

the process of outdiffusion and subsequent desorption of the volatile SiO from thermal Si/SiO_2 was evidenced more directly by x-ray photo-electron spectroscopy during post-oxidation vacuum annealing at 800 $°C$ [175, 176]. Nakamura *et al.* [177, 178] demonstrated, using multi-photon ionization spectroscopy, the formation of SiO molecules by the reaction of a Si surface with O_2: $O_2+2Si→2SiO$. The question remained whether the outdiffusion of gaseous SiO would influence the SiO_2 network. It was found that the SiO did indeed affect the SiO_2 network, in fact aggressively degrading it. Such information was revealed through the observation of several types of generated defects including E'_γ, E'_δ, EX, and the predominant exclusive S center. The areal defect densities of the occurring point defects as a function of the in vacuum (~1 h) annealing temperature are shown in Fig. 2.5. A specific finding was that the interaction of the SiO_2 network with SiO at elevated temperatures resulted in an increase in E'_γ density.

2.4 Experimental details

2.4.1 Samples

The samples studied were taken from high-purity pyrogene fumed silica powder of 7 nm average particle size and 380 ± 40 m^2g^{-1} surface area, with a low metallic impurity content. The samples were obtained from Sigma-Aldrich Inc., Missouri, USA. The structure of the material is amorphous. During particle formation and subsequent cooling down, interparticle collisions and subsequent fusion results in the formation of chain-like aggregates from 10 to 30 units, or, put differently, from ~0.1 to 0.2 μm in length. Since fumed silica is fabricated by burning silicon tetrachloride in an oxygen-hydrogen flame at ~1800 $°C$, nominally there should be no carbon present. During formation of the product, hydroxyl groups (3.5-4.5×10^3 μm^{-1}) become attached to some of the silicon atoms on the surface of the silica particles.

2.4.2 ESR spectrometry

Conventional cw absorption-derivative ESR measurements were performed at X (~9.2 GHz), K (~20.4 GHz), and Q-band (~33 GHz) in the temperature range 4.2-300 K. The levels of the magnetic field ($\vec{B}$) modulation B_m and incident microwave power P_μ were properly watched to avoid signal distortion. The hf signals were measured in an (out-of-phase) second harmonic mode in Q-band at relatively high modulation amplitudes (2 G)

and P_μ (5 mW). Typically, an ESR sample comprised $\sim$3 mg of fumed powder.

Separate sets of samples (fresh ones for each thermal step) were sub-jected to post-manufacture baking in vacuum (base pressure $<4\times10^{-6}$ $Torr$) for $\sim$1 h at desired temperatures (T_{an}) in the range 850-1115 $^\circ C$. To study the interaction with SiO at elevated temperatures, again separate samples were subjected to post-manufacture baking in vacuum (base pres-sure $<4\times10^{-6}$ $Torr$) for $\sim$3 h at desired temperatures (T_{an}) in the range 1005-1205 $^\circ C$. But this time each heating procedure was carried out with a suitable amount of the powder tightly sandwiched between two (fresh) slices of Si wafer (0.47 nm thick) with a standard thermal SiO$_2$ (6.5 nm) on top, the SiO$_2$ film facing the inside of the sandwich, as schematically pictured in Fig. 2.6. In this way, it was figured that in diffusing out the SiO released at the Si/SiO$_2$ interface of the slices could interact with the sandwiched fumed particles.

From previous investigations it may be anticipated that in the as-received fumed silica particles, the particular pyrolytic fabrication technique applied (oxy-hydrogen flame) may have resulted in passivation of dangling-bond type point defects by hydrogen (pictured as $\equiv$SiH, $\equiv$Si–OH formation), thus leaving possibly occurring inherent systems of defects in the diamagnetic state and hence disabling ESR detection. More specifically, for defects such as the E'_γ centers, occurring (passivated) precursor sites are pictured as the O$_3\equiv$Si–H entity at the site of an O vacancy [48, 179], while, similarly, for the $NBOHC$, O$_3\equiv$Si–OH (hydroxyl incorporation into the silica matrix) is
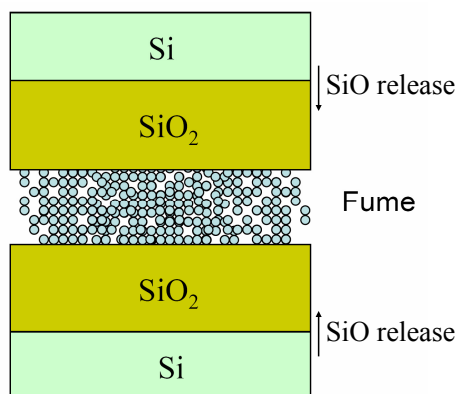
Figure 2.6: *Sketch of the Si/SiO$_2$/fumed silica/SiO$_2$/Si sandwich used for high temperature (1005-1205 $^\circ C$) SiO–fumed silica interaction treatment.*

pictured as an obvious site [48]. So, after initial ESR tests, to maximally reveal defects, samples (both in the as-received state and after additional heat treatment) were subjected at room temperature to prolonged irradiation by VUV (10 eV) photons (flux $\sim 10^{15}$ $cm^{-2}s^{-1}$) obtained from a Kr-resonant discharge lamp sealed with a MgF_2 window to photodissociate H from passivated defects, or put differently, to radiolyse defect–H bonds. Possibly, the treatment may additionally unveil strained or weak bondings (bond rupture) and diamagnetic precursor sites [62, 63]. This, however, would also add to the ultimate goal, that is, acquiring atomic scale information about the SiO_2 particles network, as these sites of defect creation, i.e., strained and/or weak bonding sites, constitute in embryo also imperfections in the a-SiO_2 matrix, although not necessarily concerning nonstoichiometry.

Early on in this work aging effects have been observed to occur in room ambient for at least one defect (*vide infra*). So ESR measurements were first performed immediately upon VUV irradiation and subsequently repeated after the samples were left in room ambient for desired times (one day to weeks). This enabled us to study the characteristics of defect modification in room ambient. For reference, measurements were also carried out on a suprasil I synthetic silica sample, obtained from Heraeus (Germany) containing [OH]$\sim$1200 ppm (by weight), [H_2O]$\leq$600 ppm, and total metal content <1 ppm, subjected to 100 $Mrad(Si)$ ^{60}Co γ-irradiation at 300 K.

2.5 ESR probing of occurring point defects

As anticipated, no ESR signal could be observed in the as-fabricated silica particles. This is ascribed, at least in part, to defect inactivation by hydrogen due to the abundance of H_2 during the flame growth. But that situation changes drastically upon VUV irradiation or after annealing at high temperature. Several signals are observed, their proper spectroscopic isolation, though, being strongly hampered by signal overlap and entanglement. As a result, while at least 5 types of signals could be assigned and analyzed, several interesting resonant responses (mostly of low intensity) remain as yet unidentified. Table 2.1 gives an overview of the observed defect densities as a function of post-manufacture heating and VUV treatment. The various types of defects observed will now be addressed separately.

The presence of SiO release during vacuum annealing at high temperatures only had a significant influence on the observations concerning the E'-type centers. Consequently, the effects of the vacuum anneal in the presence of SiO release (henceforth referred to as SiO-vac. anneal) will be

Table 2.1: *Overview of typical densities of the observed defects as a function of the anneal temperature T_{an} (vacuum anneal) and VUV treatment in fumed silica powder. Quoted values are in units of $10^{14}\ g^{-1}$. To convert the densities to units of $10^{14}\ cm^{-3}$, multiply by 2.3. Entries left blank mean that the corresponding defect could not be detected or the signal appeared too weak for reliable discrimination.*

Sample condition	$[E']$	$[LU2]$	$[OHC]$	$[EX]$	$[CH_3]$
As-received					
As-received + VUV [a]	2.2±0.5		31±3		0.08±0.01
T_{an}=850 °C		0.52±0.05			
T_{an}=850 °C + VUV [a]	2.4±0.5				0.47±0.05
T_{an}=850 °C + VUV [b]	1.0±0.5				
T_{an}=960 °C		60±6		2±1	
T_{an}=960 °C + VUV [a]	1.5±0.5	7.3±0.8		2±1	0.14±0.02
T_{an}=1005 °C				7±0.5	
T_{an}=1005 °C + VUV [a]	3±1			1.5±0.2	0.07±0.01
T_{an}=1115 °C				49±5	
T_{an}=1115 °C + VUV [a]	3.5±1			21±3	

[a] The densities given here are obtained from samples subjected to ∼1 h VUV irradiation.

[b] Several days after VUV irradiation, the sample being left in room ambient.

fully included in the following subsection dealing with the observed E'-type defects.

2.5.1 The E'-type center

Observations

The effect of VUV treatment and heat treatment in vacuum

After VUV irradiation, the SiO_2-specific E' type center (generic entity $O_3{\equiv}Si^\bullet$) is clearly detected in the as-received sample, as shown in Fig. 2.7 for X-band and in Fig. 2.8 (a) for K-band observations, as well as in the samples subjected to post-manufacture baking. A characteristic central-line two-peak powder pattern signal is observed much similar (e.g., regarding width, overall shape) to that of the common E'_γ variant [180, 46] (see section 1.2.2) in bulk silica, characterized by [4] the principal g matrix values g_1=2.0018, g_2=2.0006, and g_3=2.0003. In the K-band ESR spectroscopy a zero crossing g value of g_c=2.00058±0.00005 is typically observed [181, 182] in thermally grown SiO_2 on Si. Detailed computer
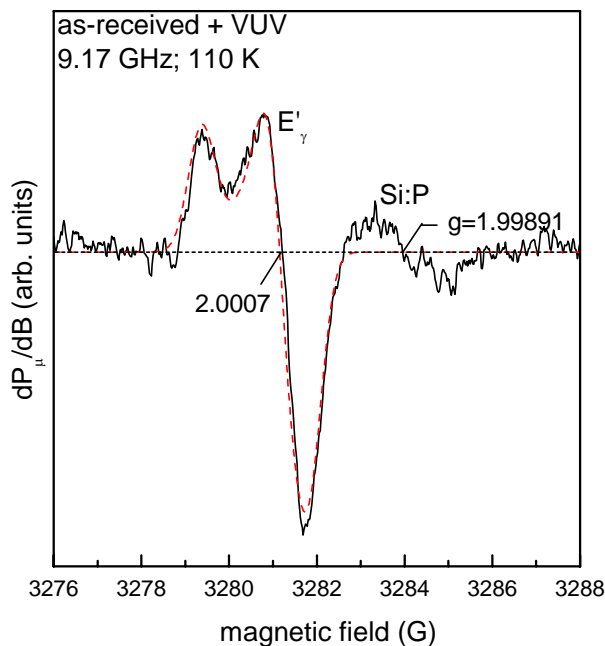
Figure 2.7: *Powder pattern derivative-absorption X-band ESR spectrum of the E′ signal measured immediate upon VUV activation of the as-received fumed silica nanoparticles, using P_μ=0.1 mW, B_m= 0.6 G, and averaging over ~50 scans.*

simulations of the presently observed spectra show slight, but convincing, variations in ESR parameters depending on the applied anneal temperature, elapsed time period between VUV irradiation and ESR measurement as the sample was kept in room ambient, and the sample temperature during the measurements.

In the as-received sample, measured immediately after VUV irradiation, the observed zero-crossing g value g_c=2.00076±0.00005 is slightly, yet well outside experimental error, larger than the one observed for irradiated thermally grown SiO_2 on Si or fused silica, i.e., g_c=2.00058±0.00005 [46, 181, 182]. As a reference the K-band spectrum for suprasil I synthetic silica subjected to 100 $Mrad(Si)$ ^{60}Co γ-irradiation at 300 K is shown in Fig. 2.8 (c). Additional heat treatment, however, affects the E' signal distinctly. Upon annealing at increasingly higher temperatures in the range T_{an}>850 °C, the zero-crossing g value gradually decreases for T_{an}→1115 °C towards the value typically measured for E'_γ in bulk silica's. There is one more remarkable observation: Pertinently, when, after VUV irradiation, leaving
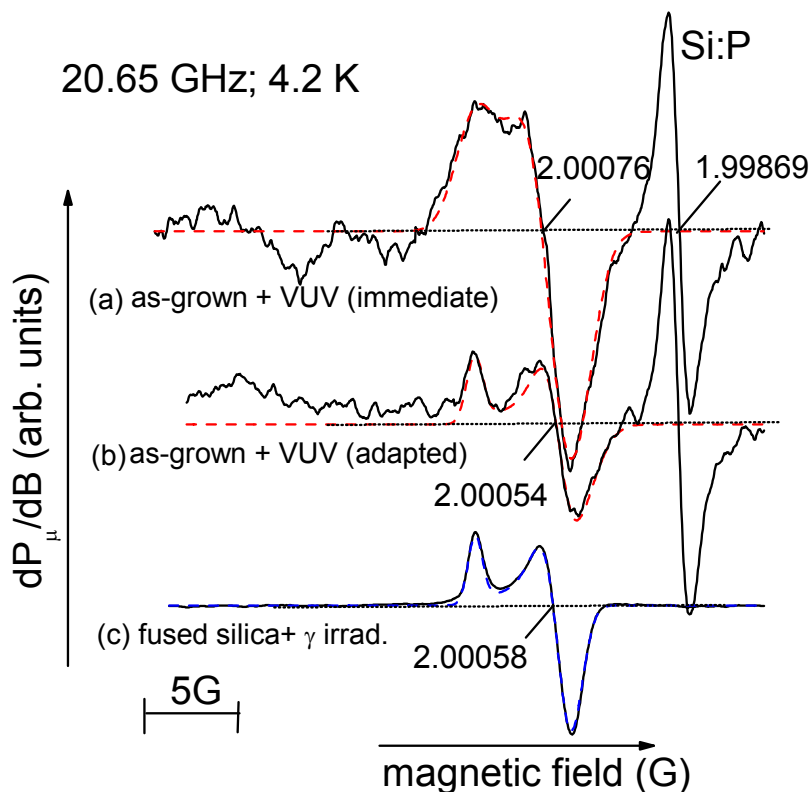
Figure 2.8: *Powder pattern derivative-absorption K-band ESR spectra ($P_\mu \sim 0.05$-0.2 nW; $B_m = 0.35$-0.5 G) observed at 4.2 K of the E′ centers in fumed silica (a) immediate upon VUV irradiation, (b) several days later the sample being left in room ambient, and (c) of the E'_γ centers in suprasil I synthetic silica subjected to $100\ Mrad(Si)\ ^{60}Co\ \gamma$-irradiation at 300 K. Dashed lines represent spectra simulations employing Gaussian broadening functions. The used g values and corresponding peak-to-peak derivative line widths are (a) $g_1 = 2.00174$; 2.1 G, $g_2 = 2.00070$; 2.3 G, $g_3 = 2.00030$; 2.2 G; (b) $g_1 = 2.00174$; 0.9 G, $g_2 = 2.00048$; 1.4 G, $g_3 = 2.00017$; 2.1 G; (c) $g_1 = 2.00175$; 0.80 G, $g_2 = 2.00057$; 1.45 G, $g_3 = 2.00032$; 1.30 G.*
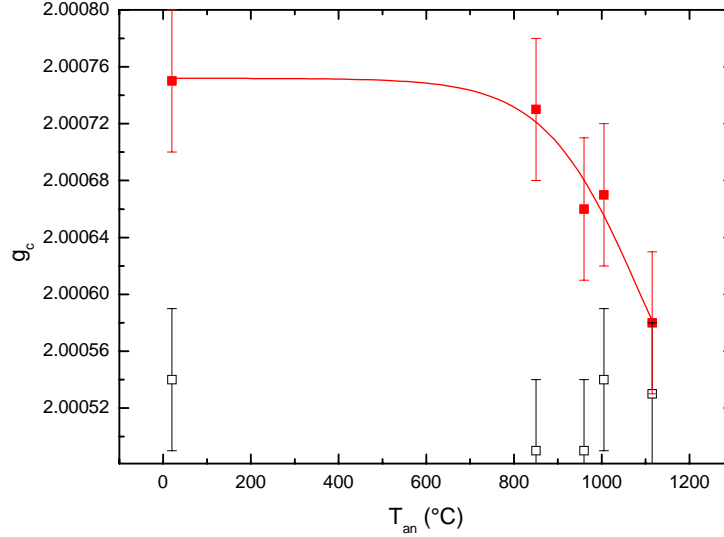
Figure 2.9: *Zero-crossing g value of the measured E′ signal (K-band; 4.2 K) as a function of post-manufacture heating in vacuum. Closed red symbols: measured immediate upon VUV irradiation. Open symbols: several days later, the samples being left in room ambient. The red curve is merely meant to guide the eye.*

the samples for substantial time ($\sim$days) in room ambient –henceforth, referred to as the *adapted state*– the zero-crossing g value has shifted about the same value (towards g_c=2.00054±0.00005) for all the samples regardless of their heat treatment including the as-grown sample [cf. Figs. 2.8 (a) and (b)]. These trends are exposed in Fig. 2.9, where g_c measured immediate upon VUV irradiation and after subsequent stay of the samples for days in room ambient, is plotted against T_{an}.

A second important ESR parameter is the displayed powder pattern line shape. A likely pertinent observation is that the shift in g_c over time in room ambient is accompanied by an attendant variation in the displayed powder pattern line shape. As illustrated in Fig. 2.8 (b) for the as-grown fumed particles, this implies, as general trend, evolution from a more blurred, broadened shape to a sharper, well expressed typical "two-peak" powder pattern pertaining to a nearly axially symmetric g matrix. A similar trend is observed as the measurements are carried out at different temperatures: The lower the sample temperature, the more blurred and broadened the powder pattern becomes, as illustrated in Fig. 2.10. At the same time a small variation in g_c is observed. Careful analysis leads to the conclusion that the latter variation in zero crossing g value is purely a consequence
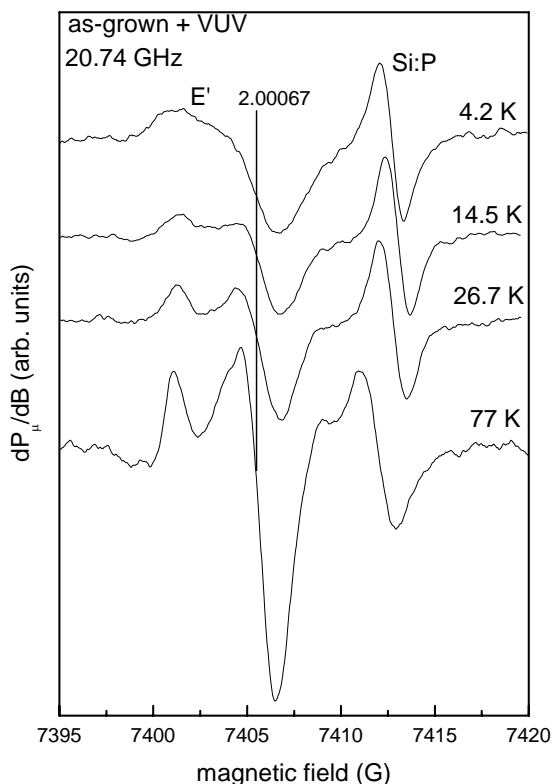
Figure 2.10: *Powder pattern K-band ($P_\mu \sim 2.5\,nW$, $B_m \sim 0.6\,G$) ESR spectra of the E' signal measured at different temperatures in the as-received sample immediate upon VUV irradiation. It should be noted that, as known, g(Si:P) is temperature dependent [16].*

of the attendant strong change in the line shape and has little to do with the g_c shifts mentioned before. As will be outlined later, it is attributed to T-dependent surface strain adaptation.

A third ESR parameter able to provide important information is the defect (E') density. Immediately upon prolonged (days-weeks) VUV activation of the as-grown particles, the maximum density that could be attained was determined as $(2.4\pm0.5)\times10^{15}\ g^{-1}$, corresponding to about 1×10^{-3} defects/nanoparticle. It should be added though that this number may not represent the maximum number of E' type centers inherent to the fumed nanoparticles, as the VUV treatment may not have exhaustively activated all defect sites present due to the small penetration depth (~ 10 nm) of the VUV photons in SiO_2 in combination with the powder nature

of the sample (geometric shadowing). However, the number may be close, given the prolonged irradiation treatment with regular intermittent stirring of the fumed powder. In support, doubling the irradiation time, indeed, did not increase any further the number of defects detected.

At this junction, it may be instructive to compare the observed E' densities with values encountered in the other macroscopic silica (silica glasses). Obviously, such comparison should be carried through most relevantly for defects produced by similar VUV treatment. A first most representative benchmark here may appear dry thermal SiO_2 grown on c-Si substrates, ubiquitously used in semiconductor IC technology and known to be of superb electrical quality, viz., in terms of point defect-related charge trapping centers. Remarkably, it is found that the measured E' density is about 100 times lower [183] than the densities typically observed [182, 181] ($\sim 1.4 \times 10^{17}$ g^{-1}) in thin ($\sim$4.1-6.5 nm thick) thermally grown dry SiO_2 on Si, indicating that the fumed silica is of superb quality in terms of malignant oxygen vacancies, that is, close to perfect SiO_2 stiochiometry or O-enriched. Further, it may be appropriate to add that the E'-type signal so far reported for thermal SiO_2 seems to be similar to the familiar E'_γ signal found in bulk silica. However, no detailed study on the hf structure of the E'_γ centers observed in thermal SiO_2 appears available yet, without doubt partially because of limited ESR sensitivity. Second, in support of the nanoparticle quality, Tsai *et al.* [184] reported the photogeneration of E'_γ centers reaching densities $\geq 10^{17}$ g^{-1} in high purity fused silica subjected to intense (40 $mJcm^{-2}$ pulses; ArF laser) 6.4 eV photon irradiation. The E' production efficiency was found to increase with higher OH content, the E' density, however, staying well below [OH].

A last but perhaps highly pertinent observation is that the observed shift in g_c over time as the sample is left in room ambient is accompanied by a striking *reduction in the E' signal intensity*. In the adapted state, the signal has reduced, in average, by factor of $\sim 2 \pm 0.5$. The experimental observed decay rate shows a slight tendency to decrease with increasing T_{an}, the variations, however, being well within experimental error.

Information on the hf interaction is well known to be a key point in atomic identification of point defects. Several attempts were made to resolve some associated (^{29}Si) hf structure, however, so far without success, which is attributed to the low density of occurring defects and strong signal overlap.
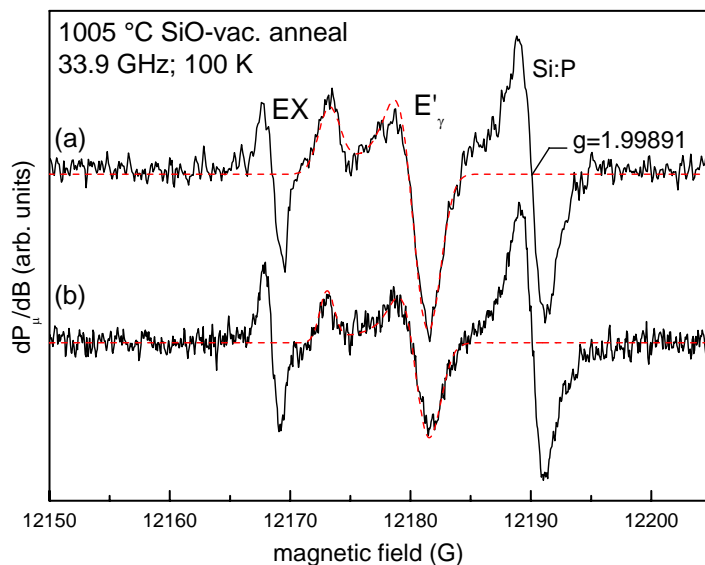
Figure 2.11: *Q-band ESR spectra of the fumed silica nanoparticles subjected to SiO-vac. annealing at 1005 °C measured at 100 K (a) immediate upon additional VUV irradiation and (b) several days later, the sample being left in room ambient. The dashed curves represent spectra simulations employing Gaussian broadening functions. The g values used for both simulations are (a) g_1=2.00168, g_2=2.00058, g_3=2.0003; (b) g_1=2.00171, g_2=2.00053, g_3=2.0003. The signal at g=1.99891 stems from a comounted Si:P marker.*

SiO impact

After the application of the SiO-vac. anneal at various temperatures followed by VUV irradiation, a characteristic central-line two-peak powder pattern signal is observed much similar (e.g., regarding width, overall shape, and g matrix) to that of the common E'_γ variant [180, 46]. Fig. 2.11 shows representative Q-band spectra recorded on a $T_{an} \sim 1005$ °C sample (a) immediately upon VUV activation and (b) several days later, the sample being left in room ambient. Both spectra could be well simulated (cf. Fig. 2.11, dashed curves) using similar ESR parameters (g value and constituent line widths).

For the various T_{an} an average drop in E' density by a factor $\sim$1.6$\pm$0.5 is observed after leaving the sample for substantial time in room ambient. Similar to the case of fumed silica subjected to simple vacuum annealing, the experimental observed decay rate shows a slight tendency to decrease
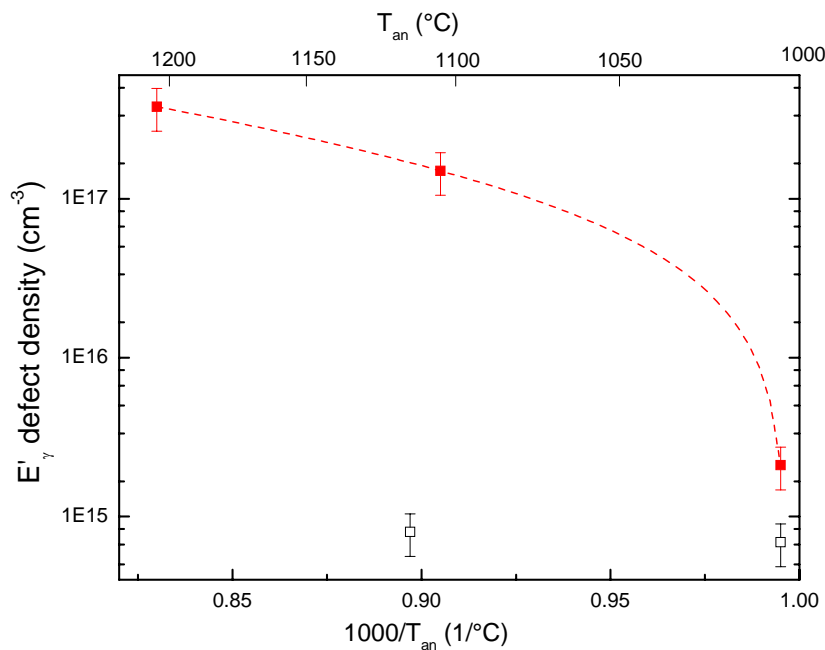
Figure 2.12: *Defect densities of the E' defect inferred from K and Q-band ESR in fumed silica subjected to a $\sim$3 h SiO-vac. anneal (solid red symbols) or a $\sim$1 h standard vacuum anneal (open black symbols) at various temperatures subjected to $\sim$1 h VUV irradiation. The measurements were performed immediately after the VUV activation. The dashed curve is merely meant to guide the eye.*

with increasing T_{an}, the variations being well within experimental error. A main finding here is that compared to ordinary vacuum annealing, the SiO-vac. anneal results in a drastic enhancement of E' density, increasing with T_{an} to a maximum defect density of $(4\pm1)\times10^{17}$ cm^{-3} attained for T_{an}=1205 $^{\circ}C$, as illustrated by Fig. 2.12. For the sample SiO-vac. annealed at $T_{an}\sim$1105 $^{\circ}C$ the attained E' density is over a 100 times larger than for the standard annealed sample.

Another interesting observation appears from Fig. 2.13 showing zoomed in representative Q-band ESR spectra of fumed silica nanoparticles subjected to SiO-vac. annealing [Fig. 2.13 (a)] and conventional vacuum annealing [Fig. 2.13 (b)] at $T_{an}\sim$1005 $^{\circ}C$ recorded immediate upon VUV irradiation. From this comparison it can be seen that the E' g_c of the nanoparticles subjected to the SiO-vac. anneal has not noticeably shifted with respect to the general bulk value ($g_c\sim$2.00058), in contrast with the g_c for the sample subjected to the vacuum anneal that has shifted upward
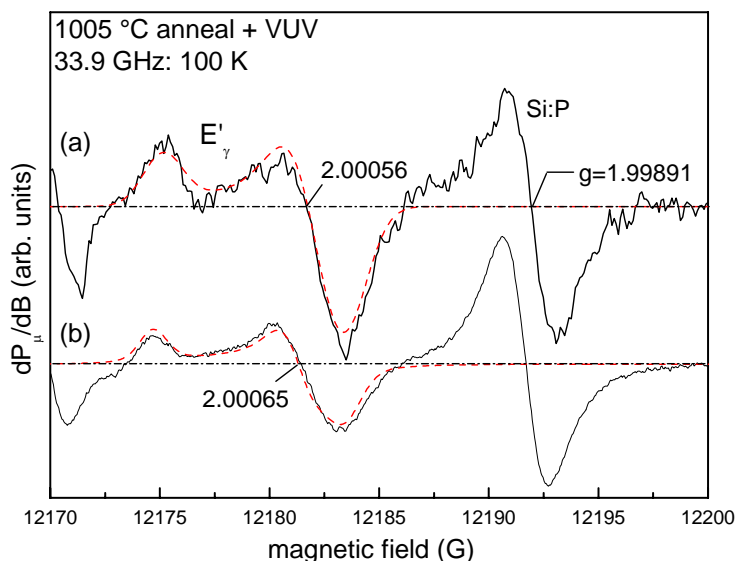
Figure 2.13: *Powder pattern Q-band ESR spectra of the E' signal measured upon VUV activation of the fumed silica nanoparticles subjected to (a) a SiO-vac. anneal at 1005 °C and (b) a standard vacuum anneal at 1005 °C. The dashed curves represent spectra simulations. The lower S/N ratio for spectrum (a) compared to (b) is due to the smaller amount of sample available.*

to ~ 2.00065.

Hyperfine structure

As mentioned before, caused by the low E' density encountered even after exhaustive VUV irradiation of the as-received and vacuum annealed fumed silica samples, we were unable to discern any hf splitting originating from the weakly abundant ^{29}Si (4.7 *at.%*) nuclei. The realized increase in E' density upon SiO-vac. annealing with additional VUV irradiation, however, enabled us to observe the ^{29}Si hf structure related to E' defects. Figure 2.14 (a) shows a typical high-power second harmonic mode Q-band spectrum observed for the fumed silica nanoparticles subjected to SiO-vac. annealing at 1105 °C and additional VUV irradiation after leaving the sample for days in room ambient. For reference we also performed a similar measurement [Fig. 2.14 (b)] on suprasil I synthetic silica subjected to 100 $Mrad(Si)$ ^{60}Co γ-irradiation at 300 K. In both samples two doublet structures are observed. The central line, largely off scale, corresponds to the E'_γ centers
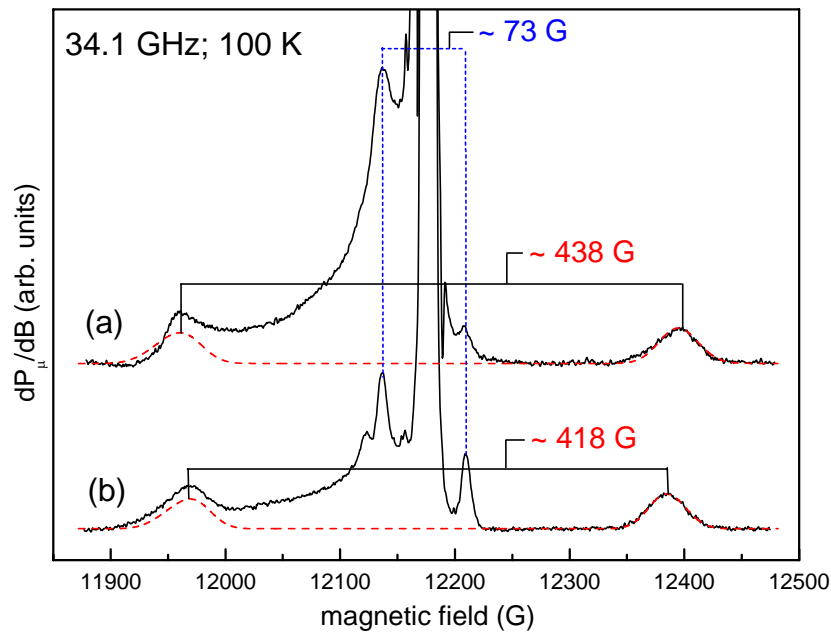
Figure 2.14: *High power (saturation) second harmonic Q-band spectra for (a) fumed silica subjected to a ~1105 °C SiO-vac. anneal and additional VUV irradiation measured at 100 K after leaving the samples for substantial time in room ambient and (b) Suprasil I synthetic silica subjected to 100 Mrad(Si) ^{60}Co γ-irradiation. The red dashed curves represent simulations of the primary ^{29}Si hf structure of the E' centers, obtained using the principal g matrix values g_1=2.0017, g_2=2.0005, g_3=2.0002 and hf parameters (a) A_{iso}=436 G, b=22 G and (b) A_{iso}=418 G, b=22 G. Spectra were aligned at the resonance field of the E' central resonance.*

with no hf splitting (unpaired electron located on ^{28}Si or ^{30}Si nuclei of I=0). The broad absorption line overlapping with the low-field parts of the doublets originates from $OHCs$. The inner hf doublet –henceforth referred to as the 73-G doublet– exhibits a splitting of 69$\pm$4 G and 73$\pm$2 G for the nanoparticles and suprasil, respectively. More zoomed-in spectra, better displaying the inner doublet in fumed silica and suprasil are shown in Fig. 2.15. As elaborated on in section 1.2.3, a similar doublet has been observed previously in various types of a-SiO$_2$ and was attributed [15, 84] to O$_2$=Si$^\bullet$-H entities with an H atom in a back bond instead of O. It should be noted that this doublet appears less prominent in the fumed silica powder than in the suprasil sample. The outer doublet (referred to as 418-G doublet) is, within the lines of this work, of more interest as it concerns the well-known primary ^{29}Si hf splitting of the E' center [51, 47]. The measured hf splittings are 438$\pm$2 G and 418$\pm$2 G for the nanoparticles
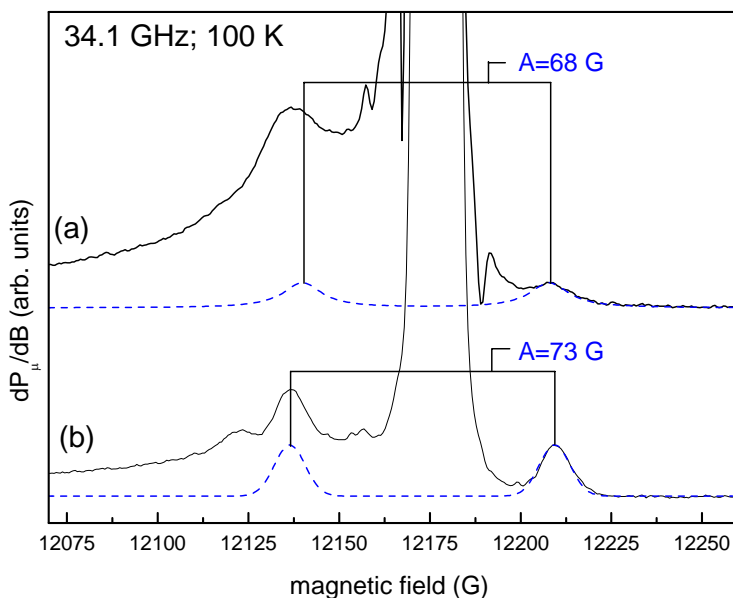
Figure 2.15: *Zoomed-in high power (saturation) second harmonic Q-band spectra for (a) fumed silica subjected to a $\sim$1105 $°C$ SiO-vac. anneal and additional VUV irradiation measured at 100 K after leaving the samples for substantial time in room ambient and (b) Suprasil I synthetic silica subjected to 100 $Mrad(Si)$ ^{60}Co γ-irradiation. The blue dashed curves represent simulations of the ^1H hf structure of the H associated E' centers (O$_2$=Si$^\bullet$–H), obtained using the isotropic g value g=2.0019 and hf parameter (a) A=69 G and (b) A=73 G. Spectra were aligned at the resonance field of the E' central resonance, and scaled to equal E' intensity.*

and suprasil, respectively (cf. Fig. 2.14), bearing out a noticeable increase in hf spitting for fumed silica.

g-value considerations

The adapted state

For purposes of assessing possible specific structural characteristics pertaining to the a-SiO$_2$ network of the studied *nm*-sized silica particles, it may appear interesting to analyze what the revealed distinct attributes of the observed E' signal, such as the principal g matrix values, may tell us about the centers' local environment within the a-SiO$_2$ matrix they are imbedded in. But before starting, as several distinct species of E' centers have been delineated over the years in glassy SiO$_2$, a basic quest concerns what particular type(s) of E' center we are actually dealing with in these fumed silica particles. Here, key information concerns the ESR observations on the particles in the *adapted state* or after post-manufacture heating at $T_{an} \geq 1100$ °C, exposing the central E' Zeeman resonances to converge to a common signal, and there is little doubt that this concerns the familiar E'_γ variant: This conclusion is based on the observed g values (g matrix, g_c) and the exhibited (nearly axially symmetric) powder pattern line shape as supported by detailed computer simulations of the observed signals [180, 46, 47].

More evidence for this conclusion is adduced by Table 1.2 where representative g value data are assembled for the relevant most prominent E'_γ-type centers reported in the literature and Table 2.2 were the current E'_γ (E'_{nano}) results are presented. From this comparison also, it follows that the SiO$_2$ nanoparticles E' signal does not concern the axially symmetric E'_β (Refs [48]) and E'_s (Refs. [49, 185]) variant nor the extreme (regarding g matrix) orthorhombic E'_α type [48]. One may remark, however, that the comparison of g matrix elements usually reported in the literature situates in the last significant digit, i.e., 10^{-4} (See, e.g., Ref. [4]). Generally, without having taken special measures (e.g., usage of accurate absolute g marker samples or ingenious high accuracy methods for *in situ* measurement of the at-the-sample magnetic field), most g value specifications do not extend beyond the fourth decimal digit (corresponding to an absolute $\vec{B}$ field determination accuracy of $\sim$0.16 G and $\sim$0.36 G for X and K-band, respectively). So, over the many g data in the literature, one encounters (slight) variations in the values reported for identical defects, urging some caution when intending to carry out comparisons –in particular, when looking for small systematic variations. To settle this, the only

Table 2.2: *Comparison of experimental principal axis g matrix values of generic E′ centers observed in this work. The g values are determined relative to a Si:P g marker. The accuracy on g is ±0.00004.*

	E'_γ [a]	E'_{nano}(bulk) [b]	E'_{nano}(surface) [c]
g_1	2.00175	2.00174	2.00174
g_2	2.00056	2.00048	2.00070
g_3	2.00030	2.00020	2.00030

[a] Observed in suprasil I synthetic silica –obtained from Heraeus (Germany) containing $[OH]\sim$1200 ppm (by weight), $[H_2 0]\leq$600 ppm, and total metal content $<$1 ppm– subjected to 100 $Mrad(Si)$ ^{60}Co γ-rays at 300 K.

[b] Observed in fumed silica 7 nm particles subjected to 10 eV photons obtained from a Kr-resonant discharge lamp (flux$\sim$10^{15} $cm^{-2}s^{-1}$) after leaving the sample for substantial time in room ambient, i.e., in the *adapted state*.

[c] Observed in fumed silica 7 nm particles immediate upon 10 eV VUV, photons obtained from a Kr-resonant discharge lamp (flux$\sim$10^{15} $cm^{-2}s^{-1}$), i.e., in the *non-adapted state*.

way out appears to first establish internal consistency. Thus, for normalization (calibration) purposes we have additionally calibrated within our ESR approach based on the usage of a single high accuracy g marker, the 'standard' most widely studied E' center produced in synthetic fused silica suprasil I by 100 $Mrad(Si)$ ^{60}Co γ-irradiation. The recorded K-band spectrum is shown in Fig. 2.8. The g matrix element results, consistent within an absolute accuracy of 2×10^{-6} between K and Q-band experiments, are included in Table 2.2 as well. Finally, in terms of g data, Table 2.2 also puts in better perspective the difference between the observed E' systems in fumed SiO_2 particles in the adapted and non-adapted state.

The non-adapted state

As the key point of focus, what then causes the notable variations in E' features –that is, shift in g_c with attendant variation in powder pattern shape– for the non-adapted (other) sample states, i.e., in the as-received state or after heating in the $T_{an}\lesssim$1100 $°C$ range, both just after VUV irradiation? Obviously, there may be various reasons.

One pertinent experimental observation is that the shift in g_c during post VUV excitation decay or after heating at $T_{an}>$850 $°C$ appears persistently

accompanied by a decrease in overall E' intensity, which would indicate that part of the ESR active centers drop out. The further interpretation could then take two points of view: A first one could start from the occurrence of only one E'_γ system, yet characterized by a profound distribution in ESR broadening parameters. The applied VUV excitation would efficiently ESR activate centers all over the distribution. Then, during the subsequent stay in room ambient (*adaptation* period), part of the E' centers, perhaps due to environmental influence, would become gradually ESR inactivated (passivated), predominantly starting with those centers pertaining to the (extreme) tails of the ESR parameter distributions. Thus, with progressing inactivation, the more standard E'_γ signal would naturally surface, characteristic of macroscopic glassy SiO_2 with more standard spreads in relevant ESR broadening parameters.

In a second scenario, the more distorted part of the E'_γ centers, making up the extended tails of the g distributions, could be rather seen as stemming from a separate, second E' system. In an idealized scheme, one could picture the first, more bulk a-SiO_2-like E'_γ system as constituting the centers located more in the center ("bulk") of the nm-sized silica particles; The second system would comprise the defects pertaining to the structurally more distorted (strained) surface and near surface layers –the *surface E' system*– more apt to environmental chemical and physical interaction (adsorption) impact. (About 23% of the molecules belongs to a monolayer ($\sim$0.29 nm) of SiO_2 entities at the surface of a 7-nm SiO_2 particle, as visualized in Fig. 2.16.) Thus, the E' signal might then rather be considered as the superposition of (at least) two overlapping signals originating from two separate E' defect systems. The first bath is dominant in the spectra of the particles in the adapted state or after post-manufacture heating at $T_{an} \geq 1100$ °C leading to the observation of signals with very similar principal g values and g value distributions as the E' systems observed in bulk silica. The surface E' system is dominant in the spectra of the as-received sample immediate after VUV irradiation giving rise to a shift in g_c and an overall more broadened spectrum.

For the remainder, the decay (adaptation) scenario upon VUV activation would be similar to the previous view: The second surface E' system would be gradually inactivated with increasing dwell time in room ambient, ultimately leaving only the first E'_γ bath. (The time delay may result from the altering accessibility by ambient species of E' centers located deeper in near surface layers). Interestingly, such a decrease in E' signal intensity has been observed before in the study of quartz crushed in vacuum [49].
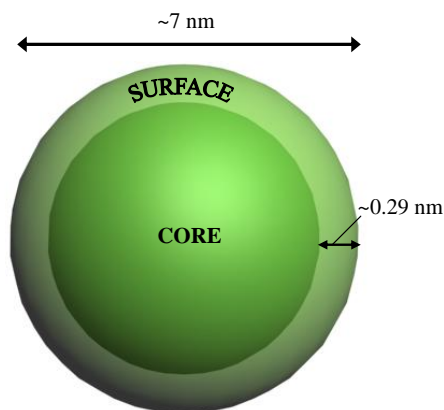
Figure 2.16: *Schematic visualization of the surface area of a ~ 7 nm fumed silica particle.*

There, an E'_γ-like (but not identical) signal was observed which could be readily modified by interaction with active gases, such as CO_2 and air. It is taken as evidence for the occurrence of surface dangling Si orbitals, i.e., the surface E' center [46, 183, 49, 185], termed E'_s, assigned to the hemicenter structure ($O_3\equiv Si^\bullet$) at the quartz grain surface. A similar sensitivity of Si dangling hybrids ($Si_3\equiv Si^\bullet$; D center) to the ambient has long ago been demonstrated at the surface of Si in cracks penetrating from the surface [186].

The surface E' systems observed in crushed silica particles and thin deposited a-SiO_2 films on Si are characterized by a closely E'_γ-like g matrix, yet with a slightly *smaller* g_c value (~ 2.0003) [46, 49] than the g_c value generally observed for the E'_γ center in bulk silica's ($g_c \sim 2.00058$), which would conflict with the current observations ($g_c \sim 2.0076$). However, here it should be remarked that in spectroscopic terms, as outlined above, the measured upward shift in g_c may well result from a substantial distribution in ESR parameters. Such spreads are well known to arise from amorphous-state disorder [4, 187], reflecting structural and strain induced site-to-site variations in Si–O–Si bond angles. Besides, it should be added that currently we deal with surfaces of nm-sized particles, which may exhibit a distinctly different dimension of distortion as compared to bulk-like grains and films. Thus, rather than counter, the current first report of such E' system from the outer layers of nm-sized silica particles might just instead be taken as evidence exposing this.

There is, however, one E'-type surface center reported that does exhibit

a *larger* g_c value than the g_c value generally observed for the E'_γ center in bulk silica ($g_c\sim2.00058$): Radzig *et al.* observed an E'-type defect center with principal g-values: $g_1=2.0003$, $g_2=2.0007$, and $g_3=2.0019$ [188, 189]. These values are very similar to those currently observed for the E' centers located in the surface layers of fumed silica. Radzig attributed the defect to a $O_2=Si^\bullet{-}OH$ entity with an OH group in a back bond, located at the surface of high purity quartz. Identification of the defect was accomplished through the observation of the primary ^{29}Si hf splitting ($A_{iso}=413\ G$; $b=19\ G$) and the small ^{1}H hf splitting ($A_{iso}=2.2\ G$; $b=0.6\ G$) [189]. The presence of such a defect site at the surface of the fumed silica nanoparticles may not be totally unexpected as extensive NMR studies [165] have pointed out that large concentrations of silanols (Si–OH groups) are present at the surface of fumed silica. If the observed surface E'-type defects in the nanoparticles would have such a OH group in the back bond, the central line should show additional structure resulting from the hf interaction with the $\sim100\%$ abundant ^{1}H nucleus. Yet, no such features could be observed in the K and Q-band spectra recorded immediate upon VUV activation of the as-received samples. However, it is possible that when measuring at these (high) frequencies the hf splitting remains unresolved as a result of intrinsic line broadening. To overcome this difficulty, X-band measurements were performed resulting in a narrow powder pattern, as shown in Fig. 2.7. If present, X-band observation should provide the best chance to resolve such hf splitting resulting from the H nucleus [190]. Yet, no such features are observed from where we conclude that for the fumed silica nanoparticles the observed g_c shift for the E' centers located in the surface layers does not concern a back bonded OH group.

The overall broadened spectra observed for the as-received sample state immediately after VUV irradiation and the strong dependence on the anneal temperature of the line width may also be understood as the result of the presence of a surface E' system. It seems reasonable to accept that the outer layers of the nanoparticles have a somewhat more distorted, more strained structure as compared to the inner core of the particles. MD computer simulations did point out that the surface has a different density and structure as compared to the interior of the cluster [156]. Furthermore, the surface can be influenced (distorted) by the presence of adsorbed atoms or impurities, such as silanols [165]. The combined effect can lead to the observed common broadening of the ESR spectra for the as-received state sample measured immediate upon VUV irradiation.

The observed dependence on observational temperature of the overall

line width can be explained by a temperature dependent surface strain adaptation. The thermal expansion coefficient α_{SiO_2} of quartz, although overall extremely low, does exhibit a clear temperature dependence, i.e., a monotonic increase, the largest relative variation (a factor ≥ 2000) occurring in the range [191] 6-75 K. Measuring at a higher temperature (77 K) can lead to some relaxation of the surface, thus decreasing the line width. A second possible explanation can be found with the adsorbed atoms. As the temperature increases the atoms can start tumbling leading to motional narrowing [192]. As will be demonstrated later, tumbling methyl radicals are indeed observed at these silica nanoparticles.

The effect of the post-manufacture heating on the E' system may also be understood within the above outlined picture. In a first view, the results may be explained by posing that with heating at increasingly higher temperatures in the range $T_{an} \geq 850$ $^\circ C$, the surface E' system is gradually eliminated, through irreversible structural network adaptation or chemical interaction with impurities leading to firm bonding. The former may appear less obvious, while the latter needs interference of impurities other than hydrogen. However, in a second more likely view, the surface E' system might just plainly be irreversibly eliminated by heating-dependent reduction of the effective sample surface area through particle sintering. Such sintering is known to start from about 850 $^\circ C$ onward, as recently re-evidenced by Uchino *et al.* [153] exposing a decrease in specific surface area with T_{an}, well mimicking (with respect to the pertinent T_{an} range) the E' g_c-vs-T_{an} dependence currently measured immediately upon VUV activation. This can be visualized by comparing Figs. 2.1 and 2.9. While we cannot discriminate between the two interpretations, the latter, given the physical facts, must at least account for part of the E' observations.

All in all, as a main result, the current data, concerning the central Zeeman resonance of the E' centers, reveal structural aspects of the nm-sized fumed silica particles different from bulk glassy SiO_2. For one, g matrix alterations are observed, assigned to enhanced amorphous state disorder and strain: Structural variations affect the spatial distribution of the unpaired electron orbital, which in turn, through the spin-orbit coupling, reflects back into the observed g factor. It is interesting to note that in recent work [193], small relative variations in g matrix elements (principal g values) observed in dry silica as a function of increasing ^{60}Co γ-irradiation (10^{-1}-10^4 kGy) have also been attributed to structural modifications reflecting back in the unpaired electron orbital, thus resulting in g shifts through the spin-orbit coupling.

In a more direct structural picture, it is known that for tetragonally arranged defects, such as the $Si_3{\equiv}Si^{\bullet}$ defect (P_b center) at the Si/SiO_2 interface, shifts in, e.g., $g_{\parallel}$ away from the average value may be directly related to variations in the unpaired bond angle θ (angle between the unpaired sp^3-like orbital direction and a Si–Si back bond). An increase in θ results in a shift in zero crossing g value towards higher values [194, 195]. Shifts in g can thus be directly translated into a more planar or pyramidal defect configuration [173, 185], which may provide useful information, also in the case of the E' center, e.g., in terms of local stress. However, no such clear relationship appears as yet established for the E' center. This will concern a next step in research, implying experimental refinement as well as, perhaps more crucially, substantial theoretical effort.

SiO impact

To analyze the influence of the presence of SiO during the SiO-vac. anneal on the fumed silica network, we compared our results obtained for the SiO-vac. anneal with those obtained for the regular vacuum anneals in the range $T_{an}{\sim}1005$-1205 °C. From Fig. 2.12 it can be seen that with the presence of SiO during the anneal, the E' density in the fumed silica particles has increased. This increase becomes gradually more drastic at higher anneal temperatures. Within the interpretation of interaction of the fumed silica network with released SiO molecules, yet without entering into atomic structural detail, this result might be understood on grounds of simple general stoichiometry: The incorporation of SiO in a $SiO_{2(x)}$ network will result in a net Si enrichment (or, equivalently, O deficiency). Thus, in the fumed silica nanoparticles, which have been evidenced to be O rich (low E' defect density), the incorporation of SiO might thus result in an increase of the number of oxygen vacancies, hence E' defect centers. For $T_{an}{\sim}1205$ °C the total E' density becomes comparable to, even slightly higher than, the density obtained for bulk thermal SiO_2 ($\sim 1.4 \times 10^{17}$ g^{-1}; standard quality) [181, 182]. It appears that the incorporation of SiO in the fumed silica network causes a serious degradation of the oxide quality in terms of oxygen vacancies. A similar increase in E' density has been observed before ascribed to the interaction of SiO with the SiO_2 network at elevated temperatures [63, 65]. However, in those cases the ESR spectra obtained for $T_{an}{\geq}1005$ °C were dominated by the S-center suggested to be of the type $Si_nO_{3-n}{\equiv}Si^{\bullet}$ (n=1, 2) [63, 66]. No S center was observed in the current fumed silica sample indicating that the nanoparticle network structure is unfavorable for S center creation.

Besides the change in defect density ascribed to SiO impact, another noteworthy difference concerns the observed g_c value of the E' signal, as illustrated by Fig. 2.13. For the standard vacuum anneal the g_c value had shifted to a somewhat higher value than the one typically observed in thermally grown SiO_2 on Si ($\Delta g_c \sim 0.0001$) due to the presence of E' centers in the surface regions of the nanoparticles, as discussed in the previous section. In the case where the SiO-vac. anneal is applied, no such shift could be observed, indicating that there is no significant fraction of surface E' centers left after the SiO-vac. anneal, in which case more of the E' centers in the (near) surface region would have turned into bulk silica properties by the SiO impact. In another opinion this could indicate that while a larger fraction of surface E' centers would still be left, their contribution to the overall observed E' signal is insufficient to cause a significant shift in the observed g_c. This would mean that a fraction of $\sim 40\%$ is insufficient to experimentally induce a measurable g shift, as indeed confirmed by independent spectral simulations. This may find some support in the generally experimentally observed trend of a decreasing decay rate with increasing T_{an}. Anyhow, it can be stated that the E' centers generated during the SiO-vac. anneal exhibit predominantly core region properties. The surface regions and the core region appear to respond differently to penetrating SiO molecules.

The primary ^{29}Si hyperfine interaction of the E'_γ-centers

Observed structure

In the previous section, it has been pointed out that monitoring the properties (e.g., g_c value) of the central Zeeman ESR signal of embedded intrinsic E' centers as a function of post-manufacture annealing and treatment (aging, VUV, and UV excitation) may provide useful information on the network structure of silica nanoparticles. As to the core region of these, no variation in the E' Zeeman signal, i.e., g_c shift, was observed compared to bulk a-SiO_2, indicating that the core is quite bulk silica-like. Uchino *et al.*, however, obtained experimental infrared and Raman data [153] indicating that the structure of the core of the nanoparticles is not fully identical to that of bulk silica. If so, most probably then these alterations in the network are too small to engender a detectable g_c shift of embedded E' centers, leaving this 'ESR route' unsuccessful. Here, the currently observed hf structure may come to the rescue (cf. Fig. 2.14). The signals are observed on fumed nanoparticle samples subjected to SiO-vac. annealing

in room ambient for substantial time, the latter resulting in suppression of the presumed surface E' system. So, the observed E' hf structure (two doublets) would also pertain to the core part of the nanoparticles.

(a)Inner doublet: We can be short about the inner 73-G doublet, actually observed with splitting of 69±4 G and 73±2 G in the nanoparticles and suprasil reference sample, respectively. Extracting the hf parameters of this doublet from the fumed silica spectrum is strongly hampered through interference of the co-present OHC signal with the low-field doublet signal, as can be seen from Fig. 2.14, resulting in a reduced accuracy (±4 G on the inferred hf splitting). To get more accurate information on the hf splitting spectral simulations were carried out using a code based on exact matrix diagonalization incorporating the Breit-Rabi formula. For this end, the high-power second harmonic spectra were assumed to resemble direct absorption shapes, an observation commented on previously [14], for which empirical evidence has been provided. For suprasil the observed hf doublet could be well simulated, as shown in Fig. 2.15, using the isotropic parameters g=2.0019 and A_{iso}=73 G; any anisotropic contributions remained unresolved. As to fumed silica, independent fitting of the hf doublet was even more severely obstructed by the overlapping OHC signal. However, by assuming that the central g value of the hydrogen associated E' center is the same in suprasil and fumed silica (as it is for E'_γ), we may circumvent this hurdle. Using this in the fitting procedure and focusing on the high-field doublet signal, we obtained A_{iso}=68 G with an estimated accuracy of ±2 G. In principle, like the primary 418-G doublet, the properties of this 73-G doublet could be perused as well to infer information about the properties of the core of the nanoparticles where the originating defects (O_2=Si$^\bullet$–H) are built in (*vide infra*). Indeed, although on the limit of experimental accuracy, there may be a decrease in hf splitting compared to the reference sample. Yet the doublet seems less amenable for that purpose for reasons such as attainable experimental accuracy (signal overlap) and the absence of a reference base linking hf structure parameters with SiO_2 network/material properties. Hence, we refrain from further hf analysis.

There is, however, one more interesting observation concerning the relative intensities of the H-doublet in fumed silica and suprasil. Observed many times before in various types of a-SiO_2, this 73-G doublet was assigned to the H-associated E'-type center O_2=Si$^\bullet$–H, the hf splitting thus originating from the interaction of the unpaired electron with a proton in a back bond [15, 84]. The defect thus signals the presence (though not exclusively, of course) of hydrogen in the silica network. In the second har-

monic mode Q-band spectra (cf. Figs. 2.14 and 2.15), this doublet appears relatively more prominent for suprasil than for fumed silica. For equal spectroscopic behavior, this suggests that fumed silica nanoparticles would contain less H. It should be added that this conclusion also assumes that the ESR-activation ratio of $E'_\gamma/O_2{=}Si^\bullet$–H defects is effectuated equally by VUV and γ-irradiation (applied to fumed silica and suprasil, respectively). Though perhaps plausible, this does not have to be a priori so, and some caution may be needed.

(b) Outer doublet: The observed second outer doublet concerns the primary ^{29}Si hf splitting of E' centers [51, 47] located in the core of the nanoparticles. The hf parameters are analyzed to attain more in depth information on the core structure. From Fig. 2.14 it can clearly be seen that the primary ^{29}Si hf splitting of the E' center is larger in the fumed silica nanoparticles than for suprasil. To obtain more detailed information about the hf structure spectral simulations were carried out. For the bulk suprasil sample the observed hf doublet could be well simulated using similar ^{29}Si hf parameters ($A_\parallel$=462 G and $A_\perp$=396 G) as reported by Griscom *et al.* for glassy silica [51]. The g values used for this fitting procedure were taken from the simulation of the central line: g_1=2.0017, g_2=2.0005, and g_3=2.0002. The parallel ($A_\parallel$) and perpendicular ($A_\perp$) hf constants are linked to the isotropic (A_{iso}) part (*s* part: Fermi contact interaction) and the anisotropic (*b*) part (*p* part: dipolar interaction) of the hf interaction through the equations:

$$
\begin{aligned}
A_\parallel &= A_{iso} + 2b, \\
A_\perp &= A_{iso} - b.
\end{aligned}
\tag{2.2}
$$

For the suprasil E' center this results in A_{iso}=418 G and b=22 G.

As can be seen from Fig. 2.14, the co-present OHC signal is badly interfering with the low-field doublet signal, particularly so for the fumed nanoparticles, exhibiting a relatively stronger OHC component. This hampered independent fitting of the primary ^{29}Si hf doublet for fumed silica. Therefore, based on various hf constants reported in the literature [51, 196], and in a similar attitude as taken before we assumed that the increase in the measured hf splitting for the E' center in fumed silica is mainly caused by an increase in the isotropic part of the hf interaction. Thus, in the fitting procedure b (=22 G) was kept constant, which enables a clear comparison with data from the literature. For the primary ^{29}Si hf parameters of the E' center in the fumed silica nanoparticles, this led to the results: $A_\parallel$=480 G and $A_\perp$=414 G or, put differently, A_{iso}=436 G and b=22 G. The inferred

A_{iso} and b values provide access to the structure of the corresponding E' centers.

E' defect structure

The first researchers to observe the primary hyperfine of the E'_γ centers in a-SiO$_2$ were Griscom *et al.* [51]. From their results, the authors obtained detailed information about the short-range structure of the amorphous network, such as, e.g., the O–Si–defect bond angle θ, using the simple expression

$$tan(\theta) = -[2(1 + \frac{b}{A_p}\frac{A_s}{A_{iso}})]^{\frac{1}{2}}, \tag{2.3}$$

where A$_s$ and A$_p$ are the hf coupling constants for 3s and 3p electrons on neutral atomic silicon. Using the values for A$_s$ and A$_p$ cited by Morton and Preston [8], as elaborated on in section 1.1.1, the values obtained for the bond angle θ in the current work are θ_{bulk}=111.86° and θ_{nano}=112.15° for the E' centers in suprasil (θ_{bulk}) and fumed silica (θ_{nano}), respectively. Assuming an accuracy of ± 2 G on the experimentally obtained isotropic hf constants, the accuracy obtained on θ is $\pm 0.03°$. The inferred value for θ is somewhat larger ($\Delta\theta = \theta_{nano} - \theta_{bulk}$) for the E' centers in the core of the nanoparticles pointing to a configurationally more pyramidal E' defect structure, as illustrated in Fig. 2.17. As to this conclusion, one may conjecture that observation of the ^{29}Si E' hf structure has been enabled through interaction with SiO at high T_{an} (E' density enhancement), which may have resulted in significant modification of the SiO$_2$ network so that the current results would not pertain to the pristine nanoparticle properties. The impact, however, on the global network structure is considered minor
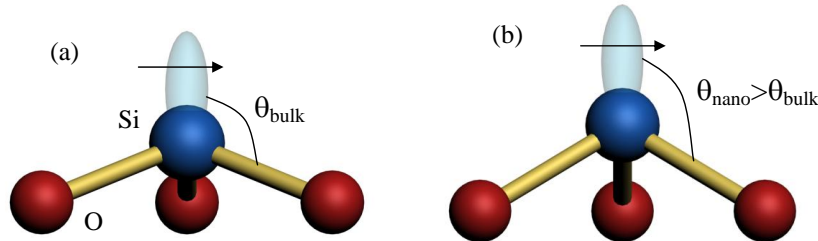
Figure 2.17: *Visualization of the structural modification of the E' center generic unit in fumed silica (b) nanoparticles to a more pyramidal defect structure compared to bulk silica (a).*

given the still low maximum density of E' defects ($\sim 1 \times 10^{17}$ cm^{-3}) in the SiO$_2$ matrix (~ 5 *at. ppm*) of the fume samples for which the hf data are currently reported ($T_{an} \sim 1105$ $°C$).

There is still one more pertinent remark that should be made concerning this defect bond angle analysis. Equation 2.3 is based on a simplified theory based on various assumptions including perfect sp^3 hybridization. It should be noted that in literature different bond angle–hf relationships exist (starting from different assumptions) resulting in different values for θ. Edwards and Fowler [197] for instance argued that in a relative ionic system such as SiO$_2$, the use of neutral atomic wave functions in Eq. 2.3 is inappropriate. They suggested the use of the wave functions from Si$^{(+1)}$, as a way to include the ionicity of the sp^3 hybridization in SiO$_2$. The ensuing modified θ–hf parameter relation results, as verified in our case, in (slightly) higher values for θ ($\theta_{nano}=113.4°$ and $\theta_{bulk}=113.7°$ for the E' center in fumed silica and suprasil, respectively) but still similar values for $\Delta\theta$ are obtained. Pacchioni and Vitiello [198] obtained from their first-principle Hartree-Fock and DFT calculations a much stronger relationship between A_{iso} and θ. For the range of values from $100°$ to $110°$, they obtained an increase in A_{iso} of 6 G for a decrease in θ of $1°$. It appears that the A_{iso}–θ relationship is very responsive to various structural/morphological parameters. However, the trends obtained even from the simplest theoretical analysis are at least qualitatively in agreement: *an increase in A_{iso} is a result of an increase in θ*. On this notion it may still be appropriate to continue using the results obtained from Eq. 2.3.

Having attained a specific quantification for a change in the structure of the E' center between bulk silica and the core of silica nanoparticles, we may want to transfer this information to assessing how it would affect other experimental quantities, such as, the g value of the ESR resonance. As already mentioned, generally, such a structural modification does not only affect the hf splitting but will also result in a g shift. However, for the core E' centers no shift could be detected, which then must mean that the variations in θ remain most probably too small to result in a detectable g shift. For the surface E' system a g shift (increase) was observed, indicating that the variations for θ would be stronger for the outer layers of the nanoparticles. But here, whether the surface E' centers have a more planar or pyramidal defect structure remains unknown as no hf structure could be resolved due to sensitivity reasons. So, unfortunately, no direct *experimental* link can be provided between a shift in g and a change in structural pyramidality. The answer may be provided by theory. However,

if assuming that the E' centers in the surface layers follow the same trend, but more pronounced, as their counterparts located in the core regions, i.e., enhanced pyramidality, than we would reach the conclusion that an increase in θ is accompanied by an increase in g. This result would be consistent with theoretical work reported for the unpaired Si bonds in a-Si and the P_b center [194, 195], where an increase in g_c value is linked with an increase in θ and hence a more pyramidal defect structure.

On the other hand, for the surface E' system (E'_s) observed in crushed silica particles discussed before [49], a smaller $g_c \sim 2.0003$ was observed accompanied by an increase in A_{iso} to ~ 466 G. If the surface E' system in fumed silica behaves in a similar way, the observed increase in g_c would be indicative for a decrease in A_{iso} and consequently in θ and thus a more planar E' defect structure. Within this picture the surface region and core region of the nanoparticles would exhibit an opposite structural behavior, e.g., where the core region is more strained, densified (*vide infra*), the surface layers would be more relaxed compared to bulk SiO_2.

Densification

While the attained atomic scale information on the structure of a specific point defect is definitely of interest on its own right, the next step beyond in analysis reaches a main goal: Very basically, it touches the potentiality of (intrinsic) point defects in providing pertinent information on larger scale structural/material physical quantities of the solid matrix these are embedded in –what can an atomic scale point defect tell us about its broader environment? The potentiality of point defects in this sense is demonstrated by many examples before, e.g., P_b defects at Si/SiO_2 interfaces [29, 202, 173], Fe-impurities in Si [203]. Assessing this is a main goal. As to the current nanoparticles, the increase observed in A_{iso} for the E' centers residing in the core of the nanoparticles as compared to bulk silica may also provide in depth information on more global structural/material parameters of the matrix the defects are embedded in. As a starting point we have compiled in Table 2.3 the results of the primary [29]Si hf splitting of the E' center for the current nanoparticles and for glassy SiO_2 reported in the literature [172, 51, 196, 199, 14, 15, 200, 201]. Over the various values, excluding densified and [29]Si implanted samples, an average hf splitting of 419 ± 4 G is attained. A substantial increase in splitting is seen to result from densification, as well as, though somewhat less, from Si implantation. As the latter was argued also to effectuate densification [201, 200], there appears a clear link between densification and enhancement of [29]Si hf splitting.

Table 2.3: *Comparison of the experimental primary ^{29}Si hyperfine splitting of E'_γ centers in silica glass.*

Hyperfine splitting (G)	Ref.	Sample	Damaging agent
423	[51]	Corning 7940	[a]
423	[51]	Corning 7943	[a]
423	[51, 14]	Suprasil I	[a]
423	[51]	Suprasil N-I	[a]
423	[51]	Dynasil 1000	[a]
423	[51]	NRL high purity precipitated silica	[a]
418	[51]	95% ^{29}Si enriched SiO_2	[a]
420	[14]	95.3% ^{29}Si enriched SiO_2	[a]
420	[14]	99.8% ^{29}Si enriched SiO_2	[a]
418	[15]	High OH silica spectrosil rods ($\sim$1200 *ppm* OH)	[a]
418	[15]	Suprasil 2 powder; high OH + OD	[a]
410	[196]	Suprasil I	[b]
410	[196]	Suprasil W1	[b]
465	[196]	Suprasil I; $\sim$24% densified	[b]
465	[196]	Suprasil W1; $\sim$24% densified	[b]
465	[199]	Suprasil I; $\sim$24% densified	[c]
440	[200]	Wet synthetic SiO_2 glass (type II, $[OH]\sim3\times10^{19}\ cm^{-3}$); ^{29}Si implanted	
420	[172]	Fused silica glass powder	[d]
420	[172]	Suprasil I	[d]
440	[201]	Dry a-SiO_2 (type II, $[OH]\leq10^{17}\ cm^{-3}$); ^{29}Si implanted	
418±2	This work	Suprasil I synthetic silica	[a]
438±2	This work	Fumed 7 *nm* SiO_2 particles; 1105 $^\circ C$ SiO-vac. anneal	[e]

[a] $\sim$100 *Mrad(Si)* ^{60}Co γ-rays.

[b] $\sim$76 *Mrad(Si)* ^{60}Co γ-rays.

[c] 248-*nm* KrF laser irradiation.

[d] $\sim$8.3$\times$10^2 *Mrad(Si)* ^{60}Co γ-rays.

[e] 10 *eV* photons obtained from a Kr-resonant discharge lamp (flux$\sim$10^{15} $cm^{-2}s^{-1}$).
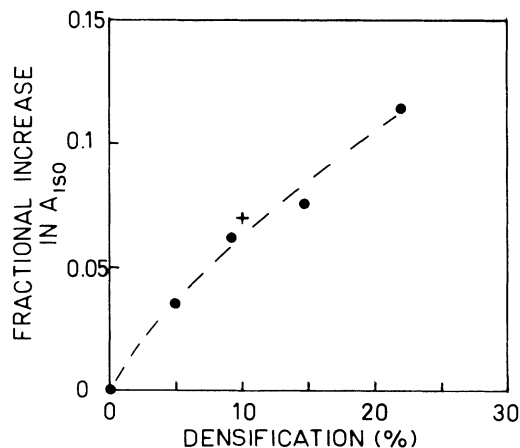
Figure 2.18: *Fractional increase of the experimentally obtained isotropic hf constant as a function of densification of the silica sample. The increase is referred to the value of 410 G found in undensified Suprasil. The cross refers to a Suprasil W1 sample and is included to demonstrate that the type of silica does not play a role. The figure is taken from Ref. [196].*

Thus, such an increase in A_{iso} has been observed before [196, 199, 200, 201] and is assigned to a densification of the SiO_2-matrix.

In a remarkable study of the hf splitting of the E' center in a-SiO_2 as a function of the density [196] for samples densified under hydrostatic pressure at high temperatures, Devine *et al.* reported an increase in A_{iso} with growing silica density, as illustrated in Fig. 2.18. Densification of the silica of 24% was observed to result in an increase of the hf splitting to $\sim$465 G, from where an increase was inferred in the length of the back bonds associated with the defected Si atom at the oxygen vacancy site, a reduction of the mean bridging Si–O–Si bond angle of the defect back bonds, and a decrease of the tetrahedral O–Si–O bond angle of the defect. These results did not depend on the type of silica studied, so it seems reasonable that their inferences can also be applied for the analysis of the current fumed silica data. In this view the obtained fractional increase in A_{iso} of 4.1% would imply a densification of the fumed silica network of 5.9%, corresponding to an increase in specific gravity to 2.33 gcm^{-3} as compared to 2.202 gcm^{-3} for undensified silica. The core of the nanoparticles are thus found to be *densified*.

But how does this densification come about in terms of modification of the SiO_2 network? In addition to ESR, Devine *et al.* also performed x-ray

scattering, Raman and NMR measurements on densified silica [204]. From these results they concluded that the densification produces a decrease in the oxygen-second-nearest-neighbor-oxygen separation (R). So, R is the minimum distance of the closest approach of two oxygen atoms belonging to adjacent SiO_4 tetrahedra. As a next crucial link, one calculation concludes that restrictions on interoxygen distances impose limits on possibly occurring ring configurations of SiO_4 tetrahedra in the SiO_2 network [205]. The description of the a-silica network in terms of the distribution of occurring n-membered rings (n=3-6) is a well known approach [See, e.g., Ref. [206] for an excellent overview], and there is a general consensus the structure to contain ring structures of different sizes [206, 207]. The average ring size in standard bulk vitreous SiO_2 is $\sim$6 [206]. The calculations infer that a decrease in R is indicative for the presence of relatively more low membered rings. At least the existence of such configurations is no longer excluded through distance considerations. On the basis of the previous inferences, our E' hf ESR data indicate an enhanced density of lower membered (SiO_4 tetrahedra) rings in the core part of silica nanoparticles compared to bulk silica. It should be borne in mind, however, that the inferences made by Devine *et al.* are based on various empirical relationships, such as, e.g., between bond angles and bond lengths. As Edwards and Fowler [197] put it: The trends predicted by this analysis are almost certainly qualitatively correct, but the relationships used are inappropriate.

Generally, we can conclude from our ESR results that the densification of the core of the fumed silica nanoparticles results in an increase in the ^{29}Si hf splitting of the E' centers located in the core, tentatively linked to a modification of the distribution in occurring ring structures in the fumed silica network. These results confirm independently those previously reported by Uchino *et al.* that the core of the nanoparticles differs from bulk silica [153] in that it would be comprised of more low (n=3 and 4) membered rings. It thus appears that through the observation of the hf structure of embedded point defects, ESR represents a powerful tool to provide us with detailed information about the network structure of the nanoparticles on atomic-scale.

2.5.2   A newly isolated ESR signal

Observations

Upon post-manufacture heating an unidentified signal (termed $LU2$) newly appears in maximum densities $(6.0\pm0.6)\times10^{15}\ g^{-1}$ ($\sim$2.5$\times$10^{-3} defect/particle),
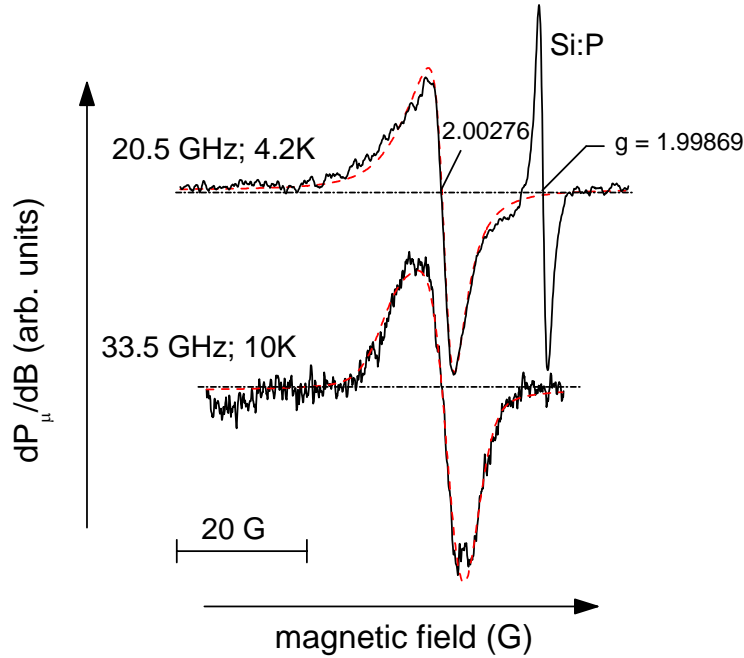
Figure 2.19: *Powder pattern K-band ($P_\mu{\sim}0.3$ nW; $B_m{\sim}0.5$ G) and Q-band ($P_\mu{\sim}40$ nW; $B_m{\sim}0.3$ G) ESR spectra of the observed signal, labeled LU2, in silica nanoparticles annealed at T_{an}=960 °C. The dashed curves represent spectra simulations (see text for parameters).*

without the additional VUV irradiation, that is required for the detection of the E' center. At K-band it appears as a single asymmetric signal of g_c=2.00276±0.00005 and peak-to-peak width ΔB_{pp}=4±0.2 G. Figure 2.19 shows K and Q-band ESR spectra observed at low T, after annealing at T_{an}=960 °C. The signals exhibit powder pattern properties, and both could be readily consistently simulated (symbols in Fig. 2.19) by one effective spin S=1/2 center, of closely axial symmetry, with one set of g matrix principal values given as $g_\parallel$=2.0041 and $g_\perp$=2.0027; Only the microwave frequency ν has been changed and the Lorentzian broadening function has been increased with ν. Other observations include: In the range 850-1115 °C, the signal intensity is found to be maximal for $T_{an}{\sim}960$ °C; Subjecting the sample to VUV irradiation decreases the intensity of the center.

It is realized, however, that the attained signal-to-noise ratio is limited. So, conforming to scientific rigor, full allowance should be made for other interpretations. For one, rather than adhering to the powder pattern of

one type of defect, e.g., the overlap of two separate signals of different
g values, which structure would also broaden with increasing microwave
frequency. Through computer simulations, this route has been carefully
analyzed. However, despite fitting over a broad range of parameter values
(g, ΔB_{pp}, line shape, relative intensity), we failed to realize a match as
satisfactory as readily obtained by the single powder pattern interpretation,
the main delimiting obstacle appearing to be the observed overall signal
symmetry, e.g., the signal measured at Q-band at 150 K constitutes a
well expressed 'two peak' powder pattern, as shown in Fig. 2.20. This is
why the powder pattern interpretation is favored. Of course, it cannot
be excluded that with still increasing the number of independent signals
(3 or more), thus concomitantly unrealistically augmenting the number
of independent fitting parameters (4 per signal), a satisfactory consistent
fit might ultimately be realized –but, obviously, at the cost of scientific
credibility.
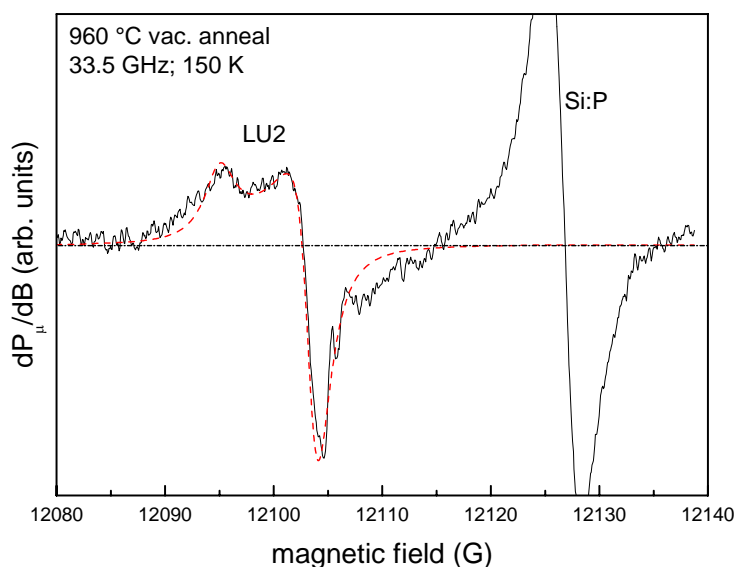
Figure 2.20: *Q-band ($P_\mu \sim 0.16$ mW; $B_m \sim 0.6$ G) ESR spectra of the observed
LU2 signal in silica nanoparticles annealed at T_{an}=960 °C, displaying a well ex-
pressed "two peak" powder pattern. The dashed curve represents the LU2 spectrum
simulation (see text for parameters).*

Discussion

Without doubt, a main key question concerns the origin of this signal. As is well known from previous studies on atomic identification of point defects, almost exclusively based on ESR analysis, conclusive determination of the nature of the originating defect necessarily requires information on the hf interaction. Identification of the defect is considered much relevant as its appearance may be closely tied to a specific characteristic of the fumed silica network, possibly different from the bulk glassy SiO_2 state. Several attempts were made to resolve associated hf structure from the background, yet so far without success, which makes that the discussion of the center's origin remains largely speculative.

Purely based on g_c, one possible candidate could be the S center ($g_c \sim$ 2.0027), tentatively assigned [62, 63, 66] to the E'-like centers $Si_nO_{3-n} \equiv Si^\bullet$ (n=1,2) –likely $SiO_2 \equiv Si^\bullet$, as elaborated on in section 1.2.2. That center was also revealed after high-T_{an} annealing in vacuum, prominently so in thermally grown SiO_2 layers on Si. However, at first sight, general line width and g matrix asymmetry considerations would disfavor this assignment.

In looking further for other models, given the measured zero crossing value g_c=2.00276, we may also consider the possibility the signal to originate from C-related defects. Indeed, many signals observed around that g value (see, e.g., Ref. [208]) have been attributed to (identified as) C-related defects, e.g., as encountered in carbonaceous materials such as mechanically damaged [209] C powder ($\Delta B_{pp} \sim$5.5 G; g=2.0027±0.0002) and a-SiC films ($\Delta B_{pp} \sim$6 G; g=2.003±0.001) [210], and as contaminants on ion-implanted glass [211] and various heat-treated surfaces [212], the latter, for quartz and glass, characterized by a width ΔB_{pp}(X-band)$\sim$1 G and g=2.0028. A singlet characterized by an approximately Lorentzian shape, ΔB_{pp}(X-band; 300 K)$\sim$1-3 G and g=2.0026±0.0002 was reported in virtually all ion-implanted glasses [211] and ascribed to surface C contamination. Along the case of heat-treated surfaces, the observed $LU2$ signal could have resulted from the annealing in vacuum. However, counter to this interpretation would appear the currently applied high T_{an} values and the non-disappearance of the ESR signal when exposed to air (room ambient) [212]. But it is well realized that for unequal circumstances (e.g., material, shape, treatment) signals may appear different, and a possible relationship of $LU2$ to carbon is not ruled out; However, it cannot be substantiated any further either. Thus, conclusive identification of this (new) defect remains still open.
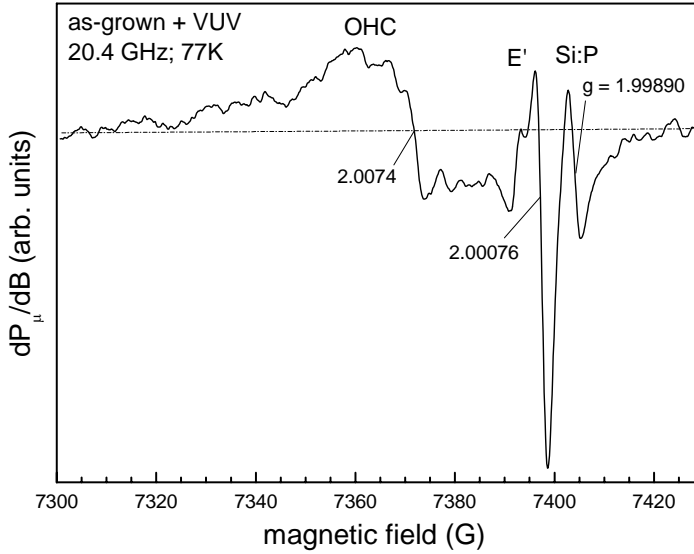
Figure 2.21: *Overall K-band ($P_\mu \sim 8$ μW; $B_m \sim 0.6$ G) ESR spectrum observed on the as-grown fumed silica sample after VUV irradiation. The OHCs clearly dominate the spectrum.*

2.5.3 The OHC type centers

Observations

Figure 2.21 shows an overall K-band spectrum measured on the as-grown sample immediate upon VUV irradiation over an extended field range at liquid nitrogen temperature. It corresponds to the totality of observed ESR signals. The most eye-catching part in this ESR spectrum, without doubt concerns the left part of the spectrum, exhibiting broad resonance features. The position and shape of the broad ESR signal(s) points to $OHCs$ [82]. The ESR signal was investigated with great care in order to assess more detailed information about the specific ESR features. The ESR resonances were monitored as a function of observational temperature, revealing some striking variations. It became clear that the broad ESR line centered at $g_c \sim 2.0074$ is the resultant of at least two resonant responses.

One of them, centered at $g_c = 2.0074 \pm 0.0005$, exhibits powder pattern properties, and could be quite well simulated (dashed curves in Fig. 2.22) in the temperature range ~ 77-100 K consistently for K and Q-band observations using a simple spin Hamiltonian of effective spin=1/2, with one set of g matrix principal values given as $g_1 = 2.0020$, $g_2 = 2.0078$, and $g_3 = 2.0670$.
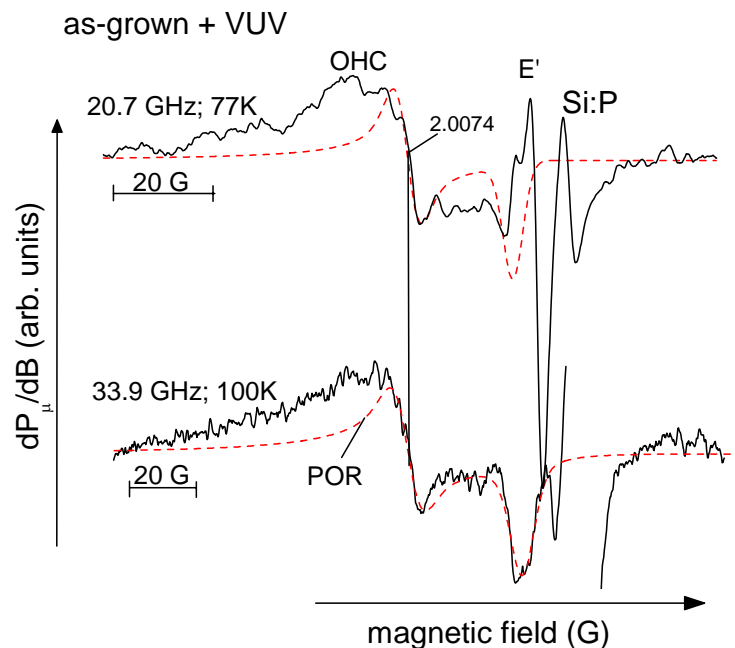
Figure 2.22: *K-band ($P_\mu \sim 8 \mu W$; $B_m \sim 0.6$ G) and Q-band ($P_\mu \sim 0.17$ mW; $B_m = 1$ G) powder pattern ESR spectra of the as-grown sample after VUV irradiation. Extreme ESR measurement parameters are used to enhance the signals in the g range 2.02-2.0015 and to saturate the other signals (E'-like center, methyl radical) present. The broad resonances centered at $g \sim 2.0074$ are ascribed to OHC centers. The dashed curves represent spectra simulations; The principal g values used for both spectra simulations are $g_1 = 2.0020$, $g_2 = 2.0078$, and $g_3 = 2.0670$.*

The latter g_3 is taken from Ref. [4], and in fact is kind of immaterial here. Interestingly, these ESR parameters are very similar to those pertaining to the well-known POR ($O_3 \equiv Si$–O–O$^\bullet$) [4]. To get more conclusive evidence several attempts were made to resolve the powder pattern peak corresponding with the g_3-component. However, these attempts failed and the signal remained beyond ESR detection, likely due to the low signal intensity and line broadening. Inferred defect densities were up to $(3.1 \pm 0.3) \times 10^{15}$ g^{-1} or about 1×10^{-3} defects/nanoparticle. The presence of $PORs$ in the nanoparticles, albeit in small densities, would indicate that fumed silica is somewhat *oxygen rich*, which would be consistent with the low density of E' centers (O vacancies) encountered.

The other part of the broad resonance line could not be assigned conclusively. There is a possibility that this line also concerns some (other) type of

$OHCs$, possibly the $NBOHC$ ($O_3\equiv Si–O^\bullet$, characterized by [4] g_1=1.9999, g_2=2.0095, and g_3=2.078). But this is more of a suggestion.

However, even in lack of full identification, we still can provide, as a useful number, an estimate of the upper limit of the density of all $OHCs$ possibly present from the added intensities of all pertinent signals. The density was determined for different VUV irradiation times in order to ensure that most, if not all, centers present are indeed ESR activated (attaining the density saturation level). This leads to a maximum number of $OHCs$ possibly present of (0.07±0.01) defects/particle, which means that only one in about every 14 particles may contain such a defect. Even if one takes *all* ESR active defects observed in the as-grown sample immediate upon VUV activation [the OHC-type centers, the E'-type center and the methyl radicals (see later)] into account still no more than one in about every 14 particles may house an ESR-active defect. The broad resonance line which can possibly be assigned to the $NBOHCs$, is indeed by far the most intense of the observed resonances.

Another observation is that the broad resonance lines, and therefore the $OHCs$ density, decreases drastically when subjecting samples to additional heat treatment.

Discussion

These observations contrast with the conclusions arrived at by Altman *et al.*, who studied the light absorption of silica nanoparticles [155]. Their experiments revealed a non-exponential behavior of light absorption in visible light, which they attributed to the presence of a large concentration of $NBOHCs$. They also suggested that the concentration of these defects amounts to such levels that they may cause narrowing of the optical energy gap through strong Coulomb disorder. The current observations, however, strongly disfavor this suggestion, at least in a statistically uniform picture, since for these defects to cause changes in the band gap there should be at least more than one defect present in each nanoparticle. Of course, defect bunching cannot be excluded, i.e., a small minority of particles could contain several to many $OHCs$ per particle, the remainder and major portion of the SiO_2 particles then being OHC free. We would have two particle subsystems in terms of OHC content. So, without contesting any of the valuable sets of date presented in Refs. [163, 164, 155], the current results would suggest that the underlying physical basis for interpretation of some results needs adaptation. Probably the explanation for the observed narrowing in optical band gap should rather be searched for in systematic

structural differences in the a-SiO$_2$ network of the nanoparticles as compared to bulk SiO$_2$.

Another point of discussion is Glinka *et al.*'s suggestion that the $NBOHCs$ are formed by the process presented in Eq. 2.1 during heat treatment of the silica nanoparticles in air at $T_{an} \geq 600$ °C and that these defects dominate the PL spectrum when the sample is pretreated at $T_{an}=900$ °C [164]. Yet, the broad ESR resonance line observed here, which can possibly be assigned to some type of $OHCs$, on the contrary, decreases drastically upon additional heat treatment. According to Eq. 2.1 not only the concentration of $NBOHCs$ but also the concentration of E'-type centers should increase since they are formed in pairs. However, no such increase in E' concentration could be observed either. These two observations make it quite unlikely for the reaction described by Eq. 2.1 to play a dominant role. In fairness, it should be mentioned that the post-manufacture heat treatments applied by Glinka *et al.* (2 *h* in air) differ from those applied in this research ($\sim$1 *h* in vacuum), which, given the nano dimensions of the particles, may be linked to the difference in result attained. This would require further investigation.
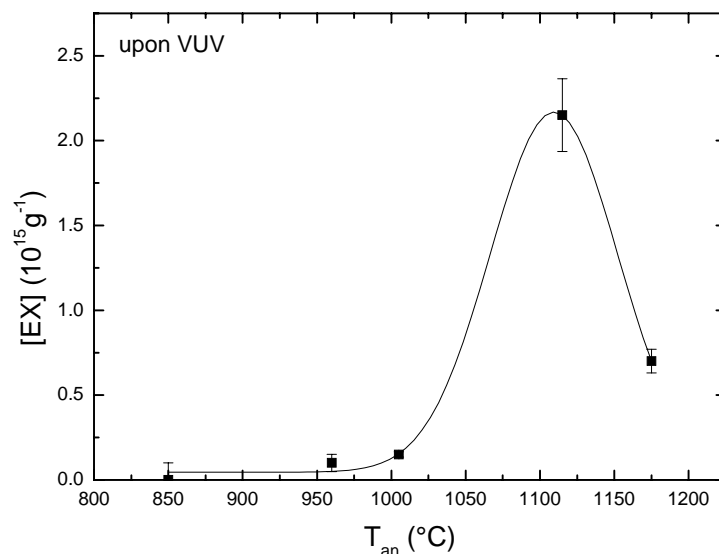
Figure 2.23: *The EX defect density upon VUV irradiation as a function of post-manufacture heat treatment in vacuum. The solid curve is merely meant to guide the eye exposing the peaked behavior of the defect generation.*

2.5.4 The *EX* center

With increasing T_{an}, another signal appears in increasing intensity. The originating defect is conclusively identified as *EX*, a SiO_2-specific center [68, 69]. In one view, it is pictured as a hole delocalized over 4 non-bridging oxygens grouped around a Si vacancy. The signal is observed from $T_{an} \geq 960$ °C on and is most intense [density up to (4.9 ± 0.5) 10^{15} g^{-1}] after annealing at $T_{an} \sim 1115$ °C; the intensity generally drops upon VUV irradiation (cf. Table 2.1). The *EX* density, measured after VUV irradiation as a function of T_{an} is shown in Fig. 2.23. A characteristic spectrum is shown in Fig. 2.24. The measured ESR parameters (g=2.0024, hf splitting A=16.4 G) are characteristic for the well known EX center. The *EX* center has been reported in various works as discussed in section 1.2.2.

2.5.5 The methyl radical

Results

A characteristic ESR spectrum (Fig. 2.25) consisting of 4 hf lines with intensity ratio 1:3:3:1 is additionally observed in the as-grown sample and in the samples annealed up to 1005 °C, measured immediate upon VUV
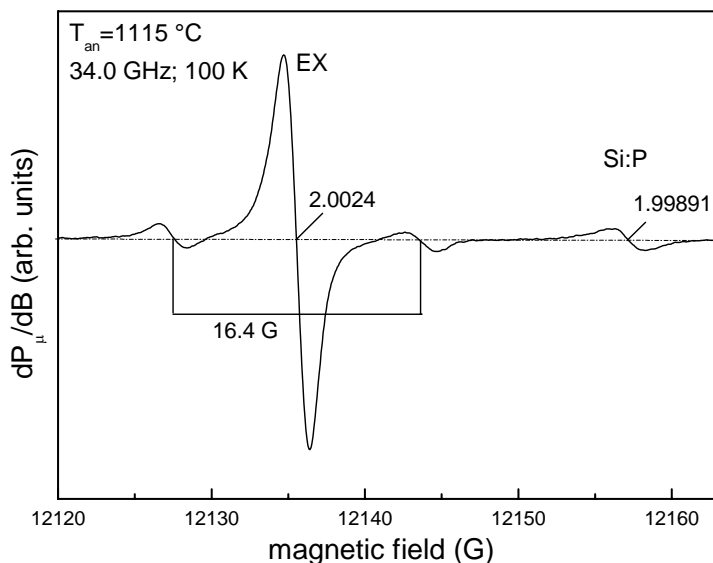
Figure 2.24: *Q-band ESR spectrum ($P_\mu \sim 0.3$ μW; B_m=1 G) of the EX center measured in the samples subjected to post-manufacture heating at T_{an}=1115 °C.*
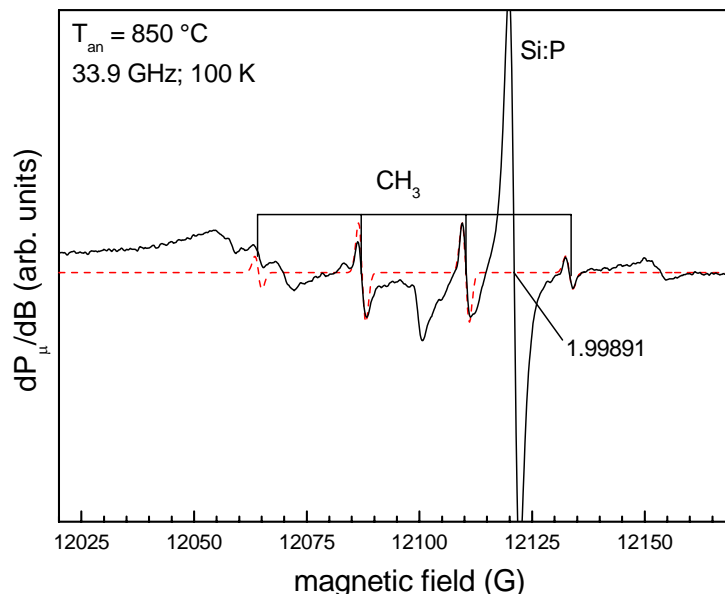
Figure 2.25: *Q-band ESR spectrum (P_μ~0.165 mW; B_m=1 G) of the CH_3 radical observed for the nanoparticles subjected to post-manufacture heating at T_{an}=850 °C. The dashed red curve represents the CH_3 radicals spectrum simulation using the parameters g=2.0026 and A=23 G.*

irradiation. This specific intensity ratio is readily explained as originating from a spin system consisting of an unpaired electron (S=1/2) interacting with three equivalent I=1/2 nuclei. Since the sample is of very high purity the most likely candidates for the nuclei are protons. The measured ESR parameters (average g value g_{av}=2.0026±0.0005; A=23±0.5 G) are indeed very similar to those observed for the methyl radical [213]. The methyl radical has previously been reported to be present in irradiated amorphous SiO_2 [214], on silica gel surfaces [215], and in some irradiated high purity synthetic silica [216]. It leaves no doubt that the observed ESR spectrum originates from the CH_3 radicals.

The total intensity of the spectra was inferred by double numerical integration of the hf component on the outer right side of the spectrum (the best resolved hf component here, the others being perturbed by signal overlap) and multiplying this intensity by 8. The density of the methyl radicals is the highest, i.e., $(0.047±0.005)\times10^{15}$ g^{-1}, for the sample annealed at T_{an}=850 °C subjected to VUV. This sample was used for further analysis. The methyl radical density as a function of post-manufacture heating in
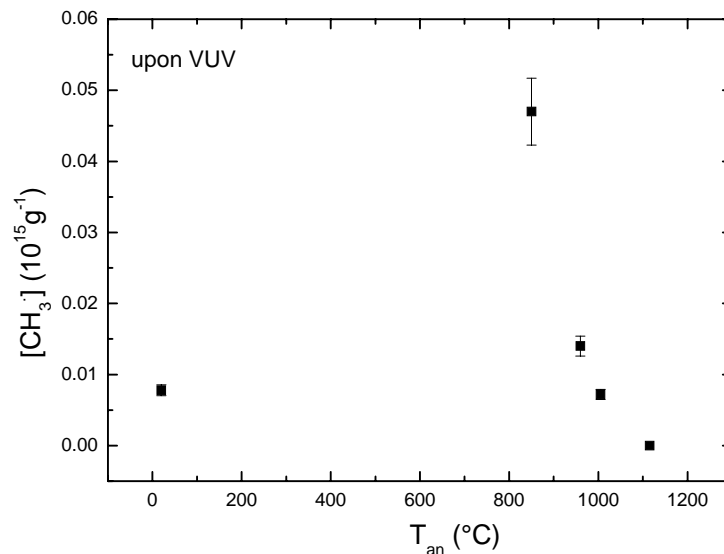
Figure 2.26: *The CH_3 radical defect density upon VUV irradiation as a function of post-manufacture heat treatment in vacuum.*

vacuum is shown in Fig. 2.26.

Analysis

As the measurements were carried out carefully with reduced modulation amplitude to avoid overmodulation, it became clear that the line widths of the four components of the observed CH_3 signals depend on the nuclear spin quantum number (M_I). This observation can be interpreted as the result of the tumbling of a spin system with anisotropies in the hf interaction and g matrix, which provides a relaxation mechanism dependent on M_I [217]. When ESR measurements where carried out at a temperature below 85 K, the ESR lines broadened beyond ESR detection. This result suggests that the radicals 'freeze' at low temperatures, substantiating that they are indeed tumbling when measured at a sample temperature of about 100 K.

The tumbling frequency can easily be calculated (see reference [215] and the references therein). Following their analysis, the line width in terms of inverse transverse relaxation time can be expressed as a sum of a secular, pseudosecular, and nonsecular part:

$$(T_2)^{-1} = (T_2)^{-1}_{sec} + (T_2)^{-1}_{pseudosec} + (T_2)^{-1}_{nonsec}. \qquad (2.4)$$
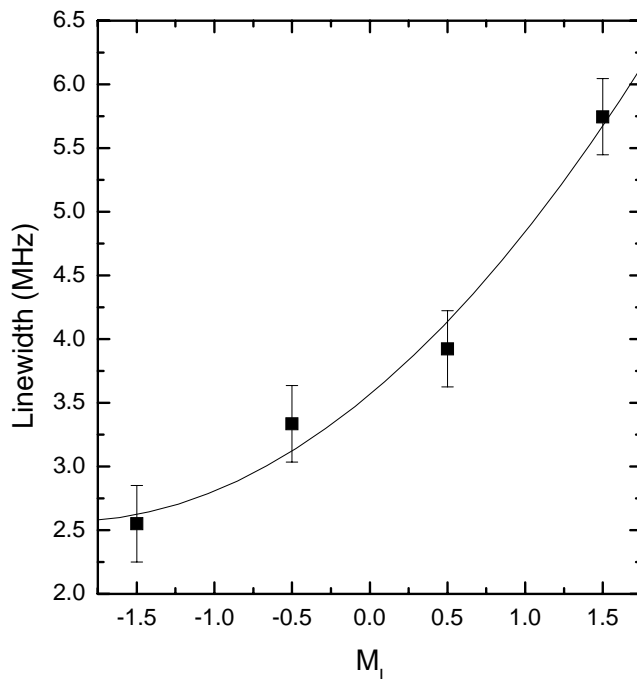
Figure 2.27: *Line widths of the four hf components of the methyl radical spectrum as a function of corresponding nuclear magnetic quantum number. The dots are the experimental points; the solid line represents the fitted curve based on Eq. 2.5 (see text).*

Since the nonsecular contribution to the line width is completely negligible and the pseudo-secular contribution is negligible to a fair approximation (∼10%), the expression for the line width can be reduced to

$$(T_2)^{-1} = a_0 + a_1 M_I + a_2 M_I^2. \tag{2.5}$$

The constants can be evaluated as:

$$a_0 = \frac{4}{45}(\Delta\gamma B)^2\tau_c + K, \tag{2.6}$$

$$a_1 = \frac{4}{15}b\Delta\gamma B\tau_c,$$

$$a_2 = \frac{1}{5}b^2\tau_c,$$

where τ_c is the correlation time, b the hf anisotropy, B the magnetic field, $\Delta\gamma$ the g matrix anisotropy, and K contains other unspecified contributions to the line width that are independent of M_I.

The line widths were measured and least squares fitted by Eq. 2.5. It should be noted that the determination of the exact line widths was somewhat hampered because of signal overlap. The measured line widths and calculated fit are shown in Fig. 2.27. The inferred constants are: a_0=3.656 MHz, a_1=1.017 MHz and a_2=0.259 MHz. If using the value b=4.5 MHz, obtained by Heller [218] for the CH_3 group in the radical $CH_3C(COOH)_2$,as an estimate for the hf anisotropy of the methyl radical, according to previous usage [216], the correlation time and thus the tumbling frequency can be calculated. In this way we find τ_c=6.39×10^{-8} s, giving 1.56×10^7 s^{-1} for the tumbling frequency. The latter value is in between the value inferred for the methyl radical trapped in irradiated high purity fused silica [216] (1.1×10^7 s^{-1}) and the value obtained for the radical adsorbed on the silica gel surface [215] (2×10^7 s^{-1}). It seems that in fumed silica the radical's rotation is slightly more hindered compared to the methyl radicals adsorbed on a silica gel surface, but less hindered by the silica network as compared to the methyl radicals present in irradiated fused silica.

It should be noted that in fumed silica the methyl radicals are possibly less stable than the ones observed in irradiated fused silica. In the latter case Friebele *et al.* still measured the same defect densities after keeping the sample for two years in room ambient [216]. In fumed silica, however, the defect densities decreased beyond ESR detection already several days after irradiation.

The appearance of CH_3 radicals is a general indicator of carbon and H contamination. This may not come as a surprise with respect to hydrogen, the abundance of which has been amply demonstrated previously by numerous techniques [160, 165]. However, although no carbon should be present during the fabrication of fumed silica, the nanoparticles are clearly C contaminated since the methyl radicals are observed in the as-grown state. Apart from possible C impurification during manufacturing, another possibility is C-contamination arising from surface adsorbance of C-containing species (e.g., CO, CO_2) from room ambient. Given the particles large surface area aspect, the latter may appear most likely. For completeness, we add that in the synthetic fused silica study using ^{60}Co γ-irradiation [216], the CH$_3$ radical formation is ascribed to radiodissociation of CH$_4$ or CO molecules trapped in the silica network during silica formation.

2.6   Summary and Conclusions

A systematic ESR study in conjunction with post-manufacture irradiation and/or annealing in vacuum in the range 850-1175 $°C$ or in the presence of SiO release in the range 1005-1205 $°C$ of fumed silica nanoparticles, reveals for the first time the presence of ESR-active point defects. Their generation and properties have been studied systematically by ESR as a function of T_{an} and VUV treatment. Several point defects inherent to the SiO$_2$ network are revealed, including E'_γ, the O_2^- ion, and the EX center. The methyl radical is also found to be present. Additionally, an as yet unidentified defect ($LU2$) is newly observed. Besides the identified ESR signals, still others are observed who could not be spectroscopically isolated or identified. The presence of these defects and their ESR properties can provide important information on the structural and chemical nature of the fumed silica nanoparticles. In particular, using the intrinsic E' defects as local atomic probes, the atomic properties of the SiO$_2$ network of the nanoparticles have been assessed. Some specific results include the following.

(1) The methyl radical is observed in the as-grown state and after post-manufacture baking in the range 850-1005 $°C$, immediately upon VUV irradiation. These $^\bullet CH_3$ centers are a familiar indicator of trace carbon and hydrogen contamination. At $T{\sim}100\ K$, it has been inferred that the radicals tumble at a frequency of $1.56{\times}10^7\ s^{-1}$. Yet, they appear unstable as their ESR signal intensity decreases beyond ESR detection several days after the VUV activation.

(2) Evidence has been found for the presence of oxygen-associated hole centers ($NBOHCs$ and $PORs$) in the as-grown samples after VUV irradiation. The dominant OHC type occurring appears to be the peroxy radical (O$_3{\equiv}$Si–O–O$^\bullet$), which would indicate that fumed silica is oxygen rich.

(3) An as yet unidentified defect, which may be linked to specific network aspects, is newly observed in the as-grown samples annealed at T_{an}=850-960 $°C$ even without additional VUV treatment. The spectral properties have been studied in detail, aiming its identification. The ESR properties include: g_c=2.00276±0.00005, closely axial symmetry, and g matrix principal values $g_{\parallel}$=2.0041 and $g_{\perp}$=2.0027. As detection of any associated hf structure has so far failed, the atomic nature of the originating defect remains largely unknown. Yet, based on specific ESR properties the center

might possibly be ascribed to $O_2Si{\equiv}Si^{\bullet}$, an E'-like center with chemically modified back bond arrangement, or to a carbon related defect center.

(4) The spectroscopic properties of the E' signal have been studied with particular interest since defect analysis can provide access to the nanoparticle structure on atomic level.

(4.1) Accordingly, changes in the zero crossing g value, line shape, and signal intensity as a function of anneal temperature, observational temperature, and elapsed time period between VUV activation and ESR measurement as the sample was kept in room ambient were carefully monitored.

The combination of all the observations on the E' signal hints at the presence of two different systems of E' centers with superposed ESR signals. It is suggested that the core of the nanoparticles exhibits a more bulk a-SiO$_2$ like structure while the surface region is of a different, more strained nature. There appears a complex strain distribution. The E' centers present in the core regions are very similar to the common E'_γ centers present in bulk a-SiO$_2$. The E' centers in the surface region, however, exhibit different properties. This can be seen as due to enhanced amorphous state disorder and strain at the surface and in near surface layers. Another important factor is that the surface E' system is possibly more apt to environmental chemical and physical interaction (adsorption) impact. As the post-manufacture temperature increases, sintering takes place decreasing the specific surface area [153] and thereby possibly the number of surface E' centers. The overall maximum E' density is small compared to standard thermal a-SiO$_2$ grown on Si, indicative of a high quality of the fumed silica particles in terms of occurring O vacancies: Only one E' center is detected in about every 1000 nanoparticles.

(4.2) In addition the influence of the presence of an (100)Si/SiO$_2$ interface during post-manufacture heating at elevated temperatures on the fumed silica nanoparticles has been studied. Through the observation and analysis of the primary ^{29}Si hf splitting of the E' centers located in the core region of the nanoparticles atomic scale information has been derived on the ring structure composition. The results demonstrate that the hf parameters are more sensitive to changes in the network structure than the g matrix.

The presumed interaction of volatile SiO at high temperatures in vacuum with the SiO$_{2(x)}$ network leads to an increase in the density of E'_γ centers, observed after VUV activation, which indicates that the fumed silica network is vulnerable for SiO attack. With SiO introduction Si enrichment

occurs leading to an increase in O vacancy (E') density. This would bring the fumed silica network closer to the compositional properties of bulk SiO_2 with known superior quality. Yet, the SiO influence does not appear to be uniform throughout the nanoparticle, as the surface regions and the core region response differently to interaction with SiO molecules.

The detection of the primary [29] hf structure of the E' centers located in the core region of the nanoparticles was enabled by virtue of the drastic increase in E' defect density resulting from the interaction of the fumed silica network with volatile SiO at high temperatures. Consistent fitting of the primary ^{29}Si E' hf structure revealed a larger isotropic hf constant for the fumed silica nanoparticles than for suprasil. As the hf parameters are linked with the O–Si–defect bond angle θ, this result indicates that θ is larger as well for fumed silica than bulk SiO_2. The latter result points to a more pyramidal defect structure for the E' centers in the core region of fumed silica particles. Moreover the observed increase in A_{iso} can be linked with a densification of the SiO_2-matrix. According to previous interpretation, this densification of the core of the nanoparticles is possibly due to a modification of the distribution of occurring ring structures in the fumed silica network suggesting the presence of more low-membered rings of SiO_4-tetrahedra.

Besides the primary ^{29}Si E' hf doublet a H-associated doublet assigned to $O_2\equiv Si^{\bullet}$–H entities was additionally observed. Relatively to the ordinary E' signal, this doublet is found to be less prominent in the spectra of fumed silica than suprasil indicating that the nanoparticles would contain less hydrogen.

As a general conclusion, the obtained results illustrate that detailed ESR studies of the specific ESR parameters such as the g and hf matrix of an embedded inherent point defect (such as E') can provide valuable information on the specific network structure on atomic-scale –in the current case, of nanosized particles. As known, the fundamental strength derives from the local probing power of the unpaired electron's wave function.

Chapter 3

P-associated defects in the high-κ HfO$_2$ and ZrO$_2$ insulators revealed by ESR

3.1 Introduction

In this chapter as well as in the next, we will step into the field of high-κ research. As aforementioned (section 1.3), excessive leakage currents encountered in metal-oxide-semiconductor field-effect transistors (MOSFETs) as the conventional a-SiO$_2$ gate dielectric is scaled down to the 1-nm range will require the replacement of the gate insulator by one of higher κ. In this chapter we will focus on ZrO$_2$ and HfO$_2$, two prominent high-κ oxides. The latter is currently considered as one of the most promising candidate high-κ dielectrics because of its favorable properties including thermal stability, suitable barrier heights for electrons and holes, and advantageous electrical properties, in part due to the existence of an ultrathin SiO$_2$ interlayer between the high-κ film and Si [20].

Nevertheless, to serve as a viable candidate the alternate dielectric must still meet various other stringent requirements, some of them not yet fully explored. One of these is that the high-κ oxide should display superb resistance to dopant penetration during necessary dopant activation anneals, as such penetration would detrimentally affect device performance. Thus, to be successful the alternate dielectric should be an excellent diffusion barrier, and consequently, the behavior of a dopant such as phosphorus is of key interest. A few works have reported on the diffusion of dopants in high-κ dielectrics [219, 220, 221]. Alarmingly, with respect to HfO$_2$-based

dielectrics, the results indicated an enhanced penetration of P through HfO$_2$ or Hf-silicates compared with standard SiO$_2$ films.

3.2   Phosphorus diffusion

Defect sites resulting from P atoms incorporated in the gate oxide may act as charge traps degrading device performance. Consequently, the presence of P atoms in the network of the gate dielectric is something one should try to avoid. Most unfortunately, this appears quite impossible. For instance, during device processing the MOSFET's source and drain are implanted with a high density of P atoms ($\sim 10^{20}$ *at.* cm^{-2}). It is not unlikely that during implantation part of the P atoms are scattered into the sides of the neighboring gate oxide. Moreover, the thermal steps necessary for dopant activation in device manufacturing may result in the diffusion of P atoms from the P-doped source and drain or, when no metal gate is used, from the P-doped poly-crystalline Si (poly-Si) gate into the high-κ dielectric.

Consequently, the problem of P penetration has been studied by several research groups [219, 220, 221]. Quevedo-Lopez *et al.* studied penetration of P through HfSi$_x$O$_y$ and HfSi$_x$O$_y$N$_z$ films in stacks consisting of a P-implanted (5×10^{15} *at.cm*$^{-2}$) poly-Si film deposited by CVD on a CVD HfSi$_x$O$_y$ (5 *nm*) or HfSi$_x$O$_y$N$_z$ film on (100)Si [219, 220]. From the secondary ion mass spectroscopy (SIMS) P depth profiles in the Si substrate
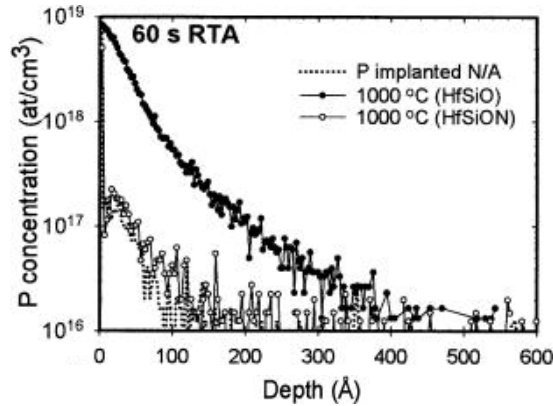
Figure 3.1: *SIMS P depth profile in the Si substrate after 1000 °C annealing for 60 s and chemical etching of the P-doped poly-Si/HfSi$_x$O$_y$ (HfSi$_x$O$_y$N$_z$)/Si stack. The dotted curve indicates the profile for the P-implanted as-grown stack. The figures is taken from Ref. [219].*

after rapid thermal annealing in the range 900-1050 $°C$, such as the one shown in Fig. 3.1 for $T_{an}\sim1000$ $°C$, the authors concluded that P penetrates through the HfSi$_x$O$_y$ layer into the Si substrate for $T_{an}\geq1000$ $°C$. The P penetration through the HfSi$_x$O$_y$ films upon annealing at these temperatures was shown to be substantially higher than for HfSi$_x$O$_y$N$_z$ films, where it was near the detection limit. The P diffusivity in the HfSi$_x$O$_y$ films is found to be at least one order of magnitude higher than those in SiO$_2$ and SiO$_x$N$_y$.

Based upon the film microstructure, studied by HRTEM, the authors propose that this enhanced P diffusion in HfSi$_x$O$_y$ is related to grain boundary formation resulting from HfSi$_x$O$_y$ film crystallization. Fig. 3.2 (a) shows their HRTEM result for a P-doped poly-Si/HfSi$_x$O$_y$/Si stack subjected to a 60 s rapid thermal anneal at 1050 $°C$, clearly displaying the crystallization of the Hf silicate film after annealing. The reduction of dopant penetration through the introduction of N into the HfSi$_x$O$_y$ films is linked with the suppression of crystallization observed in the HfSi$_x$O$_y$N$_z$ films [see Fig. 3.2 (b)]. This is attributed to both the lower Hf content in these films and the N incorporation.

Suzuki *et al.* studied the P diffusion in thick (110 nm) P-implanted (5×10^{13} $at.$ cm^{-2}) HfO$_2$ films deposited by ALCVD on Si, upon rapid thermal annealing in N$_2$ [221]. From the SIMS profiles of the P concentration in HfO$_2$, such as shown in Fig. 3.3 (a) for $T_{an}\sim1100$ $°C$, the authors extracted the diffusion coefficient (Fig. 3.3 (b)). They concluded that P
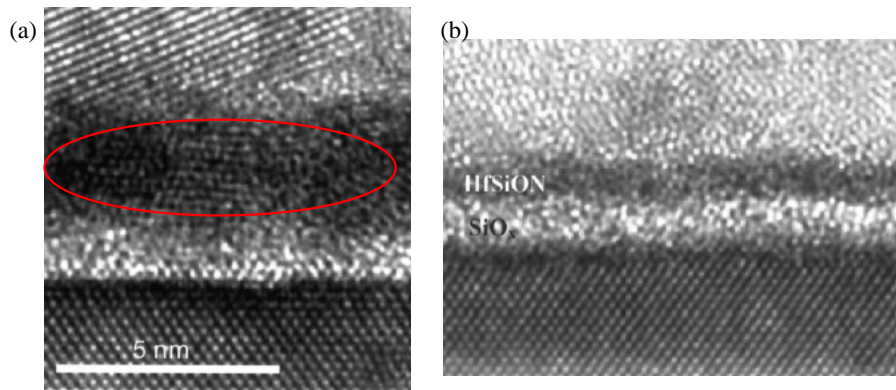
Figure 3.2: *HRTEM results for 60 s at 1050 °C annealed stacks of (a) P-doped poly-Si/HfSi$_x$O$_y$/Si (the red ellipse circles the crystalline region) and (b) poly-Si/HfSi$_x$O$_y$N$_z$/Si (no detectable crystalline region is observed). The figures are taken from Ref. [220].*
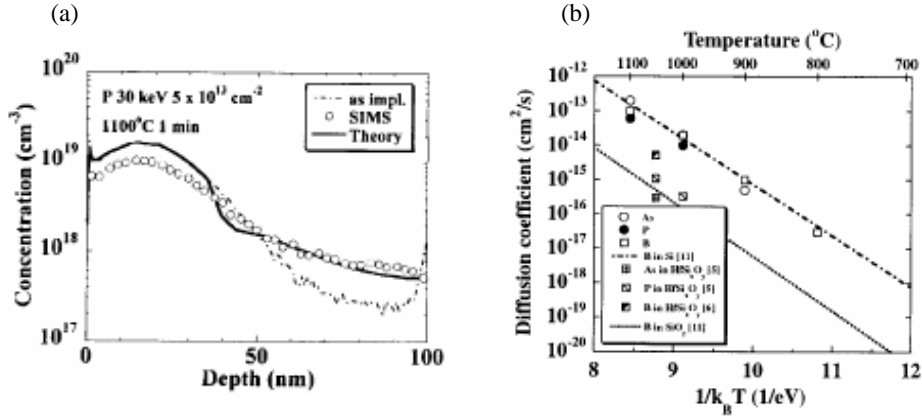
Figure 3.3: *(a) SIMS profiles of the P concentration in as-grown P-implanted ALCVD HfO$_2$ on Si and after rapid thermal annealing at 1100 °C. (b) Diffusion coefficients of As and P in HfO$_2$, and B in HfO$_2$, Si, and SiO$_2$. The figures are taken from Ref. [221].*

diffusion through HfO$_2$ is significant –two orders of magnitude higher than that of B in SiO$_2$.

Thus rather than solely focussing on finding ways to avoid P incorporation into the gate dielectric, it might be of vital importance to additionally focus on the assessment of the electrical activity of the defect sites resulting from this P penetration into the high-κ oxide. To reach this goal, atomic scale information will be required of how dopants are incorporated into the high-κ network. For this purpose ESR has been demonstrated to be the preferred technique as evidenced by the reliable identification of numerous (impurity related) point defects in various dielectrics, such as SiO$_2$. One pertinent class here concerns dopant-associated centers [4]. Indeed, ESR studies of P-associated defects in SiO$_2$-based glasses resulted in the observation and identification of several defect centers. This may be evident from the overview given in section 1.2.3 of the different P-associated defect centers so far observed in SiO$_2$-based glasses [61, 92, 13, 87, 88] and P-doped c-SiO$_2$ [85, 86].

The present chapter deals with the ESR observation of P-related point defects in two different oxides eminent in the current high-κ dielectric research, i.e., ZrO$_2$ and HfO$_2$. In each case, a similar type of defect is observed, the results indicating that the P atoms can be substitutionally incorporated in both the ZrO$_2$ and HfO$_2$ network resulting in ESR active defect centers exhibiting similar ESR parameters. In both oxides a ^{31}P hf

doublet of large splitting is observed, assigned to a P_2-type defect. The basic parameters of the defect are assessed to retrieve the defect's atomic nature which might prove essential in understanding their possible charge trapping behavior, and hence, detrimental effect on device performance.

3.3   Experimental details

3.3.1   Samples

A first set of samples consisted of 99.96% pure ZrO_2 powder of particles size <44 μm and a density of 5.89 gcm^{-3} obtained from Alfa Aesar. As main metallic impurities the powder contains <50 ppm Hf and <25 ppm Al, Fe, P, Si, and Ti. The particles are crystalline and in the monoclinic phase. After initial observation of P-associated centers by ESR a second set of samples was obtained, invoking another prominent high-κ oxide, through depositing 100-nm thick amorphous HfO_2 on p-type (100)Si substrates, using ALCVD at 300 $°C$ from $HfCl_4$ and HfO_2 precursors. Inherent to this fabrication method is that the HfO_2 films contain 2-3% H. To boost ESR detectivity the samples were implanted by P ions to densities of $\sim 10^{15}$ cm^{-2}, with the implantation energy adjusted to attain a mid-film mean projected range.

3.3.2   ESR spectrometry

Initial conventional cw absorption derivative Q-band ($\sim$34 GHz) ESR measurements were performed at 100 K on the ZrO_2 powder. The modulation amplitude (B_m) of the applied magnetic field and the incident microwave power (P_μ) were restricted to levels not causing (noticeable) signal distortion. A co-mounted Si:P marker sample [g(100 K)=1.99891] or a Li:F marker sample (g=2.00229) was used for g factor and (spin) density calibration. The latter was attained through orthodox double numerical integration of the recorded first-derivative absorption spectra of the defect and the marker. However, to circumvent saturation, in this way increasing sensitivity, the rest of the ESR measurements were performed in the second harmonic mode [14, 15] in X ($\sim$9.2 GHz), K ($\sim$20.4 GHz), and Q-band in the temperature range 4.2-300 K using relatively high modulation amplitudes and microwave powers. As outlined elsewhere, it appears that when appropriate conditions are met for a certain defect center, the second harmonic phase-quadrature (out-of-phase) spectra are identical to the absorption spectra of that defect [13, 14, 15].

Separate sets of the HfO$_2$ samples were subjected to post-implantation annealing in N$_2$ for ∼30 *min* at desired temperatures (T_{an}) in the range 300-900 °C. After initial ESR tests, to maximally reveal all defects, the samples were subjected to suitable photon irradiation. All samples were subjected to unbiased VUV irradiation (10 *eV* photons; flux∼ 10^{15} *cm^{-2}s^{-1}*) obtained from a Kr-resonant discharge lamp. The *nm*-thin HfO$_2$ films were only irradiated for a relatively short period (20 *min*), while the *μm*-sized ZrO$_2$ particles needed to be irradiated for days due to the limited penetration depth of the VUV photons and the shadowing effect with powder particles. To overcome the latter the powder was regularly stirred during irradiation. A separate set of ZrO$_2$ samples was subjected to UV irradiation (∼2-7 *eV*, obtained from a Xe-lamp) for several hours. During UV irradiation the powder was contained in a continuously rotating quartz holder put in front of the lamp. Possibly, the treatment may additionally unveil strained or weak bonding (bond rupture) and activate diamagnetic precursor sites [112].

3.4   Results

Curve (a) in Fig. 3.4 shows a typical high-power second harmonic mode [14, 15] Q-band (∼34 *GHz*) spectrum observed in 99.96% pure ZrO$_2$ powder of particle size <44 *μm* subjected to UV irradiation. Various signals appear but here we will only focus on the pair of resonance features (doublet) labeled P_2 in Fig. 3.4. From careful analysis of the saturation behavior of the different resonances, it was established that the resonance lines observed in the center region of the spectra have an origin different from the resonance lines labeled P_2. The doublet was observed in the as-received particles but became much more prominent upon VUV or UV irradiation. The doublet could be detected in both the high-power second harmonic mode [Fig. 3.4 curve (a)] and the conventional low-power derivative-absorption mode [222] [Fig. 3.4 curve (c)]. After taking the first derivative of the second harmonic mode spectrum [Fig. 3.4 curve (b)], identical spectra are obtained in both modes, attesting that both modes can reliably be used to obtain correct ESR parameters (such as, g matrix, hf tensor, and line width) of the observed defects. Additionally, the second harmonic mode measurements of the UV irradiated ZrO$_2$ powder were performed at various (measurement) temperatures T in the range 25-297 *K*. The observed doublet spectrum did not change indicating that the ESR parameters are not influenced by the observation temperature.
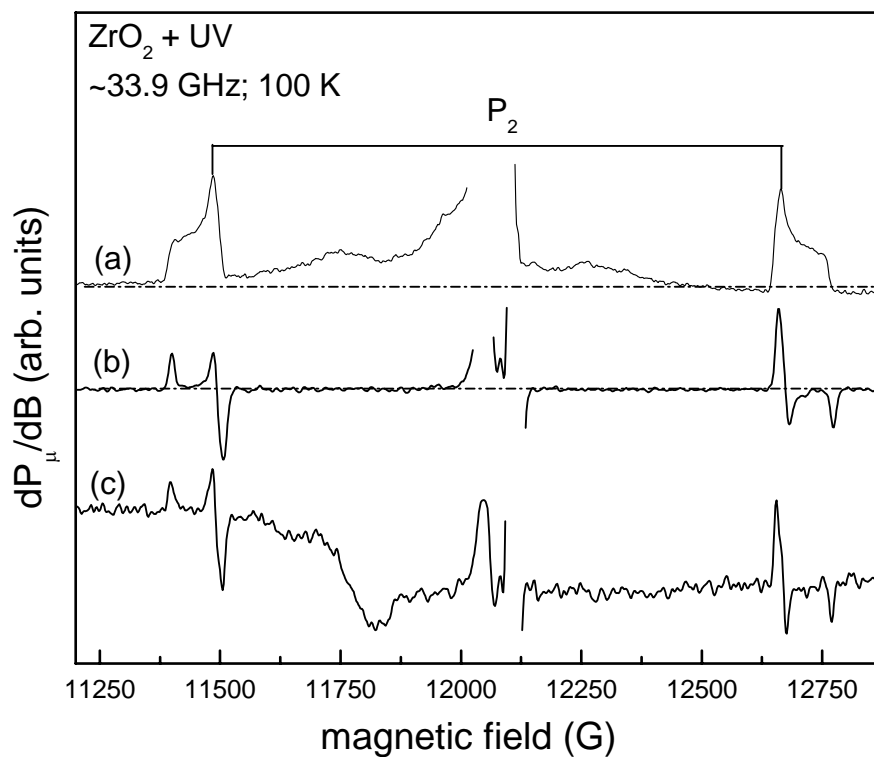
Figure 3.4: *Q-band ESR spectra of ZrO_2 powder subjected to UV irradiation measured at 100 K: (a) the high-power (saturation) second harmonic mode spectrum, (b) the first derivative of the high-power (saturation) second harmonic mode spectrum, and (c) the conventional low-power derivative-absorption mode spectrum.*

A similar doublet spectrum was observed in the P-implanted HfO_2 films on Si but only after subjecting the sample to post-implantation annealing in the range 500-900 $°C$ followed by VUV irradiation. This is illustrated in Fig. 3.5 [curve (b)] showing a representative Q-band spectrum for the HfO_2 sample subjected to post-implantation annealing at 900 $°C$, the temperature for which the doublet became the most prominent, and additional VUV irradiation. Moreover, Fig. 3.5 illustrates that the resonance lines observed in the ZrO_2 powder [spectrum (a)] and in the HfO_2 films are quite similar and, even though the ESR parameters slightly differ, seem to originate from similar defect centers.

Based on the general knowledge of powder pattern ESR line shapes, the kind of symmetry relationship between the two resonance features in one
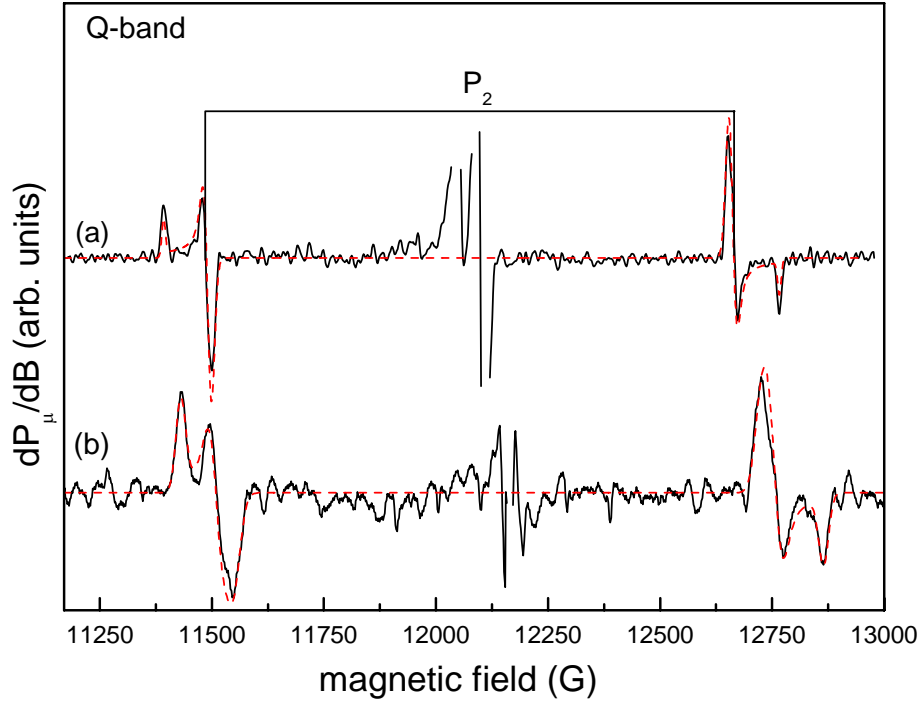
Figure 3.5: *First derivative of the high-power (saturation) second harmonic mode Q-band spectra (a) measured at 33.91 GHz at 100 K in ZrO$_2$ powder subjected to UV irradiation and (b) measured at 34.03 GHz at 4.2 K in P-implanted HfO$_2$ films on Si subjected to a 900 °C post-implantation anneal in N$_2$ and subsequent VUV irradiation. The dashed red curves represent the simulations obtained using the principal g matrix values (a) $g_1=2.0011$, $g_2=2.0007$, and $g_3=2.0007$ and (b) $g_1=1.9965$, $g_2=1.9975$, and $g_3=1.9975$, the principal hf tensor values (a) $A_1=1370$ G, $A_2=1162$ G, and $A_3=1157$ G and (b) $A_1=1425$ G, $A_2=1245$ G, and $A_3=1160$ G, a Gaussian line shape, and peak-to-peak line widths (a) $\Delta B_{pp}^1=8$ G, $\Delta B_{pp}^2=17$ G, $\Delta B_{pp}^3=17$ G and (b) $\Delta B_{pp}^1=24$ G, $\Delta B_{pp}^2=18$ G, $\Delta B_{pp}^3=24$ G.*
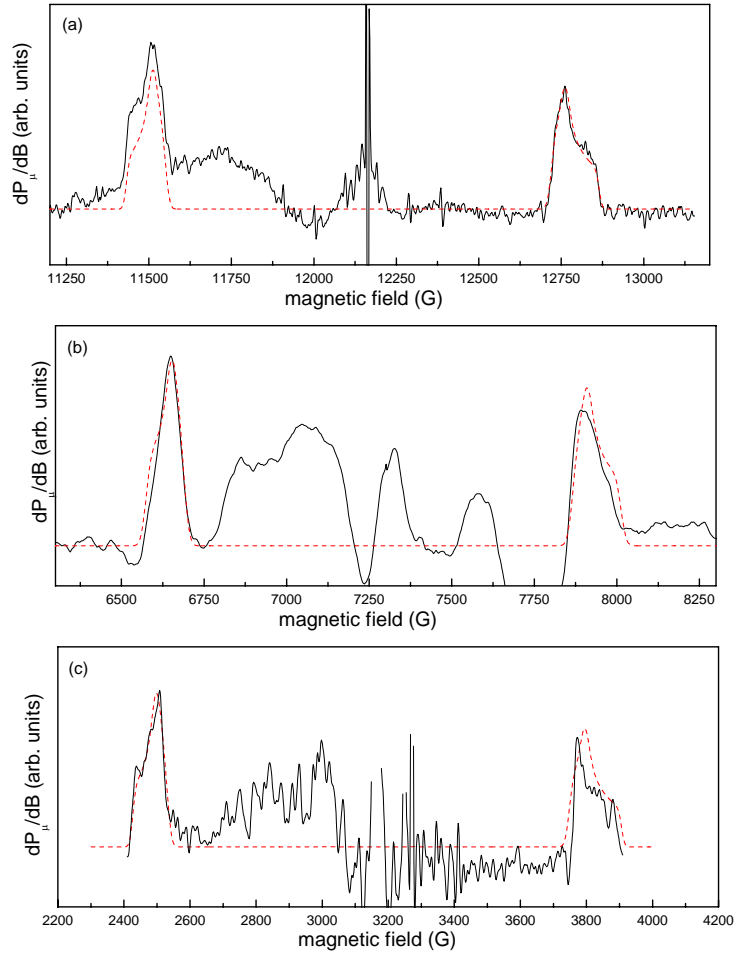
Figure 3.6: *The high-power (saturation) second harmonic mode Q, K, and X-band spectra observed in P-implanted HfO$_2$ films on Si subjected to a 900°C post-implantation anneal in N$_2$ and subsequent VUV irradiation. The dashed red curves represent the simulations obtained using, for all three spectra, the principal g matrix values g_1=1.9965±0.0004, g_2=1.9975±0.0004, and g_3=1.9975±0.0004 and the principal hf tensor values A_1=1425±10 G, A_2=1245±10 G, and A_3=1160±10 G.*

spectrum would leave little doubt about their correlated nature. Yet, to firmly establish whether the two resonance lines do form a natural doublet, complementary X ($\sim$9.2 GHz) and K-band ($\sim$20.4 GHz) ESR experiments were carried out, as illustrated by the spectra shown in Fig. 3.6 and Fig. 3.7 for the case of (100)Si/HfO$_2$ and ZrO$_2$, respectively. It appears that the doublet field splitting slightly increases ($\sim$40 G) from Q to X-band measurements, but is in first order independent of the observational frequency. The central g value (g_c) of the doublet, however, shifts significantly downward ($\Delta g_c \sim$0.064) from X to Q-band (cf. Fig. 3.7). This shift in g_c is found
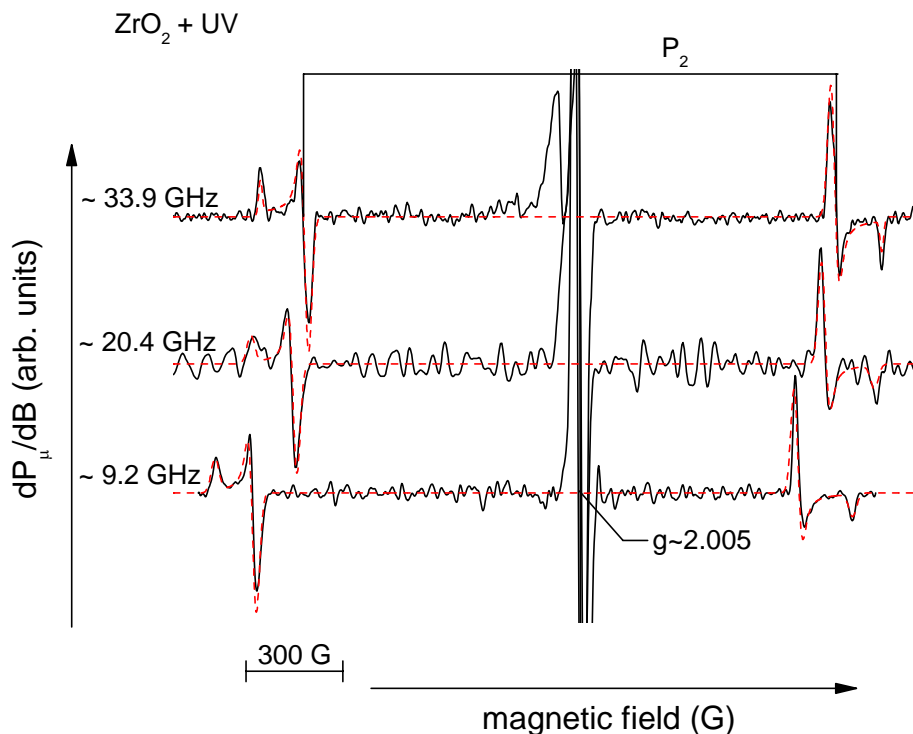
Figure 3.7: *First derivative of the high-power (saturation) second harmonic mode Q, K, and X-band spectra observed in ZrO$_2$ powder subjected to UV irradiation. The dashed red curves represent the simulations obtained using the principal g matrix values g_1=2.0011±0.0004, g_2=2.0007±0.0004, and g_3=2.0007±0.0004 and the principal hf tensor values A_1=1370±10 G, A_2=1162±10 G, and A_3=1157±10 G. The spectra are aligned at the resonance field of a main central signal at g$\sim$2.005 revealing the significant shift of the doublet as a function of observational frequency.*

to be consistent with the Breit-Rabi shift [18] expected for a hf doublet resulting from a S=1/2, I=1/2 system exhibiting such large hf splitting ($\sim$1200 G), as illustrated in Fig. 3.8 for the doublet observed in ZrO$_2$: The experimentally obtained g_c values (filled symbols) for three different microwave frequencies match within experimental error the variation in g_c values calculated using exact matrix diagonalization for a S=1/2 and I=1/2 spin system with A=1160 G and g=2.0007. Furthermore, counter to the common spectral appearance of S>1/2 centers, no ΔM_J=2 transitions at half magnetic field strength of the ΔM_J=1 transition could be observed.
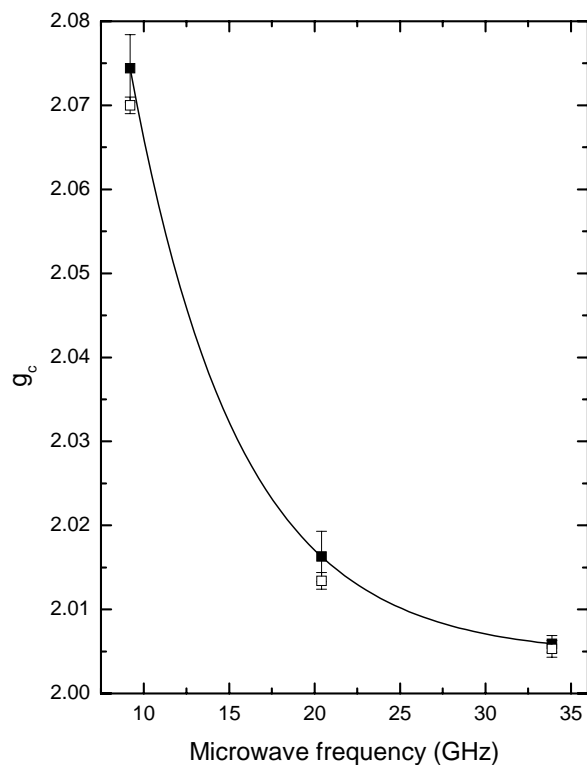
Figure 3.8: *Zero-crossing g values (g_c) of the measured P$_2$ signal in ZrO$_2$ powder subjected to UV irradiation for three different microwave frequencies. Filled symbols: experimentally obtained g_c. Open symbols: calculated g_c obtained using exact matrix diagonalization for a S=1/2 and I=1/2 spin system with A=1160 G and g=2.0007. The solid line is merely meant to guide the eye showing the upward shift of the g_c with decreasing microwave frequency.*

3.5   Analysis

Altogether these observations leave little doubt that the two signals concern a hf doublet resulting from interaction of an unpaired electron of spin S=1/2 with a closely 100% naturally abundant nucleus of spin I=1/2, rather than stemming from two dissimilar paramagnetic species. In looking for a candidate I=1/2 nucleus of 100% natural abundance which could evoke such large hf splitting ($\sim$1200 G), i.e., large nuclear moment, a quick perusal of the table of isotopes would leave only two possibilities, i.e., ^{31}P or ^{1}H. Taking into account the presence of P impurities in non-negligible amounts ($<$25 ppm) in the ZrO$_2$ powder and the P-implantation ([P]$\sim$10^{15} cm^{-2}) signal boost in the HfO$_2$ samples, ^{31}P follows as the most likely candidate nucleus involved.

3.5.1   Spectra simulations

The observed doublet spectra, exhibiting typical powder pattern properties, could be consistently described (cf. Fig. 3.5, dashed curves) by one effective spin S=1/2 and 100% naturally abundant I=1/2 center, according to the simplified spin Hamiltonian comprised of the Zeeman and hf terms, respectively

$$\mathcal{H}_{S} = \mu_B \vec{B} \cdot \hat{g} \cdot \vec{S} + \vec{S} \cdot \hat{A} \cdot \vec{I}. \tag{3.1}$$

For each of the dielectrics separately, the fitting, using a code based on exact matrix diagonalization incorporating the Breit-Rabi formula, could be consistently performed with one set (within experimental error) of $\hat{g}$ and $\hat{A}$ principal values for the independent X, K, and Q-band spectra, providing high confidence in the inferred data. The fitting result is illustrated in Figs. 3.6 and 3.7 (dashed curves) for the (100)Si/HfO$_2$ and ZrO$_2$ case, respectively. The inferred effective S=1/2 Hamiltonian parameters are listed in Table 3.1. The indicated experimental accuracies on the inferred g and A values are dominated by the accuracy attained on the magnetic field sweep since for the wide scans ($>$1000 G) the magnetic field sweep is not perfectly linear. Measurements at three different microwave frequencies and thus in three different experimental setups, however, resulted not only in more reliable spectra simulations but also in a reduction of the derived experimental error on the ESR parameters.

From the inferred parameters listed in Table 3.1, it may be noticed that the hf doublets observed in ZrO$_2$ and HfO$_2$ are quite similar, strongly suggesting that both may originate from nominally the same defect center similarly embedded in a yet different oxide network. Quite naturally, as

well expected for non-identical environment, there will emerge some (small) differences in the obtained ESR parameters as can be seen from Fig. 3.5 and Table 3.1. Compared to the HfO_2 case, the defect center observed in the ZrO_2 powder exhibits ESR parameters closer to axial symmetry, the hf splitting is smaller, the principal g values are closer to the free electron g value, and the line widths are smaller.

3.5.2   Structural model

Having established pertinent ESR parameters and accepting the P-related nature of the observed defect centers the next step in analysis would attempt to assess the structural model. In that search, let us be guided by a comparison of our results with ESR data of P-associated defects previously detected in other oxides, in particular those in doped silica glasses [4, 61, 92, 13, 87, 88]. Characteristic for the defects observed in the current study is the very large hf splitting, a property only observed for two types of P-associated defects in SiO_2 based glasses, i.e., P_1 and P_2. Comparing our g and hf data with those from literature (cf. Table 1.3 and 3.1) the currently observed defects appear to be most similar to the P_2 defect (exhibiting the largest hf splitting) observed in, e.g., P_2O_5-SiO_2 glass [61] and P-implanted α-quartz [85, 86], assigned to a P substituting a Si atom. So, mainly based on a comparison of the Hamiltonian parameters, we assign the currently observed defect centers in HfO_2 and ZrO_2 to P_2-type defects.

In SiO_2 the P_2 center has been ascribed to a P substituting a Si atom: A phosphorus atom of formal oxidation step +5 has taken the place of a silicon atom of oxidation state +4, hereby introducing a "precursor" defect that provides a coulombic trapping potential for an electron. This model was confirmed by an ESR study of single-crystal P-doped α-quartz. [85, 86] Based on the observed symmetry properties of the defect it was suggested that the P_2 defect consists of a P atom back bonded to 4 O atoms, with the P nucleus considerably displaced. As mentioned, this model of substitutional P in α-quartz has recently been confirmed by theory [89, 90].

3.5.3   LCAO analysis

Proceeding with the analysis of the observed P_2-type defects, it might be interesting to determine the s (α^2) and p character (β^2) of the orbital composition of the unpaired electron and its localization (η^2) on the central P atom [4]. To ease comparison we will do this in accordance with previous studies of P_2 in SiO_2, using the LCAO approximation elaborated on in

Table 3.1: *Comparison of the ESR parameters of the P$_2$ defect embedded in different oxides. Estimated accuracies on inferred g and A values in this work ([a], [b]) are ±0.0004 and ±10 G, respectively.*

	g_1	g_2	g_3	A_1 (G)	A_2 (G)	A_3 (G)	α^2	β^2	η^2
c-HfO$_2$ [a]	1.9965	1.9975	1.9975	1425	1245	1160	0.33	0.67	0.83
c-ZrO$_2$ [b]	2.0011	2.0007	2.0007	1370	1162	1157	0.33	0.67	0.79
c-SiO$_2$ [c]	2.0012	2.0032	1.9991	1229	1087	1075	0.39	0.61	0.61
a-SiO$_2$ [d]	2.001	2.001	2.001	1300	1150	1150	0.40	0.60	0.63

[a] P$_2$ in P-implanted HfO$_2$ subjected to post-implantation annealing in the range 500-900 °C and VUV (10 eV) irradiation.

[b] P$_2$ in ZrO$_2$ powder with <25 *ppm* P subjected to VUV (10 eV) or UV irradiation (see text).

[c] P(I) variant of P$_2$ in α-quartz subjected to x-ray irradiation (see Ref. [85, 86]).

[d] P$_2$ in P$_2$O$_5$-SiO$_2$ glass subjected to γ-ray or x-ray irradiation (see Refs. [4, 61]).

section 1.1.1. The results of such a LCAO analysis are also compared in Table 3.1 together with data on the P_2 defect in silica based glasses and quartz compiled from literature. In each case the atomic coupling constants calculated for the neutral ^{31}P atom by Morton and Preston [8] were used as those are currently regarded as the most accurate. It should be noted, however, that in previous works different values for A_s and A_p were used resulting in different inferred values for α^2 and β^2 than the ones reported in Table 3.1.

From the comparison, it appears that the main difference concerns the localization: the unpaired electron of P_2 in HfO$_2$ or ZrO$_2$ is stronger ($\sim$31%) localized on the central P atom than in SiO$_2$. The unpaired electron orbital composition, however, is also different: the proportion of the p to the s character has increased ($\frac{\beta^2}{\alpha^2} \sim 2$) for P_2 in the high-κ oxides compared to P_2 in SiO$_2$ ($\frac{\beta^2}{\alpha^2} \sim 1.5$). Some structural variations are of course expected when substitutionally embedding P in different matrices (environments), reflecting in the unpaired electron sp hybrid which will result in modification of g and A values.

3.5.4 Defect densities

Next, we may wonder about the fraction of P impurity atoms that ultimately end up as an ESR-active P_2 defect. For the P_2 defects in ZrO$_2$ an accurate defect density could be obtained as the centers could be detected using conventional first-derivative ESR, giving, after prolonged UV irradiation a density of $\sim 1 \times 10^{15}$ g^{-1}, which means that at least 1% of the P impurities (<25 *ppm*, as specified) results in an ESR active point defect.

The experimental situation is less favorable for the (100)Si/HfO$_2$ case as due to excessive saturation in combination with the limited amount of sample vailable, the P_2 signal could not be correctly measured (unacceptable signal distortion present or signal not observable at all) using conventional ESR. Quantitative determination of defect densities from second harmonic saturation spectra, however, is not straightforward [13] and requires extreme care. The amplitude of the second harmonic mode spectra depends in a complex way on the relaxation times of the defect centers and on various experimental parameters such as the modulation amplitude, the modulation frequency, and the microwave power [13].

Only via an indirect calibration procedure linking the correct first-derivative low-power ESR spectra of P_2 in ZrO$_2$ with the high-power second harmonic saturation spectra, an estimate could be made of the P_2 density in the HfO$_2$ samples along the following procedure: For both the ZrO$_2$ and

the HfO$_2$ samples a second harmonic Q-band spectrum was recorded of the doublet using the same experimental parameters. Each second harmonic measurement was immediately followed by a conventional first-derivative measurement of the co-mounted marker again under the same experimental conditions for both samples. This way the quotients can be determined of the intensity of the doublet, obtained through single numerical integration of the second harmonic spectrum, to the intensity of the marker, obtained through double numerical integration of the first-derivative marker spectrum. Assuming that the relaxation times for P_2-type centers in both high-κ dielectrics are comparable, the ratio of the quotients will be equal to the ratio of the total number of P_2-type defects in the two materials. Knowing the P_2 density in the ZrO$_2$ sample, this resulted in a total of $\sim$4$\times$10^{13} and $\sim$9$\times$10^{12} P_2 defects in the ZrO$_2$ sample subjected to UV irradiation and in the HfO$_2$ sample subjected to post-implantation annealing at 900 $^\circ C$ and VUV irradiation, respectively. It appears that the total number of P_2 defects actually in the cavity when measuring the HfO$_2$ sample is more than 4 times lower than when measuring the ZrO$_2$ sample, accounting for the lower signal to noise ratio of the HfO$_2$ spectra (cf. Figs. 3.5, 3.6, and 3.7).

In this way, for the HfO$_2$ sample subjected to a post-implantation anneal at 900 $^\circ C$ and VUV irradiation an estimated defect density of $\sim$5$\times$10^{12} cm^{-2} was obtained, which would indicate that about $\sim$0.5% of the implanted P atoms results in a P_2 defect –a fraction quite comparable with the ZrO$_2$ case and P_2 in atomic pressure CVD deposited BPSG films on Si subjected to VUV irradiation, electron, and hole injection [13]. It should be noted, however, that the inferred defect densities probably concern just lower limits as the VUV or UV irradiation applied here might not have been completely exhaustive in activating precursor sites into the ESR active state.

3.6   Discussion

In the HfO$_2$ samples the P_2 center is only observed after post-implantation annealing at $T_{an} \geq 500$ $^\circ C$ and additional VUV irradiation. The temperature of the necessary "turn on" post-implantation anneal step is close to the known onset temperature for crystallization of the HfO$_2$ film into a mixture of tetragonal and monoclinic phases, with, notably, the monoclinic phase strongly dominating [223, 224]. Hence, we suggest that the crystallization is accompanied by part of the implanted P atoms then taking the required
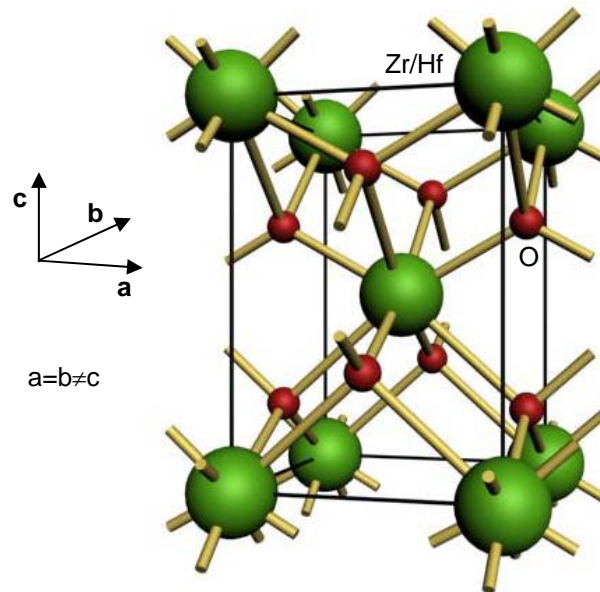
Figure 3.9: *Illustration of the unit cell of the lattice structure of tetragonal HfO_2 or ZrO_2.*
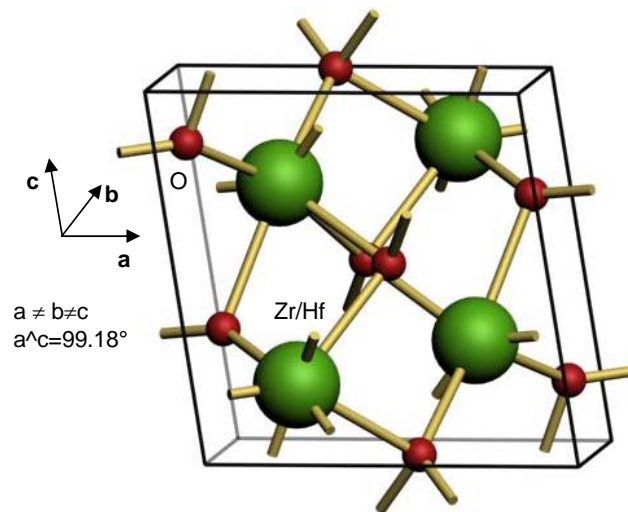
Figure 3.10: *Illustration of the unit cell of the lattice structure of monoclinic HfO_2 or ZrO_2.*

substitutional position in a particular crystalline phase. Information regarding the latter may be inferred from the fact that the P_2 center was also found to become more prominent upon annealing at higher temperatures. Indeed, it has been shown that the volume fraction of the tetragonal phase in the HfO$_2$ film decreases with increasing temperature [223], the film almost completely converting into the monoclinic phase upon annealing at $T_{an} \sim 900$ °C. Apparently the P_2 defect preferentially appears in the monoclinic phase. Figure 3.9 and 3.10 illustrate the unit cell for the tetragonal and monoclinic phase of HfO$_2$ or ZrO$_2$, respectively. For the ZrO$_2$ powder no post-implantation anneal step was necessary to observe P_2. This result is still consistent within the above picture as the as-received ZrO$_2$ particles are in the monoclinic crystalline phase, where the P impurities were incorporated during high-temperature particle formation, during which (part of) the P atoms could take a Zr substitutional position.

We thus have reached the result that the P_2 defects observed in both high-κ oxides studied are very similar and both pertain to the monoclinic oxide phase. Looking deeper, these findings seem well founded as the structural parameters for m-HfO$_2$ and m-ZrO$_2$ are almost identical (cf. Table 3.2) [225]. Quite naturally, the small differences in the hf parameters of P_2 in both oxides just reflect the small differences in the structural parameters. Comparing, however, our results with those for P_2 in c-SiO$_2$ [85, 86], the hf parameters were found to deviate more substantially. This can be seen as originating from the different network structure of the α-quartz,
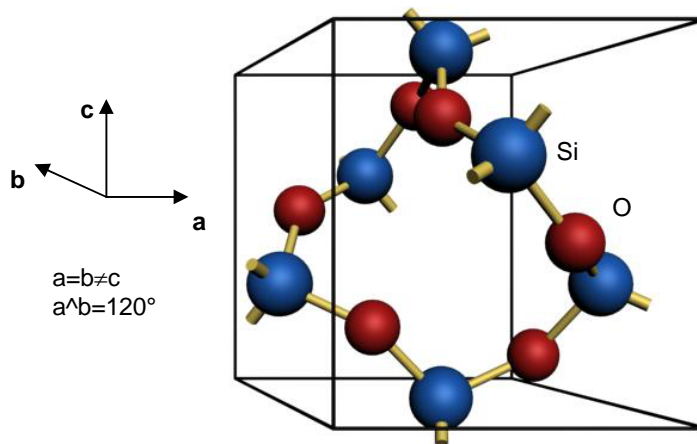
Figure 3.11: *Illustration of the unit cell of the lattice structure of trigonal α-quartz.*

Table 3.2: *Comparison of experimental structural parameters for the monoclinic phase of chemically prepared HfO_2 and ZrO_2 powder, and for the trigonal phase of SiO_2 (e.g., α-quartz). Lattice parameters a, b, and c are in Å.*

	a	b	c	monoclinic angle β
m-HfO$_2$ [a]	5.1156	5.1722	5.2948	99°11'
m-ZrO$_2$ [a]	5.1454	5.2075	5.3107	99°14'
t-SiO$_2$ [b]	4.92	4.92	5.41	/

[a] Values taken from Ref. [225]. The accuracy on a, b, and c is ±0.0005. The accuracy on β is ±0°05'.
[b] Values taken from Ref. [226]. The accuracy on a, b, and c is ±0.01.

i.e., trigonal phase as illustrated in Fig. 3.11 [226]. A steric model for the adduced P_2-type defect in HfO_2 is depicted in Fig. 3.12. Thus, the P_2-type defect may seem ubiquitous to all binary oxide glasses, where the fine details of difference in structure may be addressed by theory.

After post-implantation heat treatment at $T_{an} \sim 500$ °C the P_2 centers in the HfO_2 samples were still found to reside in an ESR-inactive state (or at least, too low an ESR active fraction). Irradiation by VUV was required to observe the hf doublet. In the ZrO_2 powder this activation step was not necessary but additional VUV or UV irradiation did drastically increase the defect density. A possible reason for the photonic impact is that (part of) the P-defects are ESR inactive due to the presence of a charge compensator [85, 86]. The VUV or UV irradiation would then cause charge transfer resulting in the proper ESR active state. However, no evidence was found for the presence of such a charge compensator. A second possibility is that (part of) the centers are left ESR inactive due to binding with H. The VUV or UV photons would then photodissociate H from the passivated defects [112]. The latter scenario is quite likely, especially for the HfO_2 samples as these films contain 2-3% H [227].

Having provided evidence that for both high-κ oxides a sizeable fraction ($\sim$0.5-1%) of the P atoms results in a P_2 defect, we should draw attention to their potential operation as charge traps, which would make them detrimental for device performance [220, 221, 13]. There seems little doubt about this: In SiO_2 it has been concluded theoretically as well as experimentally that the P_2 defects act as a hole trap [87, 93]. Whether the P_2
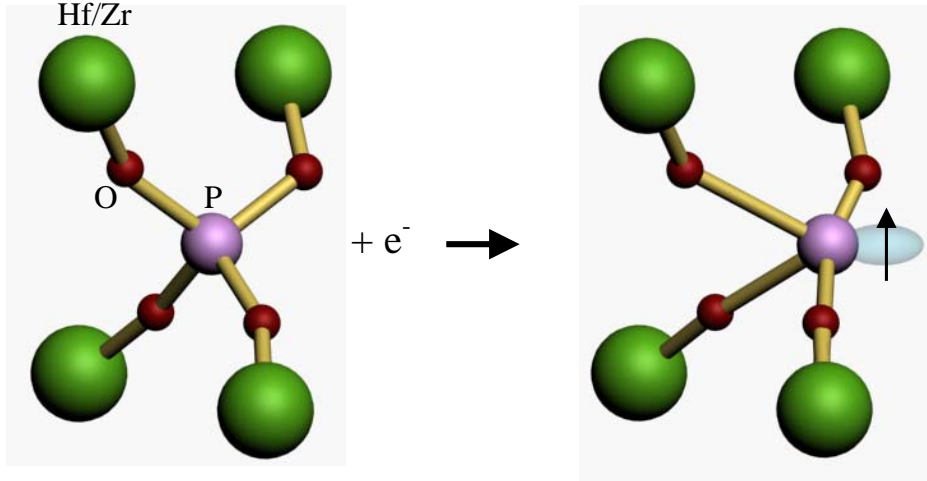
Figure 3.12: *Proposed conceptual model and the formation of the ESR-active P$_2$ defect in ZrO$_2$ and HfO$_2$, formally adopting 2-fold coordinated O atoms.*

defects observed in the current high-κ oxides will also act as hole traps depends on the position of the energy level of the defects in the band gap of the oxides. For this theory could provide valuable information to eventually establish the charge trapping behavior of the P_2 defects embedded in HfO$_2$ and ZrO$_2$ [228]. The matter becomes even more crucial as recent studies indicate enhanced P diffusion through HfO$_2$ compared to SiO$_2$ [220, 221].

3.7 Conclusions

In summary, we have reported on the observation by ESR of phosphorus related point defects in two prominent high-κ oxides, i.e., ZrO$_2$ and HfO$_2$. These donor related defects exhibit similar ESR parameters and are both assigned to a P_2-type center, largely based on comparison with the well known P-associated defects in silica. Thus the defect is ascribed to a P^{4+} atom substituting for Zr or Hf in the monoclinic phase of the ZrO$_2$ and HfO$_2$ matrix, respectively, where based on elemental LCAO analysis, the unpaired electron is found to be strongly localized on the P atom. A sizeable fraction of the incorporated P impurities was found to result in ESR active P_2-type defects. As these may act as detrimental charge traps in the oxide, the results of recent studies pointing out enhanced P diffusion through HfO$_2$ compared to SiO$_2$, may urge one to establish the latter into more detail to evaluate the potential effect on MOS-based device operation. This

will require correlative studies combining ESR with electrical and optical methods, backed up by theoretical insight.

In search of the replacement of the standard SiO_2 gate insulator in MOS-FETS by a high-κ dielectric such as HfO_2, one major obstacle encountered is the generally enhanced trap density in the metal oxide based layer. Worse even, (enhanced) migration of dopant impurities resulting in additional traps during necessary dopant-activation thermal steps may add one more element to this concern. The current work represents an initial step in atomically identifying potential charge traps in favored high-κ oxides for device application.

Chapter 4

Paramagnetic point defects in (100)Si/LaAlO$_3$ structures: nature and stability of the interface

4.1 Introduction

In the previous chapter we focussed on those high-κ oxides that will replace the conventional SiO$_2$ gate oxide in order to overcome present day and near future scaling issues. However, due to the inevitable presence of an SiO$_2$-type interlayer as discussed in section 1.3.1, the implementation of HfO$_2$ or nitrided hafnium silicates will only provide a temporary solution. The presence of such a 'low-κ' interfacial SiO$_x$ layer in Si/high-κ structures, even though possibly providing the scope of realizing standard Si/SiO$_2$ interface quality, increases the net EOT. If the interlayer is pure SiO$_2$ its physical thickness (d_{SiO_2}) is added to the net EOT:

$$EOT_{net} = EOT_{high-\kappa} + d_{SiO_2}, \qquad (4.1)$$

putting severe restrictions on the physical thickness of the high-κ dielectric. For example, to obtain a net EOT of 1 nm, the presence of an SiO$_2$ interlayer of 0.5 nm mandates a 50% decrease of the high-κ oxide physical thickness.

Optimization of the EOT would thus instruct to look for a Si/high-κ insulator system without such an SiO$_x$ interlayer. And of course, it is

hoped that this can be achieved hand in hand with simultaneously realizing an Si/high-κ layer interface of superb electrical quality –the ultimate goal of the high-κ research. Additionally, the EOT can be improved when the new high-κ oxide has an even larger κ value. Several high-κ oxides are currently studied such as, e.g. CeO$_2$ [100], Pr$_2$O$_3$ [229], Y$_2$O$_3$ [230], Er$_2$O$_3$ [231], Lu$_2$O$_3$ [232], and LaAlO$_3$ [233], the latter being one of the most promising candidates of the higher-κ dielectrics.

4.2   The (100)Si/LaAlO$_3$ structure

Park and Ishiwara projected that the Si/LaAlO$_3$ structure could be a possible candidate [234] as inferred from depositing the first LaAlO$_3$ thin films (κ=20-27) on (100)Si using molecular beam deposition (MBD) [235]. Later, Edge *et al.* concluded through an intensive study combining Auger electron spectroscopy, infrared absorption, MEIS, XPS, and HRTEM –an HRTEM image is shown in Fig. 4.1– that as-grown LaAlO$_3$ films deposited by MBD on (100)Si at a temperature of 100 $^\circ C$ have less than 0.2 $\mathring{A}$ of SiO$_2$ at the Si/LaAlO$_3$ interface [233]. They also showed that these structures have additional favorable properties such as a 6.2 eV band gap of the LaAlO$_3$ layer and band offsets of (1.8$\pm$0.2) eV for electrons and (3.2$\pm$0.1) eV for holes [121]. Lu *et al.* studied amorphous LaAlO$_3$ films deposited on (100)Si by laser MBD in the temperature range 300-700 $^\circ C$ in oxygen containing
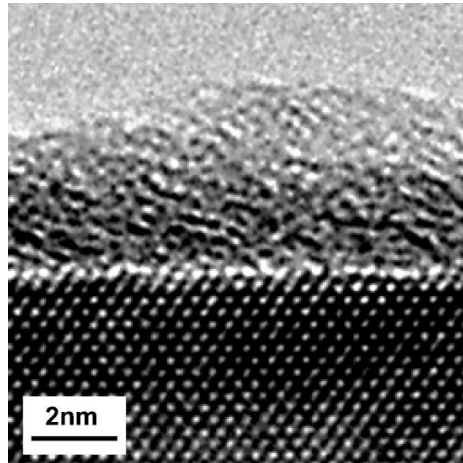
Figure 4.1: *Cross-sectional HRTEM image of 10 $\mathring{A}$ of amorphous LaAlO$_3$ on (100)Si showing no interfacial SiO$_x$ layer. The figure is taken from Ref. [233].*
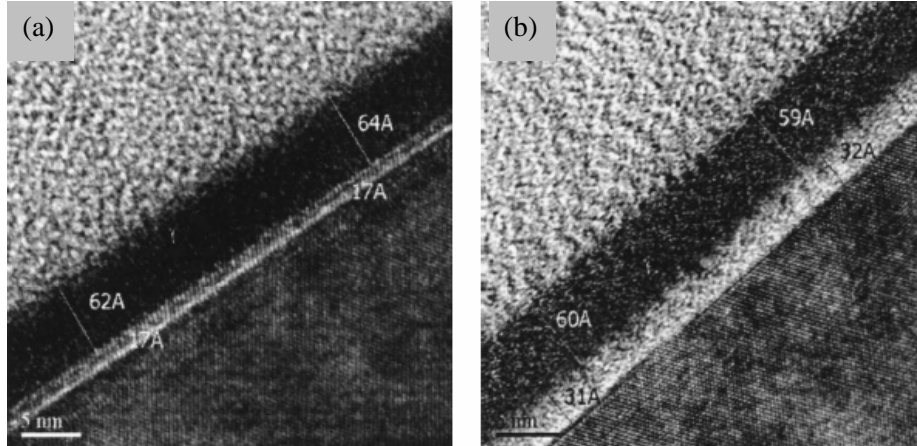
Figure 4.2: *Cross-sectional HRTEM pictures of LaAlO₃ films deposited on (100)Si at different substrate temperatures: (a) 500 °C and (b) 700 °C. The figures are taken from Ref. [236].*

ambient. Here, HRTEM measurements revealed the presence of an interfacial layer, with thickness increasing with substrate temperature, introduced during film deposition [236], as shown in Fig. 4.2. The LaAlO₃ films remained amorphous after post-deposition annealing (PDA) at 1000 °C in N_2 or O_2, but were found to exhibit a better thermal stability in contact with Si when annealed in an N_2 ambient. Applying still a different deposition method, another work [237] reported on a study of LaAlO₃ films grown on Si using CVD. Also here, the analysis revealed the occurrence of an interlayer between the oxide and the Si substrate inferred as made up of compositionally graded La-Al-Si-O silicate rather than pure SiO_x. In a recent paper Sivasubramani *et al.* reported on a study of amorphous LaAlO₃ grown on (100)Si by MBD studied as a function of post deposition rapid thermal annealing (RTA) for 20 s in flowing N_2 [238]. The LaAlO₃ films were capped in situ with ∼100 $\mathring{A}$ of Al_2O_3 in order to protect the film surface from hydroxyls. They found the (100)Si/LaAlO₃ system to be very stable. A change in the structure of LaAlO₃ from amorphous to polycrystalline takes place only after a 935 °C RTA, nicely illustrated by the AFM images and XRD spectra shown in Fig. 4.3. Through SIMS profiling as a function of thermal treatment, shown in Fig. 4.4, they showed that upon annealing at higher T_{an}, the crystallization is followed by La and Al penetration into the Si after RTA at temperatures 950 °C.

In light of the above results, it appears of interest to get more in depth information on the true interfacial nature of Si/LaAlO₃ structures and the
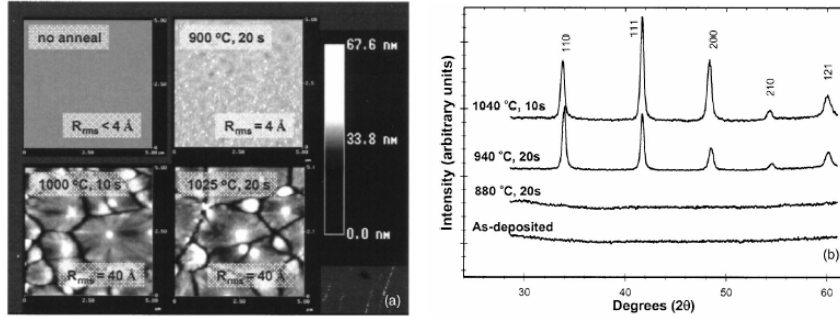
Figure 4.3: *(a) AFM images (area=25 μm^2) of the capped Al$_2$O$_3$/LaAlO$_3$/Si(100) stack before and after thermal treatments at different RTA conditions. (b) XRD spectra of the stack following RTA treatments in flowing N$_2$. The peaks correspond to all of the expected reflections of crystalline LaAlO$_3$. The figures are taken from Ref. [238].*
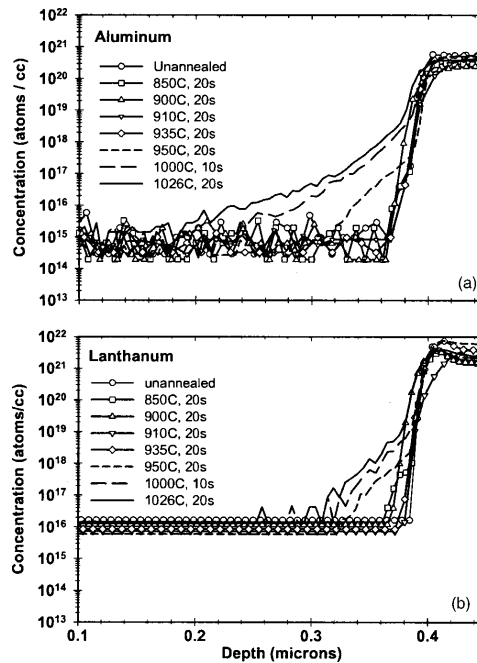
Figure 4.4: *Backside SIMS concentration vs. depth profile for (a) Al and (b) La before and after RTA treatments of Al$_2$O$_3$/LaAlO$_3$/Si stacks in flowing N$_2$. The depth scale up to ∼0.4μm corresponds to the Si subtrate, followed by the 1000 Å thick LaAlO$_3$ film. The figures are taken from Ref. [238].*

consequences of PDA treatments. The scope of the present work is to attain structural information on atomic scale by monitoring paramagnetic point defects in (100)Si/LaAlO$_3$ structures with the oxide thin films grown by MBD as a function of the PDA temperature (T_{an}). We will demonstrate, through the occurrence/absence of interface specific (P_{b0}, P_{b1}) and/or interlayer associated (EX) point defects, the appearance, additional growth and modification of a SiO$_x$ interlayer at T_{an}>800 $^\circ C$. At anneal temperatures up to 800 $^\circ C$, the Si/LaAlO$_3$ interface is found to be abrupt and thermally stable. A SiO$_x$ interlayer is formed after annealing in the temperature range T_{an}∼800-860 $^\circ C$. However this interlayer starts to break down after PDA at T_{an}∼930 $^\circ C$, possibly resulting in silicate formation (T_{an}∼1000 $^\circ C$).

4.3 Experimental details

4.3.1 Samples

Details about the samples studied can be found elsewhere [233, 121]. In short, uniform LaAlO$_3$ thin films (10-40 nm) were grown by MBD in an EPI 930 MBE chamber modified for the growth of oxides [239] on Si substrates. The latter were one-side polished commercial 8 *inch* Si wafers (p-type; n$_a$∼(3-6)×10^{15}Bcm^{-3}). Prior to deposition the native SiO$_2$ on the Si wafers was in situ thermally removed in ultrahigh vacuum at a substrate temperature of 950 $^\circ C$ (as measured with a pyrometer). Subsequently, using elemental sources, La, Al, and molecular oxygen (99.994%) at a background pressure $6×10^{-8}$ $Torr$ were codeposited on the substrate at ∼100 $^\circ C$. The La and Al fluxes from the effusion cells were each 2×10^{13} $at.cm^{-2}s^{-1}$. As analyzed by Rutherford backscattering spectroscopy, this resulted in closely stoichiometric layers (La:Al mol ratio=1±0.05).

4.3.2 ESR spectrometry

From these wafers, ESR slices of 2×9 mm^2 main area were cut with their 9-mm edge along a <0$\bar{1}$1> direction. Cutting damage was removed through selective chemical etching of backside and edges. Thermal stability of deposited LaAlO$_3$ layers and interfaces was analyzed by subjecting samples to isochronal (∼10 min) PDA at desired temperatures between 630 and 1000 $^\circ C$ generally in a 1 atm N$_2$ + 5% O$_2$ (99.995%) ambient or pure N$_2$ (99.999%) using a conventional resistively heated laboratory facility. Several sets of samples were used for the various thermal steps. As an

additional test related to potential ESR activation/maximalization of dia-magnetic defects some samples were subjected for $\sim$10 s to 10.02 eV VUV photons (flux $\sim$5$\times$10^{14} $cm^{-2}s^{-1}$) obtained from a Kr resonant discharge lamp or to short positive corona charging (3 μA for 10 s) in room ambient.

Conventional cw slow-passage K-band ESR measurements were carried out at 4.2 K, as described elsewhere [29], for the applied magnetic field $\vec{B}$ rotating in the ($0\bar{1}1$)Si substrate plane over an angular range Φ_B=0-90°, with respect to the [100] interface normal $\vec{n}$. A co-mounted Si:P reference sample of g(4.2 K)=1.99869$\pm$0.00002 was used for g factor and spin density calibration, with the latter performed through orthodox double numerical integration of the detected derivative-absorption spectra. The attained absolute and relative accuracy is estimated at $\sim$30% and $\sim$10%, respectively. Typically, an ESR sample was comprised of 10-12 slices HF (5% in H$_2$O) dipped immediately before taking ESR data. Signal averaging ($\sim$typical 100 scans) was routinely applied to enhance spectral quality.

4.4   Experimental results and analysis

4.4.1   Observed defects: P_b's and EX

Figure 4.5 presents an overview of representative ESR spectra, observed with $\vec{B}\|\vec{n}$ on the as-deposited (100)Si/LaAlO$_3$ structures and after different PDA steps in N$_2$ + 5% O$_2$ ambient. Within spectral accuracy, no ESR active defects could be observed on the as-grown samples, the situation remaining unaltered for annealing up to $T_{an}\leq$800 °C. However, upon annealing in the temperature range $T_{an}\sim$860-970 °C, a resonance signal is observed at zero crossing g=2.0060$\pm$0.0001 with ΔB_{pp}=(7$\pm$1) G, exhibiting distinct angular anisotropy. To trace the signal's origin, a coarse g map was composed for $\vec{B}$ rotating in the ($0\bar{1}1$) plane. As shown in Fig. 4.6, the obtained data could be well fitted by an axial symmetric system (cf. solid curves in Fig. 4.6) with principal g values $g_\|$=2.0017$\pm$0.0001 and $g_\perp$=2.0082$\pm$0.0001. These results match those obtained for the g pattern of the P_{b0} defect in standard thin Si/SiO$_2$ systems, as elaborated on in section 1.2.1 (see Fig. 1.6), leaving little doubt about the signal's origin. It appears that the (100)Si/LaAlO$_3$ interface has become Si/SiO$_2$-type, evidencing that a SiO$_x$-type interlayer has formed.

Here, we should add that some of the PDA steps at representative temperatures were also carried out in pure (99.999%) N$_2$. Generally, these led to similar ESR results as those for the O$_2$/N$_2$ ambient, with no outspoken effect on P_{b0} appearance. So, while it cannot entirely be excluded that the
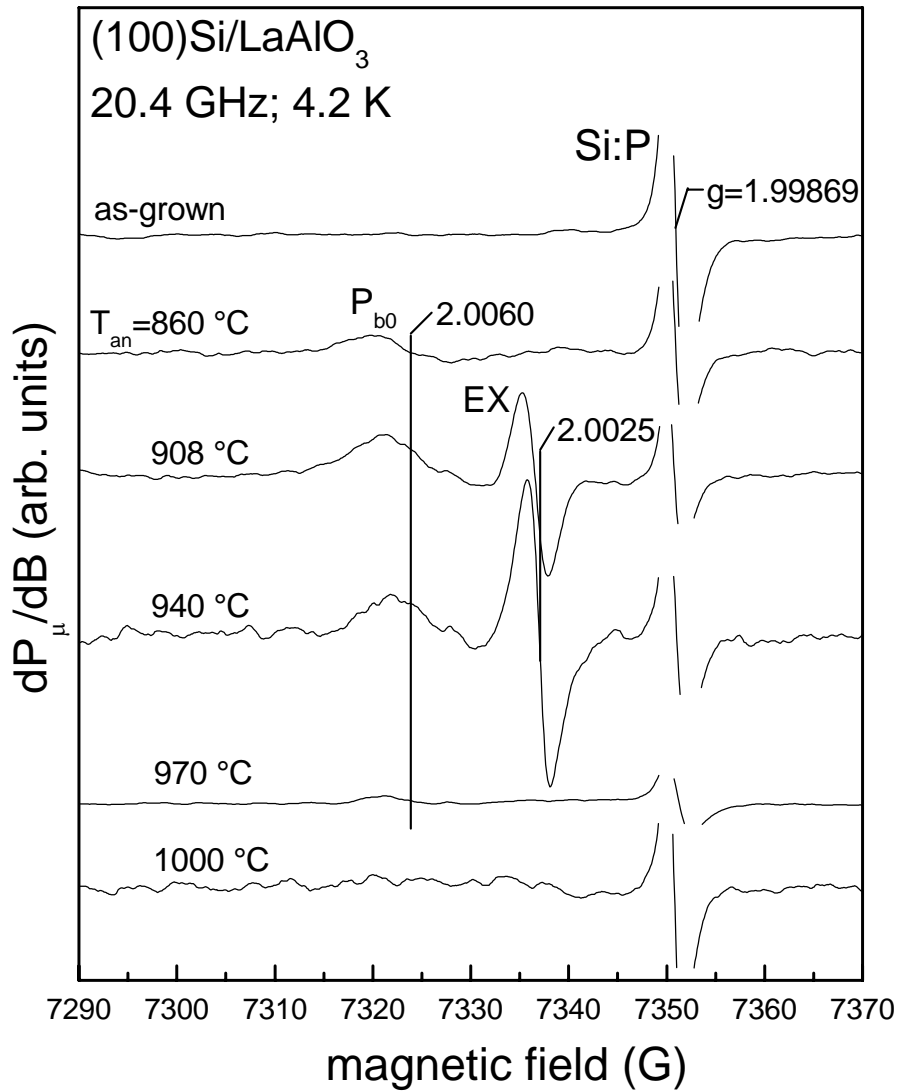
Figure 4.5: *Representative derivative-absorption K-band (B_m=0.6 G; $P_\mu \sim$2.5 nW) ESR spectra measured at 4.2 K with applied magnetic field $\vec{B}$ perpendicular to the interface of (100)Si/LaAlO$_3$ structures subjected to different steps of post-deposition annealing in N$_2$ + 5% O$_2$ (10 min). Spectral heights have been normalized to equal marker intensity and sample area. The signal at g=1.99869 stems from a co-mounted Si:P marker sample.*
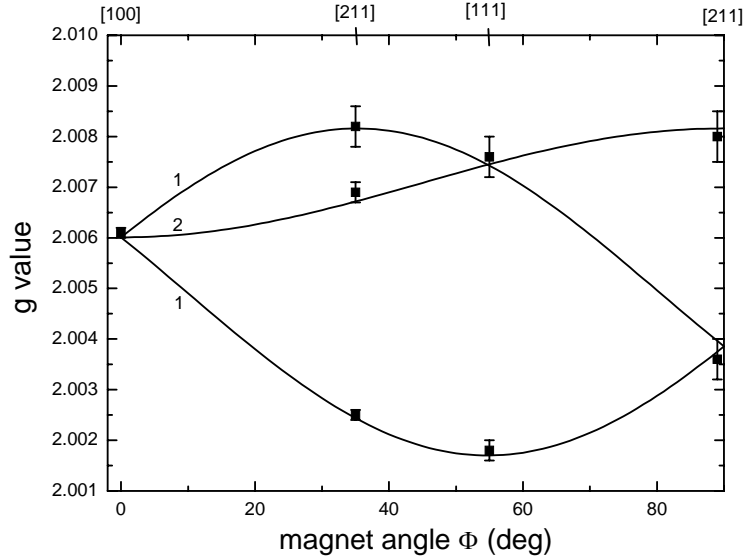
Figure 4.6: *Coarse angular g map of the observed resonances, ascribed to P_{b0} for $\vec{B}$ rotating in the plane with respect to the interface normal $\vec{n}$ observed in a (100)Si/LaAlO₃ structure subjected to a post-deposition anneal at $\sim$900 $^\circ C$ for $\sim$10 min. The curves represent the optimized fitting of the various branches for axial symmetry yielding $g_\parallel$=2.0017$\pm$0.0001 and $g_\perp$=2.0082$\pm$0.0001, within experimental accuracy in agreement with the P_{b0} data for standard thin thermal oxide/Si structures, affirming the P_{b0} assignment. The added numbers indicate relative branch intensities expected from the standard defect model, also matching experimental observation.*

presence of O_2 in the anneal ambient might have promoted the Si/SiO$_x$ interface formation, its effect is not conclusive.

As can be seen from Fig. 4.5, one more signal is observed after annealing in the range $T_{an}\sim$888-940 $^\circ C$ at g=2.0025$\pm$0.0001. It could be conclusively identified as the EX signal from the observed accompanying hf doublet ($\sim$16.1 G splitting) centered around this g value, typical for this defect. This is evident from Fig. 4.7 showing a zoomed-in representative spectrum of the EX center observed in the sample subjected to a 940 $^\circ C$ anneal and additional VUV irradiation. As outlined in section 1.2.2, the EX defect is an SiO$_2$ associated center, well known from studies of bulk SiO$_2$ and various kinds of Si/SiO$_2$ structures [77, 67, 68, 69, 71, 36, 63, 72, 73, 75].

In the as-deposited and PDA treated samples, no LaAlO$_3$-specific point defects could be observed. Quite surely, though, point defect sites will be present, but reside in a diamagnetic state, making them invisible for ESR
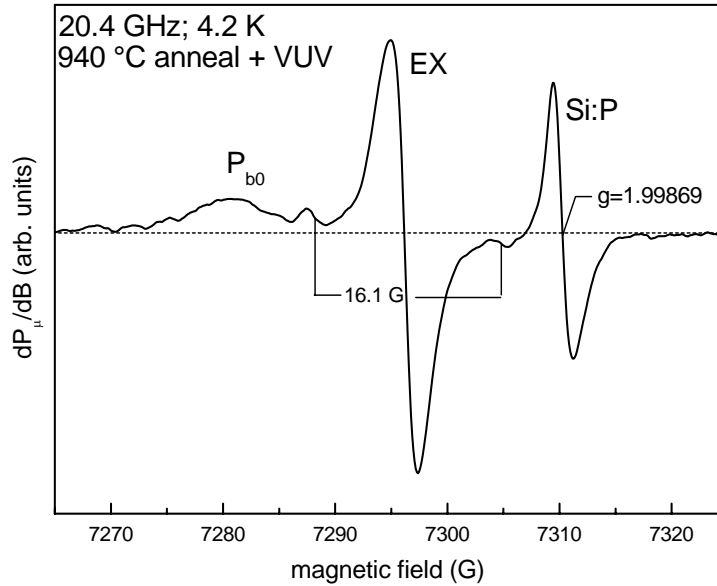
Figure 4.7: *Derivative-absorption K-band ESR spectrum improved through signal averaging (∼200 scans) of the observed defects measured at 4.2 K on (100)Si/LaAlO₃ subjected to post deposition annealing in N_2 + 5% O_2 (10 min) at 940 °C and additional VUV irradiation.*

detection. So to probe deeper it was aimed to maximally reveal defects in the oxide as well as at the interface, through subjecting some samples to additional VUV irradiation –known to be a most efficient means for both oxide [240, 168, 241] and interface defects in Si/SiO₂– to photo-dissociate H-terminated dangling bonds and to possibly additionally unveil weak or strained bonds [169, 242]. Still any evidence for LaAlO₃-associated defects remained lacking as no ESR spectral changes were noticed.

Importantly as one more result, this finding thus also indicates that no P_b-type defect system remained hidden or was left partially passivated –as could be expected from the H-free fabrication process of the samples. In the same spirit, some samples where additionally subjected to positive corona charging, applied for a very short time though to avoid impairing H-related effects inherent to such method [117], to possibly put diamagnetic defects in the LaAlO₃ in the correct charge state for ESR detection. Yet, in spite of these efforts, detection of any LaAlO₃-related defects still failed.

4.4.2 Defect densities vs. T_{an}

Monitoring the densities of the observed defects, P_{b0} and EX, as a function of PDA treatment revealed various interesting aspects about the nature and stability of the (100)Si/LaAlO$_3$ interface. The main PDA results (5% O$_2$ + N$_2$) are compiled in Fig. 4.8 showing the density of observed defects as a function of PDA temperature. Various items are worth noting:

No ESR signals, in particular no P_b-type defects could be observed in the as-deposited Si/LaAlO$_3$ structure. On the basis of the latter criterion it evidences, with atomic level sensitivity, that there is no SiO$_x$-type interlayer present or that this interlayer is at least substantially thinner than [243] 3 Å –an abrupt interface– which is in good agreement with previous results [233]. This is in sharp contrast with other stacks of (100)Si with high-κ layers, such as Al$_2$O$_3$, HfO$_2$, and ZrO$_2$, where the presence of such an interlayer appeared inevitable, even in the as-deposited state, which was revealed by ESR [112, 113, 118, 77, 115, 114, 116]. The abrupt interface remains unaltered even during subsequent annealing up to $T_{an}{\sim}800$ °C, indicating that the interface is thermally stable.

After annealing at $T_{an}{\sim}860$ °C an SiO$_x$-type interlayer has formed, as evidenced by the observation of P_{b0} defects. Upon annealing at a slightly higher temperature $T_{an}{\sim}888$ °C, the SiO$_2$-associated EX defect appears, so, delayed over ${\sim}30$ °C in terms of T_{an}. This observation corroborates the presence of an SiO$_x$-type interlayer and also indicates an additional growth of the interlayer. The defect was not observed in the sample annealed at $T_{an}{\sim}860$ °C even though the presence of an SiO$_x$-type interlayer in this sample is signaled by the observation of P_{b0} defects. It suggests that a minimal thickness of the SiO$_x$ interlayer is needed for (ESR) detectable formation of EX defects, at least more substantial than required for effective Si/SiO$_x$-interface formation. The need of a minimal thickness of SiO$_2$ for EX detection has been reported before for dry thermal SiO$_2$ on Si [69]. Thus the retardation in EX appearance vis-à-vis P_{b0} would indicate an additional growth (or modification) of the interlayer. The interlayer thickness, however, is unknown. In broader context, it is interesting to note that the generation of EX centers upon annealing at elevated temperatures in oxygen-containing ambients appears symptomatic for stacks of high-κ metal oxide layers on Si [77].
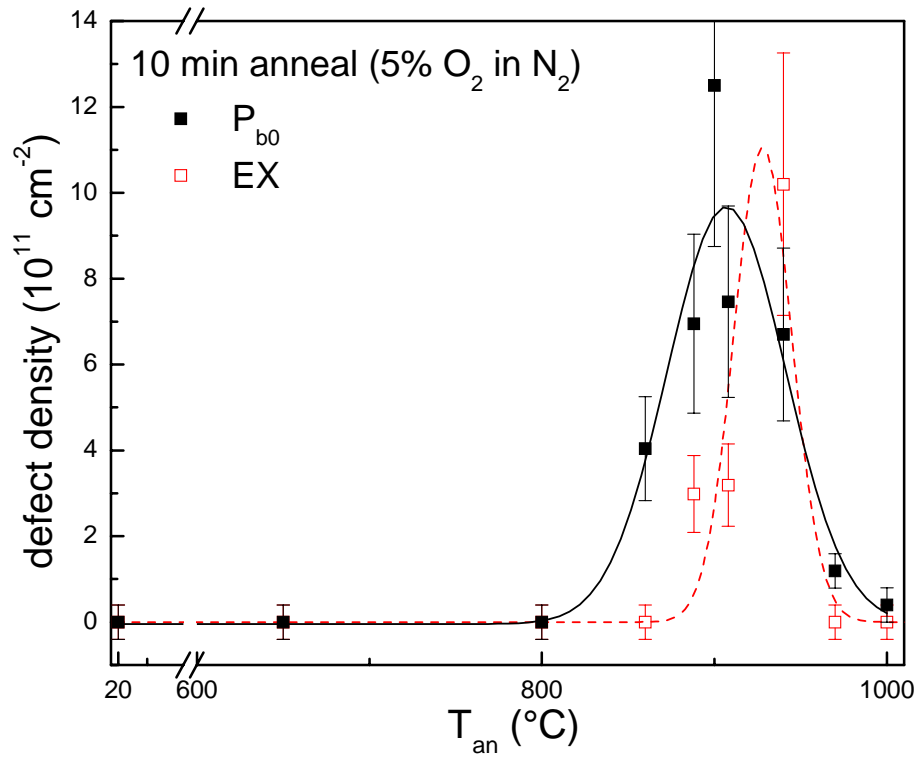
Figure 4.8: *Compilation of the inferred defect densities in $(100)Si/LaAlO_3$ entities as a function of the post deposition isochronal annealing in $N_2 + 5\% O_2$ (10 min) for P_{b0} and EX centers, represented by black closed and red open symbols, respectively. The solid and dashed traces are Gaussian curves, merely meant to guide the eye in exposing the peaking in defect generation and the somewhat lagging behind (~ 30 °C) of EX production vis-à-vis P_{b0} appearance. Data points at zero defect density symbolize failure of signal detection.*

4.5   Discussion

4.5.1   Interlayer formation and disintegration

Monitoring of occurring point defects as a function of PDA treatment, additional VUV irradiation, and corona charging revealed interesting information on the annealing induced structural/compositional changes in the interface region. Compiling the thermal evolution of the observed defect densities, hereby displaying all main results, Fig. 4.8 will guide the discussion and interpretation. Prominently, the defect density vs. T_{an} curves show a peaked behavior, simulated by Gaussian curves. The maximum P_{b0} density, $[P_{b0}]\sim(1.3\pm0.3)\times10^{12}\ cm^{-2}$, is obtained at T_{an}=900 $^\circ C$ while the maximum EX density, $[EX]\sim(1.0\pm0.3)\times10^{12}\ cm^{-2}$, is obtained at a slightly higher PDA temperature T_{an}=940 $^\circ C$. On the account of P_{b0}, it appears that for annealing from T_{an}>900 $^\circ C$ onward, the interface starts to break up first, where it is interesting to note that, in the range $T_{an}\sim$900-940 $^\circ C$, the EX density still increases while the P_{b0} density already starts to decrease.

So, the overall picture emerging from the curves in Fig. 4.8 is that, as compared to P_{b0}, the manifestation of the EX peak is delayed in terms of T_{an}. The true character of the Si/SiO$_x$-type interface is disrupted first (elimination of interfacial Si dangling bonds), but for $T_{an}\geq$940 $^\circ C$, the defects rapidly disappear altogether, pointing to drastic disintegration of the interfacial region, i.e., elimination of the 'pure' SiO$_x$ component. For clarity, this disappearance of the ESR-active centers is not due to inadvertent H-passivation, as verified by applying additional VUV irradiation after some PDA steps. The structural/chemical change breaking up the interlayer seems to first affect the P_{b0} defects located at the interface before it affects the interlayer associated EX defects.

4.5.2   Influence of oxide crystallization and interdiffusion

It is interesting to put the currently acquired atomic level information in terms of occurring point defects in the perspective of previous morphological/compositional studies [233, 238, 235, 236] on the Si/LaAlO$_3$ structure. Using such methods, recent work [238] has investigated the thermal stability of (100)Si/LaAlO$_3$/Al$_2$O$_3$ stacks against RTA in N$_2$ ambient at 850-1040 $^\circ C$ for 10-20 s. As observed by atomic force microscopy and X-ray diffraction (Fig. 4.3), the work reports that RTA from 900 $^\circ C$ onward starts to induce changes in surface morphology, together with initiation of

the transformation of the amorphous to polycrystalline state, in agreement with previous results on LaAlO$_3$ films produced by different methods. SIMS profiling shows that substantial penetration of Al and La atoms into the Si substrate occurs for RTA at or above 950 $^\circ C$, with in fact any penetration effects remaining below the detection limit for $T_{an} \leq 935$ $^\circ C$, as can be seen from Fig. 4.4.

Our ESR data may well fit within this morphological picture: In terms of T_{an}, we may link the initiation of the formation of a Si/SiO$_x$-type interface with the very early onset of LaAlO$_3$ film crystallization, followed by some more substantial SiO$_x$-type interlayer growth with increasing T_{an}. For clarity, though, the appearance of the P_{b0} centers cannot be directly linked to the grain boundary regions per se, as this would conflict with the observed ESR spectral anisotropy in registry with the crystalline (100)Si surface. Then, for T_{an} further increasing above $\sim$940 $^\circ C$, the progressing interdiffusion chemically destroys the pristine nature of the SiO$_x$ component (possibly silicate formation) resulting in the obliteration of the SiO$_{2(x)}$-specific point defects. It is possible that the onset temperature for La and Al out diffusion in the current case is somewhat lower considering the applied longer PDA treatment times (10 min) as compared to previous RTA work (10-20 s).

Also, within the interpretation, it appears we detect the initiation of crystallization of the amorphous LaAlO$_3$ film somewhat at lower T_{an} than in previous work [238]. Again, this may partly have resulted from the applied longer anneal times in conjunction with the presence of O$_2$ in the anneal ambient. Yet, it may as well bear out the fact that ESR is prone to detect interfacial reshaping in a very embryotic state, ahead of standard morphological/compositional methods.

4.5.3 Absence of P_{b1} defects

The observation of the P_{b0} defect indicates that a Si/SiO$_2$-type interface has formed. As demonstrated, the obtained ESR parameters such as g value, line width and defect density are indeed very similar to those characteristic for thermal Si/SiO$_2$ interfaces. There is, however, one remarkable apparent dissonance: No P_{b1} (g_1=2.00577, g_2=2.00735, g_3=2.0022) centers could be detected. As outlined in section 1.2.1, the P_{b1} center also concerns an unpaired sp^3 hybrid at a threefold Si atom part of a strained Si–Si dimer ($\equiv$Si–Si$^\bullet$=Si$_2$), thus basically chemically identical to the P_{b0} center, yet physically different, e.g., regarding hybrid orientation, bond strain, and structural relaxation [38]. Generally, the P_{b0} and P_{b1} centers are almost

invariably observed in tandem at the (100)Si/SiO$_2$ interface, although relative intensities may vary. So, the question arises as to the absence of the P_{b1} defect, at least below ESR sensitivity, at the current Si/SiO$_{2(x)}$-type interface formed during PDA of (100)Si/LaAlO$_3$ entities. There may be several reasons. One considered here concerns interfacial strain. Pertinently, the P_{b1} center may be less prominent, even absent beyond the detection limit in Si/SiO$_2$ entities grown at low oxidation temperatures or after particular PDAs. In previous work [244], it has been outlined this would not just be the result of the small oxide thickness per se, as compared to more standard SiO$_2$ thicknesses ($\geq$10 nm). Rather, P_{b1} formation would require a minimum amount of oxide (interface) relaxation as generally inherently established during oxidation at high temperatures. So, as a possibility, sufficient interface relieve may not have been attained in the current case, not even for PDA steps up to 950 $°C$. Possibly, in this the top LaAlO$_3$ layer plays a constraining role.

4.6   Conclusions

The ESR technique has been successfully applied to assess the nature of the interface in (100)Si/LaAlO$_3$ entities and thermally induced alterations. It is found that the (100)Si/LaAlO$_3$ structure exhibits a high quality and robust interface in terms of dangling bond-type interface defects, stable under extended thermal anneals up to $\sim$850 $°C$, even in O$_2$-containing ambient.

Upon annealing at $T_{an} \geq$860 $°C$ a SiO$_x$-type interlayer is formed as evidenced by the appearance of P_{b0} interface defects, an effect likely forerunning or heralding the onset of crystallization of the a-LaAlO$_3$ film. At somewhat higher anneal temperature, the EX defect is observed the delay in appearance vis-à-vis P_{b0} pointing to additional growth of the SiO$_x$-type interlayer. However upon annealing at temperatures $T_{an} \geq$930 $°C$, the Si/SiO$_x$-nature of the interlayer starts to break up again, resulting in fast, likely compositional, transformation with increasing T_{an} as signalled by the disappearance of the SiO$_x$ related defects altogether. It is ascribed to invasive diffusion of La and Al into the Si substrate, possibly resulting in silicate (interlayer) formation.

Generally, ESR has emerged as a viable technique to trace thermally induced structural/compositional alterations in Si/insulator entities through probing the incorporation of interface/interlayer related point defects. The method takes a separate position in the sense that it may reveal such

changes on atomic level where standard morphological/structural analyzing tools simply fall short, or detect these in an earlier stage before the latter may achieve.

Chapter 5

Origin of optical absorption in the range 4.8-4.9 eV and 5.7-5.9 eV in silica implanted with Si or O.

5.1 Introduction

The optical activity of defects in SiO_2 has been of interest for many years due to the crucial role they may play in the performance of SiO_2-based opto-electronic devices [245, 246, 247]. Consequently, the optical absorption of these glasses has been intensively studied. An extensive overview is given in Ref. [248]. The optical spectra, however, generally consist of broad bands, rather than of separate sharp lines. Because of this, the disentanglement of the various optical absorption bands and their attribution to certain defect centers is a difficult task. Quite often optical absorption measurements are combined with ESR in an attempt to correlate optical absorption bands with ESR spectra. It should be noted, however, that ESR spectroscopy only detects paramagnetic defect sites, while this is not a restriction for optical absorption.

Here we will compare the optical absorption spectra in the range 4.8-4.9 eV and 5.7-5.9 eV, measured and analyzed by Magruder *et al.*, with the ESR spectra of two series of silica samples implanted with various concentrations of Si or O.

The broad absorption band detected around 4.8 eV was first attributed to NBOHCs [249]. But, while a good correlation was reported between

this optical absorption band and the ESR signal of the NBOHCs in some studies, a poor correlation was found in others [250]. Based on combined optical and ESR measurements Hosono and Weeks attributed this band to PORs [251]. Alternatively it was suggested that the 4.8 eV band is caused by interstitial ozone molecules, as the absorption spectrum of gas-phase O_3 was found to be similar [252, 253]. Skuja *et al.* suggested that the 4.8 eV band consists of two closely overlapping bands attributed to NBOHCs and interstitial O_3 [254]. They also reported [255] interstitial oxygen molecules, O_2, in silica and Awazu and Kawazoe [252] describe the interaction of the interstitial molecules with the interstitial oxygen atom to form the ozone molecule. Thus there are at least three optical absorption bands in the range 4.8-4.9 eV attributed to O related defects including NBOHCs, PORs, and interstitial O_3.

The optical absorption band between 5.7 and 5.9 eV has often been assigned to E' type defect centers. Weeks and Sonders [256] demonstrated that the amplitude of the first derivative of the ESR absorption spectrum of the E' center and the intensity of an optical absorption band at 5.85 eV had a correlation coefficient R=0.999. They showed that the energy of the band maximum increased from 5.80 to 5.85 eV and the full width at half maximum (FWHM) amplitude decreased from $\sim$0.9 to $\sim$0.63 after bleaching with a mercury lamp. The authors [256] further suggested that there were three or more optical absorption bands between 5.5 and 6.0 eV. Based on bleaching experiments with 5.0 eV laser light on type III and IV silica samples, Weeks *et al.* [257] proposed a band with a maximum between 5.8 and 5.9 eV that was not paramagnetic. One work reports on a shift in optical band maximum with changes in the E'_γ features (zero crossing g value and line shape), which they attributed to the modification of the E'_γ structure [258]. The energy of the band maximum increased from 5.75 to 5.83 eV. Nishikawa *et al.* [259], using type III and IV silica samples, observed that the absorption maximum for the E' optical band was $\sim$5.7 eV. Their data on the correlation of the density of the E' center and the band maximum amplitude gave a correlation coefficient R$\sim$1 for both types of silica. The absence of experiments on the effect of bleaching and anneal treatments on the band maximum for their samples leaves open the question of the contribution of other bands between 5.4 and 6.0 eV to the energy of the band maximum.

Magruder and his collaborators [260, 261, 262] have measured the optical absorption in type III silica samples in which the excess Si, x, was 0.02 $at.\% < x < 3$ $at.\%$ and excess oxygen, y, was 0.02 $at.\% < y < 3$ $at.\%$ in
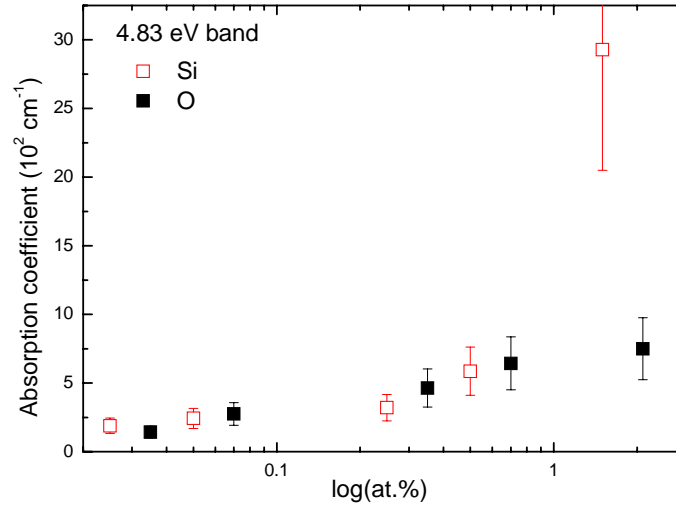
Figure 5.1: *The amplitudes for the band fit data for a 4.83 eV band as a function of the logarithm of the atomic percent of implanted ions for both Si and O implanted silica samples*
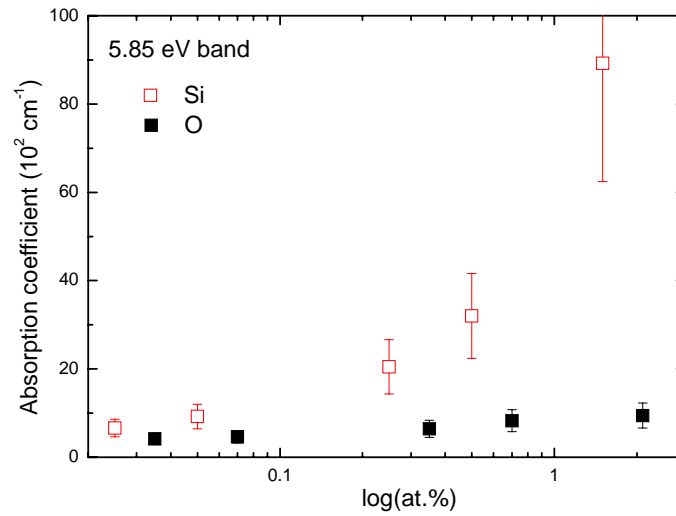
Figure 5.2: *The amplitudes for the band fit data for a 5.85 eV band as a function of the logarithm of the atomic percent of implanted ions for both Si and O implanted silica samples*

the layer in which the implanted ions were located. They then used the absorption bands reported in literature, attributed to intrinsic states, to fit the observed absorption in a series of samples implanted with O and a series of samples implanted with Si. Here the word intrinsic means that the states are a consequence of different configurations of Si and O. Linear and non-linear fitting techniques were used. From these fits the absorption coefficient for the 5.85 and 4.83 eV bands were inferred.

Here we will compare variations in the optical absorption coefficients as a function of implanted ion concentration, shown in Figs. 5.1 and 5.2, with the variations of defect densities of occurring point defects detected by ESR in samples cut from the optical samples. All information about the optical absorption measurements and the analysis of the optical data can be found in Refs. [260, 261, 262, 263, 264].

5.2   Experimental details

5.2.1   Samples and ion implantation

Multiple energy implants of Si and O were employed to produce an approximately constant volume concentration of the implanted element into the face of 2-cm diameter disks of about 1 mm thick type III (Corning 7940) silica. The computer code, PROFILE, was used to calculate the energies and concentrations required to form this constant concentration. The ion energies varied from 35 to 320 eV, and the resulting depth profiles were constant to within $\pm 5\%$ over a depth range 60 to 640 nm below the SiO_2 surface for the Si implants and from 100 to 670 nm for the O implants. A 2 cm diameter face of each sample (Corning 7940) was implanted uniformly. Implantation parameters and nominal area densities as a function of energy have been previously reported [260, 262] as well as implant conditions. Here we give the *at.*% concentration in the implanted layer in Table 5.1.

5.2.2   ESR spectrometry

Conventional cw absorption-derivative K ($\sim$20.3 GHz) and Q-band ($\sim$33 GHz) ESR measurements were performed in the temperature range 77-100 K. The modulation amplitude B_m and incident microwave power P_μ were reduced to levels at which neither signal distortion nor saturation was observed. Since the accurate determination of defect spin densities is a main aim in the current work, the latter is very important when point defects

Table 5.1: *Concentration in at.% of Si or O uniformly implanted in a surface layer of SiO_2 of $\sim$ 600 nm.*

Implanted Si (at.%)	Implanted O (at.%)
0.025	0.035
0.05	0.07
0.25	0.35
0.5	0.7
1.5	2.1

with spin relaxation times $>10^{-4}$ s such as the E' center in silica [265] are concerned.

The ESR samples were bars of about $1\times1\times16$ mm^3, cut from the centers of the 2 cm diameter optical samples. For g factor and defect (spin) density calibration, use was made of a calibrated Si:P marker sample co-mounted with the sample and recorded in the same trace. This arrangement makes the determination of the relative defect densities quite reliable. Signal averaging was applied (typically 50-100 scans for K-band and 100-300 scans for Q-band) to increase the signal to noise ratio.

As stated, a key result expected from ESR spectroscopy is a reliable and accurate inference of the densities of the various types of implantation induced spin active defect centers. Generally these various ESR components overlap and, as well known from ESR spectroscopy, in fact from any spectroscopy, their reliable decomposition poses a formidable task for which there is no straightforward remedy. It is very rare that the observed ESR spectrum would be comprised of only a few, in magnetic field, sufficiently separated individual components to enable each of them to be reliably integrated separately. Clearly, we cannot handle the problem by just trying to fit the experimental spectrum by a sum of a number, n, of theoretical spectra through a statistically optimizing program. A satisfactory fit can always be obtained, no wonder, in view of the many adjustable parameters involved ($\geq$4 for each component, a priori all unknown), but must be regarded as unreliable, to say the least. Instead, in good practice, we resort to experimental help, i.e., measuring as a function of some varied external parameters such as microwave frequency, temperature, and P_μ, to help in

discriminating the various responses and to get a good impression of their separate appearance. In addition, computer simulation of some 'known' components –powder patterns in the current case– may help. Generally, in this work with respect to defect density inference, the best results are obtained when determining the densities of separate signals relative to the Si:P intensity standard through orthodox double numerical integration of the measured dP_μ/dB spectra. (Obviously, one cannot solely rely on the component amplitude.) Since this was often not possible due to component overlap, most spectra had to be computer simulated first, thus rendering it more difficult to get accurate defect densities.

5.3   ESR results

5.3.1   Oxygen implanted samples

In the oxygen implanted samples the E'_γ center [266], the POR [267, 81], the $NBOHC$ [82], and an unknown signal (OS) were observed. Some of the K and Q-band spectra recorded for the different oxygen implanted samples
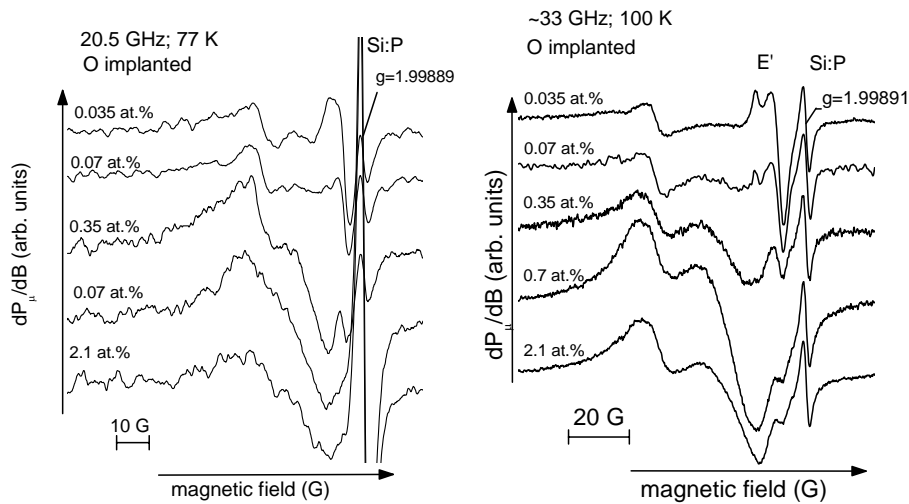
Figure 5.3: *Overview of measured K and Q-band ESR spectra on fused silica for the different O implantation doses. As a measure of dose, the curves are labeled by the calculated at.% of O atoms implanted in a layer ∼600 nm thick, over which the concentration is approximately constant. The size of all samples studied was nominally identical. The signal at g=1.99891 stems from a co-mounted Si:P marker sample. Signals are scaled to equal marker intensity.*

are shown in Fig. 5.3.

Both the K and Q-band spectra of the OS exhibit powder pattern properties (cf. Fig. 5.4), and both could be readily and consistently simulated by an effective spin S=1/2 center with one set of g matrix principal values given as g_1=2.0022, g_2=2.0033, and g_3=2.0088. Examples of the signal simulation are shown in Fig. 5.4. The center could only be observed in the samples implanted with the larger oxygen concentrations ($\geq$0.35 $at.\%$), from where we suggest that the center is oxygen excess related.

As mentioned before, due to component overlap, the $NBOHC$, POR, and OS had to be simulated to determine the proper spin densities. The g values used for these simulations are shown in Table 5.2. Fig 5.4 shows examples of such simulations. Table 5.3 and Fig. 5.5 give an overview of the defect densities obtained from the ESR measurements as a function of the

Table 5.2: *Principal g values used for the simulation of the defects in the O implanted a-SiO$_2$ samples.*

Defect	g_1	g_2	g_3
POR	2.0017±0.0001	2.0074±0.0001	2.067 [a]
$NBOHC$	2.001±0.0001	2.0095±0.0001	2.078 [a]
OS	2.0022±0.0001	2.0033±0.0001	2.0088±0.0001

[a] g value taken from literature [81].

Table 5.3: *The density of the various ESR defects in the O implanted samples.*

O implanted silica $(at.\%)$	E' $(10^{15}\ mm^{-3})$	$NBOHC$ $(10^{15}\ mm^{-3})$	POR $(10^{15}\ mm^{-3})$	OS $(10^{15}\ mm^{-3})$
0.035	1.7±0.5	6±2	18±5	(N.D.) [a]
0.070	0.7±0.2	4±1	17±4	(N.D.) [a]
0.350	0.5±0.1	(N.D.)^a	32±9	13±4
0.700	0.08±0.02	(N.D.)^a	36±10	42±13
2.1	0.028±0.008	(N.D.)^a	26±8	18±5

[a] N.D. means not detected; estimated below <4×10^{15} mm^{-3}.
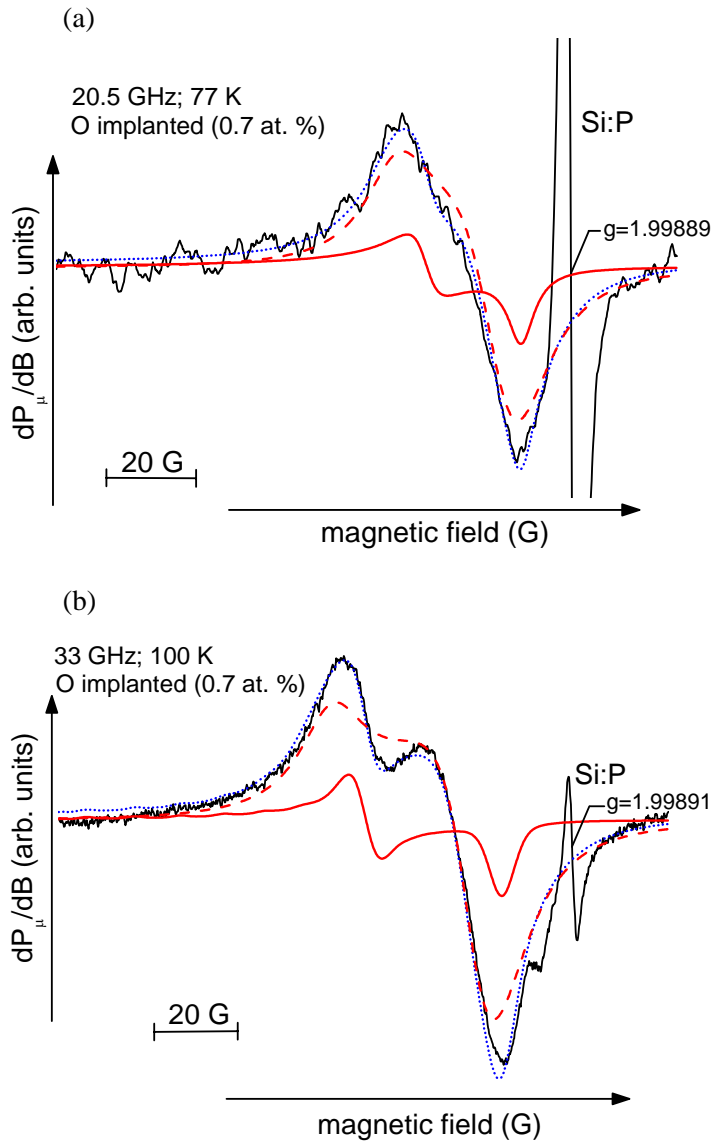
Figure 5.4: *ESR spectra of the 0.7 at.% O implanted samples measured in K-band (a) and Q-band (b), exposing the appearance of an additional signal labeled OS. Consistent fitting of the observed spectra (black solid curves) led to decomposition into two (powder pattern) spectra attributed to the OS (red dotted curves) and the POR (red solid curves) with the principle g values shown in Table 5.2. The blue dotted curve represents the sum of the two simulations.*
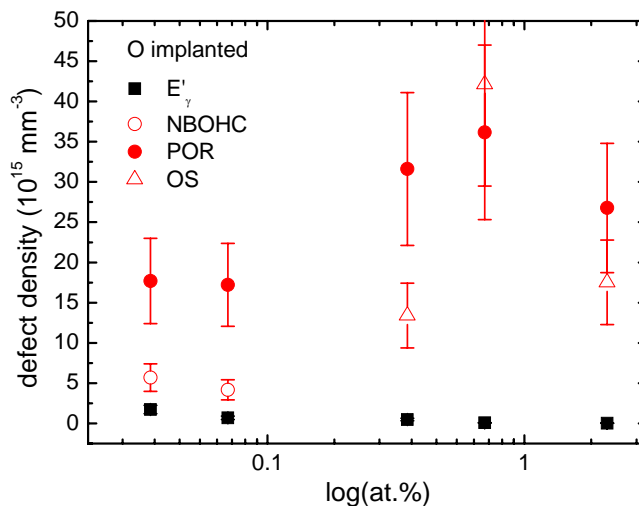
Figure 5.5: *Plot of the density of each component of the measured ESR spectra in the O implanted samples as a function of the implantation concentration.*

implanted O concentration. From Table 5.3 it can be seen that for the O implanted samples, $NBOHCs$ could only be detected in the samples with the two smallest concentrations. The $PORs$, by contrast, are detected in all the samples with changes $<15\%$ for the first two concentrations and then approximately a factor of two increase for the other three concentrations. In the spectrum of the sample with an O implantation of 0.35 $at.\%$ another defect center, labeled OS, is detected, which density increases by approximately a factor of 3 for the next concentration, but then decreases by a factor greater than 2 for the largest concentration.

5.3.2 Silicon implanted samples

Several defects could also be observed in the Si implanted samples including the E'_γ center, the POR, and a hf doublet with a splitting of 73 G and a zero crossing g value g_c=2.0014±0.0001. Corrections for second order hf effects bring the g value to g=2.00135±0.0001. A similar doublet has previously been observed in SiO_2 thermally grown on Si after VUV irradiation, and was attributed to O_2=$Si^\bullet$–H (see section 1.2.3). The $NBOHC$ is possibly present, however, there is no clear experimental evidence likely because of sensitivity reasons.

In the samples with the larger Si implanted concentrations, an additional component is observed as a shoulder situated on the low-field flank of the
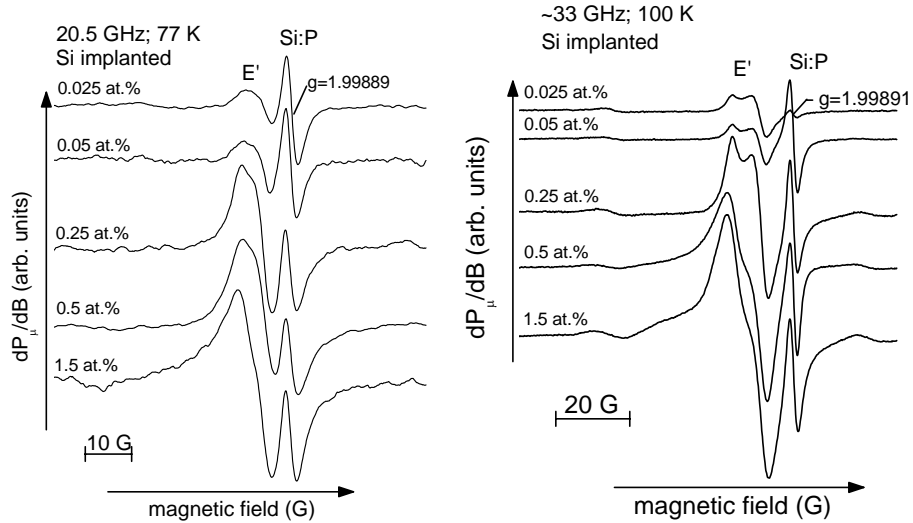
Figure 5.6: *Overview of measured K and Q-band ESR spectra on fused silica for the different Si implantation doses. As a measure of dose, the curves are labeled by the calculated at.% of Si atoms implanted in a layer ∼600 nm thick, over which the concentration is approximately constant. The size of all samples studied was nominally identical. The signal at g=1.99891 stems from a co-mounted Si:P marker sample. Signals are scaled to equal marker intensity.*

E' spectrum. The E' density was determined through double numerical integration of the measured signal. The additional component was included in these integrations, as the component resolution was considered unreliable preventing an accurate estimation of this underlying component. The determined E' densities for the samples with the largest Si implanted concentrations thus include the density of the additional center, which, therefore, may be overestimated. An estimate of the upper limit of the defect density of the underlying component is $\sim 2 \times 10^{16}$ mm^{-3}. The g value and peak-to-peak line width of this signal are estimated to be $g=2.0026 \pm 0.0005$ and $\Delta B_{pp}=(10 \pm 5)$ G, respectively.

An overview of the K and Q-band spectra recorded for the various Si implanted samples at different implantation concentrations is given in Fig. 5.6. The total number of E' defects observed in the Si implanted samples with the largest Si concentrations –see Table 5.4– is one of the largest reported in literature and, based on the derived E' densities for the samples with the two largest Si implantations, we suggest a saturation of the E' density for these samples.

The POR ESR signals had to be simulated to determine the proper de-

Table 5.4: *The density of the various ESR defects in the Si implanted samples.*

Si implanted silica $(at.\%)$	E' $(10^{15}\ mm^{-3})$	73 G doublet $(10^{15}\ mm^{-3})$	POR $(10^{15}\ mm^{-3})$
0.025	3±1	(N.D.)[a]	15±5
0.05	2.2±0.7	0.09±0.03	12±4
0.25	20±6	0.28±0.08	14±4
0.5	48±15	1.1±0.3	(N.D.)[b]
1.5	70±21	1.0±0.3	(N.D.)[b]

[a] N.D. means not detected; estimated below $\leq 0.07 \times 10^{15}\ mm^{-3}$.
[b] N.D. means not detected; estimated below $\leq 4 \times 10^{15}\ mm^{-3}$.

Table 5.5: *Principal g values used for the simulation of the POR defect in the Si implanted samples.*

Defect	g_1	g_2	g_3
POR	2.0014±0.0001	2.0072±0.0001	2.067[a]

[a] g value taken from literature [81].

fect densities; The principal g values used for these simulations are shown in Table 5.5. Figure 5.7 shows an example of such a simulation. No spectral simulations were carried out to determine the E' spin densities since we assume that more accurate results could be obtained from straightforward double numerical integration of the measured component. Indeed, the shape of the E' component varies with the implanted concentration. Table 5.4 and Fig. 5.8 give an overview of the inferred defect densities as a function of the Si implantation concentrations.

Since S=1 centers have been reported previously in silica and SiO_2 single crystals [268, 269, 270, 271] we have made measurements at half the field strength of the $\Delta M_J=1$ transitions, to trace possible $\Delta M_J=2$ transitions. In neither the Si nor the O implanted samples did we detect such transitions. On the basis of previous observations [272], the detection limit is estimated at about 1×10^{12} defects in the sample.
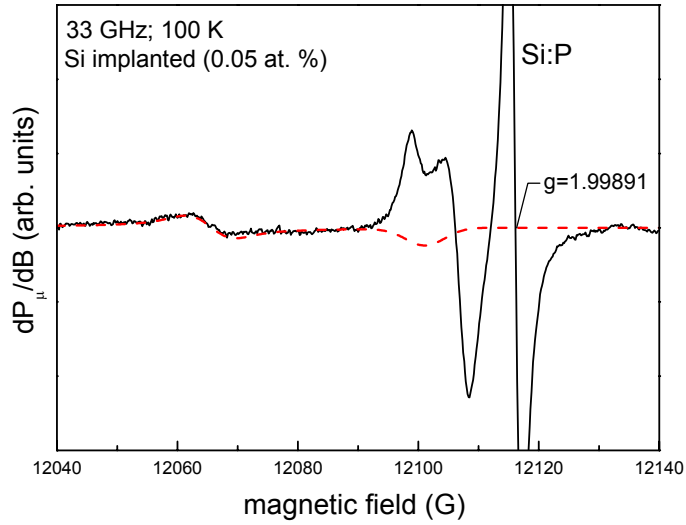
Figure 5.7: *Q-band ESR spectrum of the 0.05 at. % Si implanted samples. The dashed curve represents the simulation of the POR using the principal g values listed in Table 5.5*
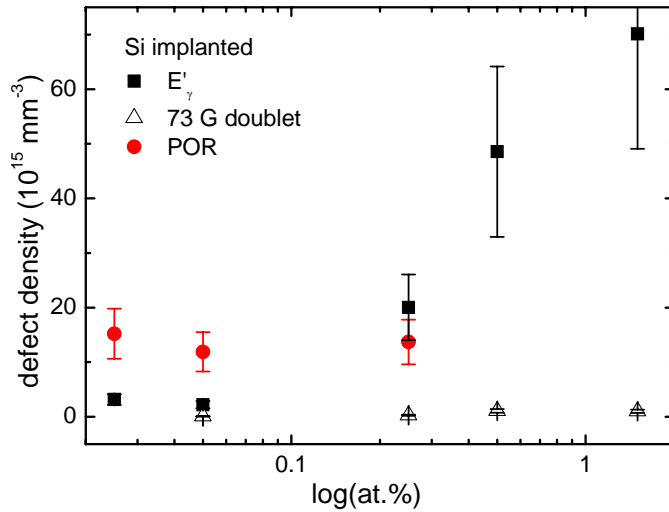
Figure 5.8: *Plot of the density of each component of the measured ESR spectra in the Si implanted samples as a function of the implantation concentration.*

5.4 Analysis and discussion

5.4.1 The 4.8-4.9 eV optical absorption band

Comparison of optical and ESR data

When comparing the optical absorption data for the 4.8-4.9 eV band with the ESR date, the E'-type defects can be excluded in this discussion as these are known to absorb in the 5.7-5.9 range, as discussed later. Before starting, it should be noted that in this comparison of optical band intensities with ESR defect densities the relative errors must be considered. In the case of ESR defect densities we estimate that the absolute error is $\sim \pm 30\%$. In the case of the intensities of the optical bands the error in the measured optical densities is $\pm 5\%$. The error in the intensities of the bands fitted to the data are more difficult to estimate. Four bands between 4.8 and 4.9 eV with FWHM between 0.2 and 0.5 eV make the estimate of errors uncertain. Magruder *et al.* guessed that the errors are $\sim \pm 50\%$. The relative errors were estimated at $\pm 20\%$. Because of these relatively large errors in the inferred defect densities and band intensities, the comparison of the defect densities and the optical absorption coefficients is tentative.

The optical data (cf. Fig. 5.1) show that the 4.83 eV absorption has a monotonic increase from the smallest to the largest O concentration. For these *O implanted* samples the POR is detected in all samples but only increases by a factor of ~ 2 over the range of concentrations covered in these samples, while the 4.83 eV band increases by a factor of ~ 5. However, here we should note that we have additionally detected an ESR signal, labeled OS, in the samples with 0.35 $at.\%$ of O and larger. Assuming that, as suggested above, the OS center is due to an O related species, and adding its density to that of the $NBOHCs$ and $PORs$, the maximum total increase in the added density of all ESR active O related defects obtained when comparing the 0.035 $at.\%$ and the 0.7 $at.\%$ samples, is a factor of ~ 3.2 (cf. Table 5.3). This factor is still smaller than the maximum increase (factor ~ 5) obtained optically. Moreover, the total ESR defect density decreases for the largest O implantation dose (2.1 $at.\%$), while the optical absorption still increases. These findings indicate that in addition to the three ESR active O related defects (POR, $NBOHC$, and OS) possibly absorbing in the range 4.8-4.9 eV, at least one additional, probably diamagnetic, O related center is formed which contributes to the absorption.

There are various theoretical calculations of the energy states of various O related defect configurations in silica. Pacchioni and Ierano [273] have calculated the energies for transitions from the ground state to the first

excited state of a $NBOHC$ (2.2 eV), of a POR (6.7 eV), of a bridging O_2 (6.8 eV), and of a hydroxyl ion bonded to a Si (7.6 eV). In the case of the $NBOHC$, the authors suggest that there is a possibility of a transition at $\sim$5 eV in agreement with the experimental results. In the case of the other O related defects the calculated energies are more than 1 eV greater than 4.8-4.9 eV. Also, we note that the theoretical link between absorption at 4.83 eV and the ESR active POR is qualitative.

Prior work has attributed the optical absorption between 4.8 and 4.9 to three types of oxygen related defects, $NBOHCs$, $PORs$, and O_3 molecules [252, 248]. To our knowledge, it has not been suggested that some of the absorption could be due to Si related centers. In the *Si implantation case* measurable absorption (cf. Fig. 5.1) is generated after the smallest implanted concentration, but increases only by a factor of 1.6 for the next two concentrations. It increases by a factor of $\sim$2 in the samples with 0.5 $at.\%$ and then in the samples with 1.5 $at.\%$ the increase is a factor of 15 over the absorption in the smallest concentration sample. Based on this increase for the largest implanted concentration we propose that there is an incubation concentration for Si related defects, or, possibly, more types of defects, and that the density of these defects formed increases when there is a sufficient density of Si ions to form the Si configuration that absorbs in the range 4.8-4.9 eV.

The fact that the absorption between 4.8 and 4.9 eV, after Si implantation for the three smallest concentrations, is of approximately the same magnitude as the optical absorption for all the O samples, the much smaller densities of the $PORs$ and the lack of detection of $NBOHCs$ for the Si implanted samples (Table 5.4) indicates that the absorption in all Si implanted samples is due to different defect centers, presumably Si excess related. We suggest that the much larger increase in optical absorption for the two largest concentrations is due to an increase in the probability of forming the Si configuration which absorbs between 4.8 and 4.9 eV, with increasing Si concentrations. Based on these observations we suggest that in the Si implantation case there is at least one Si related defect center absorbing in the 4.8-4.9 eV range. This defect center is probably diamagnetic as there is no evidence for a correlated ESR signal. In the Si implantation case, the ESR data show that the contribution to the absorption by the detected O related defects (POR) is negligible.

Diamagnetic oxygen related defects

Based on the increase in absorption after the largest O-implantation concentration compared to the lower O-implantation concentrations and the decrease in the defect densities of the ESR active O related defects, we suggest that in addition to these three defects still another O related defect is formed which contributes to the absorption and is probably diamagnetic. Richard *et al.* [274] have calculated the energy of formation of defects and have shown that the dominant defect is the oxygen interstitial which forms charged and neutral peroxy bridges. These calculations indicate that the the probability of forming an oxygen interstitial O_2^- is much smaller than the probability of forming the peroxy structures. Nishikawa *et al.* [275] attributed an absorption band observed at 3.8 eV to the neutral peroxy bridge ($\equiv$Si–O–O–Si$\equiv$). If the attribution is correct then such a configuration cannot contribute to absorption between 4.8 and 4.9 eV. Based on their discussion it appears that the charge state of the O_2 molecule is -2, it is bonded to two Si, and is, therefore, diamagnetic. In the optical absorption measurements of the current samples performed by Magruder *et al.*, no absorption band at 3.8 eV was present. However, the assignment of the optical absorption band at 3.8 eV to the peroxy bridge has been questioned by Awazu and Kawazoe [252] leaving the possibility that the neutral peroxy bridge still absorbs at $\sim$4.8 eV, and could provide a non-ESR active contribution to the absorption. Another possibility is that diamagnetic interstitial O_3 molecules account for absorption in the 4.8 eV range [253].

The OS center

As aforementioned we suggest that the OS center is O related. But what kind of O related species could account for the observed OS signal? From previous works and compilations [276, 277], a first general observation appears that most O associated defects can be excluded as viable candidates since they generally have principal g values with at least one g value much larger than those inferred for the OS signal. Based on the principal values of the g matrix, for example, it is impossible to assign the OS center to the interstitial ozonide O_3^- ion (g_1=2.018, g_2=2.011, and g_3=2.002) as observed by Griscom and Friebele [270] in high-potassium content SiO$_2$. Instead, the closest match so far in terms of g values can be found for the 'so-called' O_3^- complexes (g_1=2.008, g_2=2.0045, and g_3=2.003) adsorbed on SiO$_2$ surfaces [276]. But, in keeping with scientific rigor, it should be

added that the issue on the identification of the O_3^- ion, viz. regarding the so-called O_3^- complexes and anomalous O_3^- ions, is not quite satisfactory yet [276, 277]. So, we conclude that the atomic source of the OS signal is unknown. Conclusive assignment would, at least, need additional information on hf structure.

In line with the possible assignment of the diamagnetic O related defect described above, another possible candidate responsible for the OS signal is the positively charged peroxy bridge, perhaps also absorbing at around 4.8 eV. According to Richard *et al.* [274], its formation energy is smaller than for the neutral peroxy bridge. This complies with the experimental observation that the OS center would contribute a (significantly) smaller part to the 4.8 eV absorption band than the neutral state (cf. Fig. 5.1 and Table 5.3), which is diamagnetic. So, the charged peroxy bridge may also be the origin of OS.

Diamagnetic silicon related defects

Based on the comparison of the optical data and ESR data for the Si implanted samples, we suggest that there is at least one diamagnetic Si related defect center that absorbs in the range 4.8-4.9 eV. Next we consider some of the possible Si configurations that could produce such a defect. The calculations of Pacchioni and Ierano [273] give transition energies for the neutral $O_3Si–SiO_3$ defect of 7.5 eV (a dimer), and for the $O_3Si–Si–SiO_3$ defect of 6.3 eV (a trimer). Clearly, these energies are much larger than the transition Magruder *et al.* observed between 4.8 and 4.9 eV. Since in the Si implanted samples, the observed change in absorption is small, i.e., a factor of $\sim$1.6 increase over the first three concentrations, approximately a factor of $\sim$2.5 increase compared to the smallest concentration for the fourth concentration, and then a much larger enhancement by a factor of $\sim$15 compared to the smallest concentration for the 1.5 $at.\%$ Si concentration, the Si state may be a cluster of Si's, perhaps, forming a tetragonal structure.

5.4.2   The 5.7-5.9 eV optical absorption band

Comparison of optical and ESR data

To ease comparison, the optical absorption coefficients at 5.85 eV as a function of the log of the implantation concentrations are plotted on the same graph as the E' defect densities (see Fig. 5.9). Figure 5.9 (a) shows that the optical absorption at 5.85 eV increases with increasing O *implantation* concentration while the E' defect density decreases by a factor of $\sim$60. This
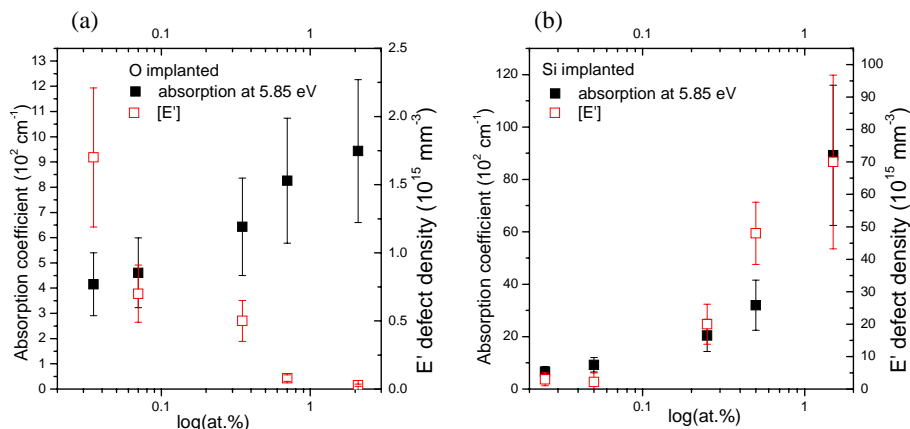
Figure 5.9: *Absorption coefficient at 5.85 eV and the E′ defect density as a function of (a) O and (b) Si implantation concentration.*

difference is incompatible with the hypothesis that the absorption at 5.85 *eV* would only be due to *E′* defects. The current data is, to us, a convincing proof of the existence of another optical band or bands between 5.8 and 5.9 *eV*, as suggested previously [256, 257, 248]. Based on the fact that the absorption between 5.8 and 5.9 *eV* increases with increasing O concentration we suggest that the additional absorption is due to an O related defect. The defect center is probably diamagnetic since no corresponding ESR components could be detected.

In the case of the *Si implanted* samples, as shown in Fig. 5.9 (b), the optical absorption and the E'_γ density increase with increasing implantation dose. The absorption coefficient at 5.85 *eV* increases approximately proportional with the Si concentration –more than a factor of 25 increase between the smallest and the largest concentrations. Within the estimated reasonable errors, we conclude that there is a good qualitative correlation (correlation coefficient R=0.93) between the optical absorption data and the *E′* ESR data for these Si implanted samples. This correlation is consistent with the data of Weeks and Sonders [256] and their inference that the largest fraction of the absorption at 5.85 *eV* in their samples was due to the *E′* center.

However, from a different point of view, we emphasize 'reasonable error' noting that accuracies of determining absorption coefficients and defect densities are reduced when there are overlapping optical bands and ESR components. Along this line, we may dispute the validity of the correlation between the *E′* densities and the optical absorption coefficient shown in

Fig. 5.9 (b) for the two largest Si concentrations. In fact, we may consider the E' data for these two largest concentrations as suggestive for the onset of E' density saturation, while the optical data does not indicate such a saturation. If we assume that the differences between the two sets of data are larger than the estimated errors, the increase in the optical absorption cannot be due to the E' centers, leading us to the conclusion that another band develops at these concentrations that absorbs between 5.8 and 5.9 eV. Since no other ESR active defects, not even S=1 centers, are detected that can account for another band, the defect is probably diamagnetic. Furthermore, it is likely that this defect is Si related since it occurs in the samples with the largest Si implanted concentrations.

Next we might consider some Si configurations that could account for this additional absorption band. The energy of the transition from the ground state to the first excited state of the neutral oxygen vacancy has been calculated as 7.5 eV [273]. If this value is correct then obviously the absorption of this state will not contribute to the absorption between 5.8 and 5.9 eV. With increasing amounts of implanted Si the probability of forming a state in which a two-fold coordinated O_2=Si: defect is formed increases. The charge state of such a site could be 0, +1, or +2. The 0 and the +2 states would be diamagnetic. For the 0 charge state the calculated energy of the first transition is between 5.3 and 5.8 eV [273]. Thus this configuration could be the source of the additional absorption between 5.8 and 5.9 eV and would be consistent with the possibility of a second Si related defect in the 5.7-5.9 eV range that begins to appear at higher concentrations of implanted Si.

E' density

Saturation of the E' density as a function of the implantation dose has been observed previously. According to Antonini *et al.* [278] comparing various damaging agents, saturation in E' density is obtained for irradiation of vitreous SiO_2 with 1 MeV protons at the $\sim 10^{17}$ $particles/cm^2$ dose, 46.5 MeV nickel ions at $\sim 10^{15}$ $particles/cm^2$, and for 1 MeV electrons at $\sim 10^{17}$ $particles/cm^2$. Bogomolova et al. [279] even reported a decrease in E' density for different ion implantations at high doses ($>6 \times 10^{15}$ $ions/cm^2$) in a-SiO_2.

In Fig. 5.9 (b) is shown that the density of E' centers in Si implanted samples increases with Si dose to the order of 5×10^{19} cm^{-3}, approximately one E' defect per two implanted Si ions (the maximum Si implantation dose of 1.5 $at.$ % corresponds with the implantation of $\sim 9 \times 10^{19}$ Si atoms per

cm^3), which is a very large fraction. However, this density is of the same order as the maximum density obtained for 2 MeV proton irradiation [278] and for one case of neutron irradiation [280]. Moritani et al. [281] reported an E' density of more than 10^{20} $spins/g$, which is rather close to their evaluated concentration of the displaced oxygen atoms. Weeks reported that the E' defect densities in four different commercial silica samples and one synthetic crystal sample, irradiated with neutrons in a nuclear reactor to doses ranging from 10^{17} to 3×10^{20} cm^{-2}, saturated at densities between 2×10^{19} cm^{-3} and 4×10^{19} cm^{-3} [266]. So, the currently observed maximum defect density of the E' centers is consistent with previous observations.

The measured shape of the E' ESR spectra induced by Si ion implantation differs from that of the E' signal observed in γ-irradiated silica [4]. These changes become more pronounced for the samples with the largest Si concentration. We attribute these effects to a larger inhomogeneous broadening of the ion implanted samples due to a larger distribution in principal g values, in turn originating from larger distortions of the local environment of the E' defects and to increasing dipole-dipole interactions between the E' spins with increasing densities.

Additional ESR component

As mentioned before (see section 5.3.2), an additional component is observed on the low-field flank of the E' component in the samples with the largest Si concentrations. A similar center has been observe before, which was assigned to a trivalent Si atom back bonded to two O atoms and one Si atom [279, 201]. However, since no hf interaction originating from this center was ever observed, the assignment should be considered merely suggestive. Considering the observed g value and line width, a possible candidate could be S center, tentatively assigned to the E' like centers Si_nO_{3-n}=$Si^\bullet$(n=1,2), likely SiO_2=$Si^\bullet$, i.e., the structure proposed in previous works [63, 66] and discussed in section 1.2.2. We note that in the current case, the resolution of this component is adversely affected by overlap with the E' center. In absence of observed hf structure it is not possible to fully identify this defect.

5.5 Summary and conclusions

The main conclusion of this comparison of the densities of defect centers observed by ESR and of the optical absorption in the range 5.7-5.9 eV, and especially in the range 4.8-4.9 eV, is that there are still a lot of unknowns

concerning the origins of the optical absorption. It appears that many paramagnetic as well as diamagnetic defect centers might possibly contribute to the absorption in these ranges. The attribution of an optical absorption band to one specific defect center (as has been done before [256] for the E' center and the 5.85 eV absorption) is not straightforward and requires extreme care. Additional contributions of other defect centers absorbing in the same range can easily be overlooked due to strong overlap of signals.

In the silica samples implanted with O concentrations ≥ 0.35 $at.\%$, a so far unknown ESR component, labeled the OS center, has been resolved with principal g values, g_1=2.0022, g_2=2.0033, and g_3=2.0088, as inferred from consistent computer simulations of K and Q-band ESR spectra. As the defect is not observed in the Si implanted samples, it is likely O related. It may be that this additional O related defect contributes to the absorption between 4.8 and 4.9 eV. A possible assignment of the OS center comes from the comparison of the observed principal g values with g values taken from literature, pointing towards the direction of the 'so-called' O_3^- complex. Another possibility of its atomic origin is the peroxy bridge in the paramagnetic charge state +1. It should be kept in mind, however, that as long as no hf structure can be observed, these assignments are purely suggestive and probably one mighty think of many other possible atomic origins for the OS center.

From the data on the O implanted samples it could be concluded that besides the ESR active defects (POR, $NBOHC$, and OS) that possibly (not certainly) contribute, there should be at least one diamagnetic defect also contributing to the absorption in the 4.8-4.9 eV range. Combining the data with literature, this extra absorption center could possibly be interstitial ozone molecules or the neutral peroxy bridge.

From the data we could also conclude that beside the E' center there is another defect, probably O related, that contributes to the optical absorption between 5.8 and 5.9 eV.

We report for the first time evidence for a band due to a Si related defect (or defects) absorbing between 4.8 and 4.9 eV. Based on the dependence of the optical absorption of this probably Si related defect on the Si implantation concentration –the formation probability of this Si related state appears implant concentration dependent– we suggest that possibly Si clusters form.

The data on the Si implanted samples show that in these samples, the E' center is the main defect responsible for the 5.8 eV absorption band. The optical absorption between 5.8 and 5.9 eV and the inferred E' densities cor-

relate within the experimental error for the three smallest concentrations. Based on the trend to saturation of the E' density at the largest concentrations of implanted Si and the absence of such a clear trend to saturation in the optical absorption we conclude that another optical band is formed related to a configuration of Si ions that absorbs between 5.7 and 5.9 eV and that is probably diamagnetic.

Summary and conclusions

In this work ESR has been used in conjunction with post-manufacture irradiation and annealing to observe, monitor and characterize point defects in the functional oxides SiO_2 (nm-sized fumed silica particles and O and Si implanted bulk SiO_2) and ZrO_2, and in Si/high-κ stacks (P-implanted $(100)Si/HfO_2$ and $(100)Si/LaAlO_3$). This way information could be obtained concerning e.g., the specific oxide network structure, the occurrence of impurity related charge traps, and the nature and stability of the Si/high-κ interface. The main results are summarized below.

The subject of chapter two is the study of point defects in fumed $\sim$7 nm-sized silica nanoparticles using X, K, and Q-band ESR following 10 eV irradiation to photodissociate H from passivated defects. Various types of ESR-active point defects are revealed including the familiar E' center (generic entity $^\bullet Si \equiv O_3$), EX, the POR, the methyl radical, and an unknown closely axially symmetric center ($g_\parallel$=2.0041, $g_\perp$=2.0027). Besides the $PORs$, large numbers of other oxygen-hole type defects appear to be present also. The exhaustive number of all oxygen-hole centers, including the $PORs$, is determined at $\sim$0.07 defects/nanoparticle, making this kind of defect highly unlikely as playing a substantial role in narrowing of the optical band gap, in contrast with previous suggestion.

The main results of this chapter were obtained through monitoring of the observed E' defects as a function of post-formation heating [in vacuum in the range 850-1115 $^\circ C$ or with the sample brought into contact with "bulk" Si/SiO_2 entities in vacuum at elevated temperatures in the range 1005-1205 $^\circ C$ (SiO-vac. anneal)] and treatment (aging, VUV excitation), allowing us to assess specific physicochemical structural aspects of the nanoparticles. Experimental evidence was presented for the presence of two different systems of E' centers. The specific ESR parameters (e.g., $\hat{g}$ matrix) of the E' centers of one batch are are found to be very similar to those of the E'_γ center in bulk fused silica, while the second batch exhibits a different zero crossing g value and line shape, attributed to variations in

local structure. It is inferred that the latter E' system pertains to the outer SiO_2 layers, exposing a structural nature different from bulk glassy SiO_2.

The SiO-vac. anneals resulted in a drastic increase in E' defect density with increasing T_{an}, which enabled us to resolve the primary ^{29}Si hf structure of the E' centers located in the core region of the nanoparticles. Detailed analysis of the observed hf spectra reveals several interesting items pointing to a modification of the specific network structure of the core region of the nanoparticles. An increased hf splitting of 438 ± 2 G is observed compared to bulk silica (418 ± 2 G) indicating that the core part E' centers exhibit a more pyramidal defect structure. Moreover, the increased primary hf splitting indicates that the core of the fumed silica particles is densified, possibly associated with the presence of more low-membered rings in the nm-sized silica network.

In a next chapter the observation by ESR of P-related point defects in nm-thick P-implanted HfO_2 films on (100)Si after annealing in the range 500-900 $°C$ and in ZrO_2 powder –two oxides prominent in current high-κ insulator research, is reported. Based on the principal g matrices and hf tensors inferred from consistent X, K, and Q-band spectra simulations and comparison with established P-associated defects in silica, both centers appear similar in nature and are assigned to a P_2-type defect –a P substituting a Hf or Zr atom. Both centers were observed in the monoclinic phase of the high-κ oxides with the unpaired electron strongly localized on the P atom. A sizeable fraction of the incorporated P impurities was found to result in ESR active P_2-type defects. Within the concern about dopant penetration out of Si into the high-κ layers on top, identification of the dopant-associated defects in the latter appears crucial to which the present basic results provide fundamental access; The centers may operate as detrimental charge trapping sites.

The atomic nature of the interface in (100)Si/$LaAlO_3$ structures with nm-thin amorphous $LaAlO_3$ layers of high dielectric constant ($\kappa\sim20$-27), deposited directly on clean (100)Si by molecular beam deposition at ~100 $°C$, is assessed in chapter four through probing of paramagnetic point defects. On the as-grown samples K-band ESR indicated the absence of an Si/SiO_2-type interface in terms of the archetypal Si-dangling bond-type Si/SiO_2 interface defects (P_{b0}, P_{b1}). With no P_b-type defects observed, this state is found to persist during subsequent annealing (1 atm N_2 or 5 % O_2 in N_2 ambient) up to $T_{an}\sim800$ $°C$, referring to a thermally stable abrupt Si/$LaAlO_3$ interface, quite in contrast with other high-κ metal oxide/Si structures. However, in the range $T_{an}\sim800$-860 $°C$ a Si/SiO_2-type inter-

face starts forming as evidenced by the appearance of P_{b0} defects and, with some delay in T_{an}, the EX center –an SiO_2 associated defect, attesting to significant structural/compositional modification. The peaking of the defect density vs. T_{an} curves indicates the SiO_x nature of the interlayer to break up again upon annealing at $T_{an} \geq 930$ °C, possibly related to crystallization and/or degrading silicate formation. No specific $LaAlO_3$-specific point defects could be traced.

In the last chapter we tried to determine some of the sources of optical absorption between 4.8 and 4.9 eV and between 5.8 and 5.9 eV by combining our ESR measurements with the optical absorption measurements made from 2.0 to 6.5 eV by Magruder, Weeks, and Weller in two separate series of type III silica samples, one implanted with Si and one with O. Several ESR active defects were observed including the E'_γ center, the $NBOHC$, the POR, a possibly oxygen related center, labeled OS, and a component around g=2.0026. As expected, it was found that in the Si case that the E' center is the main defect responsible for the 5.8 eV band. The trend to saturation of the E' density at the largest concentrations of implanted Si and the absence of such a trend in the optical absorption, however, suggest that another defect center, probably Si-related and diamagnetic, absorbs between 5.7 and 5.8 eV. In the O implantation case, the comparison of the observed increasing optical absorption at 5.85 eV with the observed decrease in the E' defect density with increasing O concentration, indicates that an oxygen related band is created and and its intensity increases with increasing O concentration. From comparing the changes in absorption between 4.8 and 4.9 eV with the changes in the defect densities of the various ESR components, we conclude that there are three ESR-active defect centers (POR, $NBOHC$, and OS) that possibly contribute to the optical absorption between 4.8 and 4.9 eV. The data also indicate the presence of an extra O-related diamagnetic contributor to the absorption in the 4.8-4.9 eV range in the O implantation case and a Si-related diamagnetic contributor in the Si implantation case.

Finally, we conclude with some possible perspectives for future research. In this work two high-κ oxides on (100)Si, i.e., HfO_2 and $LaAlO_3$ were studied promising for future applications. Recently, the HfO_2-based MOSFET has even been taken into production. However, to meet the projected advancements in semiconductor based technology many other high-κ layers on Si or on other semiconductors (e.g., Ge, GaAs) will need to be tested. More intense ESR work will be needed to characterize, e.g., the nature and stability of the high-κ/semicondictor interface and point defect (intrinsic

or impurity related) in the oxide that can act as detrimental charge traps.

In the high-κ oxides ZrO_2 and HfO_2 we succeeded in the observation and characterization of dopant (P) associated defects. This resulted in a proposition for a possible model for these observed P_2-type defect. However, to fully asses the charge trapping behavior of these defects more theoretical insight is needed. Hopefully the current experimental breakthrough will encourage theoreticians to start modeling these P_2-type defects in high-κ oxides.

Not only the impurity (dopant) associated point defects but also the intrinsic point defects possibly present in the high-κ oxides are of vital importance for the performance and reliability of MOS-based devices. According to theory, the dominant defects in HfO_2 are oxygen vacancies exhibiting defect energy levels in the band gap of the oxide. Up to now, however, no convincing experimental evidence has been presented in the literature for the presence of such large concentrations of oxygen vacancies. One of the key challenges for ESR researchers in the near future will be to provide the undeniable experimental proof for the presence of the much-discussed "oxygen vacancy".

Bibliography

[1] J. E. Wertz and J. R. Bolton, *Electron Spin Resonance: Elementary Theory and Practical Applications*, (McGraw-Hill, New York, 1972).

[2] C. P. Poole, *Electron Spin Resonance: A Comprehensive Treatise on Experimental Techniques*, (Interscience Publishers, John Wiley & Sons, New York, 1967).

[3] A. Abragam and B. Bleany, *Electron Paramagnetic Resonance of Transition Ions*, (Clarendon Press, Oxford, 1970).

[4] D. L. Griscom, *Glass: Science and Technology*, volume 4B, edited by D. R. Uhlmann and N. J. Kreidl (Academic Press, N.Y., 1990), p. 151.

[5] P. J. Mohr and B. N. Taylor, Rev. Mod. Phys. **77**, 64 (2005).

[6] W. Kohn and J. M. Luttinger, Phys. Rev. **97**, 883 (1955).

[7] R. G. Barnes and W. V. Smith, Phys. Rev. **93**, 95 (1954).

[8] J. R. Morton and K. F. Preston, J. Magn. Reson. **30**, 577 (1978).

[9] A. K. Koh and D. J. Miller, At. Data Nucl. Data Tables **33**, 235 (1985).

[10] C. G. Van de Walle and P. E. Blöchl, Phys. Rev. B **47**, 4244 (1993).

[11] G. D. Watkins and J. W. Corbett, Phys. Rev. **134**, A1359 (1964).

[12] G. Feher, Bell Syst. Techn. J. **36**, 449 (1957).

[13] R. Fuller, H. Evans, C. Gamten, B. Czagas, M. Morrison, D. Decrosta, R. Lowry, P. Lenahan, and C. Frye, IEEE Trans. Nuc. Sci. **43**, 2565 (1996).

[14] D. L. Griscom, Phys. Rev. B **20**, 1823 (1979).

[15] T. E. Tsai and D. L. Griscom, J. Non-Cryst. Sol. **91**, 170 (1987).

[16] A. Stesmans, J. Magn. Res. **76**, 14 (1988).

[17] A. Stesmans and G. Devos, Phys. Stat. Sol. **110(a)**, 615 (1988).

[18] G. Breit and I. I. Rabi, Phys. Rev. **38**, 2082 (1931).

[19] G. Wilk, R. M. Wallace, and J. M. Anthony, J. Appl. Phys. **89**, 5243 (2001).

[20] M. Houssa, L. Pantisano, L.-Å. Ragnarsson, R. Degraeve, T. Schram, G. Pourtois, S. De Gendt, G. Groeseneken, and M. M. Heyns, Mat. sci. and Eng. R **51**, 37 (2006).

[21] *International Technology Roadmap for Semiconductors*, (Semiconductor Industry Association, San Jose, CA, **2005**).

[22] S. E. Pratsinis, Prog. Energy Combust. Sci. **24**, 197 (1998).

[23] W. J. Stark and S. E. Pratsinis, Powder Technology **126**, 103 (2002).

[24] K. L. Brower, Appl. Phys. Lett. **43**, 1111 (1983).

[25] G. J. Gerardi, E. H. Poindexter, P. J. Caplan, and N. M. Johnson, Appl. Phys. Lett. **49**, 348 (1986).

[26] A. Stesmans and V. V. Afanas'ev, Phys. Rev. B **57**, 10030 (1998).

[27] R. Helms and E. H. Poindexter, Rep. Prog. Phys. **57**, 791 (1994).

[28] K. L. Brower, Phys. Rev. B **38**, 9657 (1988).

[29] A. Stesmans, Phys. Rev. B **48**, 2418 (1993).

[30] Y. Nishi, Jpn. J. Appl. Phys. **10**, 52 (1971).

[31] P. J. Caplan, E. H. Poindexter, B. E. Deal, and R. R. Razouk, J. Appl. Phys. **50**, 5847 (1979).

[32] E. H. Poindexter, P. J. Caplan, B. E. Deal, and R. R. Razouk, J. Appl. Phys. **52**, 879 (1981).

[33] A. Stesmans, Appl. Phys. Lett. **48**, 972 (1986).

[34] A. Stesmans and V. V. Afanas'ev, J. Appl. Phys. **83**, 2449 (1998).

[35] A. Stesmans and V. V. Afanas'ev, Appl. Phys. Lett. **72**, 2271 (1998).

[36] H. J. von Bardeleben, C. Ortega, A. Grosman, V. Morazzani, J. Siejka, and D. Stievenard, J. Luminescence **57**, 301 (1993).

[37] F. C. Rong, J. F. Harvey, E. H. Poindexter, and G. J. Gerardi, Appl. Phys. Lett. **63**, 920 (1993).

[38] A. Stesmans, B. Nouwen, and V. V. Afanas'ev, Phys. Rev. B **58**, 15801 (1998).

[39] A. Stesmans and V. V. Afanas'ev, J. Vac. Sci. Technol. **B16**, 3108 (1998).

[40] W. Futako, M. Mizuochi, and S. Yamasaki, Phys. Rev. Lett. **92**, 105505 (2004).

[41] A. Stesmans and V. V. Afanas'ev, Appl. Phys. Lett. **68**, 2723 (1996).

[42] A. Stesmans and V. V. Afanas'ev, Appl. Phys. Lett. **68**, 2076 (1996).

[43] A. Stesmans, J. Appl. Phys. **88**, 489 (2000).

[44] K. L. Brower, Phys. Rev. B **42**, 3444 (1990).

[45] A. Stesmans, Phys. Rev. B **61**, 8393 (2000).

[46] W. L. Warren, E. H. Poindexter, M. Offenberg, and W. Müller-Warmuth, J. Electrochem. Soc. **139**, 872 (1992).

[47] R. H. Silsbee, J. Appl. Phys. **32**, 1459 (1961).

[48] D. L. Griscom, Nucl. Instrum. Methods in Phys. Research B **1**, 481 (1984).

[49] G. Hochstrasser and J. F. Antonini, Surf. Sci. **32**, 644 (1972).

[50] R. A. Weeks, J. Appl. Phys. **27**, 1376 (1956).

[51] D. L. Griscom, E. J. Friebele, and G. H. Sigel Jr., Solid State Commun. **15**, 479 (1974).

[52] F. J. Feigl, W. B. Fowler, and K. L. Yip, Solid state Commun. **14**, 225 (1974).

[53] J. K. Rudra and W. B. Fowler, Phys. Rev. B **35**, 8223 (1987).

[54] T. Uchino, M. Takahashi, and T. Yoko, Phys. Rev. Lett. **86**, 5522 (2001).

[55] T. Uchino and T. Yoko, Phys. Rev. B **74**, 125203 (2006).

[56] J. F. J. Conley, P. M. Lenahan, H. L. Evans, R. K. Lowry, and T. J. Morthorst, J. Appl. Phys. **76**, 2872 (1994).

[57] L. P. Trombetta, G. J. Gerardi, D. J. Di Maria, and E. Tierney, J. Appl. Phys. **64**, 2434 (1988).

[58] D. Herve, J. L. Leray, and R. A. B. Devine, J. Appl. Phys. **72**, 3634 (1992).

[59] V. V. Afanas'ev and S. A., J.Phys.: Condens. Matter **12**, 2285 (2000).

[60] E. Holzenkämpfer, F. W. Richter, J. Stuke, and U. Voget-Grote, J. Non-Cryst. Solids **32**, 327 (1979).

[61] D. L. Griscom, E. J. Friebele, K. J. Long, and J. W. Fleming, J. Appl. Phys. **54**, 3743 (1983).

[62] A. Stesmans and V. V. Afanas'ev, Appl. Phys. Lett. **69**, 2056 (1996).

[63] A. Stesmans, B. Nouwen, and V. V. Afanas'ev, Phys. Rev. B **66**, 045307 (2002).

[64] A. Stesmans, B. Nouwen, D. Pierreux, and V. V. Afanas'ev, Appl. Phys. Lett. **80**, 4753 (2002).

[65] A. Stesmans and V. V. Afanas'ev, Microel. Eng. **36**, 201 (1997).

[66] A. Stirling and A. Pasquarello, Phys. Rev. B **66**, 245201 (2002).

[67] A. Stesmans, Phys. Rev. B **45**, 9502 (1992).

[68] A. Stesmans and F. Scheerlinck, Phys. Rev. B **50**, 5204 (1994).

[69] A. Stesmans and F. Scheerlinck, J. Appl. Phys. **75**, 1047 (1994).

[70] S. M. Prokes and W. E. Carlos, J. Appl. Phys. **78**, 2671 (1995).

[71] W. E. Carlos and S. M. Prokes, J. Appl. Phys. **78**, 2129 (1995).

[72] A. Baumer, M. Stutzmann, M. S. Brandt, F. C. K. Au, and T. S. Lee, Appl. Phys. Lett. **85**, 943 (2004).

[73] R. P. Wang, Appl. Phys. Lett. **88**, 142104 (2006).

[74] N. Fukata, J. Chen, T. Sekiguchi, S. Matsushita, O. T., N. Uchida, K. Murakami, T. Tsurui, and S. Ito, Appl. Phys. Lett. **90**, 153117 (2007).

[75] M. Dohi, H. Yamatani, and T. Fujita, J. Appl. Phys. **91**, 815 (2002).

[76] H. J. von Bardeleben, J. L. Cantin, J. J. Ganem, I. Trimaille, and E. P. Gusev, *Defects in High-κ Gate Dielectric Stacks, NATO science series*, p. 249, edited by E. P. Gusev (Springer, 2006), p. 249.

[77] A. Stesmans and V. V. Afanas'ev, J. Appl. Phys. **97**, 033510 (2004).

[78] B. B. Triplett, P. T. Chen, Y. Nishi, P. H. Kasai, J. J. Chambers, and J. Colombo, J. Appl. Phys. **101**, 013703 (2007).

[79] H. Kusumoto and M. Shoji, Jpn. J. Appl. Phys. **17**, 1678 (1962).

[80] D. L. Griscom, J. Non-Cryst. Solids **31**, 241 (1978).

[81] E. J. Friebele, D. L. Griscom, M. A. Stapelbroek, and R. A. Weeks, Phys. Rev. Lett. **42**, 1346 (1979).

[82] M. Stapelbroek, D. L. Griscom, E. J. Friebele, and G. H. Sigel Jr., J. Non-Cryst. Solids **32**, 313 (1979).

[83] D. L. Griscom and E. J. Friebele, Phys. Rev. B **24**, 4896 (1981).

[84] J. Vitko Jr., J. Appl. Phys. **49**, 5530 (1978).

[85] Y. J. Uchida, J. Phys. Soc. J. **42**, 1937 (1977).

[86] Y. Uchida, J. Isoya, and J. A. Weil, Am. Chem. Soc. **83**, 3462 (1979).

[87] P. Lenahan, C. A. Billman, R. Fuller, H. Evance, W. H. Speece, D. Decrosta, and R. Lowry, IEEE Trans. Nuc. Sci. **44**, 1834 (1997).

[88] M. Fanciulli, E. Bonera, S. Nokhrin, and G. Pacchioni, Phys. Rev. B **74**, 134102 (2006).

[89] J. Laegsgaard and K. Stokbro, Phys. Rev. B **61**, 12590 (2000).

[90] J. Laegsgaard and K. Stokbro, Phys. Rev. B **65**, 075208 (2002).

[91] R. A. Weeks and P. J. Bray, J. Chem. Phys. **48**, 5 (1968).

[92] W. L. Warren, M. R. Shaneyfelt, D. M. Fleetwood, P. S. Winokur, and S. Montague, IEEE Trans. Nuc. Sci. **42**, 1731 (1995).

[93] J. Robertson, *Proceedings of Symposium on the Physics and Technology of Amorphous SiO$_2$*, edited by R. A. B. Devine (Plenum Press, N.Y., 1988), p. 91.

[94] M. A. Quevedo-Lopez, M. El-Bouanani, B. E. Gnade, R. M. Wallace, M. R. Visokay, M. Douglas, M. J. Bevan, and L. Colombo, J. Appl. Phys. **92**, 3540 (2002).

[95] J. Robertson, Eur. J. Appl. Phys. **28**, 265 (2004).

[96] E. P. Gusev, M. Copel, E. Cartier, I. J. R. Baumvol, C. Krug, and M. A. Bribelyuk, Appl. Phys. Lett. **76**, 176 (2000).

[97] C. R. Krug, E. B. da Rosa, R. M. de Almeida, J. Morais, I. J. Baumvol, T. D. M. Salgado, and F. C. Stedile, Phys. Rev. Lett. **85**, 4120 (2000).

[98] P. D. Kirsch, C. S. Kang, J. Lozano, J. C. Lee, and J. G. Ekerdt, J. Appl. Phys. **91**, 4354 (2002).

[99] B. Gallas, A. Brunet-Bruneau, S. Fisson, G. Vuye, and J. Rivory, J. Appl. Phys. **92**, 1922 (2002).

[100] Y. Nishikawa, T. Yamaguchi, M. Yoshiki, H. Satake, and N. Fukushima, Appl. Phys. Lett. **81**, 4386 (2002).

[101] M. R. Visokay, J. J. Chambers, A. L. Rotondaro, A. Shanware, and L. Colombo, Appl. Phys. Lett. **80**, 3183 (2002).

[102] M. H. Cho, Y. S. Roh, N. Whang, K. Jeong, H. J. Choi, S. W. Nam, D. H. Ko, J. H. Lee, N. I. Lee, and K. Fujihara, Appl. Phys. Lett. **81**, 1071 (2002).

[103] M. Copel, M. Bribelyuk, and E. Gusev, Appl. Phys. Lett. **76**, 436 (2000).

[104] M. Houssa, M. Tuominen, N. Naili, V. V. Afanas'ev, A. Stesmans, S. Haukka, and M. M. Heyns, J. Appl. Phys. **87**, 8615 (2000).

[105] M. Copel, Appl. Phys. Lett. **82**, 1580 (2003).

[106] J. H. Lee and M. Ichikawa, J. Appl. Phys. **92**, 1929 (2002).

[107] M. Gutowski, J. E. Jaffe, C. L. Liu, M. Stoker, R. I. Hedge, R. S. Rai, and P. J. Tobin, Appl. Phys. Lett. **80**, 1897 (2002).

[108] M. Houssa, A. Stesmans, M. Naili, and M. M. Heyns, Appl. Phys. Lett. **77**, 1381 (2000).

[109] J. R. Chavez, R. A. B. Devine, and L. Koltunski, J. Appl. Phys. **90**, 4284 (2001).

[110] V. V. Afanas'ev and A. Stesmans, Appl. Phys. Lett. **80**, 1261 (2002).

[111] R. J. Carter, *Intern. Workshop on Gate Insulators*, edited by S. Ohmi, F. Fuijta, and H. S. Momose (Jpn. Soc. of Appl. Phys., Tokyo, 2001), p. 94.

[112] A. Stesmans and V. V. Afanas'ev, J. Phys.: Condens. Matter **13**, L673 (2001).

[113] A. Stesmans and V. V. Afanas'ev, Appl. Phys. Lett. **80**, 1957 (2002).

[114] S. Baldovino, S. Nokrin, G. Scarel, M. Fanciulli, G. T., and M. S. Brandt, J. Non-Cryst. Solids **322**, 168 (2003).

[115] J. L. Cantin and H. J. von Bardeleben, J. Non-Cryst. Solids **303**, 175 (2002).

[116] B. J. Jones and R. C. Barklie, Microelectron. Eng. **80**, 74 (2005).

[117] A. Stesmans and V. V. Afanas'ev, Appl. Phys. Lett. **82**, 2835 (2003).

[118] A. Y. Kang, P. M. Lenahan, J. F. Conley Jr., and R. Solanski, Appl. Phys. Lett. **81**, 1128 (2002).

[119] M. Copel and M. C. Reuter, Appl. Phys. Lett. **83**, 3398 (2003).

[120] M. L. Green, E. P. Gusev, R. Degraeve, and E. Garfunkel, J. Appl. Phys. **90**, 2057 (2001).

[121] L. F. Edge, D. G. Schlom, S. A. Chambers, E. Cicerrella, J. L. Freeouf, B. Holländer, and J. Schubert, Appl. Phys. Lett. **84**, 726 (2004).

[122] B. H. Lee, L. Kang, R. Nieh, W. J. Qi, and J. C. Lee, Appl. Phys. Lett. **76**, 1926 (2000).

[123] M. Houssa, M. Naili, C. Zhao, M. M. Heyns, and A. Stesmans, Semicond. Sci. Technol. **16**, 31 (2001).

[124] M. J. Torralvo, M. A. Alario, and M. A. Soria, J. Catal. **86**, 473 (1984).

[125] C. Morterra, E. Giamello, L. Orio, and M. Volante, J. Phys. Chem. **94**, 3111 (1990).

[126] F. R. Chen, G. Coudurier, J. F. Joly, and J. C. Vedrine, J. Catal. **143**, 616 (1993).

[127] V. Ramaswamy, B. Tripathi, D. Srinivas, A. V. Ramaswamy, R. Cattaneo, and R. Prins, J. Catal. **200**, 250 (2001).

[128] A. Y. Kang, P. M. Lenahan, and J. F. Conley Jr., Appl. Phys. Lett. **83**, 3407 (2003).

[129] S. Wright and R. C. Barklie, J. Mater. Sci. in Semicond. Proc. **9**, 892 (2006).

[130] S. Wright and R. C. Barklie, J. Mat. Sci.: Mat. in Electr. **18**, 743 (2007).

[131] C. B. Azzoni and A. Paleari, Phys. Rev. B **40**, 6518 (1989).

[132] C. B. Azzoni and A. Paleari, Phys. Rev. B **40**, 9333 (1989).

[133] J. Matta, J. F. Lamonier, E. Abi-Aad, E. A. Zhilinskaya, and A. Aboukaïs, Phys. Chem. Chem. Phys. **1**, 4975 (1999).

[134] Q. Zhao, X. Wang, and T. Cai, Appl. Surf. Sci. **225**, 7 (2004).

[135] E. V. Frolova and M. I. Ivanovskaya, Mater. Sci. Eng. C **26**, 1106 (2006).

[136] V. M. Orera, R. I. Merino, Y. Chen, R. Cases, and P. J. Alonso, Phys. Rev. B **42**, 9782 (1990).

[137] H. Liu, L. Feng, X. Zhang, and Q. Xue, J. Phys. Chem. **99**, 332 (1995).

[138] A. Adamski, Z. Sojka, K. Dyrek, and M. Che, Sol. State Ion. **117**, 113 (1999).

[139] M. G. Cattania, A. Gervasini, F. Morazzoni, R. Scotti, and D. Strumolo, J. Chem. Soc. Faraday Trans. 1 **85**, 801 (1989).

[140] A. Martínez-Arias, M. Fernández-García, C. Belver, J. C. Conesa, and J. Soria, Catal. Lett. **65**, 197 (2000).

[141] R. Ben-Michael, D. S. Tannhauser, and J. Genossar, Phys. Rev. B **43**, 7395 (1991).

[142] M. Occhiuzzi, D. Cordischi, and R. Dragone, J. Phys. Chem. B **106**, 12464 (2002).

[143] K. K. Ermakovich, V. N. Lazukin, J. V. Chepeleva, and V. I. Aleksandrov, Sov. Phys. Solid State **18**, 1022 (1976).

[144] R. I. Merino, V. M. Orera, E. E. Lomonova, and S. K. Batygov, Phys. Rev. B **52**, 6150 (1995).

[145] I. V. Bobricheva, I. A. Stavitsky, V. K. Yermolaev, N. S. Kotsarenko, V. P. Shmachkova, and D. I. Kochubey, Catal. Lett. **56**, 23 (1998).

[146] W. Känzig and M. H. Cohen, Phys. Rev. Lett. **3**, 509 (1959).

[147] A. Stesmans, V. V. Afanas'ev, F. Chen, and S. A. Campbell, Appl. Phys. Lett. **84**, 4574 (2004).

[148] A. Stesmans, V. V. Afanas'ev, F. Chen, and S. A. Campbell, Mat. Sci. in Semicond. Processing **7**, 197 (2004).

[149] J. L. Gole, Z. L. Wang, Z. R. Dai, J. Stout, and M. White, Colloid Polym. sci. **281**, 673 (2003).

[150] K. D. Y., G. R. Kowach, D. W. Johnson Jr., S. Bhandarkar, and H. Du, J. Non-Cryst. Solids **342**, 18 (2004).

[151] H. K. Kammler and S. E. Pratsinis, Chem. Eng. Process. **39**, 219 (2000).

[152] M. A. Siddig, S. Radiman, L. S. Jan, and S. V. Muniandy, Colloids and Surf. A: Pysicochem. Eng. Aspects **254**, 215 (2005).

[153] T. Uchino, A. Aboshi, S. Kohara, Y. Ohishi, M. Sakashita, and K. Aoki, Phys. Rev. B **69**, 155409 (2004).

[154] T. Uchino, A. Sakoh, M. Azuma, M. Takano, M. Takahashi, and T. Yoko, J. Phys.: Condens. Matter **14**, 11111 (2002).

[155] S. I. Altman, D. Lee, J. D. Chung, J. Song, and M. Choi, Phys. Rev. B **63**, 151402(R) (2001).

[156] A. Roder, W. Kob, and K. Binder, J. Chem. Phys. **114**, 7602 (2001).

[157] I. V. Schweigert, K. E. J. Lehtinen, M. J. Carrier, and M. R. Zachariah, Phys. Rev. B **65**, 235410 (2002).

[158] A. J. Hurd, D. W. Schaefer, and J. E. Martin, Phys. Rev. A **35**, 2361 (1987).

[159] T. Campbell, R. K. Kalia, A. Nakano, F. Shimojo, K. Tsuruta, P. Vashishta, and S. Ogata, Phys. Rev. Lett. **82**, 4018 (1999).

[160] B. C. Bunker, D. M. Haaland, T. A. Michalske, and W. L. Smith, Surf. Sci. **222**, 95 (1989).

[161] H. Saito and T. Hyodo, Mater. Sci. Forum **255-257**, 463 (1997).

[162] T. Uchino and T. Yamada, Appl. Phys. Lett. **85**, 1164 (2004).

[163] Y. D. Glinka, S. H. Lin, and Y. T. Chen, Phys. Rev. B **66**, 035404 (2002).

[164] Y. D. Glinka, S. H. Lin, and Y. T. Chen, Appl. Phys. Lett. **75**, 778 (1999).

[165] C. C. Liu and G. E. Maciel, J. Am. Chem. Soc. **118**, 5103 (1996).

[166] S. M. Prokes, W. E. Carlos, L. Seals, S. Lewis, and J. L. Gole, Mater. Lett. **54**, 85 (2002).

[167] A. Stesmans and V. V. Afanas'ev, Phys. Rev. B **54**, R11129 (1996).

[168] D. L. Griscom, J. Appl. Phys. **58**, 2524 (1985).

[169] A. Pusel, U. Wetterauer, and P. Hess, Phys. Rev. Lett. **81**, 645 (1998).

[170] B. A. Morrow and I. A. Cody, J. Phys. Chem. **80**, 1995 (1976).

[171] G. J. Young, J. Colloid Sci. **13**, 67 (1958).

[172] D. L. Griscom and M. Cook, J. Non-Cryst. Solids **182**, 119 (1995).

[173] J. T. Yount, P. M. Lenahan, and P. W. Wyatt, J. Appl. Phys. **77**, 699 (1995).

[174] R. Tromp, G. W. Rubloff, P. Balk, F. K. Le Goues, and E. J. van Loenen, Phys. Rev. Lett. **55**, 2332 (1985).

[175] Y. Takakuwa, M. Nihei, and M. Miyamoto, Jpn. J. Appl. Phys. Part 2 **32**, L480 (1993).

[176] Y. Takakuwa, M. Nihei, and M. Miyamoto, Appl. Surf. Sci. **117-118**, 141 (1997).

[177] K. G. Nakamura, H. Kuroki, and M. Kitajima, J. Appl. Phys. **75**, 4261 (1994).

[178] K. G. Nakamura and M. Kitajima, Appl. Phys. Lett. **65**, 2445 (1994).

[179] A. Revesz, J. Electrochem. Soc. **126**, 122 (1979).

[180] D. L. Griscom, Nucl. Instrum. Methods in Phys. Research B **46**, 12 (1990).

[181] P. G. Tello, V. V. Afanas'ev, and A. Stesmans, Microelectron. Eng. **72**, 81 (2004).

[182] A. Stesmans and V. V. Afanas'ev, J. Appl. Phys. **97**, 033510 (2005).

[183] C. L. Marquardt and G. H. Sigel Jr., IEEE Trans. Nucl. Sci. **NS-22**, 2234 (1975).

[184] T. E. Tsai, D. L. Griscom, and E. J. Friebele, Phys. Rev. Lett. **61**, 444 (1988).

[185] M. E. Zvanut, F. J. Feigl, W. B. Fowler, J. K. Rudra, P. J. Caplan, E. M. Poindexter, and J. D. Zook, Appl. Phys. Lett. **54**, 2118 (1989).

[186] B. P. Lemke and D. Haneman, Phys. Rev. B **17**, 1893 (1978).

[187] F. J. Feigl and J. H. Anderson, J. Phys. Chem. Solids **31**, 575 (1969).

[188] V. A. Radzig, Colloids and Surf. A: Eng. Aspects **74**, 91 (1993).

[189] V. A. Radzig, *Defects in SiO_2 and Related Dielectrics: Science and Technology, NATO Science Series, Series II: Mathematical and Physical Chemistry*, edited by G. Paccioni, L. Skuja, and D. L. Griscom (Kluwer Academic Publishers, Dordrecht, 2000), p. 339.

[190] A. A. Bobychev and V. A. Radzig, Kinet. Katal. **29**, 551 (1988).

[191] G. K. White, Cryogenics **4**, 2 (1964).

[192] M. S. Stoneham, Rev. Mod. Phys. **41**, 82 (1969).

[193] S. Agnello, R. Boscaino, G. Buscarino, M. Cannas, and F. M. Gelardi, Phys. Rev. B **66**, 113201 (2002).

[194] N. Ishii, M. Kumeda, and T. Shimizu, Jpn. J. Appl. Phys. **20**, L673 (1981).

[195] Y. Fu and P. A. Fedders, Solid State Commun. **84**, 799 (1992).

[196] R. A. B. Devine and J. Arndt, Phys. Rev. B **35**, 9376 (1987).

[197] A. H. Edwards and W. B. Fowler, Phys. Rev. B **41**, 10816 (1990).

[198] G. Pacchioni and M. Vitiello, Phys. Rev. B **58**, 7745 (1998).

[199] R. A. B. Devine and J. Arndt, Phys. Rev. B **42**, 2617 (1990).

[200] H. Hosono, H. Kawazoe, K. Oyoshi, and S. Tanaka, J. Non-Cryst. Solids **179**, 39 (1994).

[201] M. Mizuguchi, H. Hosono, and H. Kawazoe, Mat. Sci. and Eng. B **54**, 38 (1998).

[202] K. L. Brower, Phys. Rev. B **33**, 4471 (1986).

[203] W. Gehloff and K. H. Segsa, Phys. Stat. Sol. B **115**, 443 (1983).

[204] R. A. B. Devine, R. Dupree, I. Farnan, and J. J. Capponi, Phys. Rev. B **35**, 2560 (1987).

[205] Y. T. Thatachari and W. A. Tiller, J. Appl. Phys. **57**, 1805 (1985).

[206] L. W. Hobbs and X. Yuan, *Defects in SiO_2 and Related dielectrics: Science and Technology, NATO science series, Series II: Mathematical and Physical Chemistry*, edited by G. Paccioni, L. Skuja, and D. L. Griscom (Kluwer Academic Publishers, Dordrecht, 2000), p. 37.

[207] K. Awazu and H. Kawazoe, J. Appl. Phys. **94**, 6243 (2003).

[208] Y. Bounouh, L. Chahed, A. Sadki, M. L. Thèye, C. Cardinaud, M. Zarrabian, J. von Bardeleben, K. Zellama, and J. L. Fave, Diamond Relat. Mater. **4**, 492 (1995).

[209] G. K. Walters and T. L. Estle, J. Appl. Phys. **32**, 1854 (1961).

[210] M. H. Brodsky and R. S. Title, Phys. Rev. Lett. **23**, 581 (1969).

[211] D. L. Griscom, C. I. Merzbacher, R. A. Weeks, and R. A. Zuhr, J. Non-Cryst. Solids **258**, 34 (1999).

[212] R. C. Henderson, W. J. Polito, and J. Simpson, Appl. Phys. Lett. **16**, 15 (1970).

[213] F. Gerson and W. Huber, *Electron Spin Resonance Spectroscopy of Organic Radicals*, (Wiley, Darmstadt, 2003).

[214] W. R. Austin and R. G. Leisure, J. Appl. Phys. **80**, 6646 (1996).

[215] C. L. Gardner and E. J. Casey, Can. J. Chem. **46**, 207 (1968).

[216] E. J. Friebele, D. L. Griscom, and K. Rau, J. Non-Cryst. Solids **57**, 167 (1983).

[217] H. M. McConnel, J. Chem. Phys. **25**, 709 (1956).

[218] C. Heller, J. Chem. Phys. **36**, 175 (1962).

[219] M. A. Quevedo-Lopez, M. El-Bouanani, M. J. Kim, B. E. Gnade, R. M. Wallace, M. R. Visokay, A. Li-Fatou, M. J. Bevan, and L. Colombo, Appl. Phys. Lett. **81**, 1609 (2002).

[220] M. A. Quevedo-Lopez, M. R. Visokay, J. Chambers, M. J. Bevan, A. Lifatou, L. Colombo, M. J. Kim, B. E. Gnade, and R. M. Wallace, J. Appl. Phys. **97**, 043508 (2005).

[221] K. Suzuki, H. Tashiro, Y. Morisaki, and Y. Sugita, Jpn. J. Appl. Phys. **44**, 8286 (2005).

[222] A. Stesmans, K. Clémer, and V. V. Afanas'ev, Phys. Rev. B **72**, 155335 (2005).

[223] C. Zhao, G. Roebben, M. Heyns, and O. Van Der Biest, Key Eng. Mat. **206-213**, 1285 (2002).

194

[224] J. L. Gavartin, A. L. Shluger, A. S. Foster, and G. I. J. Bersuker, J. Appl. Phys. **97**, 053704 (2005).

[225] J. Adam and M. D. Rogers, Acta Cryst. **12**, 951 (1959).

[226] L. Levien, C. T. Prewitt, and D. J. Weidner, Am. Mineral. **65**, 920 (1980).

[227] S. Kimura, K. Iwamoto, M. Kadoshima, Y. Nunoshige, A. Ogawa, T. Nabatame, H. Ota, A. Toriumi, and T. Ohishi, *in Dielectric Films for Future ULSI Devices -Science and Technology*, (JSAP, Kawasaki, 2006), p. 126.

[228] K. Xiong, J. Robertson, M. C. Gibson, and S. Clark, J. Appl. Phys. Lett. **87**, 183505 (2005).

[229] H. D. B. Gottlob, M. C. Lemme, T. Mollenhauer, T. Wahlbrink, J. K. Efavi, H. Kurz, Y. Stefanov, K. Haberle, R. Komaragiri, T. Ruland, F. Zaunert, and U. Schwalke, J. Non-Cryst. Solids **351**, 1558 (2005).

[230] A. Dimoulas, A. Travlos, G. Vellianitis, N. Boukos, and K. Argyropoulos, J. Appl. Phys. **90**, 4224 (2001).

[231] Z. B. Fang, S. Chen, Y. Y. Zhu, Y. Q. Wu, Y. L. Fan, Y. Y. Wang, and Z. M. Jiang, Nanotechnology **18**, 155205 (2007).

[232] G. Scarel, E. Bonera, C. Wiemer, S. Spiga, M. Fanciulli, I. L. Fedushkin, H. Schumann, Y. Lebedinskii, and A. Zenkevich, Appl. Phys. Lett. **85**, 630 (2004).

[233] L. Edge, D. Schlom, R. Brewer, Y. Chabal, J. Williams, S. Chambers, C. Hinkle, G. Lucovsky, Y. Yang, S. Stemmer, M. Copel, B. Holländer, and J. Schubert, Appl. Phys. Lett. **84**, 4629 (2004).

[234] B. E. Park and H. Ishiwara, Appl. Phys. Lett. **79**, 806 (2001).

[235] B. E. Park and H. Ishiwara, Appl. Phys. Lett. **82**, 1197 (2003).

[236] X. B. Lu, X. Zhang, R. Huang, H. B. Lu, Z. H. Chen, W. F. Xiang, M. He, B. L. Cheng, H. W. Zhou, X. P. Wang, C. Z. Wang, and B. Y. Nguyen, Appl. Phys. Lett. **84**, 2620 (2004).

[237] Q. Y. Shao, A. D. Li, J. B. Cheng, H. Q. Ling, D. Wu, Z. G. Liu, N. B. Ming, C. Wand, H. W. Zhou, and B. Y. Nguyen, Appl. Phys. A **81**, 1181 (2005).

[238] P. Sivasubramani, M. J. Kim, B. E. Gnade, R. M. Wallace, L. F. Edge, D. L. Schlom, H. S. Craft, and J. P. Maria, Appl. Phys. Lett. **86**, 201901 (2005).

[239] J. Lettieri, J. H. Haeni, and D. G. Schlom, J. Vac. Sci. Technol. **A20**, 1332 (2002).

[240] J. I. Pankove, D. E. Carlson, J. E. Berkeyheiser, and R. O. Wance, Phys. Rev. Lett. **51**, 2224 (1983).

[241] A. H. Edwards, J. Non-Cryst. Solids **187**, 232 (1995).

[242] T. Vondrak and X. Y. Zhu, J. Phys. Chem. B **103**, 4892 (1999).

[243] W. Futako, T. Umeda, M. Nishizawa, T. Yasuda, J. Isoya, and S. Yamasaki, J. Non-Cryst. Solids **299-302**, 575 (2002).

[244] A. Stesmans and V. V. Afanas'ev, Appl. Phys. Lett. **77**, 1469 (2000).

[245] H. Hosono, M. Mizuguchi, H. Kawazoe, and T. Ogawa, Appl.Phys. Lett. **74**, 2775 (1999).

[246] T. Bakos, S. N. Rashkeev, and S. T. Pantelides, Phys. Rev. B **69**, 195206 (2004).

[247] Z. Y. Lu, C. J. Nicklaw, D. M. Fleetwood, R. D. Schrimpf, and S. T. Pantelides, Phys. Rev. Lett. **89**, 285505 (2002).

[248] L. Skuja, J. Non-Cryst. Solids **239**, 16 (1998).

[249] L. N. Skuja, A. N. Strelesky, and A. B. Pakovich, Solid State Commun. **50**, 1069 (1984).

[250] D. L. Griscom, J. Ceram. Soc. Jpn. **99**, 923 (1991).

[251] H. Hosono and R. A. Weeks, J. Non-Cryst. Solids **116**, 289 (1990).

[252] K. Awazu and H. Kawazoe, J. Appl. Phys. **68**, 3584 (1990).

[253] L. Skuja, M. Hirano, and H. Hosono, Phys. Rev. Lett. **84**, 302 (2000).

[254] L. Skuja, M. Mizugichi, H. Hosono, and H. Kawazoe, Nucl. Instrum. Methods Phys. Res. Sect. B **166-167**, 711 (2000).

[255] L. Skuja, B. Guttler, D. Schiel, and A. R. Silin, Phys. Rev. B **58**, 14296 (1998).

[256] R. A. Weeks and E. Sonders, *Paramagnetic Resonance*, volume 2, edited by W. Low (Academic press, N.Y., 1963), p. 869.

[257] R. A. Weeks, R. H. Magruder III, and P. W. Wang, J. Non-Cryst. Solids **149**, 122 (1992).

[258] S. Buscarino, G. Agnello and F. M. Gelardi, J. Non-Cryst. Solids **351**, 1801 (2005).

[259] H. Nishikawa, E. Watanabe, D. Ito, and Y. Ohki, J. Non-Cryst. Solids **174**, 179 (1994).

[260] R. H. Magruder III, R. A. Weeks, and R. A. Weller, J. Non-Cryst. Solids **322**, 58 (2003).

[261] R. H. Magruder III, R. A. Weeks, R. A. Weller, and R. Gaylon, J. Non-Cryst. Solids **345-346**, 284 (2004).

[262] R. H. Magruder III, R. A. Weeks, R. A. Weller, and R. Gaylon, J. Non-Cryst. Solids **351**, 1727 (2005).

[263] R. H. Magruder III, A. Stesmans, K. Clémer, R. A. Weeks, and R. A. Weller, J. Non-Cryst. Solids **352**, 3027 (2006).

[264] R. H. Magruder III, A. Stesmans, K. Clémer, R. A. Weeks, and R. A. Weller, J. Appl. Phys. **100**, 033517 (2006).

[265] J. G. Castle and D. W. Feldman, J. Appl. Phys. **36**, 124 (1965).

[266] R. A. Weeks, J. Non-Cryst. Solids **179**, 1 (1994).

[267] T. Purcell and R. A. Weeks, Phys. Chem. Glasses **10**, 198 (1969).

[268] R. B. Bossoli, M. G. Jani, and L. E. Halliburton, Solid State Commun. **44**, 213 (1982).

[269] R. A. Weeks and M. Abraham, Bull. Am. Phys. Soc. **10**, 374 (1965).

[270] D. L. Griscom and J. L. Friebele, Phys. Rev. B **34**, 7524 (1986).

[271] R. Tohmon, Y. Shimogaichi, Y. Tsuta, S. Munekuni, Y. Ohki, Y. Hama, and K. Nagasaka, Phys. Rev. B **41**, 7258 (1990).

[272] A. Stesmans, B. Nouwen, and K. Iakoubovskii, J. Phys.: Condens. Matter **12**, 7807 (2000).

[273] G. Pacchioni and G. Ierano, Phys. Rev. B **57**, 818 (1998).

[274] N. Richard, L. Martin-Samos, G. Roma, Y. Limoge, and J. Crocombette, J. Non.-Cryst. Solids **351**, 1825 (2005).

[275] H. Nishikawa, R. Tohmon, K. Nagasawa, and Y. Hama, J. Appl. Phys. **65**, 4672 (1989).

[276] M. Che and A. J. Tench, Adv. Catal. **32**, 1 (1983).

[277] L. D. Bogomolova, V. A. Jachkin, S. A. Prushinski, S. A. Dmitriev, S. V. Stefanovsky, Y. G. Teplyakov, F. Caccavale, E. Cattaruzza, R. Bertoncello, and F. Trivillin, J. Non-Cryst. Solids **210**, 101 (1997).

[278] M. Antonini, P. Camagni, P. N. Gibson, and A. Manara, Radiat. Eff. **65**, 41 (1982).

[279] L. D. Bogomolova, Y. G. Telpyakov, A. A. Deshkovskaya, and F. Caccavale, J. Non-Cryst. Solids **202**, 185 (1995).

[280] D. K. Stevens, W. J. Stur, and R. H. Silsbee, J. Appl. Phys. **29**, 66 (1958).

[281] K. Moritani, Y. Teraoko, I. Takagi, and H. Mariyama, J. Nucl. Mater. **329-333**, 988 (2004).

198

List of Publications

1. A. Stesmans, V. V. Afanas'ev, K. Clémer, F. Chen, and S. A. Campbell,
   Point defects and traps in stacks of ultra thin high-κ metal oxides on Si probed by electron spin resonance: the Si/HfO_2 system and N incorporation,
   Electrochemical Society Proceedings Volume **2005-01**.

2. A. Stesmans, K. Clémer, and V. V. Afanas'ev,
   Electron spin resonance probing of fundamental point defects in nanometer-sized silica particles,
   Phys. Rev. B **72**, 155335 (2005).

3. A. Stesmans, K. Clémer, and V. V. Afanas'ev,
   Are intrinsic point defects inadequate as origin of optical band gap narrowing in fumed silica nanoparticles?,
   J. Phys.: Condens. Matter **17**, L393 (2005).

4. A. Stesmans, K. Clémer, and V. V. Afanas'ev,
   Electron spin resonance probing of fundamental point defects in nm-sized silica particles,
   J. Non-Cryst. Solids **351**, 1764 (2005).

5. A. Stesmans, K. Clémer, and V. V. Afanas'ev,
   Electron spin probing of E'-type defects in fumed silica nanoparticles,
   Mat. Sci. and Eng. C **26**, 766 (2006).

6. R. H. Magruder, A. Stesmans, K. Clémer, R. A. Weeks, and R. A. Weller,
   Origins of optical absorption between 4.8 and 4.9 eV in silica implanted with Si or O,
   J. Non-Cryst. Solids **352**, 3027 (2006).

7. R. H. Magruder, A. Stesmans, K. Clémer, R. A. Weeks, and R. A. Weller,
   Sources of optical absorption between 5.7 and 5.9 eV in silica implanted with Si or O,
   J. Appl. Phys. **100**, 033517 (2006).

8. A. Stesmans, K. Clémer, V. V. Afanas'ev, L. F. Edge, and D. G. Schlom,
   Nature and stability of the (100)Si/LaAlO$_3$ interface probed by paramagnetic defects,
   Appl. Phys. Lett. **89**, 112121 (2006).

9. K. Beerten, J. Lomax, K. Clémer, A. Stesmans, and U. Radtke,
   On the use of Ti centers for estimating burial ages of Pleistocene sedimentary quartz: Multiple-grain data from Australia,
   Quaternary Geochronology **1**, 151 (2006).

10. A. Stesmans, V. V. Afanas'ev and K. Clémer,
    Probing point defects in stacks of ultrathin high-κ metal oxides on semiconductors by electron spin resonance: the Si/HfO$_2$ vs the Ge/HfO$_2$ system,
    Electrochemical Society Proceedings Volume **2006-01**.

11. K. Clémer, A. Stesmans, and V. V. Afanas'ev,
    Observation of a P-associated defect in HfO$_2$ nanolayers on (100)Si by electron spin resonance,
    Appl. Phys. Lett. **90**, 142116 (2007).

12. K. Clémer, A. Stesmans, and V. V. Afanas'ev, L. F. Edge, and D. G. Schlom,
    Analysis of the (100)Si/LaAlO$_3$ structure by electron spin resonance: nature of the interface,
    J. Mat. Sci. and Eng. **18**, 735 (2007).

13. A. Stesmans, K. Clémer, and V. V. Afanas'ev,
    Electron spin resonance observation of a P-associated defect in HfO$_2$ films on (100)Si,
    Microel. Eng. **84**, 2358 (2007).

14. K. Clémer, A. Stesmans, and V. V. Afanas'ev, L. F. Edge, and D. G. Schlom,
    Paramagnetic point defect in (100)Si/LaAlO$_3$ structures: nature and

stability of the interface,
J. Appl. Phys. **102**, 034516 (2007).

15. K. Clémer, A. Stesmans, and V. V. Afanas'ev,
Paramagnetic intrinsic point defects in nm-sized silica particles: Interaction with SiO at elevated temperatures,
Mat. Sci. and Eng. C **27**, 1475 (2007).

16. A. Stesmans, K. Clémer, P. Somers, V. V. Afanas'ev,
Probing semiconductor/insulator heterostructures through electron spin resonance of point defects: Interfaces, interlayers, and stress,
Material Research Society Proceedings Fall meeting 2006 (*in print*).

17. A. Stesmans, K. Clémer, V. V. Afanas'ev,
The E′ center as a probe of structural properties of nanometer-sized silica particles,
J. Non-Cryst. Solids (*submitted*).

18. K. Clémer, A. Stesmans, and V. V. Afanas'ev,
P-associated defects in the high-κ HfO_2 and ZrO_2 insulators revealed by electron spin resonance,
Phys. Rev. B (*submitted*).

19. K. Clémer, A. Stesmans, and V. V. Afanas'ev,
The primary ^{29}Si hyperfine structure of E′ centers in nm-sized silica: probing of the microscopic network structure,
Phys. Rev. B (*submitted*).